Doctoral Thesis

A laboratory study of fluid-driven tensile fracturing in anisotropic rocks

Submitted in partial fulfilment of the requirements

for the award of the degree of

Doctor of Philosophy

of the University of Portsmouth

by

Stephan Gehne

Portsmouth, July 2018

Abstract

Fluid-driven tensile failure is a ubiquitous phenomenon in Earth sciences, as seen in examples ranging from dyke and sill injection in volcanic systems to veining and mineralisation. In the engineered environment, the method has recently been used for the intentional hydraulic fracture of water and hydrocarbon reservoirs. This has allowed the exploitation of previously uneconomic reservoirs by generating tensional fracture networks for enhanced permeability, but with the side effect of generating small earthquakes in the process. This has made the application of the technology controversial, as it generates a clear inherent risk. Although this industrial application has proven itself, it has developed in a largely uncontrolled trial-and-error approach and with little regard to the fundamental science behind the process. This is important, as to understand and predict the fracture process, the various controlling factors must be known, which is challenging in a natural environment. To address some of these gaps in knowledge, this study has developed a novel laboratory-based method to simulate the fluid-mechanical process of hydraulic fracturing. New data are presented that illustrate the combined effects of the inherent rock anisotropy, fabric and initial permeability, and how this is manifested in terms of tensile fracture initiation, propagation and geometry. To achieve this, a new apparatus to generate fluid-driven tensile fractures using a conventional triaxial cell (providing simulated burial depth) is developed. Rock physics data from the experiments (Acoustic Emission, radial strain and fluid pressures) recorded at high speed are combined with post-test micro X-ray CT imaging. For the first time, the generation and propagation of fluid-induced hydraulic fractures is made with respect to the initial rock fabric, and then linked to the generated Acoustic Emission, for direct comparison to field seismicity.

Fracture orientation is primarily controlled by the principal stresses and their orientation relative to bedding planes. However, inherent rock anisotropy, initial rock permeability and rock fabric are key controlling factors in governing fracture initiation, propagation, and fracture geometry. It has been shown that anisotropy and initial permeabilities affect fracture initiation and can lead to increased or premature failure pressures respectively. Fracture geometry strongly depends on the orientation of the inherent bedding, determining if fractures propagate parallel or normal to the bedding, and the rock fabric, resulting in planar or more tortuous fracture paths. By linking Acoustic Emission and mechanical behaviour with respect to the final fracture network, the hydraulic fracture process is decoded into distinct fracture stages: (i) maximum fluid pressure, (ii) a short period of ‘plastic’ deformation, (iii) fracture initiation, (iv) stable fracture propagation, (v) sample breakdown and finally (vi) unstable fracture propagation. This analysis shows that a combination of seismic activity, fluid injection rates and deformation are reliable indicators for imminent breakdown in anisotropic

sedimentary rocks subjected to injection fluid pressures, a critical step towards the development of an updated, engineered approach to hydraulic fracturing in an effort to reduce risks, increase controllability and to optimise gas extraction. Finally, the incremental fracture process is analysed and related to the fracture toughness (K_{IC}) using fracture energy as a proxy to show that fracture extension only occurs when fluid-driven stress increases beyond K_{IC}, whereas fracture initiation is controlled by the tensile strength. Ultimately, relating fracture behaviour in unconventional resource lithologies to induced seismicity and key mechanical and fluid injection parameters may provide for better fracture prediction during field operations, reducing the risk and improve resource exploitation.

Declaration

Whilst registered as a candidate for the above degree, I have not been registered for any other research award. The results and conclusions embodied in this thesis are the work of the named candidate and have not been submitted for any other academic award.

Word count: 65486

Acknowledgements

"It's not an experiment if you know it's going to work." (Jeff Bezos)

Fortunately, I did not count the number of experiments that did not work, but I have the slight suspicion that I am still not even. It has been a long way to get to this point and I have to thank many people who made this journey possible and most importantly, enjoyable.

Most of all, I thank Katharina Piche and Phil Benson for their endless support throughout the entire time. Kat was the important and healthy counterpart to the laboratory world, which kept me sane and always going. Especially over the last four months, her support was amazing; she accepted my mess in our living room and endured my grumpy phases without complaints.

I huge thanks to Phil for his endless support and enthusiasm, for all the guidance and all the time and effort to support and read paper drafts, posters and fellowship applications and to discuss designs, experiments and lots of other great ideas.

I thank Nick Koor and Mark Enfield, second and third supervisor, for their support and many helpful discussions throughout the project, which raised the quality of the project and my knowledge. I would like to thank past and present laboratory members, Marco, Pete, Ricardo and Emily for all the help in keeping the equipment running and making the laboratory a comfortable and enjoyable place to work in. I thank Nathaniel Forbes Inskip and Phil Meredith for a great collaboration and for introducing me to Nash Point Shale. A big thanks to Nathaniel, who, on several occasions, shared with me the load of massive shale blocks to carry them to the car, which was parked way too far away.

I am grateful for the support from Janet, Carol, Wendy, Sue and Mike in the SEES-Admin office, who made my life easier countless times, and the technical staff Geoff, Joe, James, Elaine, Zoe, Richard and Sue for all the support and providing help whenever needed. I also thank Rob, Geoff, Alex and Rachna from the Mechanical Department for introducing me into the world of micro CT imaging and helping me with many mechanical issues. I owe a huge thanks to Kate Dobson, for all her effort and time to help me with the analysis of the micro-CT data.

Just as important for this thesis was all the support from outside the University. I am indebted to my parents and to Kevin, Conny, Max, Sören, Frank, Sabine, Marie and Herbert for their endless support and encouragement and the refreshing retreats to Germany and Canada. I also thank Brandon and Charlie for their support and all the enjoyable evenings, where I could forget the project over a nice dinner and a pint. Furthermore, I thank Christie and Danny, who became great friends and running buddies.

Although there is only my name on the cover page (they do not allow multiple cover pages for all the names), this thesis has been a team effort and I am very thankful for all the support and help from everyone.

Contents

List of Tables

List of Figures

List of symbols and abbreviations

Abbreviations

AE	Acoustic Emission (laboratory seismicity)
Arr	Arrester
BSE	Back Scatter Electron
COS	Crab Orchards Sandstone
Div	Divider
HF	Hydraulic fracturing (field)
ITS	Indirect Tensile Strength
LEFM	Linear Elastic Fracture Mechanics
LP	Long-Period seismic events
MHF	Micro Hydraulic Fracturing (laboratory)
Micro-CT	X-ray Micro Computed Tomography
NPS	Nash Point Shale
SEM	Scanning Electron Microscope
SE	Secondary Electron
S-T	Short-Transverse
VT	Volcano-Tectonic earthquakes
Suffix ‘x’	indicates that bedding is parallel to sample axis
Suffix ‘z’	indicates that bedding is normal to sample axis

Symbols

Latin characters

Symbol	description
A	Surface area of the sample (m^2),
a	fracture (half-) length (mm)
a_0	initial fracture (half-) length (mm)
AE_0	onset of increased AE activity
b_s	gas slippage factor
c	cohesion (MPa)
C_m	rock matrix compressibility
C_b	rock bulk compressibility
D	sample diameter (mm)
eK_{IC}	effective fracture toughness for mode I (Pa√m)
G	strain energy release rate or crack driving force
G_C	critical strain energy release rate
$K_{(I,II,III)}$	mode I,II,III stress intensity factor (Pa√m)
$K_{(I,II,III)C}$	mode I,II,III critical stress intensity factor or fracture toughness (Pa√m)
L	sample length (mm).
M_{sat}	mass of the saturated sample (g)
M_d	mass of the oven-dried sample (g)
$maxAE$	peak acoustic emission activity (hits/s)
$maxP_{inj}$	maximum fluid injection pressure recorded (MPa)
P	applied load (MPa)
P_b	breakdown pressure re in the borehole (MPa)
P_c	confining pressure
P_d	downstream Pressure (MPa)
P_{eff}	effective pressure (MPa)
P_{frac}	fluid pressure inside the fracture (MPa)
P_{mean}	mean core pressure (MPa)
P_{inj}	fluid injection pressure (MPa)
P_{max}	maximum applied load or force (peak load) (MPa)
P_p	pore pressure (MPa)
P_{rd}	fluid pressure starts to decrease rapidly, unstable fracture
P_u	upstream Pressure (MPa)
Q	Volume flow rate (flow velocity) (m^3/s),
q	Fluid flux (Darcy's velocity) (m/s)

r	radial distance from the centre of the hole (mm)
r_i	inner diameter of sample (diameter of conduit) (mm)
r_o	outer diameter of sample (mm)
rDef	onset of radial deformation
T	tortuosity
t_P	P-wave travel time (s)
U	strain energy
V_b	bulk volume (m^3)
V_p	compressional elastic wave velocity (m/s)
W	specimen width (mm)

Greek characters

Symbol	description
α	Biot's poroelastic coefficient
α_{eff}	effective stress coefficient
β	angel of the crack plane with σ_H
γ_s	unit crack surface energy (elastic surface energy)
γ_p	plastic work per unit area of surface created (plastic surface energy)
Δa	extension in crack length (mm)
ΔP	Pressure gradient (MPa)
E	Young's Modulus (GPa)
ε_a	axial strain
ε_r	radial strain
κ	Permeability (m^2)
κ_L	liquid permeability (m^2)
κ_∞	Klinkenberg-corrected permeability (at infinite mean pressure)
μ	fluid viscosity (mPa.s)
μ	coefficient of internal friction
ρ_s	grain density (g/cm^3)
ρ_w	density of water (g/cm^3)
σ'	effective principal stresses / pressure (MPa)
σ_1	maximum principal stress (MPa)
σ_3	minimum principal stress (MPa)
σ_c	uniaxial compressive strength (MPa)
σ_H	maximum horizontal stress (MPa)

σ_h	minimum horizontal stress (MPa)
σ_n	normal stress (MPa)
σ_r	radial stress (MPa)
σ_{rr}	effective radial stress (MPa)
σ_T	tensile strength (MPa)
σ_v	vertical principal stress (MPa)
σ_θ	tangential stress (MPa)
$\sigma_{\theta\theta}$	effective tangential stress (MPa)
τ	shear stress (MPa)
τ_0	shear strength at zero normal stress (MPa)
$\tau_{r\theta}$	shear stress component (MPa)
υ	Poisson's ratio
ϕ	porosity (%)
ϕ_T	Total porosity (%)
ϕ_i	internal friction angle (°)

Disseminations

Peer reviewed journal publications

Gehne, S. & Benson, P.M., 2017. Permeability and permeability anisotropy in Crab Orchard sandstone: Experimental insights into spatio-temporal effects. *Tectonophysics*, 712–713, 589-599

In peer review

Gehne, S., Benson, P.M., Koor, N., Dobson, K., Enfield, M. & Barber, A. (submitted May 2018). Seismo-mechanical response of anisotropic rocks under simulated hydraulic fracture conditions: new experimental insights. *Geology.*

Conference presentations

Gehne, S., Benson, P.M., Koor, N., Dobson, K., Enfield, M. & Barber, A., 2017, Hydro-fracture in the laboratory: matching diagnostic seismic signals to fracture networks (Poster). *AGU Fall Meeting 2017*, New Orleans, USA,

Gehne, S., Benson, P.M., Koor, N. & Enfield, M., 2017, Fluid-driven fracture mechanics in highly anisotropic rocks: a laboratory study with application to hydraulic fracturing (Talk). *EGU General Assembly 2017*, Vienna, Austria

Gehne, S., Benson, P.M., Koor, N. & Enfield, M., 2017, Seismicity induced through fluid-driven fracturing in highly anisotropic rocks (Poster). *Schatzalp – 2nd Induced Seismicity Workshop*, Davos, Swiss

Gehne, S., Benson, P.M., Koor, N. & Enfield, M., 2017, Fluid-driven fracture mechanics in highly anisotropic rocks: a laboratory study with application to hydraulic fracturing (Talk). *Joint Assembly VMSG, TSG and BGA 2017*, Liverpool, UK

Gehne, S., Benson, P.M., Koor, N. & Enfield, M., 2016, Investigation of the fracture mechanics behaviour of the fluid-driven mechanical fracture process in a highly anisotropic shale (Poster). *Extractive Industry Geology Conference 2016*, Birmingham, UK

Gehne, S. & Benson, P.M., 2015, The effect of inherent and induced anisotropy on geomechanical rock properties in mudrocks (Talk). *Geomechanical and Petrophysical Properties of Mudrocks*, Workshop, The Geological Society, London, UK

Gehne, S., Benson, P.M., Koor, N. & Enfield, M., 2015, Hydraulic fracturing – Simulation in the laboratory (Poster). *EURO conference on Rock Physics and Geomechanics 2015*, Ambleside, UK

Gehne, S. & Benson, P.M., 2014, Permeability Hysteresis in tight, anisotropic rocks (Poster). *The challenge of studying low permeability materials: Laboratory, in situ (field) and numerical methods*, Workshop, Paris, France

Scholarships and bursaries

- Extractive Industry Geology (EIG) Scholarship, 2015
- Schatzalp Travel Fellowship, 2017
- TSG Travel Bursary, 2017

1 Introduction

1.1 Unconventional Resource Reservoirs

Hydrofracturing is a common process in many areas of pure and applied geosciences, such as magma and dyke intrusions (e.g. Rubin, 1993; Tuffen and Dingwell, 2005), the development of mineral veins (e.g. Gudmundsson and Brenner, 2001) and the intentional hydraulic fracturing of impermeable rock formations in the hydrocarbon and geothermal energy industries (e.g. Bennion et al., 1996; Vinciguerra et al., 2004; Wang et al., 2014). Especially in the exploitation of unconventional hydrocarbon resources, hydraulic fracturing has become a common and critical technique for oil and gas reservoir stimulation to produce hydrocarbons economically from low permeability rock formations (Zoback et al., 1977; Stanchits et al., 2011; Gandossi, 2013). This technique enabled one of the biggest and most influential (and controversial) developments in the energy sector in recent years; the exploitation of "unconventional reservoirs" loosely defined as sedimentary formations that are too low in porosity or permeability to extract hydrocarbons by using a conventional well. By intentional creating new porosity and increasing permeability, the extraction of hydrocarbons (both oil and gas), from unconventional reservoirs has transformed the US energy landscape resulting in the growth of total natural gas and oil production (Wang et al., 2014). Unlike conventional reservoirs of sandstone or carbonate formations, which are usually buoyancy-driven deposits occurring as discrete accumulations in structural and/or stratigraphic traps (Law and Curtis, 2002) (Figure 1-1), unconventional reservoirs have a very low permeability ($<20 \times 10^{-15}$ m^2) and are frequently composed of shale and occasionally, tight (cemented) sandstone and carbonate rocks.

Although there is no sharp boundary between conventional and unconventional reservoirs, unconventional reservoirs are frequently described by their characteristics based on permeability and their compositions that might suggest trapped pockets of hydrocarbon. In general, sedimentary rock formations containing hydrocarbon resources with a permeability below 0.1mD are commonly classed as unconventional reservoirs (Lee and Hopkins, 1994) (Figure 1-2).

Due to this low permeability, unconventional reservoirs are not economic unless the well is stimulated to enhance permeability and expose more of the reservoir to the wellbore (Boyer et al., 2011). Furthermore, unconventional reservoirs are also characterised by a petroleum system and fluid trapping mechanism, unlike conventional reservoirs here the source rock may also act as the reservoir rock with the potential for hydrocarbon resources to extend across large areas of the basin (Figure 1-1). Due to this, there are several different types of

unconventional hydrocarbon resources depending on the hydrocarbon type and the rock formation: (1) Shale gas is defined as natural gas of biogenic or thermogenic origin formed and stored in a fine-grained, organic-rich shale, which is source rock and reservoir rock at the same time. The gas can be stored in pores and fractures, or accumulated on the surface of organic particles in a shale reservoir (Jarvie, 2012a). (2) Tight gas or oil are hydrocarbon resources produced from very low permeability rock formations (generally lithologies such as highly cemented/tight sandstone and limestone), that must be stimulated to create sufficient permeability to allow natural gas or oil liquids to flow at economic rates (Boyer et al., 2011). These tight rock formations act as reservoir rock only with hydrocarbons migrating from a separate source rock into the reservoir over time. (3) Shale oil has been generated *in-situ* in organic-rich mudstones or shales and is stored in these organic-rich intervals or juxtaposed, continuous organic-lean intervals (Jarvie, 2012b). (4) Coal-bed methane, which is natural gas formed during coal formation and is adsorbed to the surface of matrix pores within the coal or natural fractures due to increased reservoir pressures (Wang et al., 2014). (5) Natural gas hydrates are methane molecules stored within a crystal structure, typically ice or water, and formed under high pressures and low temperatures in permafrost zones and deep water (Wang et al., 2014). Following the success in the US, many other countries such as China, South Africa, Australia (Warner, 2011), Poland, Ukraine, Germany (Andruleit et al., 2012), France, Sweden and UK (Andrews, 2013) have evaluated their natural shale gas resource potential (Lechtenböhmer et al., 2012; Kuuskraa et al., 2013; Wang et al., 2014). Countries worldwide with potential for shale gas resources and estimates of technically recoverable shale gas resources across the globe are shown in Figure 1-3.

The discovery of considerable volumes of hydrocarbon resources within tight sedimentary rock formations in the UK, with large volumes of Carboniferous strata in the Midlands and in the Jurassic strata of the Weald Basin (Selley, 2012) (Figure 1-4), has led to a resurgence of interest on the fundamental fracture properties of shale

However, this poses a new challenge. Although the large scale process has proven itself, it has developed in a trial-and-error approach, especially in the USA. Here, high pressure water is injected into the formation generating new families of fractures in a relatively piecemeal fashion, and with little regard to the fundamental science behind the process. This is a critical gap in our knowledge. In this study, a new controlled laboratory method has been designed, and used to fracture samples of shale under controlled conditions. For the first time, this holistic rock physics approach links the fundamental fracture mechanics of the rock to key parameters of fluid pressure/injecting rate, and with respect to the applied confining pressure.

Most importantly, by encapsulating the specimen in a purpose designed engineered rubber jacket fitted with eleven ports for Acoustic Emission sensors (the laboratory analogue to tectonic earthquake activity), the fluid-mechanical data are evaluated through the seismicity generated by the tensile fracturing. This is an important addition, as in the field, local earthquakes (magnitude 2.3 and 1.5) have previously been recorded during fracture stimulation near Blackpool, Lancashire (UK). This may have been enhanced by the structural complexity of UK shale basins, which typically comprise a series of small fault-bounded sub-basins. Unlike many shale gas formations in North America which have a relatively simple sub-horizontal structure, those in the UK (and in Europe generally) are often folded and faulted on a variety of scales (e.g. Jackson and Mulholland, 1993). Those of Carboniferous age show an especially complex structure, due to an extended history of geological deformation spanning 300 million years. In April 2018, the drilling company Cuadrilla completed the first horizontal shale gas well in the UK with a depth of 2,700 metres and lateral extension of 800m through a gas-rich area beneath its site off Preston New Road, near Blackpool. This well explores the West Bowland Sub-basin where up to 2 km of gas-bearing organic-rich shale has been confirmed (Kuuskraa et al., 2013). And in July 2018, Cuadrilla has been granted the final consent for exploitation by the UK government. The main stratigraphic targets for shale exploration in the UK are the Carboniferous Mississippian (Early Namurian), the Upper Jurassic Kimmeridge and the Lower Jurassic Lias formations, all of which contain organic-rich, marine-deposited shales (Figure 1-5) (Kuuskraa et al., 2013; Harvey and Gray, 2013; Hough et al., 2014).

The deposition of these organic-rich shales is associated with global sea level changes at periods of global high levels (Hough et al., 2014). The early Numerian shales, including the Bowland shale, are found in the Carboniferous Pennine Basin which includes several sub-basins such as Bowland, Cleveland, Cheshire, West Lancashire, Northumberland, East Midlands, Gainsborough, and Midland valley (Figure 1-4). The prospective Kimmeridge and Lias formations contain oil-prone shale and are highly probable for shale oil development (Kuuskraa et al., 2013). They are located in the Wessex and Weald basins in southern England (Figure 1-4). The technically recoverable shale resources of the UK are estimated at 26 Trillion cubic feet (tcf) of shale gas (Figure 1-3) and 0.7 billion barrels of shale oil, where 96% of the shale gas are assumed to be located in the Carboniferous shale region in northern England (Kuuskraa et al., 2013; Andrews, 2013). Based on a 1.6Tcf annual gas consumption in the UK (National statistics, Department for Business, Energy and Industrial Strategy, 2018) this resource would provide Britain with energy for about 16 years.

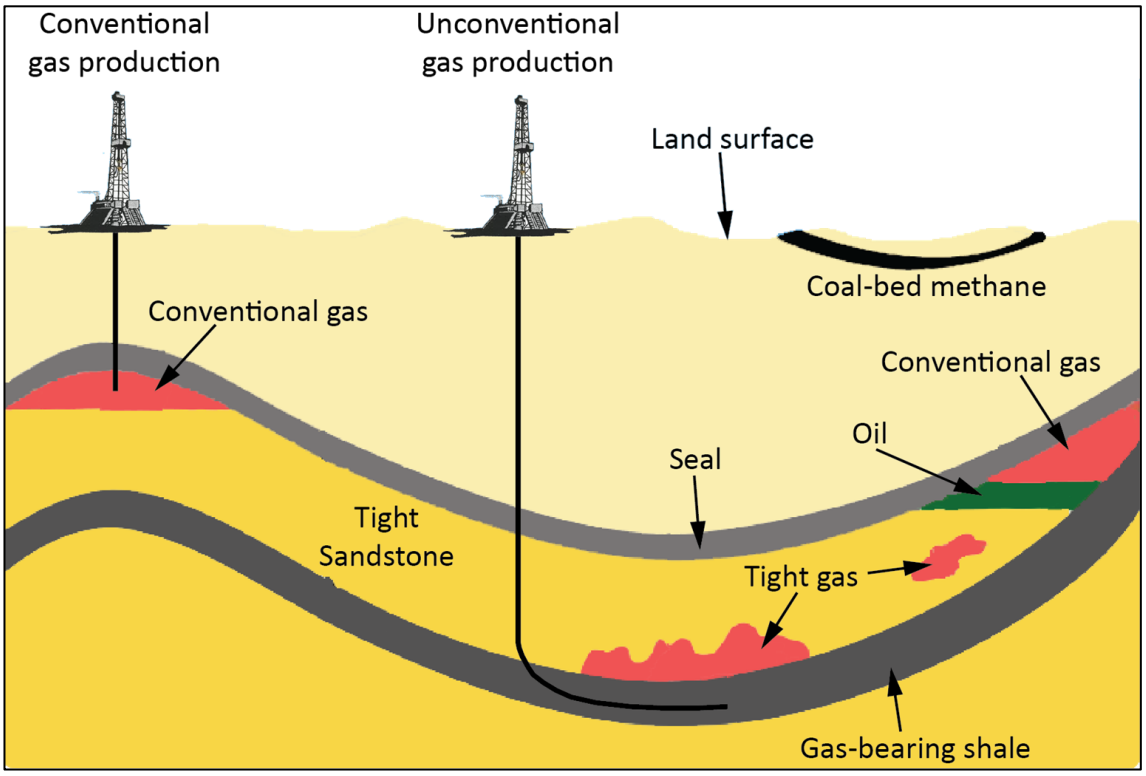

Figure 1-1: Schematic of conventional and unconventional resources (Source: EIA US Energy Information Administration)

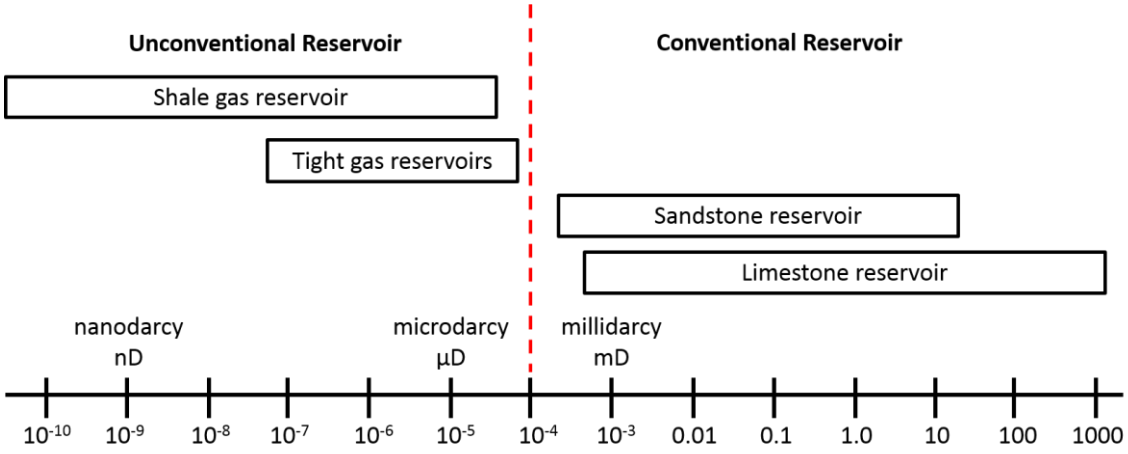

Figure 1-2: Unconventional and conventional reservoirs defined by permeability. Modified from Navarette et al. (2013).

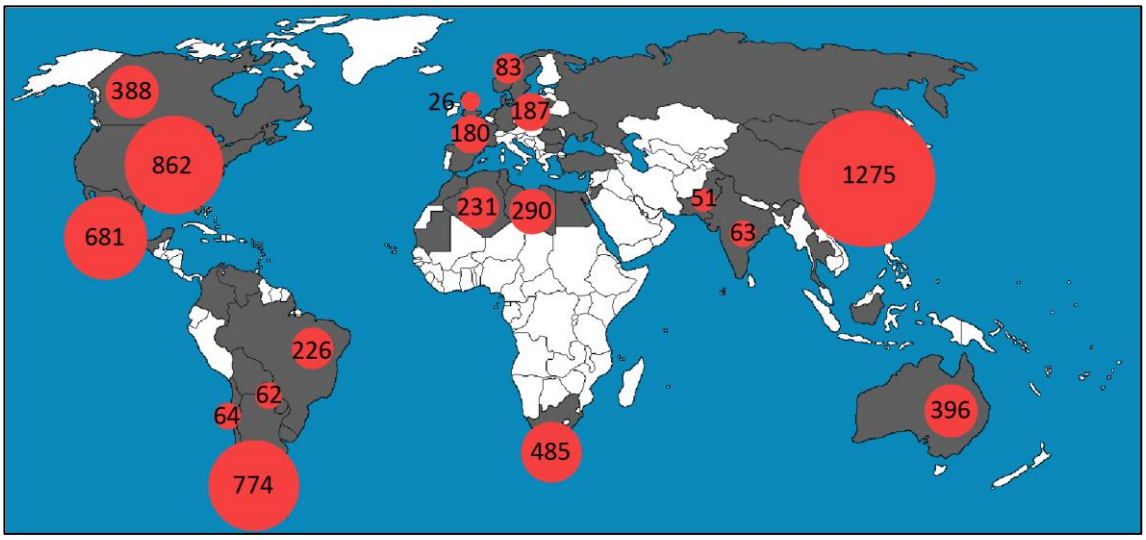

Figure 1-3: Estimates of technically recoverable shale gas resources (trillion cubic feet) (red circles); countries with potential for shale gas resources are highlighted in grey. Data from Kuuskraa et al. (2013).

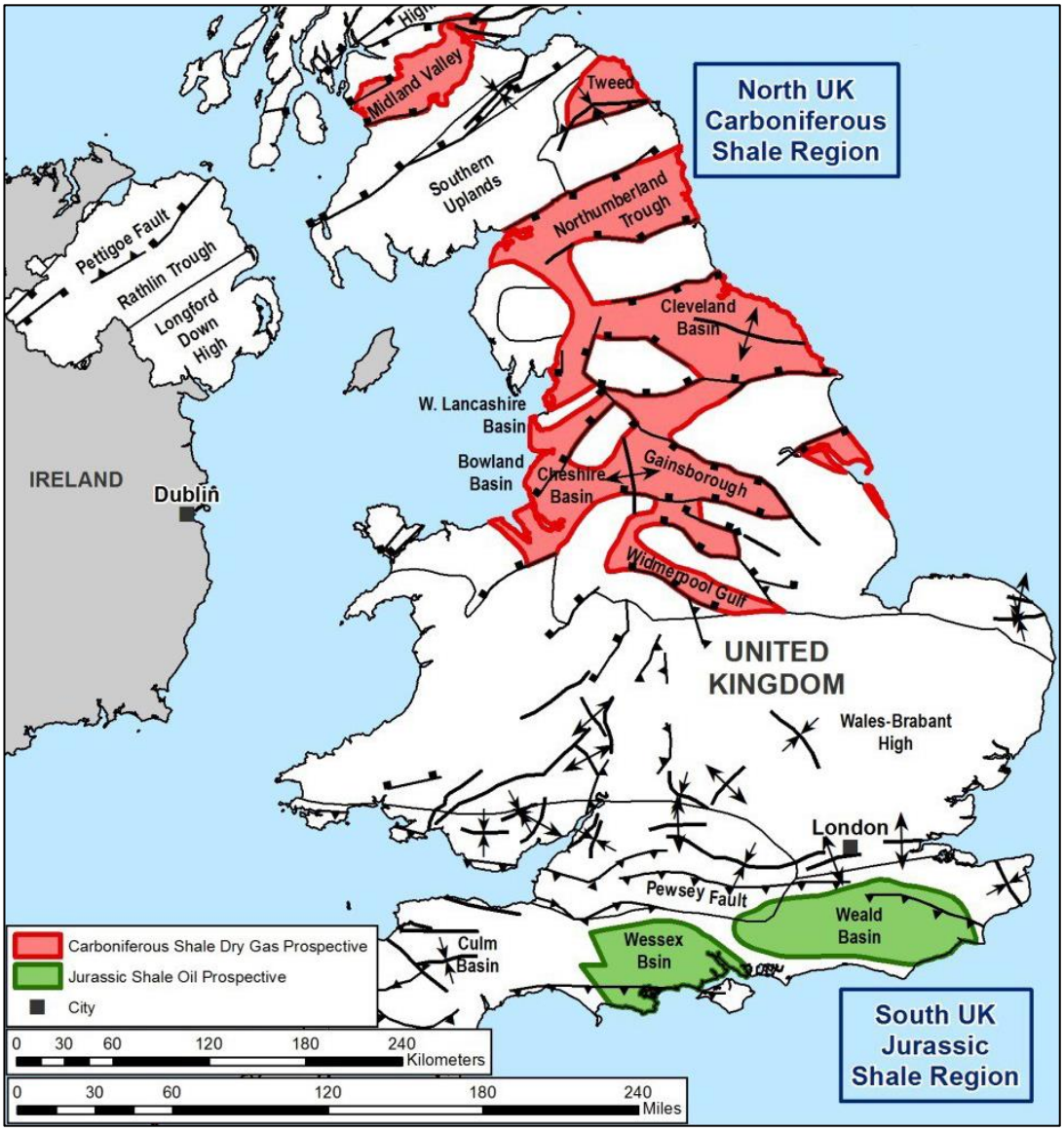

Figure 1-4: Shale basins in the UK. Image from Kuuskraa et al. (2013).

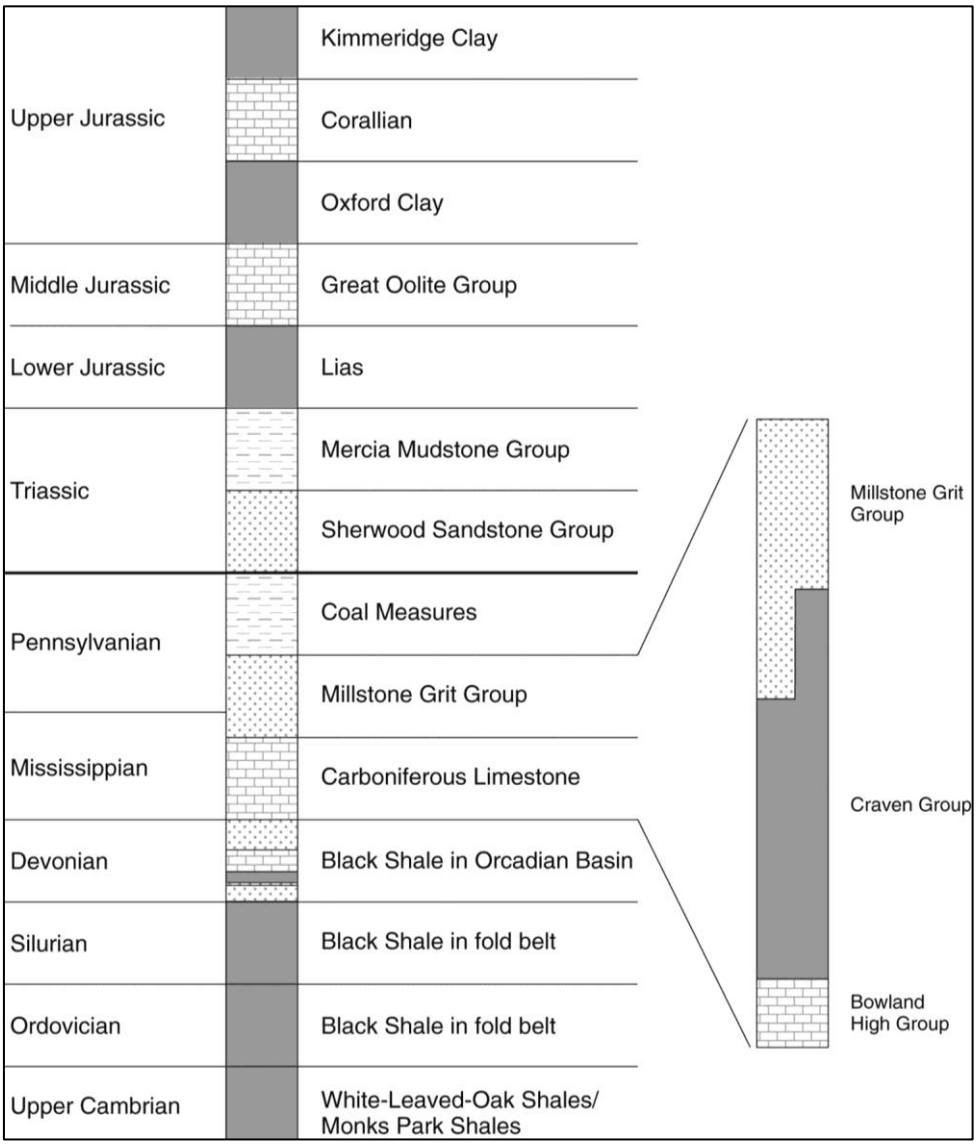

Figure 1-5: Stratigraphic column showing UK formations that contain organic-rich shales. From Smith et al. (2010).

1.2 Stimulation of Shale Gas Reservoirs

During hydraulic fracturing stimulation, fluid is pumped into a wellbore at rates higher than the radial fluid flow into the surrounding rock, which is a function of the permeability of the rock mass. This leads to a pressure build up inside the borehole until the pressure is sufficient to induce new fractures at the borehole wall and/or to re-open and/or further propagate pre-existing discontinuities. Fractures extend until the rate of fluid loss into the formation exceeds the pumping rate (Reinicke et al., 2010) and create a high-conductivity pathway and a larger surface area in contact with the reservoir in order to extract pore fluids. The first hydraulic fracturing treatment experiments for stimulation were performed in the Hugoton gas field in Kansas in 1947 by Stanolind Oil. In 1949, Halliburton Oil Well Cementing Company performed the first commercial fracturing treatment in Oklahoma and Texas and within the first year,

about 330 wells were treated, increasing the production by 75%. During the 1950's, the application of hydraulic fracturing increased rapidly to up to 3,000 wells per month (Montgomery and Smith, 2010). However, the commercial breakthrough of hydraulic fracturing was only realised due to key technological advances such as horizontal drilling, new hydraulic fracturing fluids and multi-stage fracturing methods.

Technology advance in hydraulic fracturing

Whereas vertical wells access tens or hundreds of meters of a flat lying formation, horizontal wells extend the range of fracturing sideways along the targeted rock formation to thousands of meters. Furthermore, horizontal wells reduce the number of drilling pads, reducing the surface disturbance, and are able to reach areas where vertical wells cannot (Vidic et al., 2013). Significant technological improvement in drill bit technology, top-drive drilling rigs and steerable motors and rotary systems, as well as azimuthal real-time logging-while-drilling imaging to prevent unexpected drilling events and a more effective steering made horizontal wells more economical by the late 1990's (Jennings, 2011; Dusseault, 2013). Another key factor was the use of "slick" water as a fracturing fluid; this is a low viscous mixture that could be rapidly pumped down a well to deliver a much higher fluid pressure to the rock than before and allows the pumping of high volumes of proppant at low concentrations. Furthermore, these low viscosity fluids create a more efficient fracture network and reduce the risk of blockages within the fracture (Gandossi, 2013). The third important advance was the application of multi-stage fracturing, with up to 60 stages, significantly increasing the surface area of the fracture and allowing gas extraction from a much larger volume of rock (Montgomery and Smith, 2010). Finally, 3D seismic imaging has contributed by enabling cost-effective but detailed analysis of new gas development regions to develop a detailed geological understanding, including the presence of faults and natural fractures, characterise reservoirs and extract seismic-derived properties such as stress maps to support drilling and surface infrastructure planning (Jennings, 2011).

The full industrial, field-based hydraulic fracturing process consists of several stages, which can vary between different sites (Cuss et al., 2015):

(1) Drilling of the well and installation of a production casing, to protect the surrounding lithologies.
(2) The casing is perforated at the desired position (within the gas bearing formation) and a section of the well is isolated.
(3) The isolated section is then stimulated by creating a network of cracks via high pressure fluid injection, which is the process of hydraulic fracturing. Proppants in the fluid (e.g. sand) remain in the new fractures to keep them open after the stimulation process.

The perforation and stimulation procedure might be repeated several times along the horizontal well. Finally, the well is depressurised, which creates a pressure gradient and gas starts to flow out of the rock into the well. An overview of the process is given in Figure 1-6.

1.3 Microseismicity during hydraulic fracturing

Microseismicity surrounding hydraulic fractures during multistage horizontal fracturing has been well documented (e.g. Pearson, 1981; Rutledge and Phillips, 2003; Warpinski et al., 2012; Eaton et al., 2013; Hurd and Zoback, 2012). Several studies investigated the seismic characteristics of these microseismic events and have reported the occurrence of long-period seismic events and "tremor-like" events in various reservoirs during hydrofracture (Das and Zoback, 2011; Mitchell et al., 2013; Kumar et al., 2016; Bame and Fehler, 1986; Ferrazzini et al., 1990). Despite differences in the duration, amplitude and frequency, Kumagai and Chouet (2000) recognized the similar characteristics of the hydraulic fracturing long-period events and long-period events and tremors associated with magmatic and/or hydrothermal fluid injection beneath volcanoes, which is plausible as in both cases fluid is injected into a rock, fracture or fracture system. In the field of volcano seismology, the analysis of such low frequency microseismicity already has an extensive literature. Here, seismic signals associated with volcanic activity and their seismic signatures have been studied (e.g. Chouet, 2003) linking fluid-mechanical seismic events with significant long-period and tremor activity (Chouet, 1996). In volcanic seismology, signals are further separated into two main families; (1) volcano-tectonic earthquakes (VT), representing brittle response of the rock, and (2) long-period events (LP) and tremors, representing volumetric sources driven by pressure disturbances associated with fluid flow (Kumagai and Chouet, 2000). LP earthquake events are characterised by an emergent high frequency onset, followed by a harmonic monochromatic coda, similar to that of a tremor, which consist of continuous harmonic vibrations (Chouet, 1996). To investigate the source mechanism of both LP and tremor, Chouet (1988) used the fluid filled crack model originally proposed by Aki et al. (1977). This model considers a perturbation of a fluid-filled crack which resonates, generating a slow wave propagating along the crack wall due to the abrupt impedance contrast at the rock-fluid interface, and demonstrating a likely link between pressure perturbations, fluid flow, and long-period seismicity.

Das and Zoback (2011) investigated a series of hydraulic-LP events similar to tectonic tremor sequences observed in subduction zones and fault boundaries. These events were recorded during passive seismic monitoring of a multi-stage hydraulic fracturing field experiment in the Barnett Shale in Texas and lasted for 10-100 seconds with the main energy in the frequency band 10-80Hz. LP events were also observed during a multi-stage fracture simulation in the

Cardium formation in west central Alberta, Canada (Das and Zoback, 2013) and during a study in the Canadian Montney gas reservoir (Eaton et al., 2013), although with lower energy and in lower numbers compared to those identified in the Barnett shale. More evidence for the link between hydraulic fracturing and seismicity was seen in Marcellus Shale in Greene County, Pennsylvania where the maximum rate of hydraulic-LP signals occurred when pumping pressure and rate were at maximum values (Kumar et al., 2016). Hydraulic-LP events in the Eagle Ford Shale were located close to the hydraulic treatment well, migrating away from the well with time (Hu et al., 2017). This suggested that the long-period events are associated with the hydraulic fracturing and possibly caused by the "jerky" opening and resonance of fluid filled cracks. All this field evidence shows that hydraulic fracturing is a complex fluid-mechanical process that generates a potentially diagnostic micro-seismic response. By better understanding this seismo-fluid-mechanical effect (e.g. slow slip along large or local faults, resonance of fluid filled cracks, fluid movement), a better understanding of the deep process may be derived, and hence contribute to improved safety and efficiency.

Importantly, seismic events associated with fluid movement have also been recorded in the laboratory when studying volcanic seismicity (Benson et al., 2008, 2010; Fazio et al., 2017). The events showed similar characteristics to the ones recorded in the field; an impulsive onset and a long low frequency coda (Benson et al., 2010; Fazio et al., 2017). Therefore, a new experimental design for combined fluid-driven tensile fracturing and combined with laboratory seismicity (Acoustic Emission) provides an opportunity to calibrate field operations and help to understand the fracturing process during hydraulic fracturing, by creating a detailed geophysical image of tensile fracture nucleation and growth in anisotropic rocks. The laboratory experiment will generate data that will help to develop our understanding of fracking in the field, and how induced seismicity can be used to better understand the process of hydraulic fracturing.

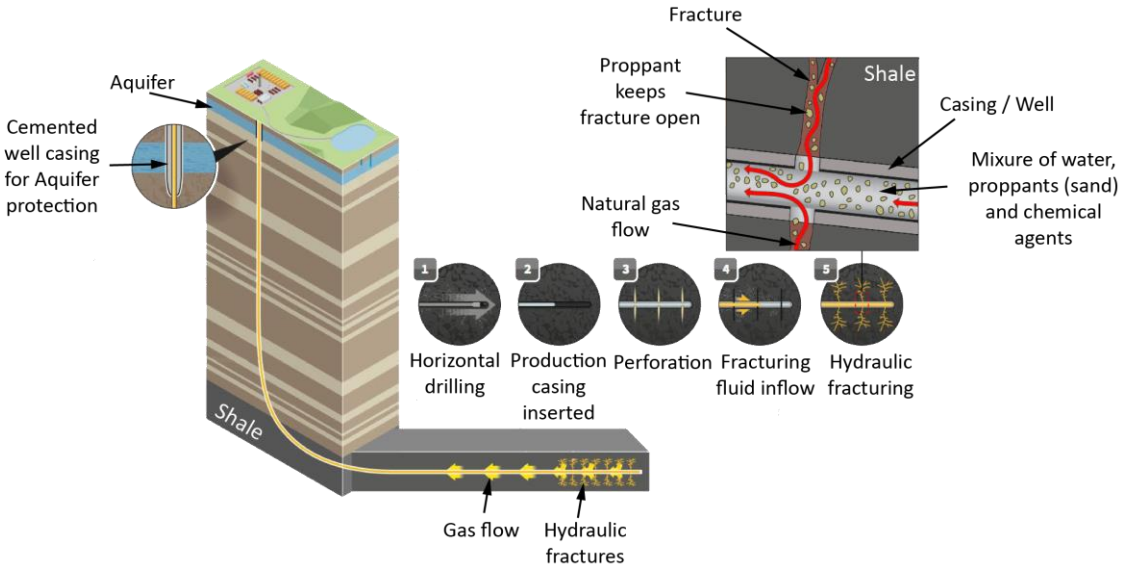

Figure 1-6: Schematic of hydraulic fracturing process for natural gas extraction from an unconventional shale reservoir; (1) the well is drilled horizontally once the targeted strata is reached, (2) production casing is inserted into the borehole and surrounded by cement, (3) perforation gun or explosives are detonated, which creates holes in the casing and induces small fractures in the rock formation, (4) fracturing fluid (mix of water, proppants (e.g. sand) and chemical additives) is pumped into the borehole and pressurised, (5) pressurised fluid creates new fractures and propagates existing ones so that trapped gas can flow to the surface. Proppants keep the fracture open to increase the flow of the gas. (3) – (5) are repeated several times for different sections along the horizontal well (modified from: image retrieved on 05/06/2018 from http://energy-reality.org/fracking).

1.4 Hydraulic fracturing experiments in the laboratory – previous work

The principal aim of hydraulic fracturing of unconventional hydrocarbon resource reservoirs is to enhance extraction and flow rates through an increased permeability. Motivated by the large scale application of hydraulic fracturing, the interest in the fundamentals behind the process have been the focus of many studies (Table 1-1). A number of early attempts simulating hydraulic fracturing under controlled laboratory conditions have relied on the use of an inner rubber membrane (Clifton et al., 1976; Schmitt and Zoback, 1992; Vinciguerra et al., 2004) to simplify boundary conditions and to reduce complex poroelastic and leak-off effects. Following these early experiments, experiments without the inner membrane have been performed by using either cylindrical or cubical samples in uniaxial, hydrostatic, triaxial or polyaxial stress conditions (e.g. Haimson and Fairhurst, 1969b; Zoback et al., 1977; Stanchits et al., 2014a; Stoeckhert et al., 2015). These experiments were conducted to investigate various different aspects of the hydraulic fracturing process such as the breakdown pressure, relationships to rock properties and stress-field conditions, the effect of different pressurisation rates or fluids of various viscosity, and the source mechanism.

One of the key aspects in many studies has been the breakdown pressure including the relationship with far-field stresses and factors like pressurisation rate and fluid viscosity (e.g. Haimson and Fairhurst, 1969b; Ito and Hayashi, 1991; Ishida et al., 2004). A positive relationship between confining pressure and breakdown pressure has been shown for many rock types like granite, sandstone, limestone, marble and hydrostone (e.g. Haimson and Fairhurst, 1969b; Schmitt and Zoback, 1993; Brenne et al., 2013). In addition, it has been shown in many experiments that an increased pressurisation rate leads to higher breakdown pressures (e.g. Zoback et al., 1977; Haimson and Zhao, 1991; Song and Haimson, 2001; Haimson and Zhao, 1991). Ishida (2001) and Ishida et al. (2004) on the other hand, focused on the influence of different fluid viscosities and investigated the effect on the failure mechanism during hydraulic fracturing in two sets of laboratory experiments on granitic rocks using water (viscosity of 1cP) and oil (80cP) as pressurising medium. They showed that high viscosity fluids tend to induce tensile cracks while low viscosity fluids will induce shear fractures as the fluid can infiltrate into the fracture surfaces promoting shear failure events. Furthermore, when using lower viscosity fluids, Acoustic Emission sources are distributed more widely and fractures are created more three dimensionally rather than along a plane (Ishida et al., 2004, 2012). Stanchits et al. (2014b) conducted hydraulic fracturing experiments on sandstone blocks using different fluids of different viscosity and observed that injection of high-viscosity fluids results in slower fluid penetration, higher fracture width and higher breakdown pressures. However, further studies using different gasses to initiate fractures (e.g. CO_2, N_2, Ar, He)

demonstrated that the relationship between fluid viscosity and fracture morphology is not a simple linear one (e.g. Alpern et al., 2012; Li et al., 2016). Chen et al. (2015) showed that a higher viscosity yields a smoother fracture pattern in a granite, Alpern et al. (2012) and Li et al. (2016) did not find such a linear relationship between the viscosity of gasses (used as fracturing medium) and fracture geometry. In this regards, Li et al. (2016) conducted experiments on Green River Shale with different gases. The highest breakdown pressures were recorded when using CO_2, followed by N_2 and water resulting in the lowest pressure, despite N_2 exhibiting the lowest viscosity. Furthermore, CO_2 fracture surfaces were more complex compared to water induced fractures, but N_2 fractures were the least complex. Other important factors in hydraulic fracturing of sedimentary rocks are the rock fabric and an inherent anisotropy. Heterogeneities as stress localisations and local mechanical variations (pores) are known to be important for fracture initiation and propagation (Renard et al., 2009; Scholz, 1968a), with the effect of bedding planes then significantly influencing the propagation of hydraulic fractures across different lithologies (Chitrala et al., 2010; He et al., 2016). Brenne et al. (2014), using a Hoek-cell setup, investigated the effect of cleavage planes in a slate and found significant differences in breakdown pressures ranging from 5MPa (parallel bedding) to 65MPa (normal to bedding) depending on the cleavage orientation relative to the borehole. Ishida (2001) used granites with different grain sizes to investigate the effect of rock fabric texture on the source mechanism and demonstrated that the number of tensile events increased relatively with decreasing grain size. He et al. (2016) performed hydraulic fracturing experiments on hollow cylinder samples of sandstone, granite and shale to investigate different fracture extension patterns in the different rock types. They observed that the tortuosity of the fracture path increased with increasing grain size.

The studies mentioned so far, focused primarily on the fracturing process of hydraulic fracturing. However, a key indicator to evaluate the effectiveness of fracturing is the fracture conductivity, defined as the product of fracture permeability and fracture aperture, which plays a key role in the evaluation of long term production of shale gas wells (Tan et al., 2018). Thus, the ability to capture the evolution of hydraulic fracture conductivity under various conditions in the laboratory is also important for analysing well performance and optimizing fracturing design. Many studies have experimentally investigated the permeability of artificial fractures (sawn or split samples) and the effect of proppants using triaxial or shear-box devices (e.g. Kranz et al., 1979; Davy et al., 2007; Bernier et al., 2007; Kassis and Sondergeld, 2010; Zhang et al., 2013). Bernier et al. (2007) conducted hydraulic fracture tests on hollow samples within a triaxial device. They observed 4–5 order of magnitude increases in permeability from initial values between 10^{-22} and 10^{-19} m^2. Guo et al. (2013) carried out an experimental study of

fracture permeability on cores from a shale formation of the Shengli Oilfeld to explore the effects of fracture surface roughness, fracture registration, confining pressure, proppant type and proppant distribution mode on fracture permeability. They found that the permeability of aligned fractures (unpropped and without fracture offset) increased about 1–3 orders of magnitude over shale matrix permeability. However, fracture permeability also depends on factors such as fracture compressibility, fracture roughness and fracture surface offset as well as effective stress and rock strength (Kassis and Sondergeld, 2010; Guo et al., 2013; Tan et al., 2018). Through a series of tests on fractured Barnett shale, Kassis and Sondergeld (2010) demonstrated that fracture offset enhances fracture permeability as effectively as propping does and that stress dependency of a propped fracture is stronger than for an offset fracture. The effectiveness of hydraulic fracturing is therefore closely related to the fracturing process itself, nature defined parameters such as rock properties and far-field stresses, as well as engineered factors like fluid injection rate and fluid viscosity. An understanding of these relationships is fundamental for an optimised hydraulic fracturing treatment.

Table 1-1: List of references for hydraulic fracturing laboratory experiments.

Abbreviations: cyl = cylindrical specimens, cub = cuboid specimens, sle = experiments with jacketed boreholes.

Sample material: and = andesite, cem = cement, dia = diatomite, dol = dolomite, gab = gabbro, gla = glass, grn = granite, hyd = hydrostone, lim = limestone, mrb = marble, phy = pyrophyllite, pls = plaster,

PMMA = polymethyl methacrylate, rhy = rhyolite, sha = shale, sla = slate, slt = rock salt, sst = sandstone.

Author	Focus of experiments	Cyl	Cub	Sle	Material
Hubbert and Willis (1957)	Confirm theoretical results	x			gelatin
Haimson and Fairhurst (1969b)	Initiation, orientation and location of hydrofractures, development of theoretical criteria	x	x		hyd
Haimson and Fairhurst (1969b)	Effect of fluid infiltration	x	x		mrb, grn, dol, sst, hyd
Haimson and Avasthi (1973)		x	x		sla
Zoback et al. (1977)	Effect of pressurisation rate and influence of pre-existing cracks	x			sst, gab
Zoback et al. (1977)	Effect of pressurisation rate and influence of pre-existing cracks		x		sst, gab
Lockner and Byerlee (1977)	Location and orientation of fracture planes	x			sst
Abou-Sayed et al. (1978)	Supply material properties for field interpretations	x		x	sha
Daneshy (1976)	Effect of rock properties on fracture propagation	x			sst, lim
Solberg et al. (1980)		x			grn
Anderson (1981)			x		sst, lim
Warpinski et al. (1981)		x			sst, tuff
Blanton (1982)			x		sst, lim

Author	Focus of experiments	Cyl	Cub	Sle	Material
Lockner et al. (1982)		x			greywacke
Winter (1983)		x		x	sst
Rummel (1987)	Derive material properties for field data interpretation	x	x		grn, sst, lim, mrb, gab, slt
Ito and Hayashi (1991)	To verify theoretical breakdown pressures		x	x	and
Haimson and Zhao (1991)	Size and pressurisation rate effects on hydraulic fracturing	x			grn, lim
Schmitt and Zoback (1992)	Diminished pore pressures and dilatancy prior failure	x			grn
Schmitt and Zoback (1993)	Infiltrations effects during hydraulic fracturing	x			grn, glass
Ishida et al. (1997)	Effect of injected water in hydraulic fracturing		x	x	grn
Song and Haimson (2001)	Effect of pressurisation rate and initial pore pressure	x			sst
Ishida (2001)	Effect of viscosity of injection fluid		x	x	grn
Ishida et al. (2004)	Effect of viscosity of injection fluid		x	x	grn
Vinciguerra et al. (2004)	Comparison of experimental and numerical results for MHF	x		x	sst
Chitrala et al. (2010)		x			lim, sst, phy
Chitrala et al. (2012)	Microseismicity and fracture morphology	x			sst, phy
Stanchits et al. (2012a)	Initiation and growth of hydrofractures in sandstone		x		sst

Author	Focus of experiments	Cyl	Cub	Sle	Material
Stanchits et al. (2012b)	Effect of fluid viscosity on fracture initiation and propagation		x		sha
Alpern et al. (2012)	Effect of different fluids		x		PMMA
Brenne et al. (2013)	Comparison of sleeve and non-sleeve fracturing	x		x	mrb, lim, sst, and, rhy
Brenne et al. (2014)	Effect of bedding orientation	x		x	sla
Stoeckhert et al. (2014)	Effect of bedding orientation and pressurisation rates	x			and, rhy, sst, lst, sla, mrb
Stanchits et al. (2014a)	Effect of discontinuities in sandstone and shale		x		sst, sha
Stanchits et al. (2014b)	Onset of hydraulic fracture initiation in sandstone		x		sst
Goodfellow (2015)	Energy budget of hydraulic fracturing	x			grn
Gan et al. (2015)	Effect of fluid infiltration and exclusion on breakdown pressures		x		PMMA
Molenda et al. (2015)	AE location		x	x	rhy, sst, sla
Alber et al. (2015)	Effect of bedding orientation		x	x	sla
Stoeckhert et al. (2015)	Fracture propagation in slate and sandstone		x	x	sst, sla
Chen et al. (2015)	Effect of viscosity on fracture propagation and morphology		x		grn
Pradhan et al. (2015)	Fracture behaviour and morphology	x			sst, chalk

Author	Focus of experiments	Cyl	Cub	Sle	Material
Li et al. (2016)	Effect of different gas compositions on fracture propagation and morphology	x			sh
Diaz et al. (2016)	Effect of cleavage anisotropy on fracture behaviour in granite	x			grn
He et al. (2016)	Fracture pattern comparison of three rock types	x			sst, grn, sha
He et al. (2018)	Effect of bedding orientation on fracture propagation direction	x			sha

A more detailed overview is given in Appendix A.1, including sample dimensions, bedding orientation and injection fluid.

1.5 Nature of research (objectives) and thesis outline

Hydraulic fracturing is rapidly gaining importance in the engineered environment and despite the potential to add significant gas resources in many countries in Europe (Andrews, 2013), environmental and public safety concerns around groundwater contamination and seismicity prevent wider exploitation (Howell, 2018; Currie et al., 2017). Public concerns can be alleviated by improving the control we have on fracture formation, which requires an improved rock mechanics understanding of the fracture networks that are produced by fracking operations. This is especially true in the usually complex shale gas reservoirs in the UK (e.g. Bowland Shale) and Europe. So far, the success of hydraulic fracturing and shale gas exploration has largely been based on empiricism through field experiments and operations.

A detailed relationship between breakdown pressure, burial depth (pressure) and rock characteristics as well as the controlling factors of the fracturing process remain unclear. This uncertainty of the deep geological and geotechnical processes combined with the signals recorded as seismic data lead to the necessity for new empirical (laboratory) testing. Despite several studies investigating fluid-driven fracturing in the laboratory (Chapter 1.4), the micromechanics of the fracturing process and the interplay between the inherent anisotropy of the rock, the initial permeability of the rock mass, the fluid overpressure needed to generate new tensile fractures, and the seismicity generated, are not fully understood. In addition, there is still no general theory or relationship between breakdown pressure, burial depth (pressure), tensile strength (including fracture toughness) and geological properties of the rock to define the hydraulic fracturing process and predict breakdown pressures. This is not surprising given the inherent complexity when rock fabric size, permeability, *in situ* stresses, inherent rock anisotropy, fluid viscosity and pressurisation rate are taken into account. However, these relationships are critical to develop an updated, engineered approach to hydraulic fracturing in an effort to reduce risks, increase controllability and to optimise gas extraction.

This study aims to address this gap in understanding by simulating the generation of hydraulic fractures and relating this to rock fabric, orientation of bedding planes and seismicity using new laboratory rock physics methods. A comprehensive suite of laboratory controlled experiments are conducted with the focus on the understanding of the progressive hydraulic fracturing process and the influence of boundary conditions, which are predetermined by nature such as in-situ stresses, mechanical and geological properties of the rock including strength, heterogeneities, rock fabric, permeability, anisotropy and discontinuities. The main objectives of this work are:

(1) The development of the equipment and experimental protocol to simulate hydraulic fracturing under controlled laboratory conditions in a triaxial pressure apparatus,
(2) To analyse and understand the hydraulic fracturing process over time and with respect to the inherent anisotropy, rock fabric and initial permeability of the rock,
(3) To quantify the hydro-mechanical and the seismo-mechanical relationship as well as the influence of mechanical rock properties on hydraulic fracture propagation and fracture geometries,
(4) To unravel the interplay between the evolution of the fluid-driven fracturing progress and the seismic character of the resultant micro-earthquakes.

To achieve this, hydraulic fracturing simulation in the laboratory is combined with high resolution recording of mechanical parameters, geophysical imaging through acoustic emission and post-test micro X-ray CT imaging. Hydraulic fracturing (fluid-driven tensile fracturing) is a complex process and simply evaluating the fluid pressure curve does not capture the entire complexity of the fracturing process. Therefore, to better understand progressive fracturing and the controls on the developed fracture network, hydraulic fracture is here simulated via direct pressurisation, recording mechanical and acoustic data at a high resolution to accommodate the dynamic fracture process. Some of the complexity is addressed by simultaneously measuring radial deformation, fluid injection pressure and microseismicity in relation to the initial material anisotropy using a holistic rock-physics approach. Fluid pressure and seismicity are monitored using continuous high frequency recorders (0.1 μs sampling rate) synchronised with mechanical parameters (at 0.1 ms sampling rate). This permits different fracturing stages to be detected by linking seismic and mechanical behaviour to the resulting fracture network. To investigate the effect of the inherent anisotropy, two rock types were used and compared with experiments conducted with different orientations (stress, σ_v) to the bedding plane. By creating a detailed mechanical and geophysical image of tensile fracture nucleation and growth in anisotropic rocks, this work will advance our understanding of fracking in the field, and present how mechanical data and seismicity can be used to better understand and monitor hydraulic fracturing remotely. Such a system not only could become a forecasting tool, but also a means to control the fracking process to prevent avoidable seismic events and fracture extent beyond the targeted lithology. To evaluate the effectiveness of hydraulic fracturing, a new setup has been designed where fracture permeability of the hydraulically induced fracture network can be derived without any additional sample handling between fracture initiation and permeability measurements.

This thesis describes a detailed experimental study of hydraulic fracturing simulations under controlled laboratory conditions to investigate the hydraulic fracturing process over time with respect to the inherent anisotropy, rock fabric and initial permeability for a very low permeability and highly anisotropic shale (Nash Point, Wales, UK) and a low permeability and anisotropic sandstone (Crab Orchard, Tennessee USA). The laboratory data set is used to quantify relationships between fluid movement, Acoustic Emission activity and rock properties and to test a number of models that attempt to predict the breakdown pressure for reservoir formations.

The thesis is divided into four sections, (i) introduction and theoretical background, (ii) experimental equipment and methods, (iii) material description and characteristics and experimental results, and (iv) the discussion of the experimental data and modelling. These four segments are presented in seven chapters. Chapter 1 introduces the concept of unconventional reservoirs, the extraction technology and process and recorded microseismicity during the extraction. This chapter also outlines the missing knowledge and the need for experimental work as well as previous experimental work on this subject. Chapter 2 outlines the theory of rock failure in the brittle regime, and describes the fracture conditions of a borehole in the field and thick-walled cylinders used in the laboratory as well as the use of acoustic emission in rock mechanics. In chapter 3, the author describes the development of the experimental equipment used for the hydraulic fracturing simulations and the experimental protocol in detail. Chapter 4 introduces the rock material (type) used for this study and describes the petrography and the petrophysical and mechanical properties of the rocks types. Additionally, properties of the shale rock used for this study are compared to properties of well-known gas bearing shales from the US. Chapter 5 details the experimental results of the hydraulic fracturing tests and the micro X-ray CT imaging. Chapter 6 discusses the laboratory data including a detailed interpretation and description of the fracturing process and the influence of confining pressure, anisotropy, rock fabric and initial permeability. Well established hydraulic fracturing models are compared to the experimental data and a new approach to estimate fracture toughness at elevated pressures and under hydraulic fracturing conditions is presented. Finally, chapter 7 summarises the findings of this work and draws a number of conclusions. Recommendations for further studies are given based on the findings of this research.

2 Simulation of hydraulic fracturing in the laboratory

2.1 Theories of rock failure in the brittle regime

Rock failures are common occurrences in nature and controlled rock deformation is a necessary task in many branches of engineering geology and civil engineering. Consequently, a thorough understanding of rock mechanics, rock deformation, and rock strength is of fundamental importance. Rocks deform when they are subjected to a load and will fail when their strength is exceeded by the applied stress. The failure can occur in compression or in tension, with the failure mechanism describing the process of failure by which a rock is permanently damaged, ultimately leading to the dynamic propagation of fractures, decreasing stress, and failure of the rock. There are typically three main types of deformation associated with the behaviour of solid materials: (1) reversible elastic – applied stress leads to deformation, which is reversible when stress is removed (e.g. rubber or spring), (2) irreversible plastic (ductile) – irreversible deformation of material and associated with permanent change of shape or volume (e.g. synthetics and plastics, that can be moulded and keep the new shape), and (3) brittle – almost instantaneous loss of strength with little or no plastic deformation and associated with a drastically reduced strength and irreversible change that penetrates atomic bonds (e.g. glass and ceramics). Brittle materials absorb relatively little energy prior to failure. These three idealised scenarios are visualised for a perfectly elastic, a perfectly plastic and perfectly brittle material in stress-strain diagrams in Figure 2-1 and idealised stress train models for typical stress-strain patterns in rocks are shown in Figure 2-2.

However, the fracturing of rocks is a complex process, and can only be described to a certain extent using mathematical and phenomenological models. A typical stress-strain curve for a rock (Figure 2-3), derived usually from uniaxial loading tests, shows axial stress plotted against the associated axial strain. At low stress levels, the initial region of the stress-strain curve is non-linear and represents the closure of microcracks in the sample. This phase is not always present as it depends on the crack density and crack geometry of the sample. This is followed by a linear elastic behaviour of the rock, where the strain is proportional to the stress. From this part of the curve, the Young's modulus, a measure of the material stiffness, may be derived. Beyond a certain strain, the yield point, the rock cannot sustain pure elastic behaviour and plastic deformation starts to occur. It is assumed that new microcracks are nucleated at this point leading to a strain-softening behaviour. As the stress continues to increase, stable crack growth occurs resulting in a strain softening behaviour until the specimen approaches its peak stress (strength). Here, cracks coalesce resulting in the dynamic failure of the rock sample (Martin and Chandler, 1994; Brady and Brown, 2005).

This behaviour of rock, and the mechanical failure process are influenced by many factors such as external stress conditions, temperature, mineral composition, porosity, discontinuities, heterogeneities and anisotropy. Plastic deformation occurs usually under conditions of high temperature and pressure, or at low strain rates so as to give atoms time to shift in response to the stress through mechanisms such as dislocation creep. However, at the earth surface and in depths up to a few kilometres, brittle deformation is far more common (Brace and Kohlstedt, 1980; Kirby, 1980) and has been the focus of many studies, including this one. In the last century, so-called failure criteria have been developed for the brittle regime, establishing relationships between the three principal stresses (σ_1, σ_2 and σ_3) to forecast the likely failure conditions (stress) of a rock given a set of input conditions. To date, there have been two different approaches for developing these theories in the brittle regime. The first approach uses empirical data to define a criteria of failure that agrees with the observed failure conditions. They are intended to provide a basis for calculating failure conditions in practical situations involving more general states of stress and therefore do not explain the physical mechanisms behind the failure. The most commonly used ones are the Mohr-Coulomb failure criteria and the Hoek-Brown failure criteria, both described in this chapter, and are considered phenomenological methods. The second approach attempts to develop an underpinning physical model of the brittle fracture process to explain essential aspects of the mechanism of fracture, and thus provide a failure criteria that is applicable to general states of stress. This has resulted in the Griffith theory of brittle failure. It should be noted that the Griffith theory is only applicable to the initiation of failure on the scale of microcracks, whereas the strength observations by Mohr and Coulomb and Hoek and Brown refer to the macroscopic failure. In order to explain the failure criteria some technical terms used in the field of fracture mechanics, and in this chapter, are now defined (Bieniawski, 1967a; Whittaker et al., 1992):

- FAILURE → is a process by which a material changes from one state of behaviour to another one.
- STRENGTH FAILURE → is the failure process by which a material changes from a state in which its load-bearing capacity is either constant or increases with increasing deformation to a state in which its load-bearing capacity is decreased or has even vanished.
- FRACTURE → is the failure process by which new surfaces in the form of cracks are formed in a material, or existing crack surfaces are extended. Various conditions and stages of fracture can be visualised, namely:

  - Fracture Initiation → is the local failure process by which one or more cracks pre-existing in a material start to extend (Griffith concept). It indicates the onset of crack extension and is confined to the vicinity of the crack tip.
  - Fracture Propagation → is the global failure process by which cracks in a material are extending, thus it is a stage subsequent to fracture initiation and represents the process of crack extension from the crack tip to the boundaries of the material, resulting in the catastrophic failure of the stressed material. Fracture propagation may be distinguished between two types of fracture propagation; stable and unstable.
  - Stable fracture propagation → is the failure process of fracture propagation in which the crack extension is a function of the loading and can be controlled accordingly.
  - Unstable fracture propagation → is the failure process of fracture propagation in which the crack extension is also governed by factors other than the loading, thus becoming uncontrollable.
- RUPTURE → is the failure process by which a structure (e.g. a specimen) disintegrates into two (or more) pieces.
- BRITTLE FRACTURE → is defined as fracture that exhibits no or little permanent (plastic) deformation.
- DUCTILE FRACTURE → is defined as fracture that is preceded by a clear phase of plastic deformation.

The transition from stable to unstable fracture propagation is determined by the critical energy release during fracturing, a concept first introduced for brittle metals by Irwin (1957) and later adapted for rock mechanics by Bieniawski (1967c). Bieniawski (1967c) argued that the process of unstable crack propagation is governed by the crack growth velocity. Accordingly, the transition is associated with a critical fracture propagation velocity, which is slow below and fast above the critical energy release, and a critical crack length (Figure 2-4). In the brittle-tensile regime, fracture initiation and fracture propagation take place in very quick succession whereas in the brittle-compression regime, the process of fracture propagation is considerably slower, depending on strain rate (Martin and Chandler, 1994). In compression, the rupture of the material occurs primarily from fracture propagation and crack coalescence (Bieniawski, 1967a; Whittaker et al., 1992). The existence of an extensive array of microcracks around the main crack tip has been shown by Hoagland et al. (1973). This overview of fracture mechanics is supported by numerous researchers in the field (e.g. Whittaker et al., 1992; Hudson and

Harrison, 2000; Brady and Brown, 2005; Paterson and Wong, 2005; Jaeger et al., 2009; Zoback, 2007).

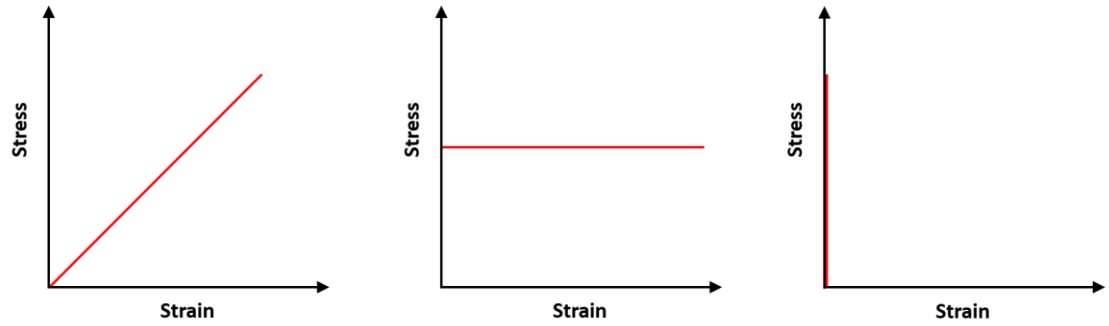

Figure 2-1: Stress-strain relationships for (a) ideal elastic, (b) ideal plastic, and (c) brittle deformation.

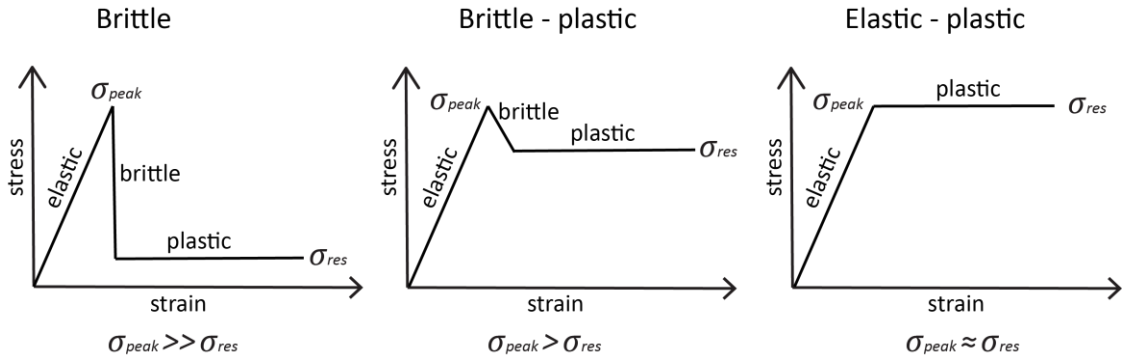

Figure 2-2: Idealised stress-strain behaviour models of rocks; σ_{peak} is the peak strength of the rock and $\sigma_{res}$the residual strength.

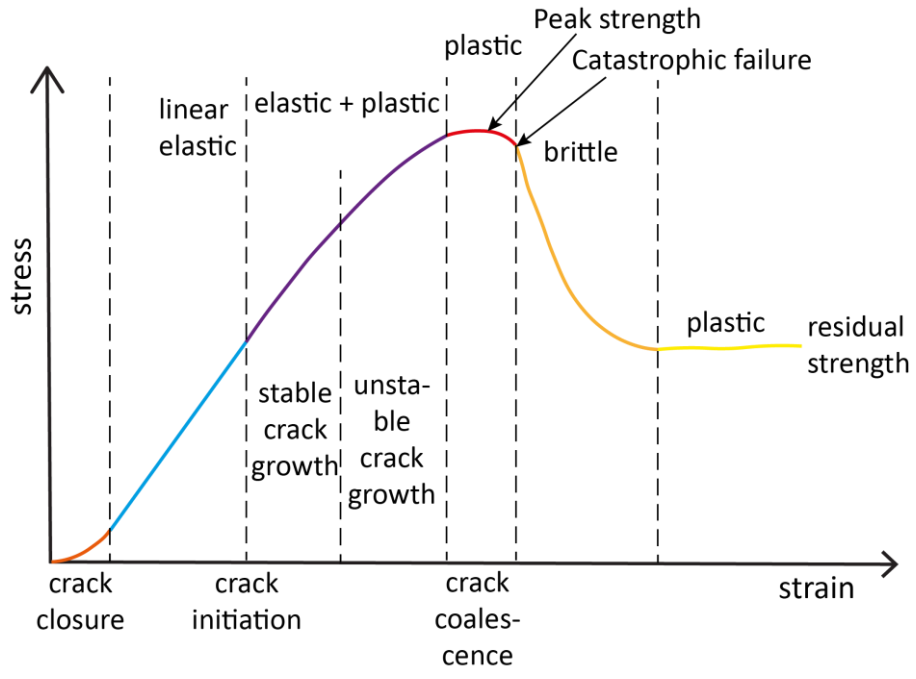

Figure 2-3: Stress-strain curve for rocks in a uniaxial compression test. Modified from Martin and Chandler (1994) and Hudson and Harrison (2000).

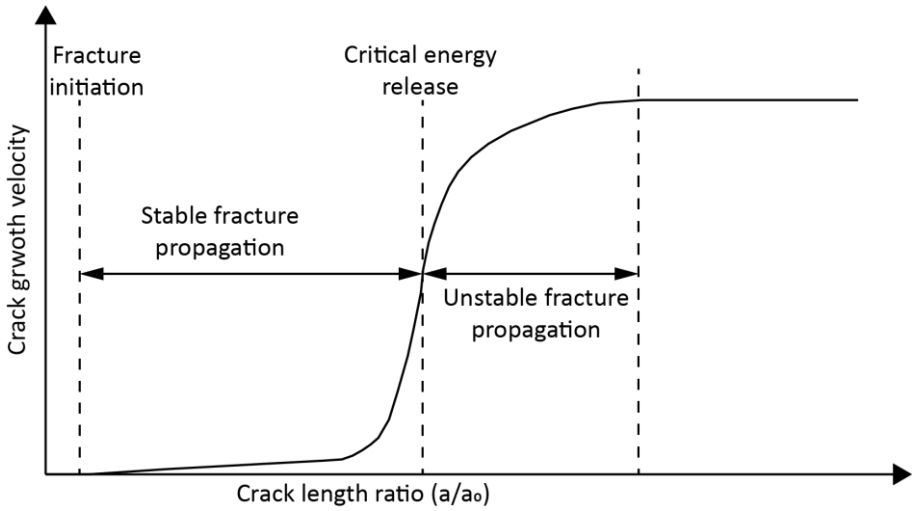

Figure 2-4: Crack growth velocity related to crack length ratio, experimentally determined for norite rock. Modified after Bieniawski (1967b).

2.1.1 Macroscopic failure criterion

One of the earliest failure criteria for brittle rock was the Mohr-Coulomb failure criterion, which describes shear failure under compressive stress (Jaeger et al., 2009). Coulomb (1776) postulated that the shear strength of any rock (or soil) depends on two parameters: a constant cohesion and a normal-stress dependent friction component. The latter is given as internal friction angle or coefficient of internal friction. Based on laboratory investigation, Coulomb concluded that failure in a rock or soil occurs due to the shear stress acting on a plane within the sample. Therefore, the criteria states that shear failure will occur on a plane a-b (Figure 2-5) if the following conditions are satisfied (Lockner and Beeler, 2002):

$$\tau = c + \mu\sigma_n \qquad 2\text{-}1$$

where: τ and σ_n are shear and normal stress and c = cohesion and μ = coefficient of internal friction.

The coefficient of internal friction is related to the angle of internal friction by $\phi = tan^{-1} * \mu$, where ϕ is the angle of the failure envelope with the σ-axis. Thus, the criteria can be stated using either term. The classic Mohr diagram (Figure 2-6) is a graphical representation of the Mohr-Coulomb failure criterion, showing how the failure envelope defines cohesion as the intersection with the τ-axis, and μ as the slope of the failure envelope line (Figure 2-6a). Mohr's circle can be easily constructed from laboratory triaxial compression tests using confining pressure as σ_3 and the peak (specimen failure) stress as σ_1. The point of failure in the $\sigma - \tau$ space on the circle is the contact point with the envelope. Several experiments (results) are thus required to construct a reliable failure envelope using this method (Zoback, 2007). For

tensile failure to occur, the tangent to the Mohr circles are simply extrapolated to $\tau = 0$, where the tensile failure condition $\sigma_3 = \sigma_T$ is defined with σ_T being the tensile strength of the rock (Cosgrove, 1995). Furthermore Cosgrove (1995) also demonstrated that the fracture orientation depends on the differential stress ($\sigma_1 - \sigma_3$) with tensile fractures forming parallel to σ_1 if the differential stress is relatively large. As the differential stress decreases towards zero, tensile fractures therefore develop with their crack normal's randomly orientated, but with their long axes parallel to the principal stress direction. However, as will be demonstrated below, these views are over simplistic, with a tendency to significantly overestimate tensile strength, in particular.

Applying the stress transformation equations (Brady and Brown, 2005) to the failure criteria (equation 2-1) gives

$$\sigma_n = \frac{1}{2}(\sigma_1 + \sigma_3) + \frac{1}{2}(\sigma_1 - \sigma_3)cos2\beta \qquad 2\text{-}2$$

and

$$\tau = \frac{1}{2}(\sigma_1 - \sigma_3)sin2\beta \qquad 2\text{-}3$$

Substituting equation 2-2 for σ_n and equation 2-3 for τ in equation 2-1 and rearranging for σ_1 derives the critical failure stress condition on any plane defined by β (Brady and Brown, 2005) as

$$\sigma_1 = \frac{2c + \sigma_3[sin2\beta + tan\phi(1 - cos2\beta)]}{sin2\beta - tan\phi(1 + cos2\beta)} \qquad 2\text{-}4$$

As σ_1 increases, the maximum shear strength will be reached first on the critical plane. The orientation of this plane can be determined from the Mohr circle (Figure 2-6a) and is defined as

$$\beta = \frac{\pi}{4} + \frac{\phi}{2} \qquad 2\text{-}5$$

Where for the critical failure plane $sin2\beta = cos\phi$ and $cos2\beta = -sin\phi$, which can be used to simplify equation 2-4 to

$$\sigma_1 = \frac{2c * cos\phi + \sigma_3(1 + sin\phi)}{1 - sin\phi}. \qquad 2\text{-}6$$

The linear relationship between σ_1 and σ_3 is shown in Figure 2-6b; the gradient of the line is related to ϕ through

$$tan\,\psi = \frac{1 + sin\phi}{1 - sin\phi}. \qquad 2\text{-}7$$

Uniaxial compressional strength (σ_c) and an apparent tensile strength ($\sigma_{T\ apparent}$) are related to cohesion and internal friction angle by

$$\sigma_c = \frac{2c * cos\phi}{1 - sin\phi} \qquad 2\text{-}8$$

and

$$\sigma_{T\ apparent} = \frac{2c * cos\phi}{1 + sin\phi}. \qquad 2\text{-}9$$

As previously introduced, this derivation tends to overestimate tensile strength (in particular) with laboratory measurements showing significantly lower values as calculated from equation 2-9 (Heard, 1960; Handin et al., 1967; Mogi, 1967). The usual remedy, a tensile cut-off applied at an experimentally determined value of the tensile strength (σ_T) of the rock (Hoek and Martin, 2014), being not the most rigorous of solutions. Another disadvantage of the method is its tendency to imply the presence of major shear fractures at a particular direction, which seldom agrees with experimental observations (Wawersik and Fairhurst, 1970). Despite these pitfalls, the Mohr-Coulomb failure criteria gives a reasonable approximation for the peak compressive strength of rocks (Brace, 1964; Murrell, 1965; Carmichael, 1982; Colmenares and Zoback, 2002), and works well in the 'intermediate' range of stresses.

Although empirical, the Hoek and Brown failure criterion (Hoek and Brown, 1980) solves the issue by taking the unconfined compressive strength of a rock as a scaling parameter and adding two dimensionless factors. Using the maximum and minimum principal stresses, the peak triaxial compressive strength of a rock is described by

$$\sigma_1 = \sigma_3 + \sigma_c \sqrt{m\frac{\sigma_3}{\sigma_c} + s} \qquad 2\text{-}10$$

where σ_1 and σ_3 are the major and minor effective principal stresses at failure, σ_c is the uniaxial compressive strength of the intact rock material, and m and s are constants. Although useful for practice-based engineers, the criterion in equation 2-10 depends on the rock properties and on the extent to which the rock had been broken *before* being subjected to the failure

stresses (Hoek and Brown, 1980). Hoek and Brown (1997) established these parameters phenomenologically by studying a wide range of published experimental data, defining m for different rock types. The parameter s depends on the state of the rock to be tested. For intact rock material $s = 1$, whereas for previously broken rock $s < 1$. For a completely broken specimen or rock aggregate $s = 0$. The Hoek-Brown failure law gives a nonlinear, parabolic failure envelope, in contrast to the linear relationship of the Mohr-Coulomb criteria (Figure 2-7). A more detailed interpretation of the Hoek-Brown failure criteria has been provided by Martin (1997) and others (e.g. Martin and Chandler, 1994; Martin et al., 1999), who studied the laboratory and field behaviour of Lac du Bonnet granite.

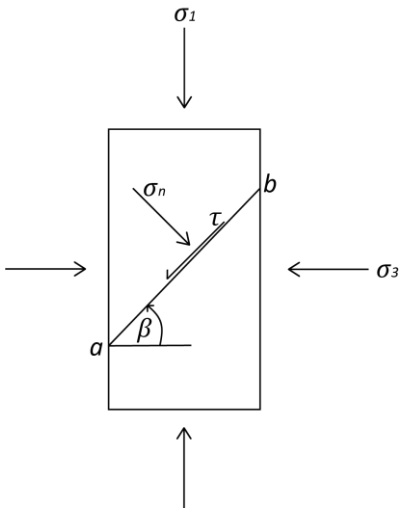

Figure 2-5: Shear failure on plane a-b. Modified from Brady and Brown (2005).

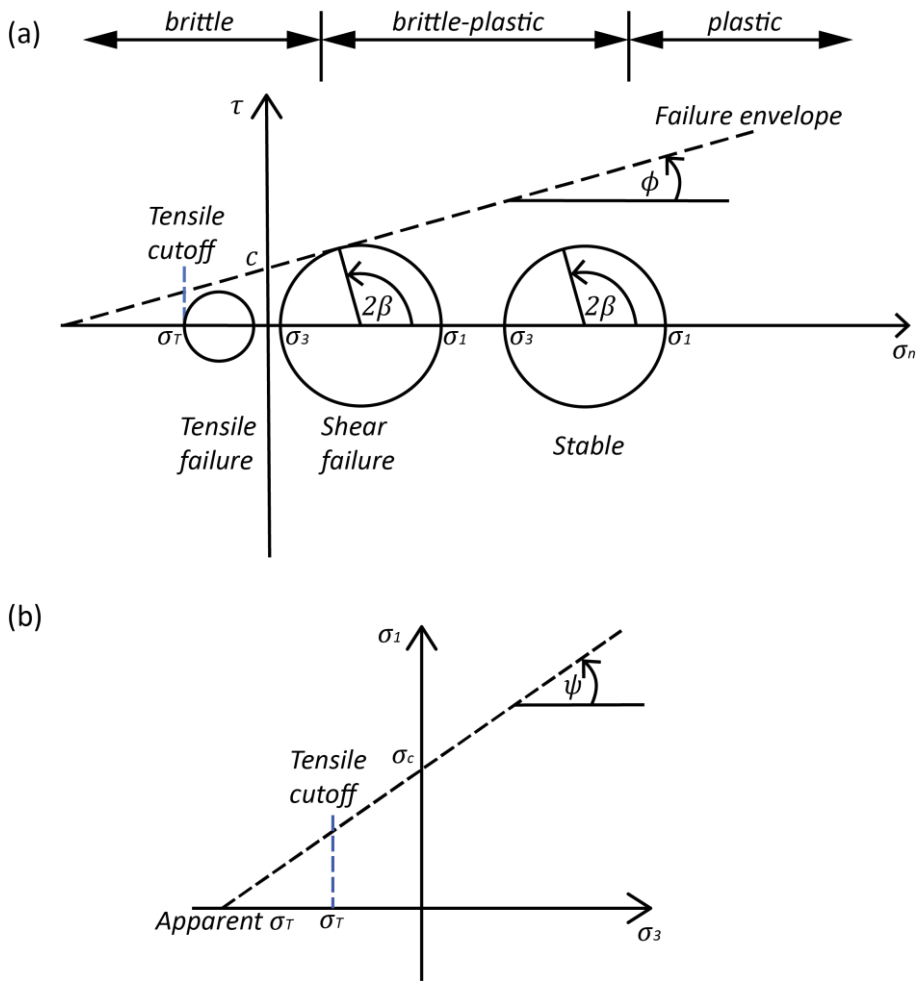

Figure 2-6: Coulomb strength envelope; (a) shear and normal stress (Mohr diagram) (modified from Nygård et al. (2006)), and (b) principal stresses (modified from Brady and Brown (2005)).The blue line indicates the tensile cut off.

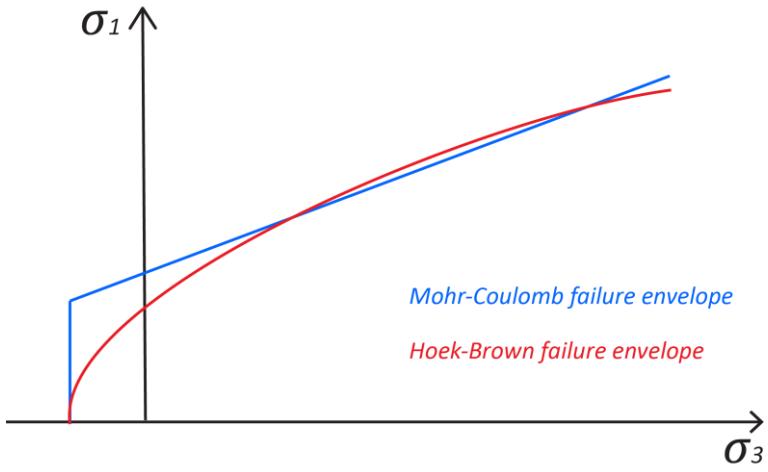

Figure 2-7: Mohr-Coulomb (blue) and Hoek-Brown (red) failure envelopes. Modified after Wyllie and Mah (2014).

2.1.2 Griffith crack theory

Another approach to the fundamental theory of rock tensile strength can be expressed simply as the energy or work required to break atomic bonds that hold atoms together (Figure 2-8), and dates back to early work on the stress concentration around a hole, with its roots in metallurgy (Inglis, 1913).

In general, the theoretical tensile strength of an ideal brittle material is related to Young's Modulus (E) (Heap, 2009) by

$$\sigma_T = \frac{E}{2\pi} \qquad 2\text{-}11$$

and calculates to be approximately 10% of the Young's Modulus (Whittaker et al., 1992). However, the measured tensile strength of brittle materials are in the order of just 0.1-1% of the Young's Modulus (Lange, 1974). Griffith (1921), building on the work of Inglis (1913), recognized the significance of pre-existing cracks which cause a significant decrease in tensile strength of a brittle material via the stress 'concentration' around microscopic cracks. Griffith (1921) proposed the first theory that qualitatively explained the discrepancy between theoretical predictions of tensile strength and laboratory measurements based on these underlying micromechanics. He postulated that brittle materials contain microscopic flaws known as Griffith cracks that act as stress concentrators and that fracture initiation is caused by large tensile stress concentrations at the ends of these internal cracks. The crack will start to extend (fracture initiation) when the tensile stress induced at or near the tip of an inherent crack exceeds the interatomic cohesive strength of the material (Hoek and Bieniawski, 1965). Based on Kirsch (1898) and Inglis (1913) stress analysis, who showed that cavities or notches in a material can magnify stresses near the crack tips, Griffith (1921) established a relationship between the fracture strength and the size of pre-existing cracks. The magnitude of stress concentrations depends on the geometry of the hole and therefore differs greatly with different shaped holes as can be seen for a circular and an elliptical hole in Figure 2-9.

The original work concentrated on fractures in materials subjected to tensile stresses, but four years later, Griffith (1924) extended his theory to include biaxial compression loading, where he proposed a critical maximum local tensile stress criterion for an open crack extending from the crack tips. Griffith's crack theory explains the far lower tensile stresses measured at failure compared to the theoretically calculated tensile strength. Numerous studies have since confirmed that the peak strength of rock decreases inversely with the square root of crack length (Brace, 1961; Olsson, 1974; Hugman III and Friedman, 1979; Fredrich et al., 1990; Wong

et al., 1996; Hatzor and Palchik, 1997), which is approximately equal to the maximum grain size (Brace, 1961; Hoek, 1965; Eberhardt et al., 1999). It follows that the smaller the crack length, the greater the stress required for fracture initiation.

Griffith (1921, 1924) also proposed the problem of theoretical brittle failure by considering an energy balance for pre-existing crack propagation, introducing a surface energy term to calculate the brittle tensile strength. The concept is based upon the condition that the energy applied by loading the sample is balanced by the elastic strain energy stored in the material and the surface energy in the free faces of the pre-existing crack. He proposed that the creation of a new crack surface due to the crack extension absorbs energy (surface energy) which is supplied by the work done by the external force and/or the release of the stored strain energy (potential energy) in the material (Whittaker et al., 1992). Therefore, sufficient potential energy must be available to overcome the resistance of crack extension which is a simple energy balance consisting of the decrease in potential energy (stored strain energy release) due to the crack extension, and the increase in surface energy due to the increase in crack surface area. This approach uses the surface energy as a measure of the local cohesive strength of the material. The model (Figure 2-10a) involves a crack, of length 2a and width 2b, within an elastic body, which is loaded by an external tensional force σ_{∞}. The small extension in crack length (Δa) is a result of the work exerted by the external boundary force. This causes a decrease in the internal strain energy (energy released) and an increase in the surface energy (energy absorbed by the formation of new fracture surfaces) as the crack extends, leading to a decrease in the total potential energy of the system (Figure 2-10b).

The critical fracture stress at which the crack will be at equilibrium can be obtained from Griffith (1921) as:

$$\sigma_f = \sqrt{\frac{2\mathrm{E}\gamma_s}{\pi a}} \qquad \textit{2-12}$$

Where: σ_f is the applied fracture stress at failure, E is the Young's Modulus, a is the half-crack length and γ_s is the unit crack surface energy (elastic surface energy) which reflects the total energy of broken bonds per unit area.

The fracture stress defines the minimum stress needed to just initiate a crack, and by definition is equal to the tensile strength of the rock. Once exceeded, the crack will propagate in an unstable manner, leading to the failure of the sample, otherwise it remains stationary (stable).

However, Bieniawski (1967a) and Ingraffea et al. (1976) showed that equation 2-12 describes a fracture initiation mechanism, rather than a failure criterion for fracture under compressive conditions. In contrast, in the tensile stress regime, fracture initiation and strength failure occur almost simultaneously, with the progress of fracture propagation virtually non-existent. This means that equation 2-12 can be seen as a strength failure criterion for fracture under tensile stress conditions (Bieniawski, 1967b; Hoek and Martin, 2014). Griffith crack theory assumes open and cylindrical cracks, but in the case of rocks, it is more common for defects to form, from which tensile cracks then nucleate from. Alternatively, such pre-existing cracks can also become cemented or closed due to external compressive stresses and in which case are considered as closed cracks. For this reason Griffith theory has since been modified to account for crack closure with the development of frictional resistance along the crack surfaces (McClintock, 1962; Murrell, 1963, 1964; Murrell and Digby, 1970; Murrell, 1964). McClintock (1962) also suggested that shear strength (τ) from closed Griffith cracks can be calculated based on the Mohr-Coulomb failure criteria:

$$\tau = \tau_0 + \mu * \sigma_n \qquad \textit{2-13}$$

where τ_0 is the shear strength at zero normal stress, σ_n is the normal stress and μ is the coefficient of friction.

Naturally, for a system under tension this is not an issue, as crack closure is absent. Griffith (1921) performed his experiments on hard glass, which is thought to be ideally brittle. However, rocks normally show a certain extent of plastic deformation near the crack tip, forming a micro cracking process zone where the material behaves plastically (Hoagland et al., 1973; Schmidt and Huddle, 1977; Schmidt, 1980; Labuz et al., 1983; Hillerborg, 1985). Therefore, Irwin (1948) and Orowan (1949) suggested Griffith's equation can be applied to brittle materials undergoing plastic deformation at the fracture tip by including the plastic work into the total elastic surface energy required to extend the crack wall (Anderson, 2017). In this case, the modified Griffith's equation is given by

$$\sigma_T = \sqrt{\frac{2\mathrm{E}(\gamma_s + \gamma_p)}{\pi a}} \qquad \textit{2-14}$$

where γ_p is the plastic work per unit area of surface created (plastic surface energy) and is typically much larger than γ_s.

Orowan (1949) found that γ_p was approximately three orders of magnitude larger than γ_s, with similar observations in rocks by Wong (1982) and Kemeny and Cook (1987). In general, the original Griffith theory is more applicable to the tensile rather than the compressive stress conditions as it strictly refers to the local failure process, i.e. facture initiation. Through various modifications (e.g. Irwin, 1948; Orowan, 1949; McClintock, 1962; Cook, 1965) the theory can also be used for the solution of practical problems in compressive stress conditions. Although Griffith's theory has its limitations, it also was the starting point to the subject of linear elastic fracture mechanics which has extensive applications in the micromechanics of brittle failure. It is therefore important to explain this concept next.

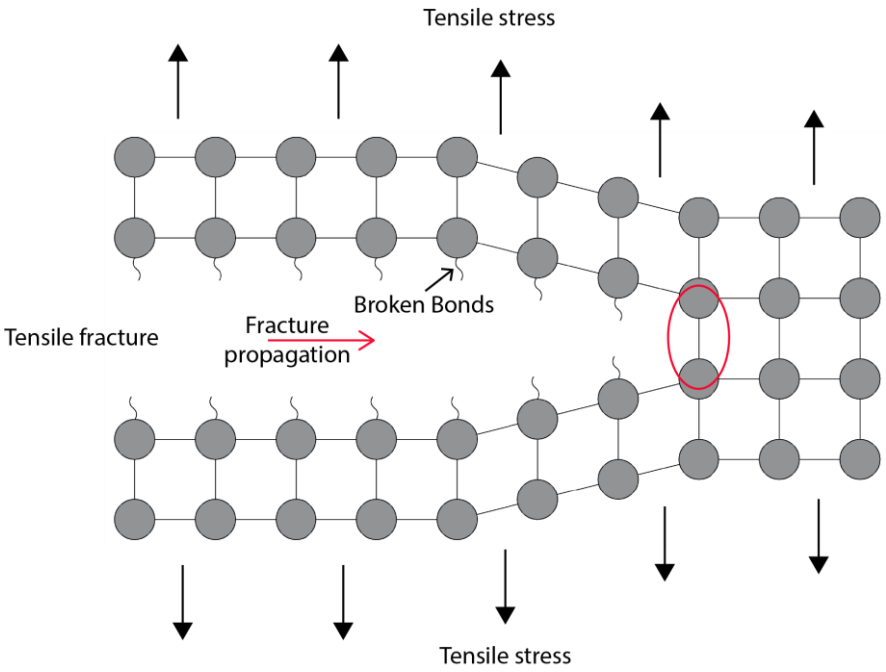

Figure 2-8: Schematic model of tensile fracturing propagation in a brittle material; red circle indicates area of increased stress intensity and plastic deformation. Modified from Anderson (2017).

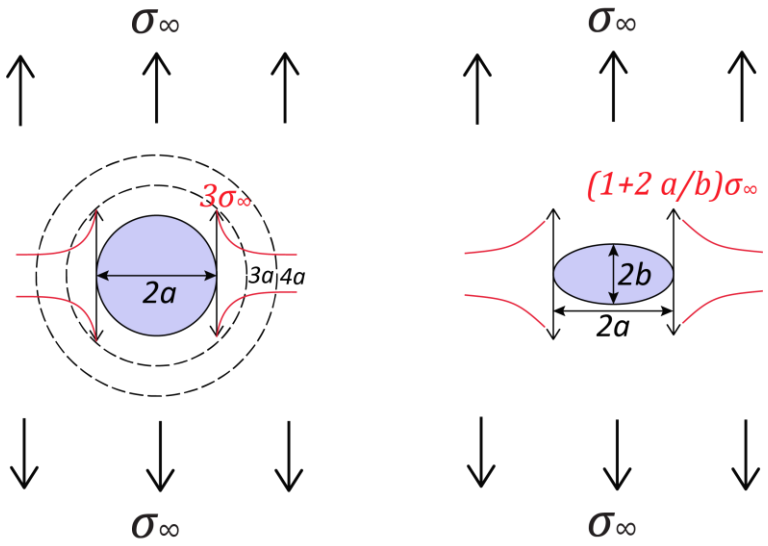

Figure 2-9: Stress concentration around (a) a circular hole and (b) an elliptical hole subjected to uniform tension (σ_∞). Based on Inglis (1913).

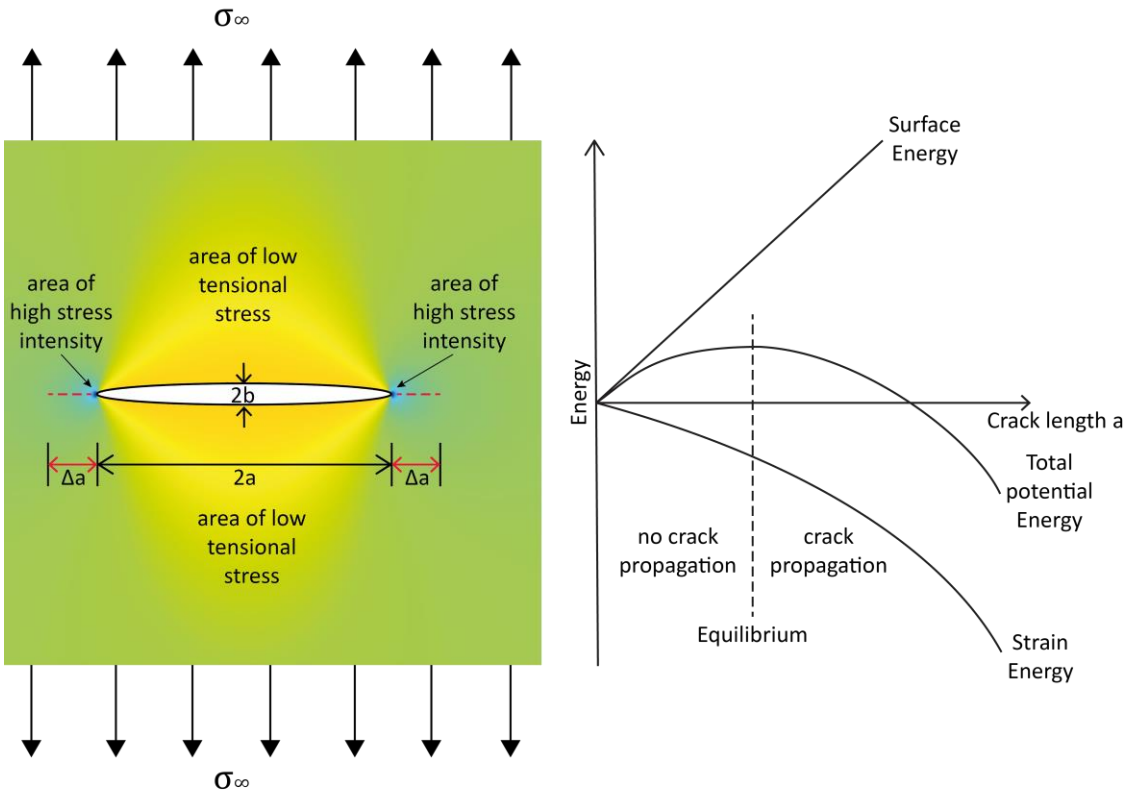

Figure 2-10: Griffith crack model; (a) Griffith static crack model for crack propagation due to local stress intensities at the crack tip (blue areas); yellow areas indicate areas of low tensile stresses due to the external stress field; Δa represents the crack extension; (b) Schematic of Griffith energy balance (total energy vs crack length). Modified from Whittaker et al. (1992).

2.1.3 Linear elastic fracture mechanics

Fracture mechanics describes the fracturing of materials with the laws of applied mechanics and macroscopic material properties and provides a quantitative concept relating fracture strength to the applied stress and the geometry of inherent defects (Irwin and de Wit, 1983). Linear Elastic Fracture Mechanics (LEFM) goes further, using linear elastic theory which tries to quantify the combination of an applied stress with a particular crack geometry that results in the extension of that crack (Knott, 1973; Chell, 1979; Broek, 2012). Consequently, LEFM extends the Griffith (1921, 1924) analysis by considering the stress tensor at the fracture tip to provide a solution for general crack problems and loading configurations. Using this approach equation 2-12 can be rearranged to:

$$\sigma_f \sqrt{\pi a} = \sqrt{2\mathrm{E}\gamma_s} \qquad 2\text{-}15$$

where: Young's Modulus E and the elastic surface energy y_s are properties of the given material.

The right hand side of equation 2-15 is a constant, indicating that fracture initiation will take place once the product of $\sigma_f \sqrt{\pi a}$, denoted as the stress intensity factor K (Irwin and de Wit, 1983), exceeds a critical value. This is known as the critical stress intensity factor or fracture toughness K_c, a characteristic material property which describes the ability of a material to resist fracture propagation (Zhu and Joyce, 2012). The stress intensity factor is a measure of the stress concentration at the crack tip for a particular fracture mode in a homogenous linear-elastic material (Irwin and de Wit, 1983) and depends on the applied stress field and the length of the crack. Once K_c has been exceeded, no more stress input is required as the crack propagation is unstable. From equation 2-12 the elastic surface energy y_s is also derived as:

$$\frac{{\sigma_f}^2 \pi a}{\mathrm{E}} = 2\gamma_s \qquad 2\text{-}16$$

The right side of equation 2-16 represents the elastic surface energy per unit crack surface which is available for crack extension (Whittaker et al., 1992) and defines the strain energy release rate or crack driving force G. Physically this describes the loss of energy per unit area of new crack during an increment of forward extension. Crack extension takes place once G reaches a critical value. Despite most of the energy being released near the crack tip, G is a global parameter and includes contributions from all parts of the system, whereas K is a local crack tip parameter. Irwin (1957) was able to establish a relationship between K and G, where K^2 is proportional to G and demonstrate the equivalence of these two parameters, which

provided the basis for the development of LEFM. As the principal of superposition applies, the relationship yields:

$$G = \mathrm{K}^2(\frac{1-\nu^2}{\mathrm{E}}) \qquad \textit{2-17}$$

where: ν is Poisson's ratio, and E the Young's modulus.

Stress intensity factor and strain energy release rate are key parameters in LEFM, and change depending on the mode of displacement. LEFM distinguishes between three different crack surface displacement modes (fracture modes), each associated with a certain stress field (Figure 2-11): (1) Mode I ("opening or tensile mode") is associated with local displacements in which the crack surfaces move directly apart perpendicular to the crack plane, (2) Mode II ("forward sliding or in-plane shearing mode"), and (3) Mode III ("anti-plane or tearing mode") are both shear modes with parallel displacements relative to the crack. Any combination of these three basic modes is referred to as "mixed mode". To distinguish the different stress intensity factors, a subscripted suffix ($\mathrm{I}-\mathrm{III}$) is added for the different fracture modes and "C" to indicate the critical stress intensity factor. The practical application of these theories (e.g. Griffith's theory and linear elastic fracture mechanics) primarily involves the determination of the stress threshold at which a crack will extend. As previously mentioned, the stress intensity factor depends on both the loading and the geometry of a crack.

The stress intensity factor for a tension crack of half-length a in an infinite plate and non-constant stresses $\sigma(x)$ acting perpendicular to the fracture surfaces can generally be calculated by integration (Paris and Sih, 1965; Tada et al., 1973):

$$K_{\mathrm{I}} = \frac{1}{\sqrt{\pi a}}\int_{-a}^{a}\sigma(x)\sqrt{\frac{a+x}{a-x}}\,dx. \qquad \textit{2-18}$$

Fracture propagation occurs once the stress intensity of the particular fracture mode $K_{(I,II,III)}$ has reached the material specific critical stress intensity factor $K_{(I,II,III)C}$ such that

$$K_{(I,II,III)} = K_{(I,II,III)C} \qquad \textit{2-19}$$

is satisfied. A typical range of critical stress intensity factors for tensile fracture of selected geological materials are shown in Figure 2-12.

2.1.4 Effect of pore pressure on the strength of rocks

Rocks are typically porous, with pore fluids exerting a significant influence on the mechanical rock properties, including strength (e.g. Handin et al., 1963; Byerlee, 1967; Murrell, 1965; Dropek et al., 1978; Cook, 1999). Two important ways that pore fluid influences rock strength are via: (1), the purely mechanical effect of the pore fluid and (2), chemical interactions between the rock and the fluid. In the first case, the pressure of the fluid causes a mechanical effect as water exerts hydrostatic pressure of the same magnitude in all directions. Therefore, the fluid in the pores counteracts the perpendicular stress component. Terzaghi (1936) first formalised this concept, known as the effective stress law, which is defined as the principal compressive stress minus the pore fluid pressure:

$$\sigma' = \sigma - \alpha_{eff} * P_p \qquad 2\text{-}20$$

where the effective stress is given by σ', principal stress σ, pore pressure P_p, and the effective stress coefficient $\alpha_{eff} = 1$.

Terzaghi's law, with coefficient $\alpha_{eff} = 1$, appears to have an empirical validity for the inelastic behaviour of rocks, including sandstone, limestone, dolomite, shale, and siltstone (Robinson Jr, 1959; Serdengecti and Boozer, 1961; Handin et al., 1963; Murrell, 1965; Dunn et al., 1973; Byerlee and Summers, 1975; Gowd and Rummel, 1977; Dropek et al., 1978; Schmitt and Zoback, 1989). However, this has often been challenged, with a number of studies showing that α_{eff} can vary depending on the properties of the rock (Zoback and Byerlee, 1975; Bernabé, 1987; Boitnott and Scholz, 1990; Gangi and Carlson, 1996; Kwon et al., 2001; McKernan et al., 2017). In the simple case of α_{eff} = 1, the effect of pore fluid on the strength is easily shown via Mohr's diagram (Figure 2-13) which assumes a saturated material under pressure. The diameter of the Mohr circle is unchanged, but translated to the left by an interval equal to the magnitude of the pore fluid pressure increase. This has the effect of shifting the circle closer to the failure envelope, promoting any affected rock mass towards failure. The reduction of shear strength can be shown mathematically by including the pore fluid pressure in the Mohr-Coulomb failure criteria:

$$\tau = c + \mu(\sigma_n - P_p). \qquad 2\text{-}21$$

The second case of rock strength weakening by pore fluid effects considers the chemical interaction of the pore fluid with the rock. Here, active pore fluids (water) activate the

mechanism of stress corrosion, whereby water molecules dissociate with the OH and H ions attaching to the Si-O2 bonds of quartz (in particular) weakening the bonds and promoting cracking. This is therefore especially prevalent at a crack tip where bonds are already stretched, and is further enhanced by acidic fluids and elevated temperatures (Atkinson, 1979a; Peck, 1983). The effect has been widely observed in quartz rich rocks, as well as limestone (Jaeger, 1963; Parate, 1973; Seto et al., 1997), coal (Price, 1960) and calcite-rich rocks (Rutter, 1972).

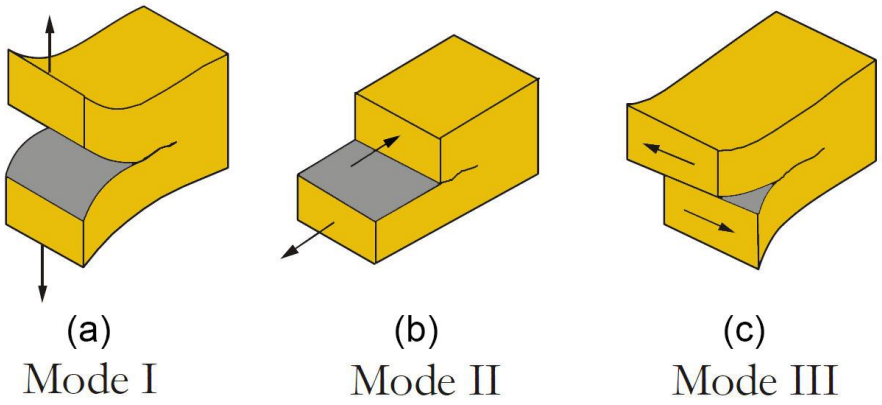

Figure 2-11: Schematic of the three basic crack surface displacement modes; (a) Mode I - tensile, (b) Mode II - in-plane shear mode, and (c) Mode III - tearing mode. Modified from Hudson and Harrison (2000).

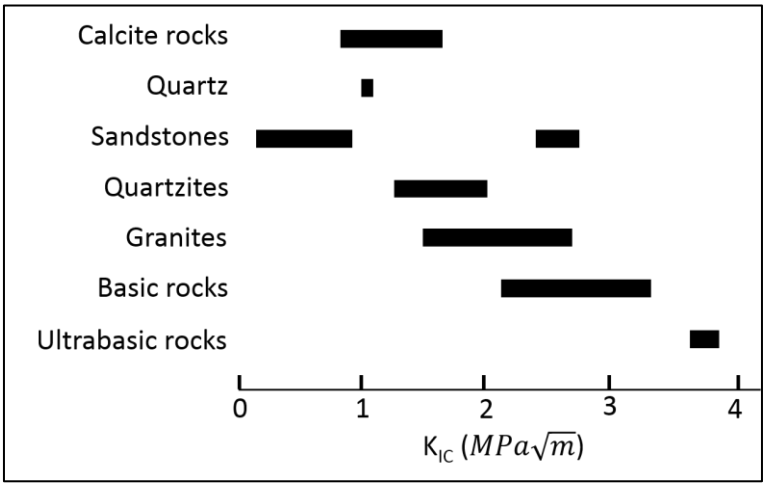

Figure 2-12: Critical stress intensity factors for tensile fracture mode (K_{IC}) of different rock types. Re-drawn from Heap (2009).

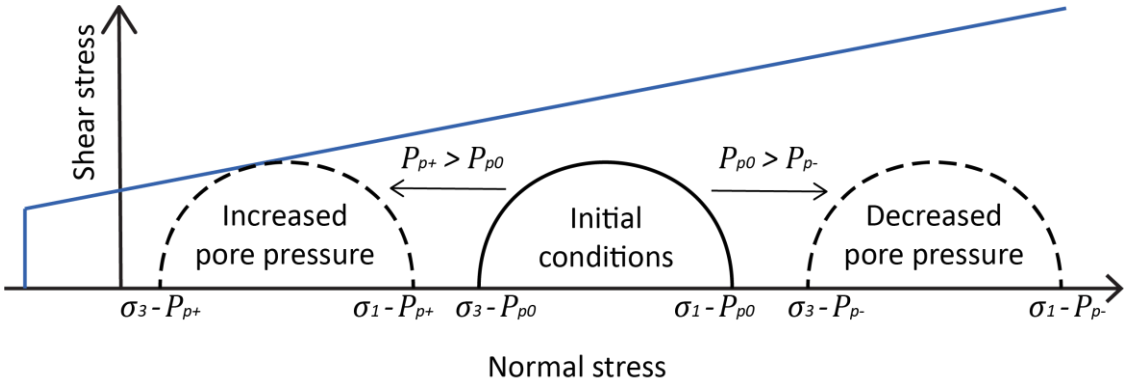

Figure 2-13: The effect of pore fluid pressure (P_p) on the strength of rock shown in the Mohr diagram. Modified from de Vallejo and Ferrer (2011).

2.2 Mechanics of hydraulic fracturing for the case of a pressurised borehole

In the previous section, the fundamentals of rock failure in the brittle regime and the effect of pore pressure on rock strength has been outlined. These are fundamental for the understanding of hydraulic fracturing and the mechanical process behind it. The following section will apply this knowledge to the engineering case of an overpressurised borehole and hence outline the fundamental mechanics of hydraulic fracturing.

2.2.1 Stress distribution around the borehole

The presence of a borehole distorts the pre-existing stress field in the rock (Figure 2-14). Here, stress concentrations develop in the direction of the principal stresses, with a concentration of compressive stress in the direction of the minimum principal stress and development of tensile stresses in the plane of the maximum principal stress. The present stresses can be separated in radial σ_r, tangential σ_θ and shear stress $\tau_{r\theta}$ components (Figure 2-14); the mathematics that describe the radial stress, tangential shear stress and circumferential stress as a function of radius from the centre and angle with respect to the principal stresses were first derived by Kirsch (1898), who provided a solution for the stress concentration around a hole in a plate subjected to a deviatoric stress.

Using the stress equations of Kirsch (1898), the stresses at a point r (outside the hole) can be expressed in polar coordinates with the centre of the hole as origin and uniaxial stress conditions (Hubbert and Willis, 1957):

$$\sigma_r = \frac{\sigma_H}{2}\left[1 - \frac{{r_i}^2}{r^2}\right] + \frac{\sigma_H}{2}\left[1 + 3\frac{{r_i}^4}{r^4} - 4\frac{a{r_i}^2}{r^2}\right] cos2\theta, \qquad \textit{2-22}$$

$$\sigma_\theta = \frac{\sigma_H}{2}\left[1 + \frac{{r_i}^2}{r^2}\right] - \frac{\sigma_H}{2}\left[1 + 3\frac{{r_i}^4}{r^4}\right] cos2\theta, \qquad \textit{2-23}$$

and

$$\tau_{r\theta} = \frac{\sigma_H}{2}\left[1 - 3\frac{{r_i}^4}{\mathrm{r}^4} + 2\frac{{r_i}^2}{r^2}\right] cos2\theta, \qquad \textit{2-24}$$

Here, σ_r denotes radial stress, σ_θ the tangential stress, and $\tau_{r\theta}$ the shear stress component; r_i is the radius of the hole, and θ-axis is parallel to the axis of the compressive stress σ_H.

Taking plane stress conditions with two regional principal stresses σ_H and σ_h at right angles, the above equations may be re-written as (Jaeger et al., 2009):

$$\sigma_r = \frac{\sigma_H + \sigma_h}{2}\left[1 - \frac{{r_i}^2}{r^2}\right] + \frac{\sigma_H + \sigma_h}{2}\left[1 + 3\frac{{r_i}^4}{r^4} - 4\frac{{r_i}^2}{r^2}\right]cos2\theta, \quad \textit{2-25}$$

$$\sigma_\theta = \frac{\sigma_H + \sigma_h}{2}\left[1 + \frac{{r_i}^2}{r^2}\right] - \frac{\sigma_H + \sigma_h}{2}\left[1 + 3\frac{{r_i}^4}{r^4}\right]cos2\theta, \quad \textit{2-26}$$

and

$$\tau_{r\theta} = \frac{\sigma_H + \sigma_h}{2}\left[1 - 3\frac{{r_i}^4}{\mathrm{r}^4} + 2\frac{{r_i}^2}{r^2}\right]cos2\theta, \quad \textit{2-27}$$

where the x-axis is aligned with the orientation of σ_H.

Stress distribution around the borehole due to internal pressure

During hydraulic fracturing, tensile fractures are generally induced by pressurising a wellbore internally using a fluid. The additional pressure inside the bore adds another stress field, which now needs to be considered. Hubbert and Willis (1957) did this by applying the Lamé solution (Timoshenko and Goodier, 1970) for stresses in a thick walled elastic cylinder, with a non-penetrating fluid. By increasing the outer radius of the cylinder, and reducing the external pressure to zero, the solution is well matched to the physics of the wellbore problem and thus to hydraulic fracturing. The stress distribution with only an internal borehole pressure is shown in Figure 2-15. The radial and circumferential stresses become (Hubbert and Willis, 1957)

$$\sigma_r = +\Delta P_w \frac{{r_i}^2}{r^2} \quad \textit{2-28}$$

$$\sigma_\theta = -\Delta P_w \frac{{r_i}^2}{r^2} \quad \textit{2-29}$$

where: ΔP_w is the increase in fluid pressure inside the borehole above the original pressure, r_i is the borehole radius and r is the distance from the centre of the hole. Note that the circumferential stress is now acting in a tensile manner.

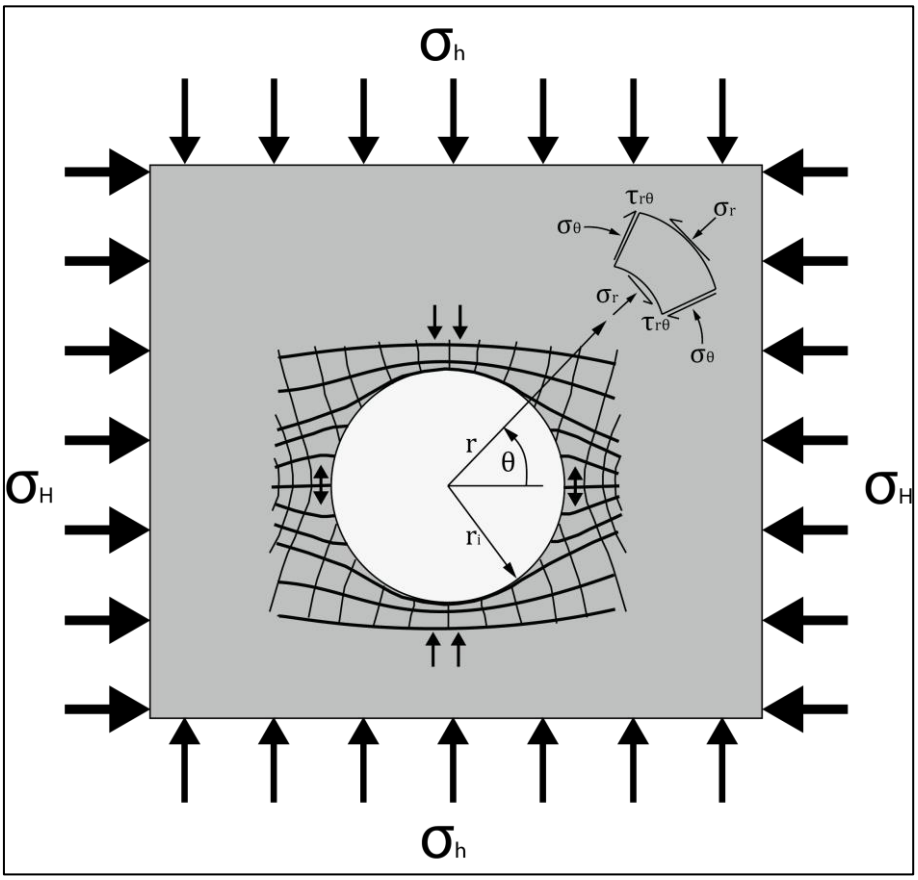

Figure 2-14: Problem geometry and nomenclature for the stress distribution around a circular hole in a biaxial stress field; stress directories indicate directions of principal stresses (σ_H and σ_h). Modified from Brady and Brown (2005).

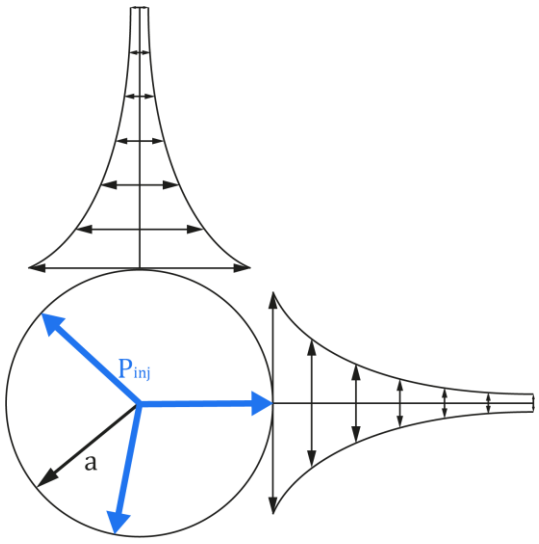

Figure 2-15: Stress distribution resulting from an internal pressure within a borehole. Modified from Hubbert and Willis (1957).

2.2.2 Continuum mechanics failure criteria for hydraulic fracturing

Linear – elastic criterion

By superimposing both the pre-existing regional stress and the internal stress, the injection pressure at which hydraulic fractures initiate (in tension) can now be derived (Hubbert and Willis, 1957). According to that model, hydraulic fractures initiate where the tensile stress is highest at the borehole wall and exceeds the tensile strength plus the minimum principal stress. In general, a hydraulic fracture will propagate along planes normal to the least principal stress, and therefore the minimum injection pressure should be equal to the least principal stress to keep the fracture open. Hubbert and Willis (1957) argued that the tensile strength of a rock can be neglected for field applications due to the abundant presence of joints with tensile strength reduced to zero. Strictly, this is not the case, especially for initially unfractured media. Adding this tensile strength of the rock finally yields the linear-elastic failure criteria for hydraulic fracturing (Scheidegger, 1962):

$$P_b = maxP_{inj} = 3\sigma_h - \sigma_H + \sigma_T - P_P \qquad 2\text{-}30$$

Where: σ_H and σ_h denote the magnitudes of the maximum and minimum principal far-field stresses perpendicular to the borehole axis, σ_T the tensile strength of the intact rock and P_P the initial pore pressure in the rock. The breakdown pressure P_b is equal to the maximum recorded fluid injection pressure ($maxP_{inj}$) in the borehole. Here, the pore pressure in the rock promotes failure by decreasing the required breakdown pressure via the conventional effective stress law.

Poro-elastic failure criterion

The linear-elastic approach does not consider poro-elastic effects caused by fluid infiltrating into the rock which adds another stress field and effects the breakdown pressure (Schmitt and Zoback, 1992, 1993). To address this shortfall of the linear elastic model, Haimson and Fairhurst (1967) proposed a poroelastic model for the calculation of the breakdown pressure to incorporate the poroelastic deformation and compressive circumferential stresses generated by the fluid infiltration (Lubinski, 1954). Haimson and Fairhurst (1967) superimposed the three different stress fields generated by: (1) non-hydrostatic regional stresses, (2) the pressurisation of the wellbore, and (3) the radial fluid flow through porous rock from the pressurised borehole into the formation due to the pressure difference between the borehole pressure and the pore pressure in the surrounding rock. For hydraulic fractures to initiate, the stress on the borehole wall needs to become tensile, which is only possible for the tangential stress. The effective tangential stress $\sigma_{\theta\theta}$ at the borehole wall is:

$$\sigma_{\theta\theta} = P_{inj} * \left(2 - \alpha \frac{1-2\nu}{1-\nu}\right) + 3\sigma_h - \sigma_H \qquad 2\text{-}31$$

The equation includes Biot's poroelastic parameter of rock, $\alpha = 1 - C_m/C_b$ (C_m is the rock matrix compressibility; C_b is the rock bulk compressibility), fluid injection pressure P_{inj} and Poisson's ratio ν (Schmitt and Zoback, 1989). Failure occurs when the tangential stress exceeds the tensile strength of the rock, $\sigma_{\theta\theta} > \sigma_T$. With $P_b = maxP_{inj}$, the breakdown pressure required to initiate hydraulic fractures (Haimson and Fairhurst, 1967) is given as:

$$P_b = \frac{3\sigma_h - \sigma_H + \sigma_T - \alpha \frac{1-2\nu}{1-\nu} P_P}{2 - \alpha \frac{1-2\nu}{1-\nu}}. \qquad 2\text{-}32$$

2.2.3 Failure criterion based on linear elastic fracture mechanics

Both the linear-elastic (equation 2-29) and poro-elastic criterion (equation 2-32) are based on the assumption that failure takes place when the effective tangential stress at the borehole wall reaches the tensile strength of the rock and do not consider the loading of crack faces by the pressurised fluid. However, this contributes to the stress intensity at the crack tip prior to fracturing and neglecting could result in overestimation of the required breakdown pressure (Abou-Sayed et al., 1978). Therefore, Abou-Sayed et al. (1978) considered a pressurised borehole in an infinite medium subjected to biaxial principal stresses with two pre-existing symmetrically opposite radial cracks (Figure 2-16) and proposed a revised model based on fracture mechanics concepts. The internal fluid pressure is assumed to act on the borehole wall and on the crack faces. For geometrical and loading conditions as shown in Figure 2-16, the breakdown pressure P_b can be obtained via (Abou-Sayed et al., 1978):

$$P_b = [1 - \mathrm{I}(\beta)] * \sigma_h + \mathrm{I}(\beta) * \sigma_H + \frac{K_{IC}}{f(a_0/r_i) * \sqrt{\pi a_0}} \qquad 2\text{-}33$$

Where: K_{IC} represents the fracture toughness for mode I (tensile), a_0 the initial crack length, r_i the borehole radius, $f(a_0/r_i)$ a function of the dimensionless crack length and borehole radius ratio, and $\mathrm{I}(\beta)$ is defined by:

$$\mathrm{I}(\beta) = \cos^2\beta - \frac{g(a_0/r_i)}{f(a_0/r_i)} * \cos 2\beta \qquad 2\text{-}34$$

where β is the angel of the crack plane with σ_H and the functions $g(a_0/r_i)$ and $f(a_0/r_i)$ have been calibrated by Paris and Sih (1965) and are given in Appendix A.2.

Another model for hydraulic fracturing based on linear-elastic fracture mechanics was suggested by Rummel (1987), who analysed the stress intensity near the crack tip by using the principal of superposition and included the stress intensity factors from discrete loading sources. These discrete loading sources are differentiated according to their cause (Figure 2-17); (1) maximum horizontal principal stress, (2) minimum horizontal principal stress, (3) internal fluid injection pressure, and (4) fluid pressure inside the fracture. In this model, the existence of a symmetrical double crack of half-length a is assumed, which is aligned along the direction of the maximum principal stress and extends from a circular borehole with the radius r_i in a intact infinite plate subjected to compressive principal stresses σ_H and σ_h. Fluid pressure is applied to the borehole and is also acting inside the fracture. This complex stress system can be described via (Rummel, 1987):

$$K_{\mathrm{I}}\left(\sigma_H, \sigma_h, P_{inj}, P_{frac}\right) = K_{\mathrm{I}}(\sigma_H) + K_{\mathrm{I}}(\sigma_h) + K_{\mathrm{I}}\left(P_{inj}\right) + K_{\mathrm{I}}\left(P_{frac}\right). \qquad 2\text{-}35$$

Where: K_I is the stress intensity for mode I crack propagation for each loading source, $P_{inj}$is the fluid pressure acting on the borehole wall and P_{frac} is the pressure acting along the crack surfaces.

The stress intensity factors resulting from the two principal stresses $K_{\mathrm{I}}(\sigma_H)$ and $K_{\mathrm{I}}(\sigma_h)$ neglect the existence of a pre-existing crack and were derived using the Kirsch solution (Kirsch, 1898):

(1) $K_{\mathrm{I}}(\sigma_H)$ → resulting from maximum principal stress

$$K_{\mathrm{I}}(\sigma_H) = -\sigma_H\sqrt{r}\, f_{\sigma_H}(b) \qquad 2\text{-}36$$

$$f_{\sigma_H}(b) = -2\sqrt{\frac{b^2-1}{\pi b^7}} \qquad 2\text{-}37$$

(2) $K_{\mathrm{I}}(\sigma_h)$ → resulting from minimum principal stress

$$K_{\mathrm{I}}(\sigma_h) = -\sigma_h\sqrt{r}\, f_{\sigma_h}(b) \qquad 2\text{-}38$$

$$f_{\sigma_h}(b) = \sqrt{\pi b}\left(1 - \frac{2}{\pi} sin^{-1}\frac{1}{b}\right) + 2(b^2+1)\sqrt{\frac{b^2-1}{\pi b^7}} \qquad 2\text{-}39$$

The other two loading sources are a result of the fluid pressure inside the borehole and inside the crack and given as:

(3) $K_{\mathrm{I}}(P_{inj})$ → resulting from the fluid injection pressure inside the borehole

$$K_{\mathrm{I}}(P_w) = P_{inj}\sqrt{r}f_{P_{inj}}(b) \qquad 2\text{-}40$$

$$f_{P_{inj}}(b) = 1.3\frac{b-1}{1+\sqrt{b^3}} + 7.8\frac{sin\left(\frac{b-1}{2}\right)}{2\sqrt{b^5}-1.7} \qquad 2\text{-}41$$

(4) $K_{\mathrm{I}}(P_{frac})$ → resulting from the fluid pressure inside the fracture

$$K_{\mathrm{I}}(P_{frac}) = P_{inj}\sqrt{r}f_{P_{frac}}(b) \qquad 2\text{-}42$$

$$f_{P_{frac}}(b) = \sqrt{\pi b}\left(1 - \frac{2}{\pi}sin^{-1}\frac{1}{b}\right) \qquad 2\text{-}43$$

In all cases (1) to (4) b is a function of the initial flaw length and the borehole radius and given as $b = 1 + a_0/r_i$.

The superposition allows the consideration of different scenarios of pressure distribution within the fracture. Here, only the scenario of a constant pressure $P_{frac} = P_{inj}$ acting over the entire length of the fracture is stated (Rummel, 1987). Finally, superposition of the different stress intensity factors above yield the breakdown pressure P_b which can be determined via (Rummel, 1987):

$$P_b = \frac{1}{f_{P_{inj}}(b) + f_{P_{frac}}(b)}\left(\frac{K_{\mathrm{IC}}}{\sqrt{r}} + \sigma_H f_{\sigma_H}(b) + \sigma_h f_{\sigma_h}(b)\right) \qquad 2\text{-}44$$

Where: K_{IC} is the critical stress intensity of the rock for pure mode I crack growth. P_b is a function of the borehole diameter and the initial length of the crack.

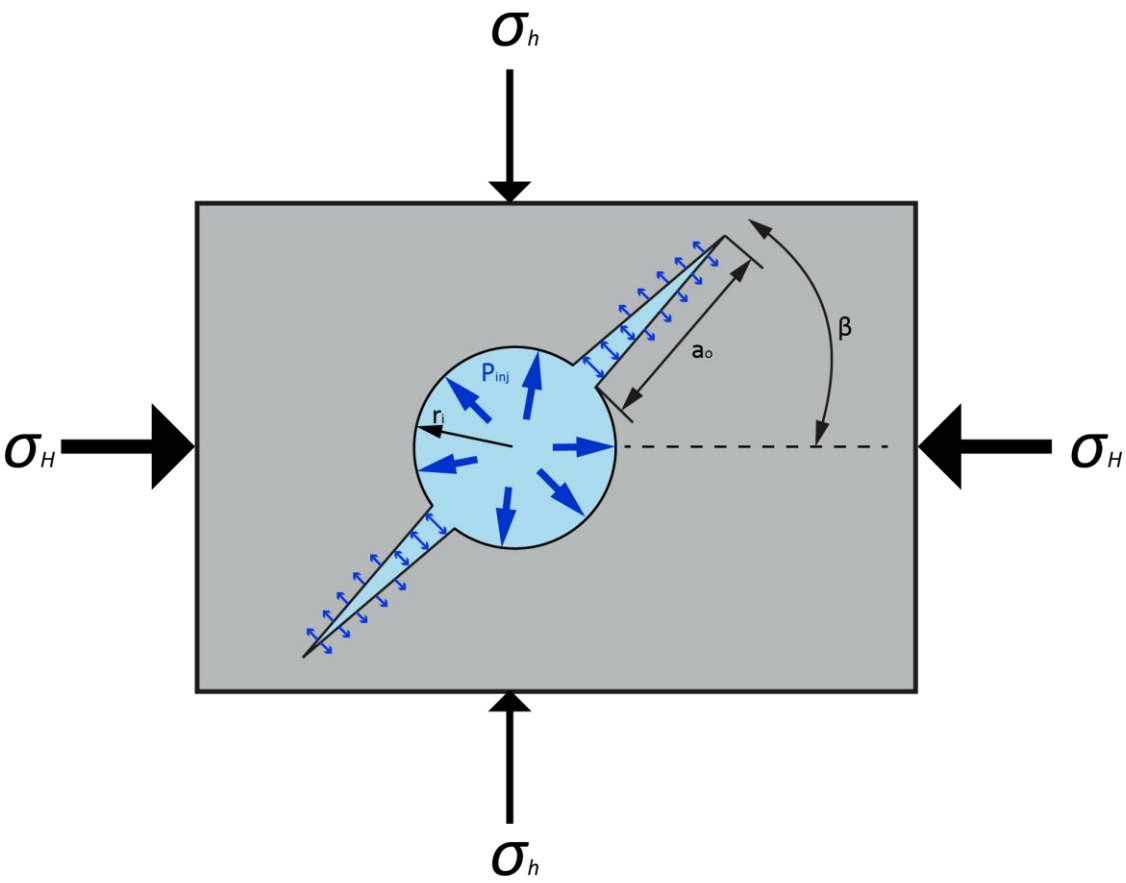

Figure 2-16: Fracture mechanics model of hydraulic fracturing with fracture in the borehole wall subjected to far-field stress and internal pressure. Modified from Abou-Sayed et al. (1978).

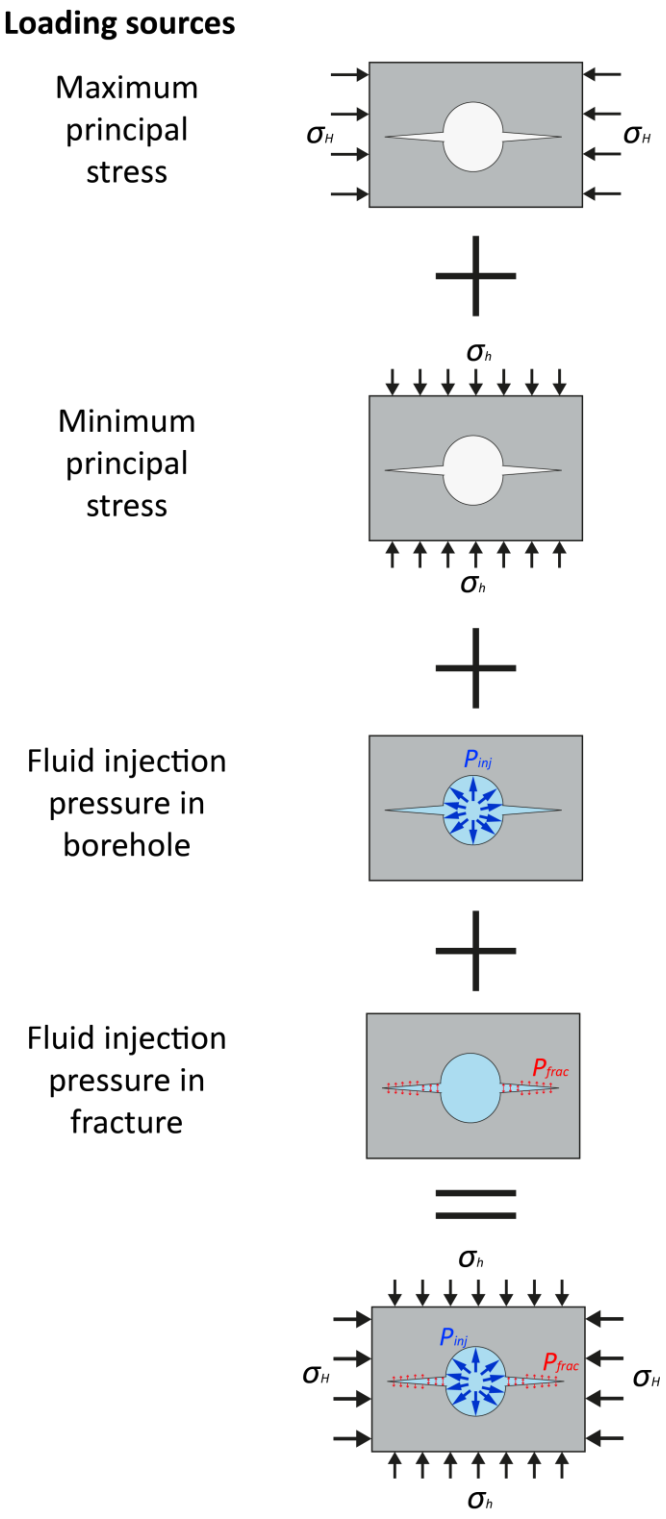

Figure 2-17: Fracture mechanics model of hydraulic fracturing derived by superposition of simplified loading sources found during hydraulic fracturing; symmetrical radial borehole under far-field stress and internal pressure. Modified from Rummel (1987).

2.3 Mechanics of internally pressurised thick-walled cylinders

In the previous section, hydraulic fracturing has been mathematically described for the general case of a borehole under field conditions. During hydraulic fracturing operations in the field (HF), sealed-off borehole intervals are internally pressurised with a fluid, where the fluid pressure is constantly increased until tensile fractures initiate and propagate (Chapter 1.2). A similar approach has been applied in the laboratory at a smaller scale, where cylindrical rock samples are fractured using fluid overpressure in a central conduit, and can be called micro hydraulic fracturing (MHF) to distinguish from field operations. However, in contrast to field operations, thick-walled cylinders have a finite outer radius and during laboratory experiments with thick-walled cylinders, the horizontal principal stresses are applied by the confining pressure P_c and are equal in all directions (Figure 2-18).

The stress distribution analysis for the thick-walled cylinders is based on the Lamé solution for an infinitely long elastic hollow cylinder (Timoshenko and Goodier, 1970). A linear-elastic solution for tangential σ_θ and radial stress σ_r distribution for a hollow-cylinder with an inner diameter r_i and outer diameter r_o subjected to internal and external boundary pressures is given by Timoshenko and Goodier (1970) as:

$$\sigma_r = \frac{{r_i}^2 {r_o}^2 \left(P_c - P_{inj}\right)}{({r_o}^2 - {r_i}^2) r^2} + \frac{P_{inj} {r_i}^2 - P_c {r_o}^2}{({r_o}^2 - {r_i}^2)} \qquad \textit{2-45}$$

$$\sigma_\theta = -\frac{{r_i}^2 {r_o}^2 \left(P_c - P_{inj}\right)}{({r_o}^2 - {r_i}^2) r^2} + \frac{P_{inj} {r_i}^2 - P_c {r_o}^2}{({r_o}^2 - {r_i}^2)} \qquad \textit{2-46}$$

Where: P_{inj} is the internal fluid injection pressure, P_c the confining pressure and r a radial distance from the axis of the cylinder. Tensional stresses are positive and compressional stresses negative.

The sum of the radial and tangential stress is constant throughout the thickness of the cylinder wall, therefore a uniform extension or compression is assumed in the direction of the axis of the cylinder (Timoshenko and Goodier, 1970). In the case of purely internal pressurisation ($P_c = 0$), equation 2-45 and 2-46 reduce to

$$\sigma_r = \frac{{r_i}^2 P_{inj}}{{r_o}^2 - {r_i}^2} \left(1 - \frac{{r_o}^2}{r^2}\right) \qquad \textit{2-47}$$

$$\sigma_\theta = \frac{{r_i}^2 P_{inj}}{{r_o}^2 - {r_i}^2}\left(1 + \frac{{r_o}^2}{r^2}\right) \qquad 2\text{-}48$$

From these equations can be seen that σ_θ is always a tensile stress and σ_r a compressive stress. The tangential stress is greatest at the borehole wall ($r = r_i$), where:

$$\sigma_{\theta max} = \frac{P_{inj}({r_i}^2 + {r_o}^2)}{({r_o}^2 - {r_i}^2)}. \qquad 2\text{-}49$$

And where $\sigma_{\theta max}$ is always numerically greater than the internal fluid pressure, but approaches P_{inj} with increasing outer radius. The internal fluid injection pressure is related to the tensile strength of the rock through (Clifton et al., 1976; Abou-Sayed et al., 1978):

$$\sigma_T = \left(P_{inj} - P_c\right) * \left(\frac{\left(\frac{r_o}{r_i}\right)^2 + 1}{\left(\frac{r_o}{r_i}\right)^2 - 1}\right) \qquad 2\text{-}50$$

The failure models for hydraulic fracturing from the borehole scenario can also be applied to the thick-walled cylinder arrangement. For $\sigma_H = \sigma_h = P_c$ the linear-elastic model (equation 2-30) reduces to:

$$P_b = 2P_c + \sigma_T - P_P, \qquad 2\text{-}51$$

and the poro-elastic model (equation 2-32) can be written as:

$$P_b = \frac{2P_c + \sigma_T - \alpha\frac{1-2\nu}{1-\nu}P_P}{2 - \alpha\frac{1-2\nu}{1-\nu}}, \qquad 2\text{-}52$$

When $\sigma_H = \sigma_h = P_c$, the angle β in the fracture mechanics model becomes irrelevant and equation 2-33 reduces to:

$$P_b = P_c + \frac{K_{IC}}{f(a_0/r_i) * \sqrt{\pi a_0}} \qquad 2\text{-}53$$

If the initial crack length a_0 is much smaller than the borehole radius ($a_0/r_i < 0.1$), equation 2-53 can be further simplified and the breakdown pressure can be determined via:

$$P_b \approx \frac{1}{2}\left(2P_c + \frac{K_{IC}}{0.6\sqrt{\pi a_0}}\right) \qquad 2\text{-}54$$

where K_{IC} represents the fracture toughness for mode I.

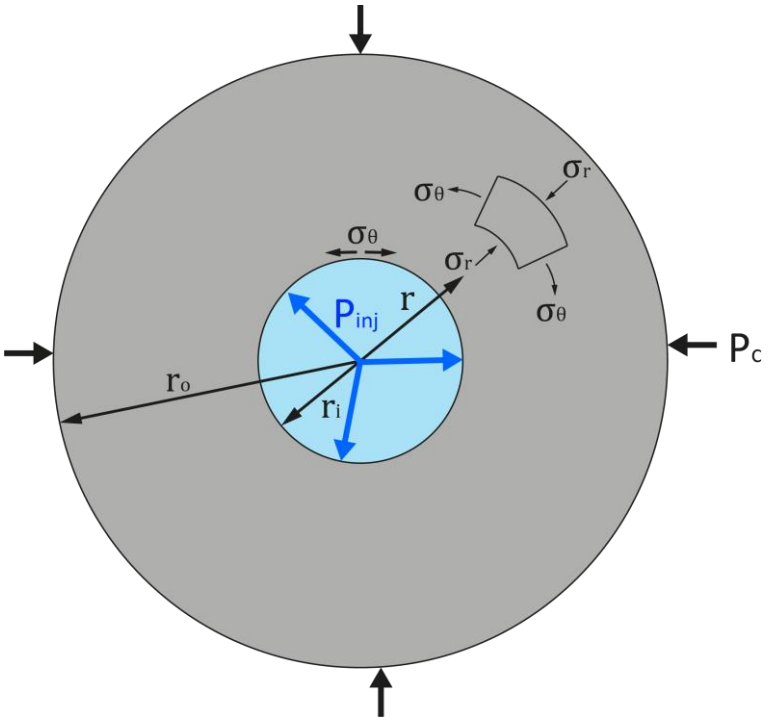

Figure 2-18: Cross sectional view of thick walled hollow cylinder of inner radius r_i and outer radius r_o subjected to an external pressure P_c and internal pressure P_{inj}. Modified from Schmitt and Zoback (1993).

2.4 Acoustic Emission (AE) as a rock mechanics tool.

Seismicity has become a key tool for monitoring many processes in the field such as volcanic activity (e.g. Malone et al., 1983; Power et al., 1994; Ohminato and Ereditato, 1997; Unglert and Jellinek, 2015), as well as engineered systems like geothermal reservoirs and mines (Collins et al., 2002; Dyer et al., 2008). Acoustic Emission (AE) is the laboratory analogue to field seismicity (Benson et al., 2007), referring to microseismic signals with much smaller energy transmitted compared to earthquakes, but with a higher frequency content (tens of kHz to MHz) as visualised in Figure 2-19. In that sense, AE can be treated as low-energy, but high frequency seismicity (Miller and McIntire, 1987; Benson et al., 2007). Acoustic emission can be used to understand the micro cracking process leading to failure and to study potential precursor phenomena by investigating the in-situ micromechanics of crack initiation, crack growth and failure of the sample under laboratory controlled conditions.

Acoustic emission is defined as a spontaneous transient elastic wave generated by the rapid release of energy within the material (Eitzen and Wadley, 1984). In rocks, localised and sudden release of elastic strain energy due to dislocation motion or crack growth causes elastic waves that travel through the material. These waves carry energy at all frequencies, but have a single or multiple distinct energy highs at specific frequencies, which can be used to characterise the event. AE laboratory studies focus mainly on the following aspects (Ohnaka and Mogi, 1982; Lockner, 1993): (1) observation of AE activity based on AE count prior to failure (or the cumulative numbers), (2) location of hypocentres of AE source events, (3) investigation of frequency characteristics, and (4) analysis of the source mechanism.

The origin of Acoustic Emission as a monitoring technique dates back to the work of Obert (1977) on geological materials in mines. Barron (1971) performed triaxial compression tests with basic AE equipment using sensors in the frequency range of 36 to 44 kHz. Byerlee and Lockner (1977) conducted the first laboratory based fluid injection tests in triaxially loaded porous rock samples accompanied by an AE monitoring system. Lockner et al. (1991) expanded on this, added an AE-based feedback loop to measure the entire stress strain curve of an axially compressed Westerly Granite. Lockner (1993) provides a review of the role of acoustic emission in the study of rocks and describes many applications. Since then, the importance of AE in geoscience has increased and many studies have been performed in the laboratory using AE to improve the understanding on the behaviour of geological material and processes. Rock deformation studies showed that seismic activity increases exponentially at the onset of fracture initiation (Martin and Chandler, 1994; Hoek and Martin, 2014). Using a multi-sensor setup, it is now common to track the 4D hypocentre location in a rock specimen of cm size, ranging from dynamic failure in volcanic basalt (Benson et al., 2007), to localised compaction

in sandstone (e.g. Baud et al., 2004; Stanchits et al., 2009; Fortin et al., 2009; Charalampidou et al., 2011), to fluid flow in porous media, both from the standpoint of rock-fluid resonance (Benson et al., 2008; Fazio et al., 2017) and mechanical stability (e.g. Thompson et al., 2005; Thompson, 2006; Thompson et al., 2009). Similar techniques have now been applied to true-triaxial apparatus (e.g. King et al., 2012; Nasseri et al., 2014).

As such, the use of AE as a laboratory tool is now firmly established as a key rock physics technique for the monitoring (Goodman, 1963; Scholz, 1968b) and localization (Mogi, 1968; Benson et al., 2007; Stanchits et al., 2014b) of fracture processes. The typical sequence of events leading to the detected AE signal on a computer is summarized in Figure 2-20. The signal generation and acquisition chain consists of four elements: (1) A source - event and wave generation, (2) wave propagation through material, (3) sensor – conversion of mechanical signal into a voltage, and (4) signal conditioning – processing of the signal for recording and interpretation usually with an amplifier and filter.

Stage (1): The AE process begins with an event, releasing elastic energy due to displacement at the particular location (source). Crack growth that instantly creates a new surface is a very good source for high-amplitude AE. As detailed earlier, cracks grow when the stress intensity exceeds a material dependent value. This can be caused by geometrical features like flaws, material changes or externally induced stresses. Another source is the collapse of pores (Fortin et al., 2006, 2007). Any fracture, flaw, pore or grain boundary is a potential AE source if strain occurs and surfaces moving relative to each other. These type of acoustic emission, where the source is created within the sample due to the processes above, is known as a passive event. In laboratory studies, active methods of AE recording are also employed regularly to characterise the rock material properties and response to mechanical or geological processes. For active AE recording, an artificial source emits a signal that travels through the material and is detected by a receiver. Examples are ultrasonic P-wave / S-wave velocity measurements or AE tomography. Stage (2): The acoustic waves propagate though the material, with the amplitude decreasing with time and distance. Attenuation is caused by geometric spreading, scattering and absorption (Hellier, 2001). These combined effects result in a decrease in amplitude of the advancing wave. In small laboratory specimens, however, attenuation is dominated by the inelastic response of the medium (heterogeneities), and the necessarily high frequencies usually used (500 to 800 kHz) for the sensors. For these reasons, for laboratory AE, attenuation is usually neglected. Stage (3): The acoustic wave is then received by several sensors mounted at known locations on the sample. AE sensors can be described as very sensitive microphones or high sensitivity geophones, converting mechanical strain waves into an electrical pulses using a piezoelectric element. Stage (4): This voltage is then conditioned by a band pass filter

to remove local 'hardware' noise and amplified, before being fed into a recording unit. Usually only a short window of the entire waveform is analysed at a time. To differentiate between real events and low amplitude background noise, a threshold amplitude is defined (Figure 2-21). The crossing of the threshold marks the start of the AE event and typical parameters of the event signal can be determined. Basic parameters include: duration time, time between first and last threshold crossing, peak amplitude, rise time, the time between first threshold crossing and peak amplitude, AE energy, the area underneath the signal curve, and AE count rate, the number of threshold crossing per unit of time.

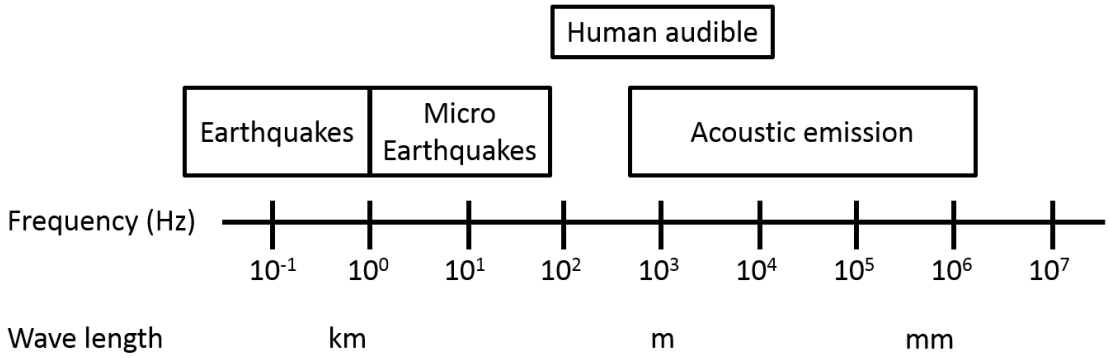

Figure 2-19: Classification of seismic signals based on the main frequency content. Modified from Hardy Jr (2005).

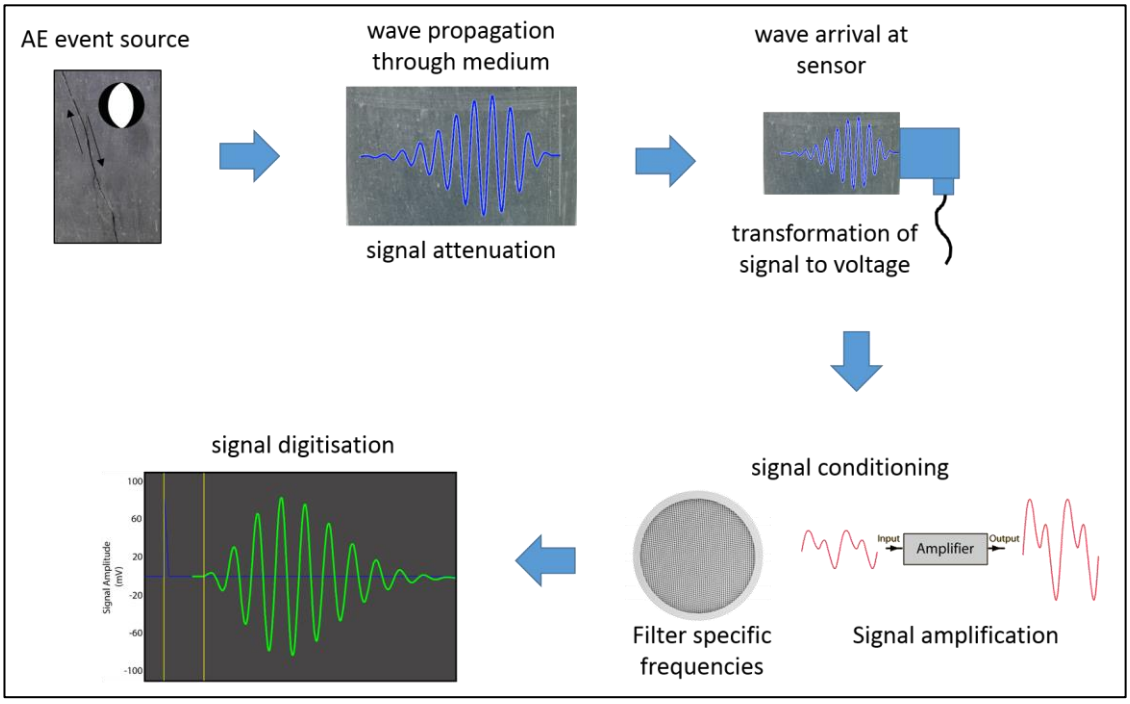

Figure 2-20: Schematic of the signal shaping chain

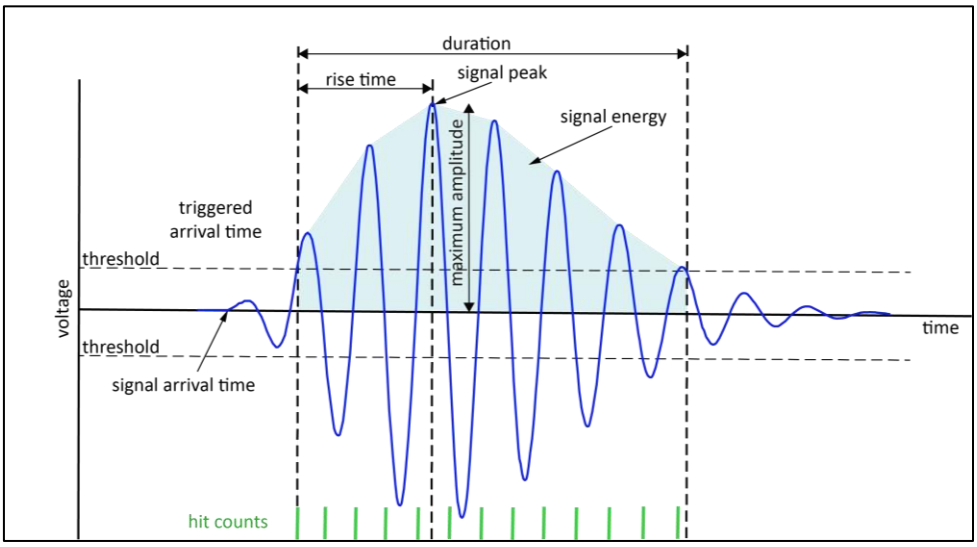

Figure 2-21: Characteristic parameters for acoustic emission signal evaluation. Modified from Grosse and Ohtsu (2008) and Zaki et al. (2015).

3 Experimental methods and equipment

3.1 Sample geometry and preparation

Coring was performed using a radial arm drilling machine fitted with a hollow, diamond tipped drill, followed by cutting and grinding to achieve right cylindrical cores of 40mm diameter and 90-95mm length. This process produces samples with a minimum diameter-length ratio of 2.25, and a parallelism accuracy of better than ± 0.1mm. When possible, test samples were cored from the same block of rock to minimise the effect of sample heterogeneity. Following sample preparation, samples were dried in an oven at 80°C for at least 24hrs. Rock samples were cored parallel (x-orientation) and normal (z-orientation) to inherent bedding (Figure 3-1). Bedding parallel to sample axis is indicated by the suffix "x" in the sample name and sample axis normal to bedding by "z". The orientation of the bedding planes in the samples has been confirmed afterwards using compressional elastic wave velocity measurements, assuming that the maxima measured V_P aligned with the direction of the bedding (e.g. Jones and Meredith, 1998; Benson et al., 2005).

In addition, specimens for hydraulic fracture tests were prepared with a central, axial-drilled conduit of 12.6mm diameter over the entire length of the sample. To date a large number of laboratory hydraulic fracturing studies have used a thick wall-ratio of the outer radius to inner radius of 10 or greater (e.g. Haimson and Fairhurst, 1969a; Zoback et al., 1977; Rummel, 1987). This has the advantage of simulating far-field conditions well although requiring a large pressure to initiate failure. Conversely, a lower wall-ratio generates a more uniform tensional tangential stress over the entire thickness of the sample wall. Here, a compromise was chosen with a wall ratio of approximately 3.2. A conduit over the full length of the sample was preferred to avoid any stress concentrations, and maintain uniform axial strain and plane stress conditions throughout the sample (mathematically described by the Lamé solution Chapter 2.3).

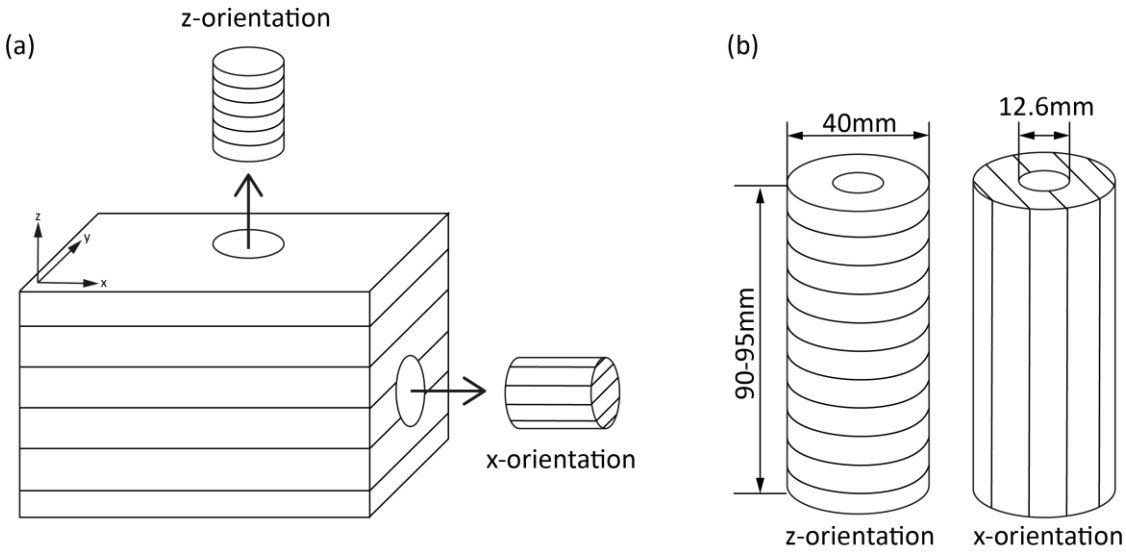

Figure 3-1: Sample preparation ; (a) Coring orientation relative to inherent bedding in rock block and (b) sample geometry and dimensions.

3.2 Equipment development

Although much equipment for tensile rock fracture is available, and methods well understood, simulating hydraulic fracturing via direct fluid pressure inside a triaxial cell required extensive development of a new, practical setup and experimental protocol. A number of equipment designs were needed to adopt the existing triaxial cell for this purpose, as detailed below.

3.2.1 Waterguide "fracker"

This simple device is needed to direct pressurised fluid into a section of the conduit, inside a sample, which is in turn inside a rubber jacket so as to impose sufficient pressure to induce tensile failure. The main design constraints were:

1. a tensile fracture needed to be initiated from a pre-defined sealed section inside the sample and that fracture was consistently initiated from the same section of the conduit,
2. the setup does not require extreme axial loads or differential stresses to maintain effective sealing,
3. avoid pressure build up or fluid migration at the top or bottom of the sample, where fluid pathways are shortest,
4. to initiate a hydraulic fracture from the exposed portion of the conduit, the injection pressure needs to exceed the confining pressure and therefore the borehole needed to be isolated from the rubber confining jacket and the confining medium,
5. the setup must not allow the mixing of the pressurising fluid with the confining fluid, to avoid contamination,

6. the setup needs to be easily adaptable for different rock types, bedding orientations and pressure conditions, and
7. employable using the existing triaxial apparatus.

From preliminary tests and background research it was clear that a downhole packer system similar to Schmitt and Zoback (1992) was required. Such a system works like a double-packer, used for field permeability measurements (Brassington and Walthall, 1985) creating a sealed section of conduit, which initiates fractures consistently from the same section of the conduit and avoids pressure build up or fluid migration at the top or bottom of the sample. The setup consists of two steel parts: the waterguide and the plug (Figure 3-2). Detailed technical drawings are provided in Appendix A.3. The lower waterguide has a hollow central stem to guide fluid into the sealed chamber, and the upper plug has a solid stem and acts as a seal only. O-rings on the top and bottom of the base plate prevent any water leakage as they create a face seal between the rock specimen and the steel guide, and the steel guide and the loading anvils respectively. An axial pressure just exceeding the fluid pressure is applied to create the axial seal, and keep the inserts in place. O-rings along the stem providing the sealing of the interval as there are pressed against the conduit wall. The length of the chamber formed by the assembly can therefore be modified by placing O-rings at different positions along the stem of the plug and water guide. Strictly, the O-rings also apply a small normal stress perpendicular to the sample axis. However, measurements of the sample diameter before and after inserting the steel guides did not show any differences, and examination of samples after the experiments did not show any O-ring induced normal stress effects. It is assumed that these effects are therefore negligible. The steel parts may be used with different diameters to vary the size of the chamber, and analyse the effect of the ratio of conduit diameter to sample outside diameter, i.e. the thickness of the wall, although this was not attempted here due to time constraints. Laboratory tests showed that the setup is reliable and produces reproducible results (as much as the natural variability of rock samples allows), with similar results observed for similar testing conditions. Therefore, all above mentioned design constraints were met.

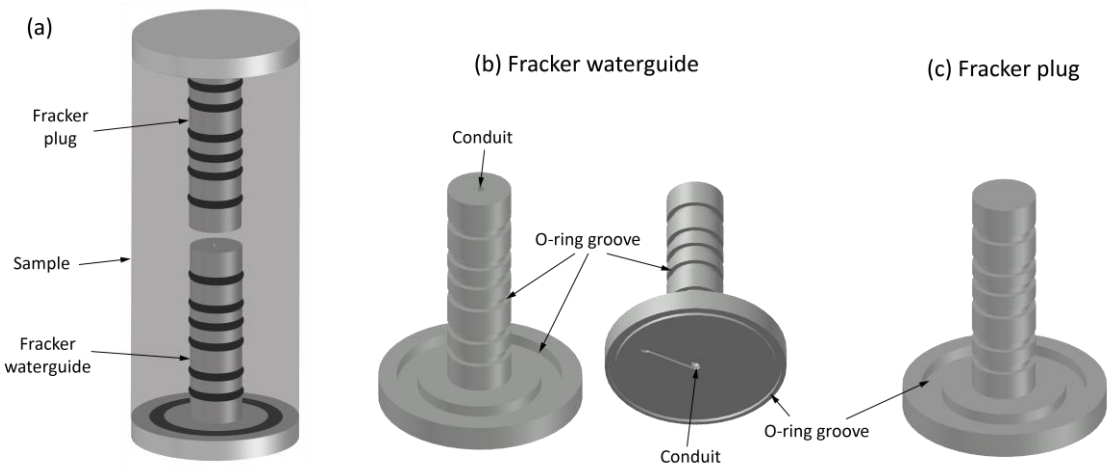

Figure 3-2: Schematic of Fracker ; (a) 3D view of Fracker setup inside the sample, (b) Fracker waterguide (top and bottom view), and (c) Fracker plug (top view, no central conduit).

3.2.2 Radial extensometers

The deformation of rock specimens (strain) is a key indicator to describe the progressive failure of rocks (e.g. Martin and Chandler, 1994). Therefore, measuring the radial deformation during the hydraulic fracturing experiments is likely to provide valuable insight, as the specimen deformation is highest in this mode due to the specific sample geometry used. For the measurements of radial deformation during the experiments inside the pressure chamber, a new approach was required as conventional methods, such as strain gauges and 'belts', could not be employed due to constraints of the triaxial and sample arrangements. The new design had to be sensitive to the micro-mm scale, as only very small deformations were expected, record at a high sampling rate, and withstand high pressures as installation was required within the pressure chamber to guarantee direct contact with the rock, putting further constraints on the size and location. Miniature 'intrinsically safe' Linear Variable Differential Transformers (LVDT, Type: PMAC-CD-Series, High temperature (up to 200°C) and pressure (up to 100 MPa) version from Macro Sensors) were selected and connected to a high-speed recording system. Two parts form the LVDT (Figure 3-3b); a body where a magnetic field is active, and a small metallic cylinder (core). Separate primary and secondary electric fields inside the LVDT body are affected by the position of the LVDT core; a conditioner (EAZY-CAL™ LVC-4000 LVDT Signal Conditioners from Macro Sensors) provides a voltage output that varies linearly depending on the core position inside the body. The LVDT's were part of a custom designed cantilever structure which is held in place by the engineered rubber jacket using the standard sensor ports. The cantilever structure consist of four cantilever arms which are free to rotate relative to each other at the corners (Figure 3-3a). The LVDT body is held by one of the cantilever arms, whereas the LVDT core is connected to another. These two cantilever arms, hence also the LVDT body and core, move relative to each other with any radial deformation of the sample (Figure 3-3d). This movement is converted into a voltage output, the magnitude depending on the degree of the movement of the LVDT core relative to the body.

Before installation, the LVDT's were calibrated for voltage output per mm movement (Figure 3-4). This allows the radial deformation of the sample to be derived by taking into account the geometry of the frame and lever-action of the trigonometry involved (1mm sample deformation providing 2mm LVDT movement, due to positioning). These "radial extensometer" (LVDTS with cantilever structure) were installed on the sample assembly above and below the pressurised chamber to measure radial deformation during the experiment (Figure 3-3c). The upper extensometer measures North-South deformation, whereas the lower extensometer measures the East-West deformation. Compressive stresses and compactive strains are considered positive. Once the required confining pressure is established, the zero

position of the LVDT's is recorded and the movement zeroed. Detailed technical drawings of the radial extensometers are provided in Appendix A.4.

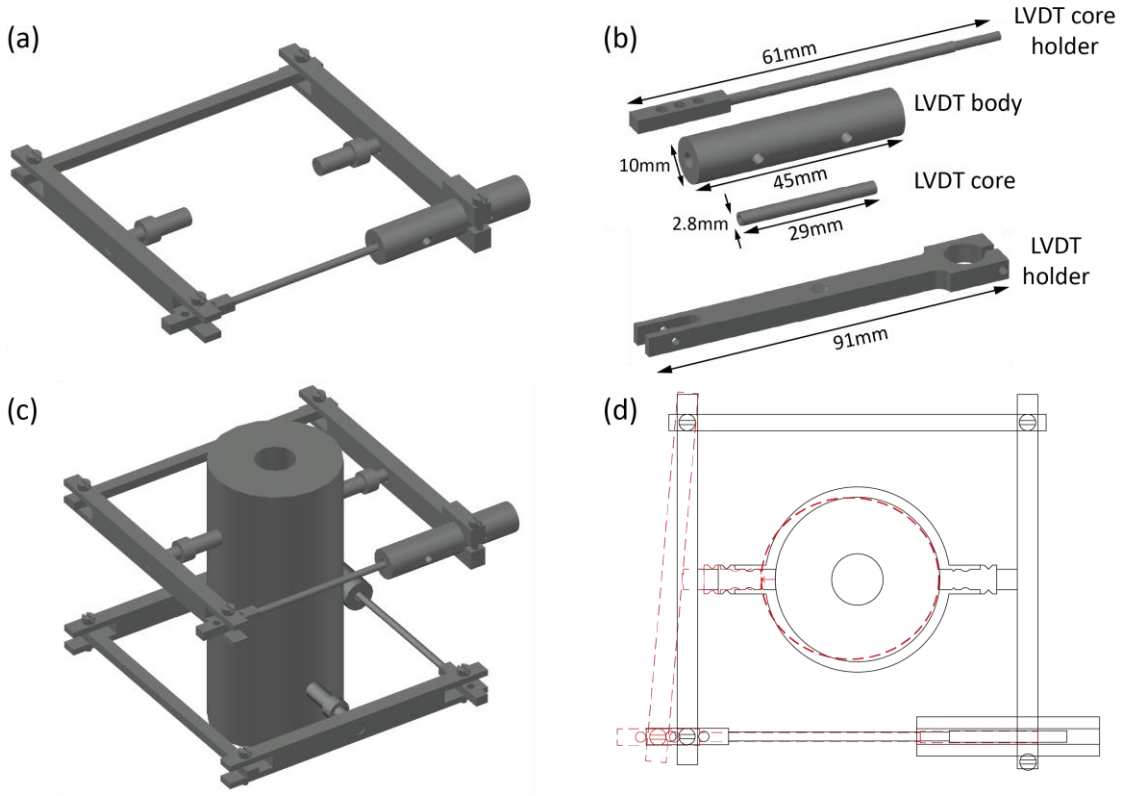

Figure 3-3: Radial extensometer ; (a) assembly 3D view; (b) LVDT parts; (c) extensometer setup with sample, and (d) schematic of radial deformation measurement (black – original position; red – new position radial deformation of sample).

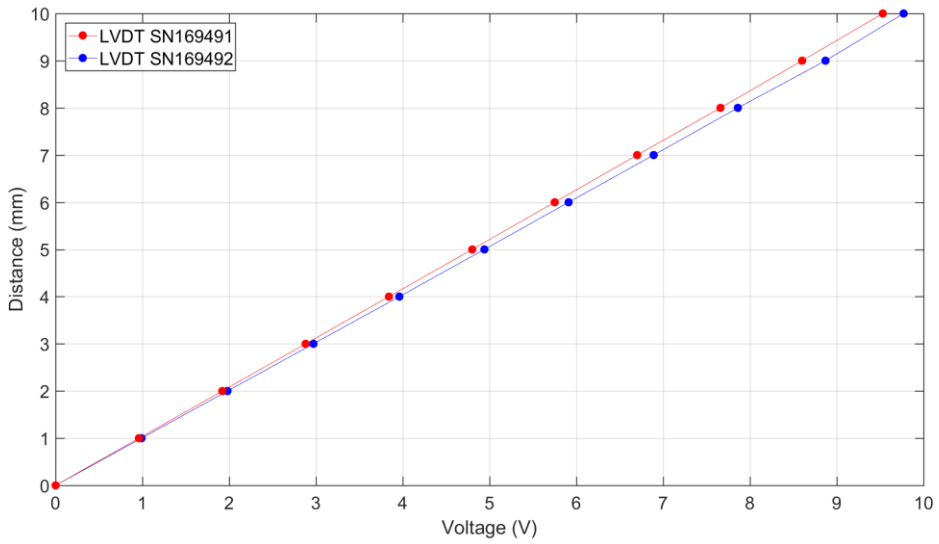

Figure 3-4: Calibration curve for miniature LVDT's.

3.2.3 Fluid separator

To evaluate the effect of different fluids to generate hydraulic fractures either the entire pore fluid injection must be re-filled with a new fluid, a time-consuming task, or some form of fluid separator added to the system. This latter solution was adopted, which needed to withstand high pressures and has a large volume to avoid refilling during the experiment. The fluid separator is a simplified pressure vessel which contains a central shuttle plug sealed by two O-rings (Figure 3-5). Detailed technical drawings are provided in Appendix A.5. The volume is 110mL, about 1/3 of the fluid pump volume and sufficient for a single hydraulic fracturing experiment. The shuttle is free movable in one dimension (along the borehole) transferring equal pressure from one fluid to the other. On both ends, flanges are screwed into the separator, again sealed by O-rings. A fine thread was used to increase the surface area, over which the applied pressure is distributed. Tests with fluid pressures up to 70MPa did not show any sign of leakage or fluid mixing. During use, the separator is installed between the fluid pressure pumps (upstream) and the fluid circuit inside the pressure chamber (downstream). The downstream side of the separator can easily be connected to the main oil reservoir of the triaxial apparatus to push fluid into the separator and move the shuttle upstream. Afterwards, the downstream is connected to the fluid pressure circuit again. The fluid pressure pumps applying pressure to the upstream site of the separator, which in turn moves the shuttle, transferring the pressure to the fluid in the downstream site. The fluid separator can be disconnected from the pressure system through valves on both sides.

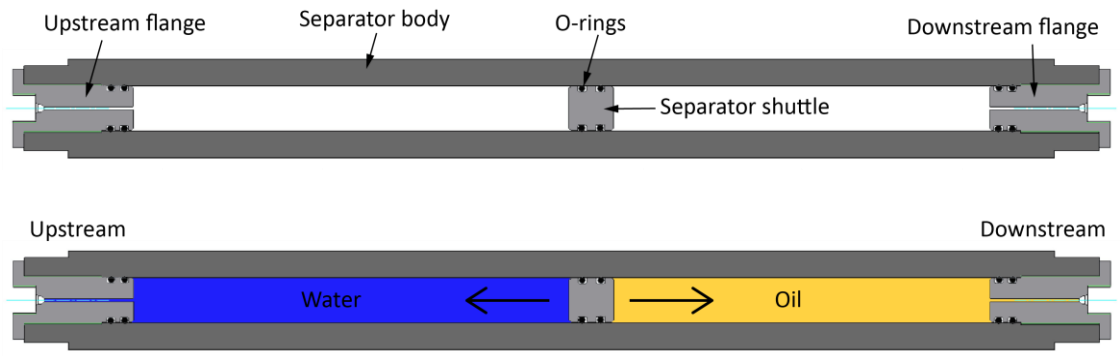

Figure 3-5: Schematic of fluid separator.

3.3 Laboratory setup and test procedure

An internally pressurised thick walled cylinder setup was chosen for these experiments, both to simulate the hydraulic fracturing architecture as close as possible, but also because this arrangement subjects the sample to a true tensile tangential stress near the conduit wall, which fails under tension. A series of hydraulic fracturing experiments were carried out by pressurising the internal bore with high pressure syringe pumps, with the sample mounted in a conventional triaxial cell (Sanchez Technologies, Core Laboratories) within a rubber jacket (Figure 3-6), allowing different confining pressure conditions (burial depths) to be tested. In detail, the apparatus incorporates a test chamber, which can be pressurised with either dry nitrogen gas (for pressures to approximately 10 MPa), or heat transfer oil (Julabo Bath fluid Thermal HS) for higher confining pressures to 100 MPa. Servo-controlled syringe pumps are used to apply axial stress via a piston-mounted pressure intensifier, which increases the 100 MPa pump pressure to a maximum 680 MPa axial stress across a nominal 40mm diameter sample. A second syringe pump provides confining pressure (oil), which is by-passed for low pressures, using a simple gas bottle/regulator.

An additional servo-controlled syringe pump supplies high-pressure pore fluid (distilled water) to the bottom end of the test sample, where the pore fluid circuit connects with the lower waterguide. This steel insert or 'waterguide' (Figure 3-6b and c) directs pressurized fluid into a sealed section of the axially drilled conduit, where the fluid applies a uniform pressure over the interval (Figure 3-7) and initiates tensile fractures from the pre-defined zone within the sample bore. The two steel inserts (described in chapter 3.2.1) create a sealed chamber in the centre of the sample using O-ring seals (Figure 3-6c and Figure 3-8b) and the pressurised volume can be expanded by removing O-rings. For all experiments, the maximum number of O-rings was used and the typical pressurised area was between 922 and 1240mm^2 (length between 17-25mm). Importantly, this arrangement does not require the use of a rubber lining inside the conduit so that the pressurized fluid is in direct contact with the rock, allowing to assess the initial generation of fractures and the competition between rock permeability and overpressure. To avoid sample failure during this preparation phase, the specimen is held in a V-block and pressure is applied normal to the bedding whilst the waveguides are inserted (Figure 3-9). Afterwards, the sample is visually inspected and the outer diameter measured again to check for eventual damage or lateral expansion (opening of bedding planes). To explore the key issue of anisotropy, and its influence on the fracture process, samples are orientated (drilled) with their bedding planes either parallel (x-direction) or normal (z-direction) to the major principal stress direction (σ_1).

The sample including the steel inserts (Figure 3-8a) is separated from the confining medium by an engineered rubber jacket (Sammonds, 1999) shown in Figure 3-6b, which is fitted with 20 ports to which sensors may be fixed to the sample whilst maintaining the seal. Here, 11 ports are used for lateral AE sensors, evenly distributed over the sample, and 4 ports for 2 extensometer, which measure sample radial deformation (Figure 3-6b and c). A typical sample setup commences by fitting the drilled samples with the steel waterguide, which is loaded together into the jacket. This entire assembly is then mounted inside the vessel, and then the radial extensometers and AE sensors are finally installed. Experiments are typically carried out in three consecutive loading phases (Stanchits et al., 2011). Firstly an initial triaxial stress (σ_1) and confining pressure (P_c) are applied until the required conditions are established, controlled by setting a stress-rate increase. A ratio between axial stress (σ_1) to confining pressure (P_c) between 2:1 and 4:1 was used, so as to establish a triaxial condition where samples were firmly held, and to prevent the subsequent injection fluid back-pressure from lifting the axial stress piston (the process of fluid-driven fracture necessarily require high injection fluid pressures). Standard triaxial deformation experiments of thick-walled cylinders did not show a significant reduction in compressional strength over the tested pressure range compared to samples with no central conduit (Figure 3-10). To be sure, during hydraulic fracture experiments the axial stress was set to never exceed 30% of the peak compressional strength of the rock. Furthermore, AE activity was closely monitored during loading to guarantee that the critical state is not approached. Secondly, to allow any seismic activity to decay to a background level, a minimum of 10 minutes was allowed before the pressurised fluid was injected. For this, distilled water was used to establish initial fluid pressure equal to confining pressure. The final stage, fluid pressure is increased at a constant flow rate until microscopic and macroscopic failure occurred. For shale, a flow rate of 1mL/min was used and when testing sandstone samples the pressure was increased with a flow rate of 5mL/min to account for the higher permeability of the sandstone compared to the shale. A constant flow rate was used instead of a constant pressurisation rate based on Zoback et al. (1977), who showed that fracture initiation pressures are rate independent when pressure is increased with a constant flow rate.

Figure 3-7 illustrates the loading configuration and accompanying stresses. As fluid pressure increases, it is clear the pressure will also attempt to move the waterguide vertically. Although a high axial stress is initially applied, as detailed earlier, during the experiment the axial stress is increased at the same rate as fluid pressure once fluid pressure was within 2 MPa of σ_1. Frictional forces additionally prevent a vertical movement of the steel guide which arise at the contact between the O-rings and the wall of the conduit.

Acoustic Emission (AE) events (passive seismicity) were recorded by eleven piezoelectric lateral sensors throughout the entire experiment. The sensors are evenly distributed around the sample, shown in Figure 3-11 both in 3D and in terms of a location map. For AE recording (digitisation of voltages) two separate systems are used, referred to as “triggered” and “continuous” data recording (Figure 3-12): this ensures that data loss is minimised, especially during the rapid fracturing process. The acquisition works in the following way. The triggered system consists of a 12 channel, 16 bit Digitizer (“Milne” acquisition unit) and a Trigger Hit Count unit which monitors the voltage level of the 12 inputs continuously, per channel at 10 MHz sampling rate. When the trigger hit count unit detects a sensor voltage above a given threshold on one channel, it triggers the digitizer to record the signal (waveform) on all channels. The recorded waveform is defined by a specified number of data points, of which a certain percentage (25%) is set before the trigger time (pre-trigger). However, due to the time needed to monitor the voltages, detect a threshold, and download the waveform to disk, the triggered system has a maximum number of events per second (about 30) that can be recorded. The triggered system is mainly used during the first two loading stages to monitor seismic activity levels. During the failure of the sample, the event rate is much higher and the trigger unit saturates, resulting in loss of data. To overcome this limitation the continuous recording system is employed in parallel, and activated during the final stage of the experiment when the fluid pressure is increased and hydrofracture imminent. This system consists of three 16 bit digitizers (“Richter” streaming units) each recording 4 channels simultaneously and continuously at 10MHz and streamed directly to a dedicated RAID0 hard disk system. Using this approach the entire signal is recorded, allowing for post-experiment processing, where the continuous waveforms are “harvested” to extract discrete events. This has the advantage that the harvesting can be run multiple times using different triggering criteria in order to maximise the number and quality of events. This is of great benefit, especially when working within the tensile failure regime, where on average, amplitudes are much lower compared to conventional compression experiments. The continuous data stream is split in minute long files to maintain a reasonable and workable file size, as each Richter unit generates a 4.3GB file per minute. Both systems are fed signals from the sensors, which filtered through a bandpass hardware filter/amplifier (“Pulser-Amplified-Desktop” or PAD unit) to remove local background noise, split, and independently amplified by 40dB and 60dB before entering the Richter and Milne unit respectively. The AE acquisition systems are visualised in Figure 3-12

The acoustic emission recording equipment (software and hardware) was supplied by Applied Seismology Consultants (ASC, now part of ITASCA), except for the sensors, which were custom designed in house by members of the Rock Mechanics Laboratory, University of Portsmouth.

Two types of sensors were used, sensitive to “high” frequencies to approximately 600kHz, and “low” frequencies to approximately 200kHz. These sensors (Figure 3-13) consist of a piezoelectric disk (active element) backed by a conductive copper plate (electrode), and a rubber/PTFE disc to insulate the electrode from a hex screw to keep the ‘stack’ in good contact with an aluminium waveguide, which sits in the engineered rubber jacket. The waveguide has a precise profile designed to fit into integrated seals in the jacket, preventing leaks. In the case of the high frequency sensors, an additional tungsten cylinder is fitted to reduce the ‘ringing’ or resonance effects of the bare unbacked PZT element, improving the signals. A combination of low frequency (LF) and high frequency (HF) sensors were used. Signals recorded by LF-sensors were filtered with a 10kHz-1MHz bandpass filter and signals recorded by HF-sensors with a 45kHz-1MHz bandpass filter. For both sensors, the frequency response has been measured. The LF-sensors are most sensitive to the 50-200kHz band, whereas the HF-sensors are sensitive in a wider band from 50-600kHz (Fazio, 2017).

The standard data recording system of the triaxial apparatus (stress, strain, fluid pressures) has a maximum recording frequency of 1 sample/second. From early preliminary tests it became obvious that a much higher sampling rate for the mechanical parameters was critical to capture the fracturing process in detail. Therefore, additional external pressure transducers (fluid pressure and axial stress) and Linear Variable Differential Transformers (LVDTs, for axial deformation) were installed and connected to a high-speed data logger (National Instruments USB X Series Multifunction DAQ) recording at 10,000 samples/second (10kHz). The NI X Series DAQ system is controlled by an application written by the author in LabVIEW, a commercially available system engineering software developed by National Instruments. The code and the user interface are attached in Appendix A.6. Bespoke radial extensometers (Chapter 0) were designed for the project to directly measure the radial deformation of the sample, and connected to the same high-speed recording system (10kHz). The high sample rate permitted a detailed analysis to be made of the mechanical response of the sample during hydraulic fracturing. However, to evaluate the seismo-mechanical response, accurate correlation of the seismic and the mechanical datasets was critical. To achieve this, the pore fluid pressure output (voltage) was split between the NI X Series DAQ system and one channel of the continuous recording system via an operational amplifier circuit (Figure 3-14). The core of the circuit is a precision current-loop receiver to convert a current input into a voltage output. The receiver consists of an operational amplifier, a resistor network, and a precision 10V reference. The operational amplifier circuit boosted the incoming current to a usable voltage between 0-2V, which was recorded by a Richter unit at 10MHz and the NI X Series DAQ system at 10kHz.

Continuous AE recording and high frequency mechanical data recording started at the same time as the fluid pressure ramp was initiated. Fluid injection pressure is recorded by both systems, so that datasets could be synchronised with a time accuracy of ±0.01ms. For experiments using oil as the pressurising fluid the same setup was used, except that a fluid-separator (details in Chapter 3.2.3) was installed between the fluid pressure pump and the waterguide to avoid oil contamination of the pump. External pressure transducers were installed on both sides of the fluid separator to compare fluid pressures. Following the fracturing experiments, samples were scanned using X-ray microcomputed tomography to identify and localise fractures.

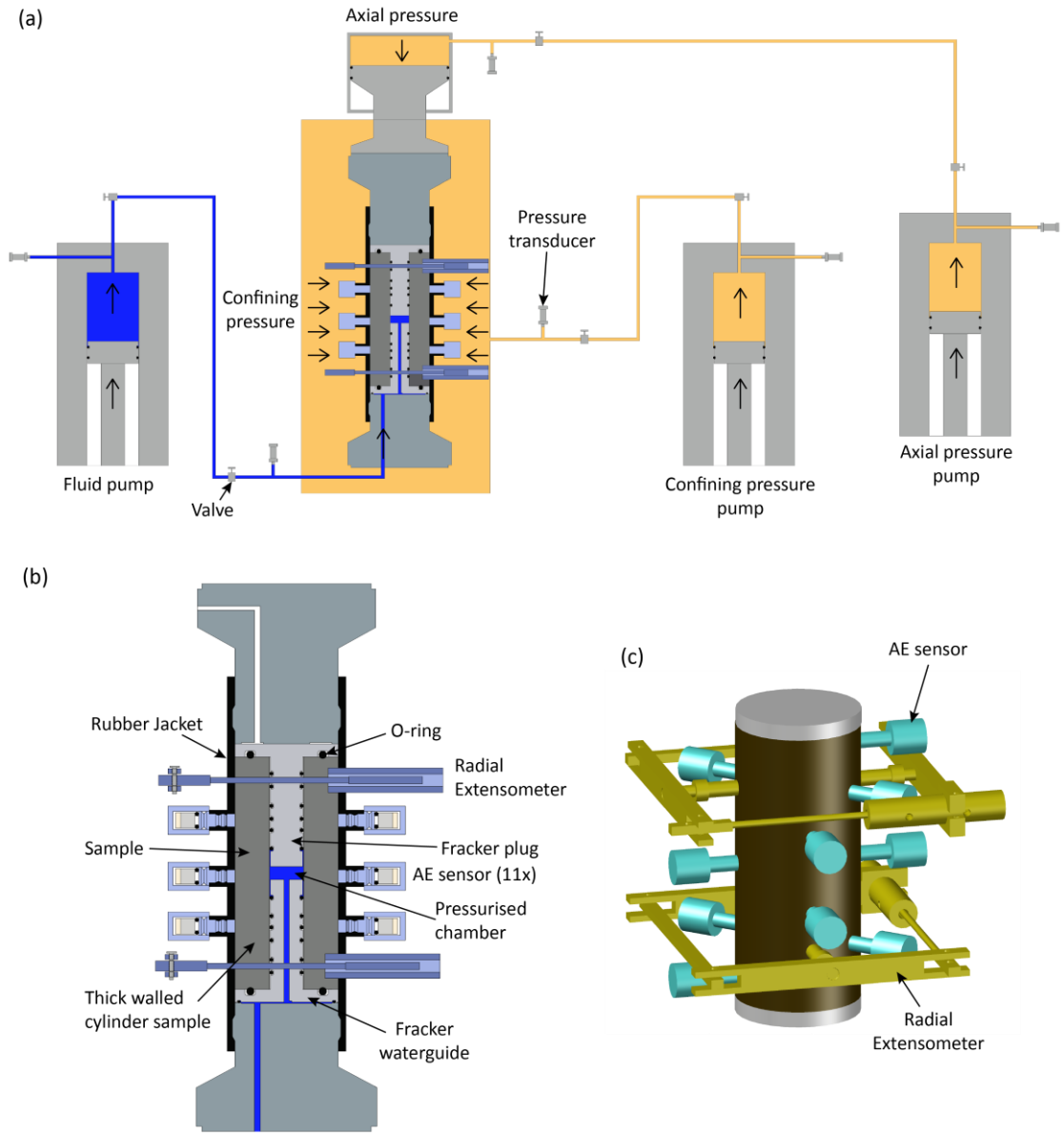

Figure 3-6: Hydraulic fracturing laboratory setup; (a) Schematic of the TRX apparatus setup for hydraulic fracturing experiment, (b) zoom in of sample setup, and (c) 3D view of the sample setup with AE sensors and radial extensometers (without rubber jacket).

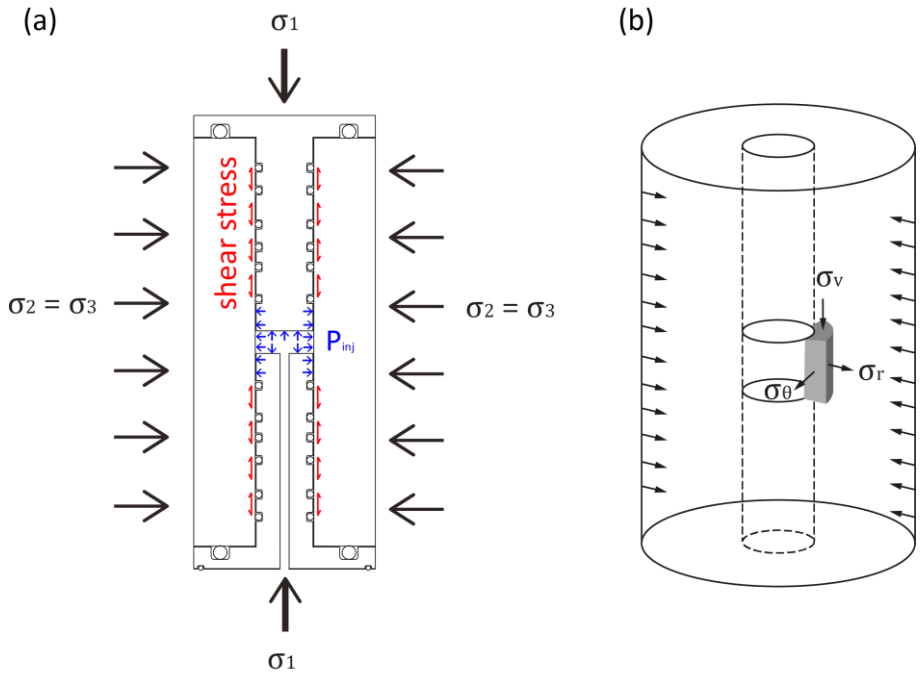

Figure 3-7: Loading configuration and accompanying stresses; (a) on surfaces and (b) inside the rock material.

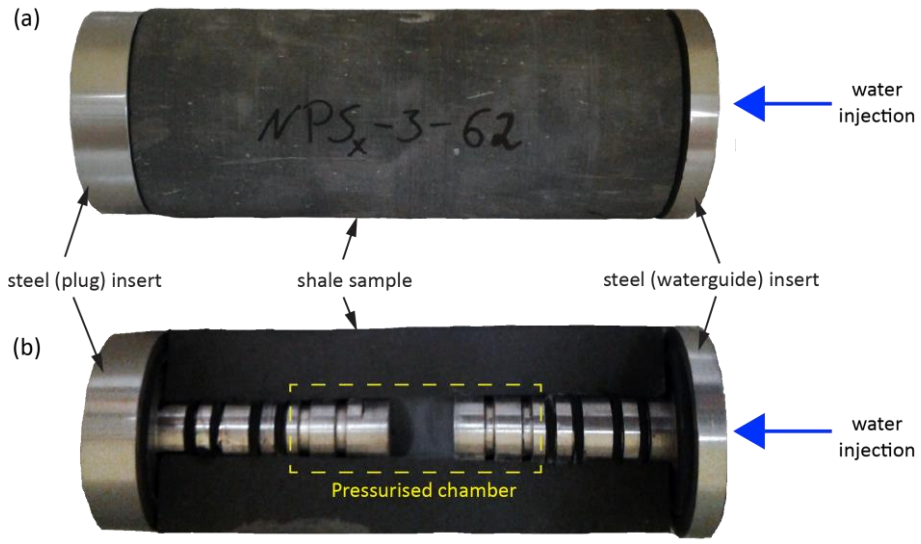

Figure 3-8: Hydraulic fracturing sample; (a) shale sample with steel inserts and (b) cut of shale sample with steel inserts showing pressurised chamber.

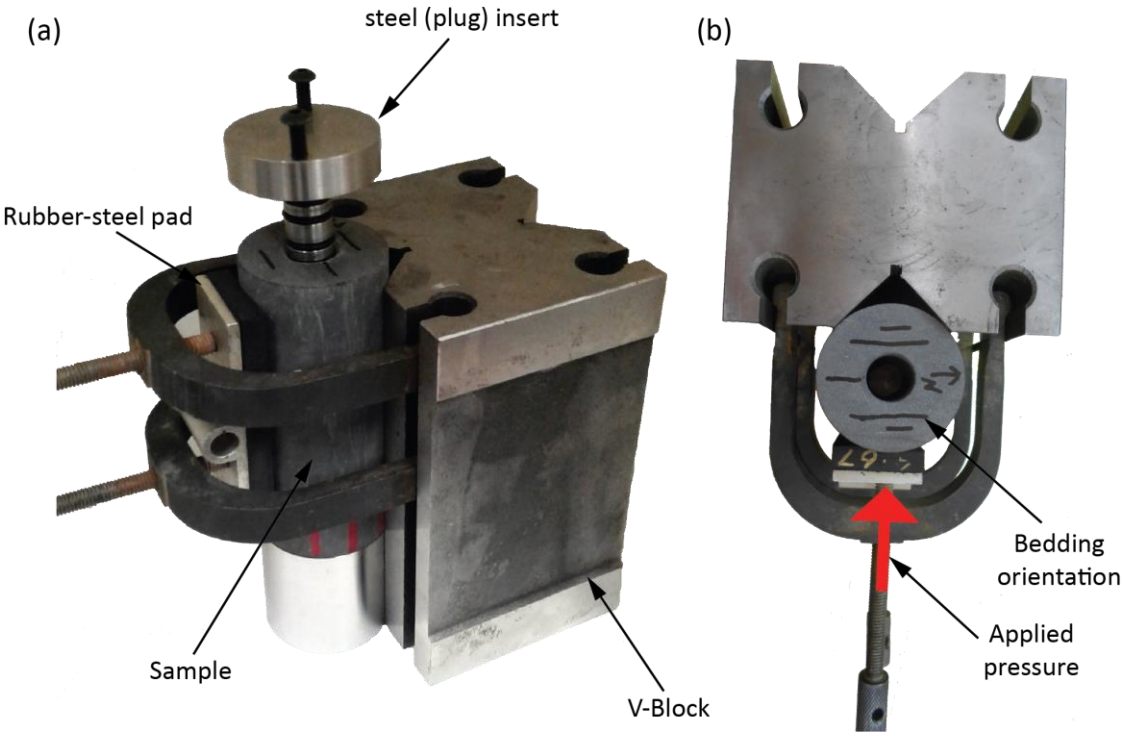

Figure 3-9: Sample support setup used when inserting the waveguide; (a) side view and (b) top view, pressure is applied by two screws and distributed over the length of the sample by the rubber-steel pad.

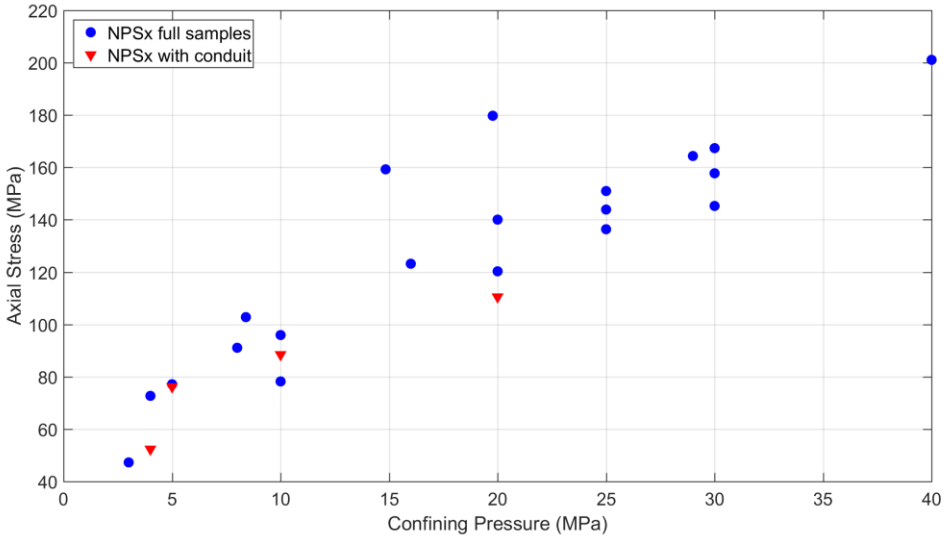

Figure 3-10: Strength comparison of full Nash Point Shale samples and samples with central conduit; axial stress applied parallel to bedding planes, triaxial experiments with Hoek-cell setup.

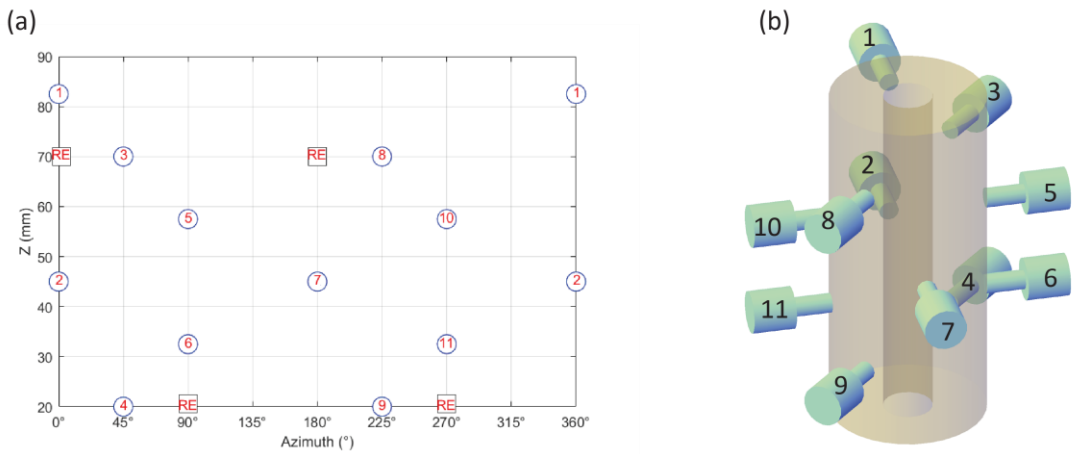

Figure 3-11: Acoustic Emission (AE) sensor configuration; (a) AE sensor location map and (b) AE sensor location 3D

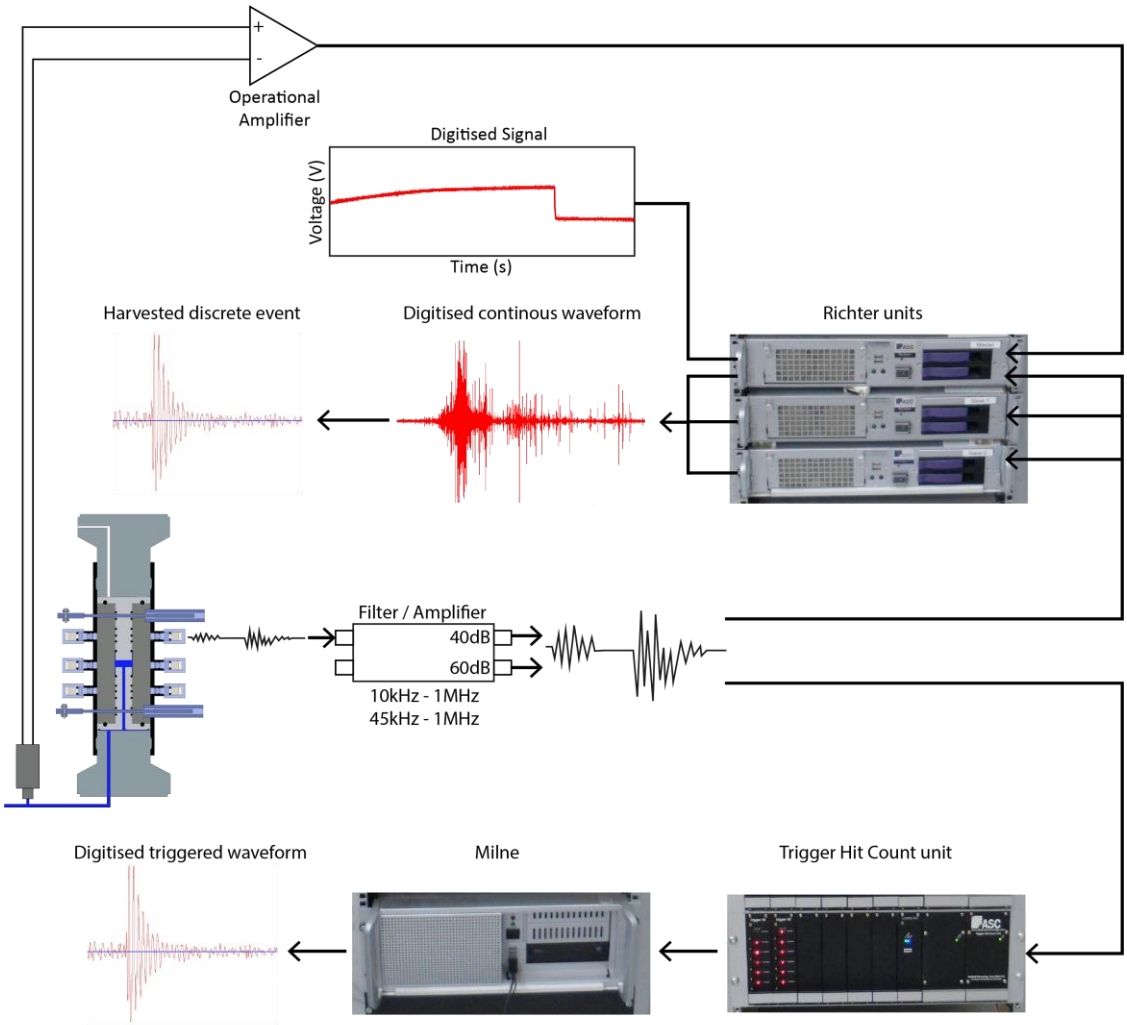

Figure 3-12: Schematic of acoustic emission acquisition system

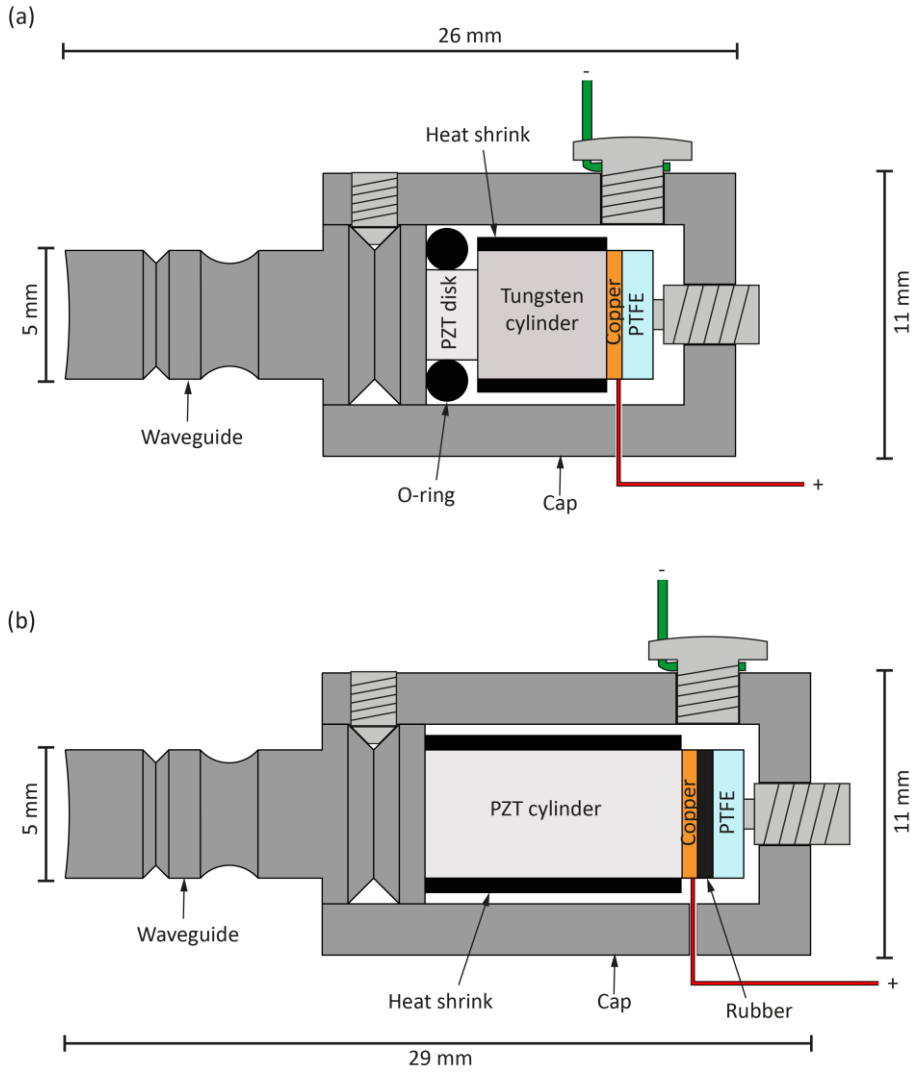

Figure 3-13: Schematic of AE sensors; (a) HF-sensor (frequency response up to 600 kHz) and (b) LF-sensor (frequency response up to 200 kHz). The PZT-crystal is isolated from the housing by an O-ring or heat-shrink. Modified from Fazio (2017).

(a)

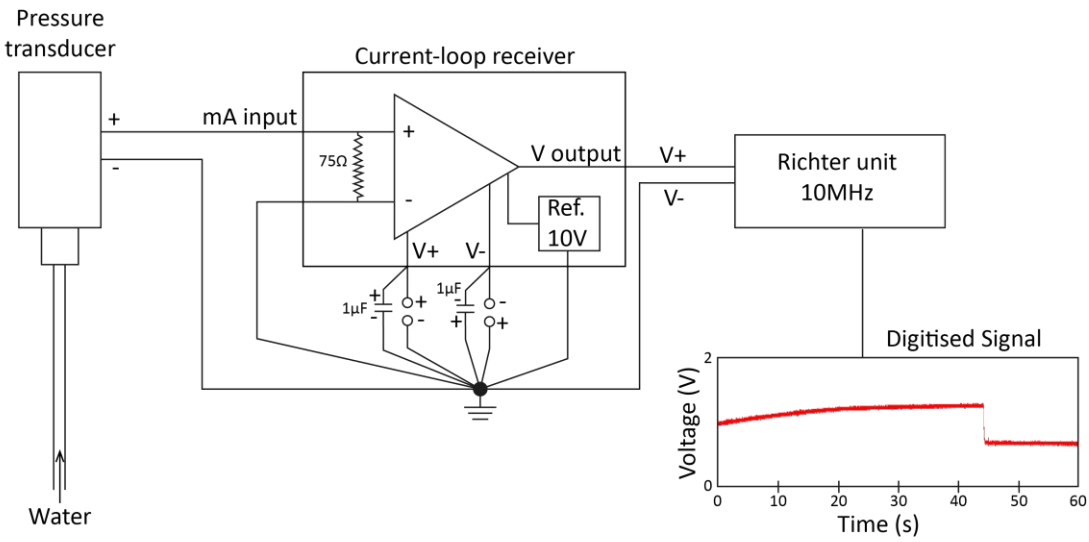

(b)

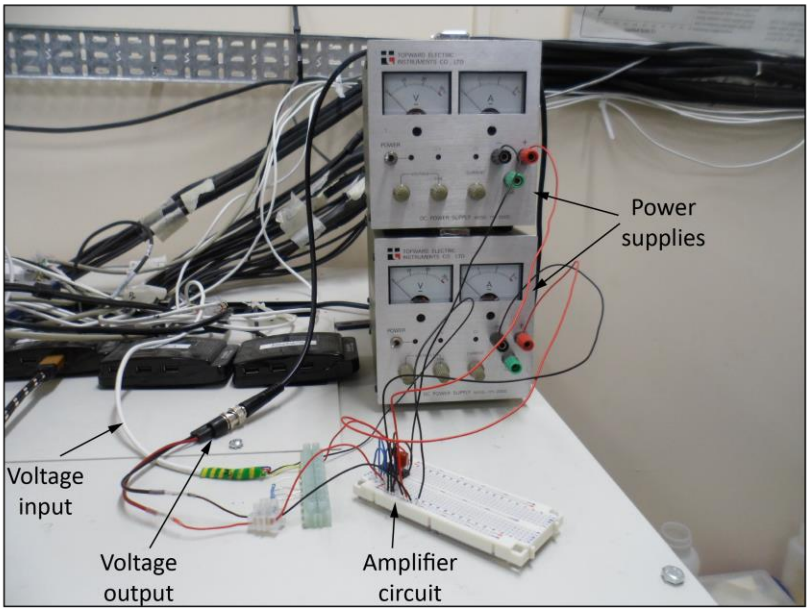

Figure 3-14: Operational amplifier; (a) schematic of signal amplifier circuit and (b) photograph of the setup.

3.4 Principals of X-ray microcomputed tomography and scanning parameters

Recent technological advances in X-ray Micro Computed Tomography (micro-CT) offer the possibility to investigate and reconstruct the three dimensional architecture of materials at scales ranging from micrometre down to atomic scales. Over the last two decades, micro-CT has been increasingly used in geosciences. Some examples are Denison et al. (1997), who used micro-CT tomography to quantitatively analyse the texture of metamorphic rocks, Ketcham et al. (2010) performing three-dimensional measurements of fractures in heterogeneous material, Dobson et al. (2016) capturing dynamic pore fluid transport processes in 4-D (3-D+time), Ma et al. (2016) and Ma et al. (2017) characterising shales in terms of porosity and organic content.

In simple terms, microcomputed tomography is an X-ray transmission imaging technique, where X-rays are emitted from a source, travel through the sample and are recorded by a detector to ultimately create a 3D-image of the sample. Scanning was performed on a Zeiss Xradia 520 Versa 3D X-ray microscope at the Technology Centre of the University of Portsmouth (Figure 3-15).

A photograph and a schematic diagram of the micro-CT system are shown in Figure 3-16. The fundamental components of the micro-CT system are the X-ray source, a sample stage, and a flat-panel detector. X-rays are generated inside the source, where a beam of electrons is accelerated by a voltage and directed onto a target (usually tungsten). The interaction of the fast-moving electrons and the target create x-rays, which are then transmitted through and around the sample (Du Plessis et al., 2017). As X-rays pass through the scanned object, some of the x-ray photons are absorbed while others are transmitted to the detector. Micro-CT requires two types of absorption; partial absorption, meaning that only some x-rays are absorbed by the material, and differential absorption, where different materials in the sample have different absorption characteristics to give a contrast (Du Plessis et al., 2017). The attenuated radiation (unabsorbed x-rays) is then collected by the detector and converted into a 2D projection image (Figure 3-17a), which consist of thousands of pixels and shows contrasts that are generated by differences in X-ray absorption arising from density differences within the sample (Denison et al., 1997). Once the image is taken, the sample is rotated by a fraction of a degree and another image is produced at the new position. At each step, several images can be taken and averaged to improve image quality and reduce noise. This procedure is repeated until the sample has rotated 360° producing hundreds or thousands of projection images, depending on the number of projections chosen. A higher number of projections improves the signal-to-noise ratio and hence image quality. After scanning, these projection

images are used to reconstruct a 3D dataset (Figure 3-17b), typically using the Feldkamp filtered back-projection algorithm (Feldkamp et al., 1984). The reconstruction process maps each voxel by using projection image representations of a particular voxel from many angles producing a representation of the actual X-ray density and hence brightness of that voxel (Du Plessis et al., 2017). These reconstructed images are also called cross sections or slices, as they show the inside of the sample as if 'sliced' along a plane. The reconstruction results in a stack of slices which can be used to view the internal structures and construct virtual three-dimensional volumetric models (Figure 3-17c).

The micro-CT procedure consist of many steps such as (1) sample preparation and mounting, (2) scanner setup and parameter selection, (3) scanning, (4) image reconstruction and (5) visualisation and analysis. Before the scan, silver paint marks were painted on each sample. These marks show in the micro-CT images and are used to determine the location of the fracture. Great care needs to be taken when preparing and mounting the sample. Movement of the sample during the scanning must be avoided as it will inevitably result in blurred images. The thick-walled cylinder samples were attached to a circular platform by using double sided tape and blue tack to fix the sample in a stable position (Figure 3-18a). Samples for high resolution scans where glued on a small pedestal using double sided tape and if necessary epoxy glue (Figure 3-18b). After the mounting, the sample was placed on the turntable inside the scanner and scan parameters were selected. X-ray voltage is highly dependant on the type, size and material composition of the sample and the most optimal material discrimination is usually obtained by using lower voltages (Du Plessis et al., 2017). However, as denser and thicker materials will absorb more x-rays, the x-ray penetration value might become too low, causing noise and potential artefacts. This makes it a challenge to find the right voltage as enough x-rays need to penetrate the sample but the lower the energy the better the resolution between the different greyscales in the images. For geological samples, the voltage should not exceed 100V, certainly never over 120kV (personal communication with Katherine Dobson, Durham University, 26/06/2017). Due to the high density of the rock material and the thickness of the samples, a glass-lead filter is placed between the source and the sample to increase x-ray transmission but also to pre-compensate for the eventual beam hardening due to the increased voltage. In combination with the filter, shale samples were imaged with 110 kV and 10 W/µA and sandstone samples at 100 kV and 9 W/µA. For all scans, between 3001 and 5001 projections were collected, with a 0.12-0.25 s exposure time, 7 or 8 images per imaging step and reconstructed using the Xradia proprietary software "ZEISS Scout-and-Scan Reconstructor" (filtered back projection) to achieve a 3D image of the sample. First a short pilot scan was taken on each fractured sample, where only a small vertical section of about 2mm in the middle of

the sample (same area as the pressurised chamber) was scanned at a resolution of about 31µm to confirm that a hydraulic fracture was created (Figure 3-19a). Additionally, the entire length (Figure 3-19b) of some samples were imaged at the same resolution to investigate any changes of the fracture network over the length of the sample. Samples of each rock type were then chosen for a high resolution imaging. The fracture location was marked on the sample to cut out the part of the sample containing the fracture (Figure 3-20). Afterwards, the cut off part of the cylinder was scanned at a lower energy (90kV and 8W) over the entire length to achieve a 3D image with a 9 microns voxel resolution. The high resolution images were used for a more detailed analysis of the fracture geomorphology (Figure 3-20d) and to create a 3D volumetric visualisation of the fracture to assess the roughness of the fracture surface and the interplay with the surrounding rock fabric. Scans took from 2hours up to 24hours depending on resolution and size of the scanned area.

Figure 3-15: Photograph of the Zeiss Xradia 520 Versa 3D X-ray microscope at the Technology Centre of the University of Portsmouth, which has been used for the micro-CT scanning in this study.

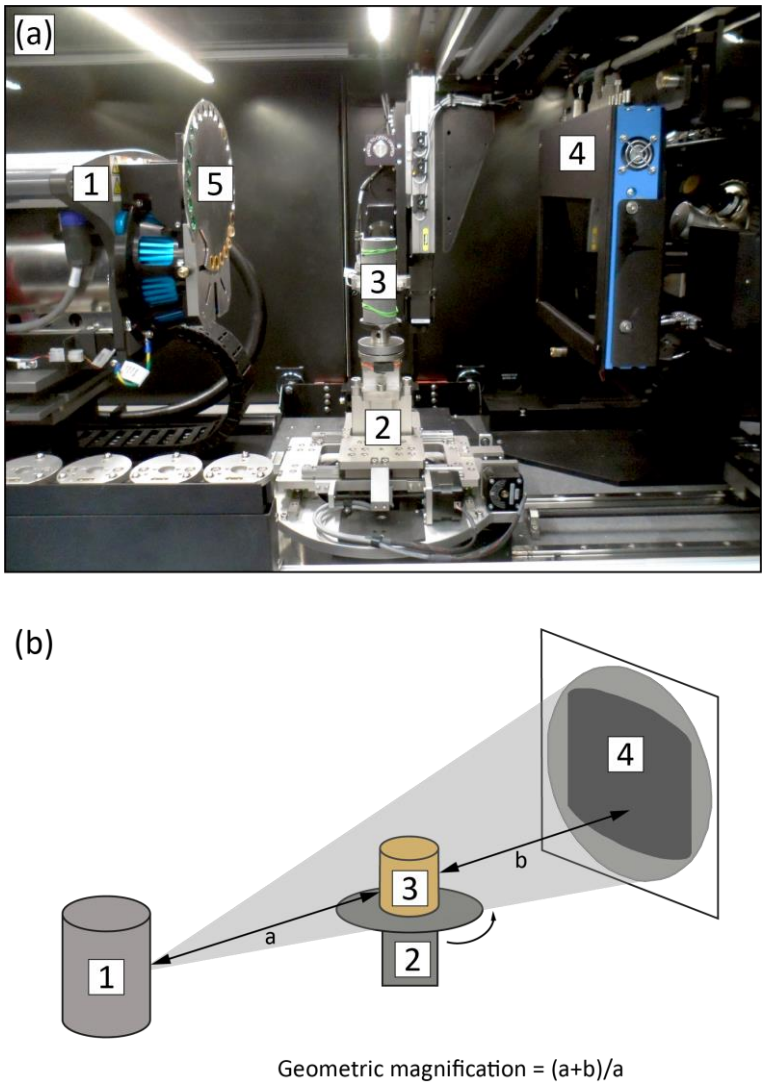

Figure 3-16: Micro-CT system; (a) Photograph of the micro-CT scanner used for this study and (b) schematic diagram of micro-CT architecture, showing the fundamental components of the setup; (1) X-ray source, (2) sample stage (turntable), (3) sample, and (4) flat-panel detector. The Zeiss Xradia 520 Versa also has a beam filtering system (filter placed between X-ray source and sample) installed with series of filters of different thickness (yellow and green) (5). The X-ray source and the Flat Panel Detector remain stationary while the sample on the turntable is rotating.

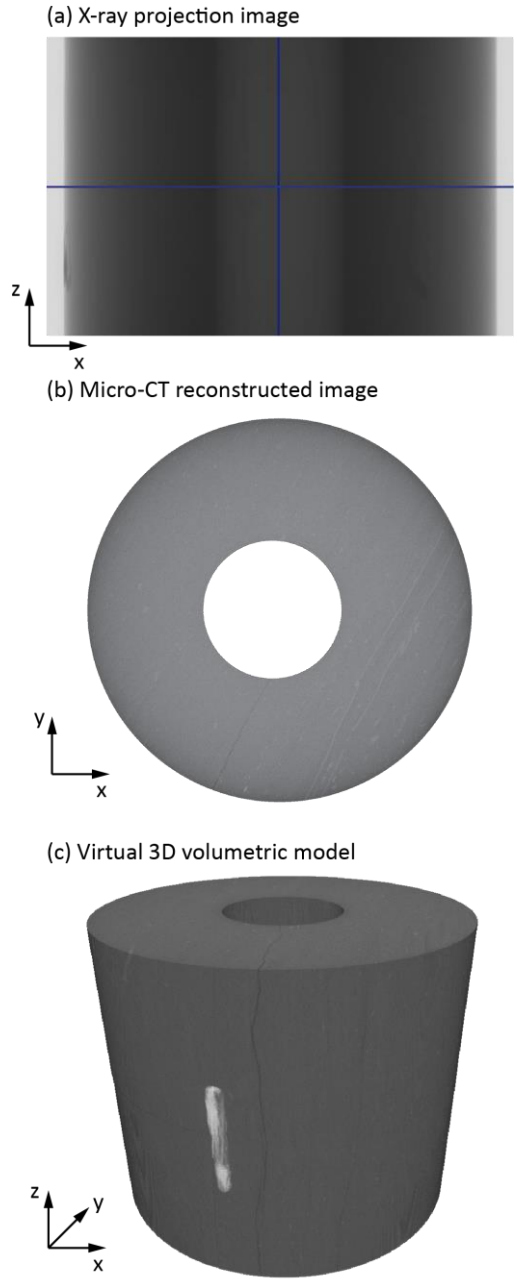

Figure 3-17: Images created during the micro-CT process; (a) X-ray projection image, (b) reconstructed image (slice) and (c) virtual 3D volumetric model.

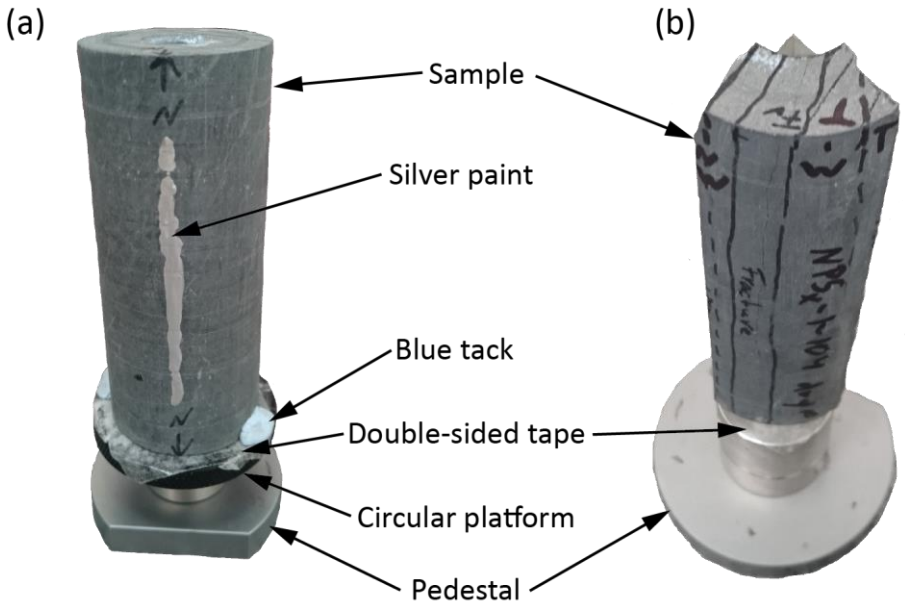

Figure 3-18: Sample preparation and mounting for micro-CT scanning; (a) thick-walled cylinder for low resolution scanning (31µm) and (b) cut sample for high resolution scanning (9µm).

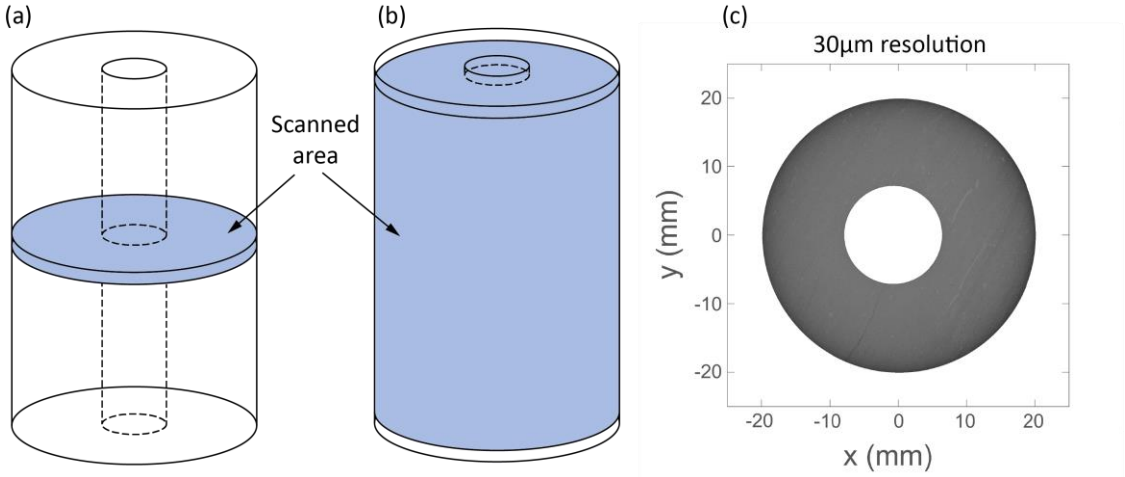

Figure 3-19: Low resolution CT imaging areas of HF samples; blue indicates the scanned area, (a) pilot scan area, (b) scan area for entire sample, and (c) example of an imaged slice at 31µm resolution.

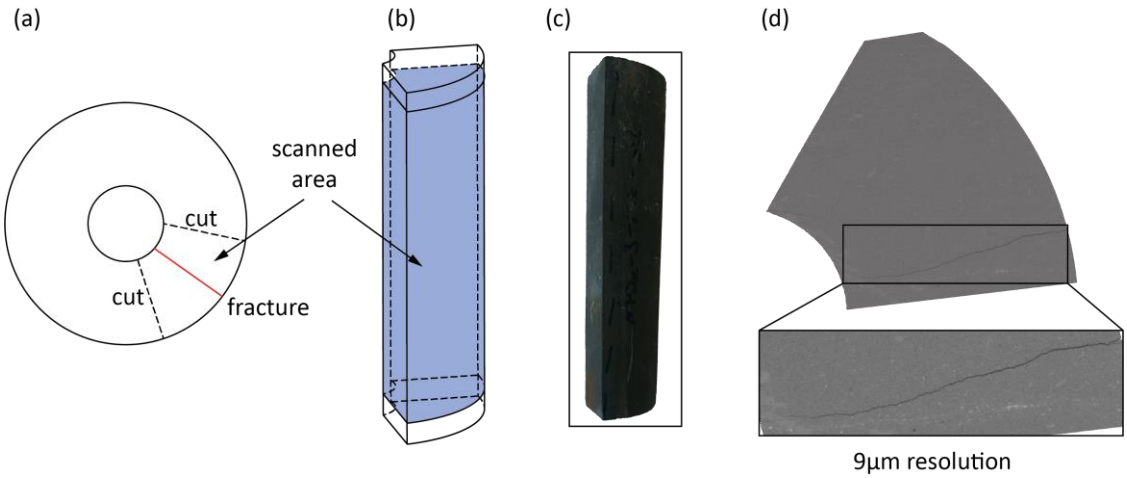

Figure 3-20: High resolution CT imaging sections; (a) section of sample for high resolution imaging, (b) scanned area of cut-off containing the fracture (highlighted in blue), (c) image of cut sample, and (d) example of an imaged slice at 9µm resolution.

3.5 Data processing

In the previous two sub-chapters, it was described how experimental and imaging data was generated for this study. This data also needs to be processed and analysed, which is described in the following section.

Mechanical and AE data processing

Hydraulic fracturing experiments produced mechanical (fluid injection pressure, radial deformation) and seismic data (continuous and triggered waveforms) which have been processed sequentially for successful experiments. All the processing has been done using either MATLAB® (matrix laboratory), which is a numerical computing environment and proprietary programming language developed by MathWorks, or InSite-Lab™, a commercially available acoustic emissions and ultrasonic survey processing software package developed by ITASCA IMaGE. The processing of the mechanical and AE data is outlined as follows:

Seismic data formatting: The continuous stream dataset was formatted using InSite-Lab. The formatting is required for visualisation and analysis of the data stream in both time and frequency domain. After formatting, the complete time-series is displayed as a waveform (voltage) (Figure 3-21a and b) and the complete frequency series as a spectrogram (Figure 3-21c). This allows for a first initial data analysis in terms of failure time so that the minute file containing the failure can be determined for further processing. Based on seismic activity of each sensor and the location of the sensors, an approximate location of the fracture can also be derived as sensors close to the fracture show signals with higher voltages.

Time synchronisation: Due to the fact that mechanical and AE data are recorded on different logging systems and at different sampling rates, a time synchronisation was necessary before further analysis could be undertaken. Time synchronisation was based on the fluid injection pressure, which has been recorded by both the continuous AE recording and the high frequency mechanical data recording. An example of the synchronisation is shown in Figure 3-22. Afterwards, the determined time synchronisation value was applied to the mechanical dataset to correct the time offset. The corrected dataset was then used for further analyses. The time synchronisation was done in MATLAB.

Harvesting and hit count: Individual triggered events have been extracted from the continuous stream dataset. The minimum noise level (Figure 3-23) across all channels is used as a triggering threshold and the number of channels to be triggered to extract an event is defined (number

of channels with high noise level plus one). A waveform length of 819.2µs was used for shale experiments and 204.8µs for sandstone experiments, which showed the clearest results for the two rock types. The harvesting was carried out in InSite-Lab. A pre-existing MATLAB-code was modified to extract a hit count file from the continuous data stream of the failure minute. The same threshold as used for the harvesting is used to count the number of hits (threshold crossing, Figure 2-21) for each channel for 0.1ms time windows (10kHz). This high resolution was required for the detailed analyses of the fracturing process and seismo-mechanical relationship.

Analysis of mechanical data: MATLAB codes were written to analyse fluid pressure and radial deformation over time. In this regards, several parameters have been determined for the fluid pressure analysis including maximum fluid pressure, fluid pressure decay rate over time (MPa/s) and the onset of rapid fluid pressure decay. The latter is determined as a break in slope in the gradient curve of the fluid pressure and afterwards verified using the fluid pressure decay rate, where fluid injection pressure is integrated with time to give a pressure rate. Furthermore, the time of radial deformation onset was determined.

Analysis of seismic data: Two aspects of the seismic data were considered during the analysis; AE hit count rate and the seismic characteristics of the waveform, including frequency content and seismic signature. The AE hit count rate was analysed using MATLAB and the onset of acoustic activity as well as the time of maximum count rate were determined. The onset of AE activity is indicated by an exponential increase of the AE hit count rate. The seismic characteristics were analysed by describing the onset and coda of the waveform using spectrograms generated with InSite-Lab. The spectrogram of the waveform represents the power-time-frequency distribution of the signal in time and the frequency content of the selected waveform.

Event type (source mechanism): First motion polarities of the harvested waveforms have been used to discriminate AE source types in tensile, shear and compressional (collapse) type events. Fracture types were distinguished by calculating the ratio between piezograms with positive and negative first motions, where the polarity of the arrival indicates whether the first motion is of compressional or dilatational character (Zhang et al., 1998). The polarity of a given event can be calculated by:

$$pol = \frac{1}{k}\sum_{i=1}^{k} sign(A_i) \qquad 3\text{-}1$$

Where: $sign\ (A_i)$ is the polarity of the first motion amplitude (positive or negative) of the i^{th} waveform in an array of k sensors. Source types are generally classified into three categories: (1) tension (T-type) $pol < -0.25$, (2) compression (C-type) $pol > 0.25$, and shear (S-type) $-0.25 < pol < 0.25$ (Zang et al., 1998).

Micro-CT image processing

The imaging dataset generated through micro-CT scanning of hydraulically fractured samples involved two categories, low (31µm) and high resolution (9µm), which resulted in two different processing approaches. The low resolution images were used for a descriptive evaluation of the developed fracture network in terms of the macro-complexity (single or multiple fractures) as well as propagation direction relative to bedding (Figure 3-19c). An approximation of fracture aperture was determined by counting the pixels along the direction of fracture width. This is based on the intensity values of the pixels as the intensity values of pixels representing the fracture (empty space, dark) are different from the ones representing intact rock (grey). However, the accuracy was limited to one pixel, i.e. the resolution of the scan (31µm) and for the lower resolution scans, apertures smaller than 30µm could not be measured accurately. Therefore an approximate aperture range was determined by counting pixels at several points along the fracture and different slices across the length of the scanned area of the sample. The images were processed using Fiji, an open-source image processing package. Adjustments to the images have been made (contrast, brightness, and grey levels) to improve the visibility of the thin fracture. The high resolution images allowed for a more detailed analysis of the fracture geometry and the segmentation of the fracture and intact rock. The geometric complexity of hydraulic fractures was quantified and evaluated by using the concept of tortuosity, which is a measure of the deviation from a straight line. Tortuosity is defined as the ratio between the sum of line segments along the pathway divided by length of a straight line between the starting and ending points (Figure 3-24) (Chen et al., 2015) and can be determined via:

$$T = \frac{\sum L}{L_0} \qquad 3\text{-}2$$

where T is the tortuosity, L the length of a single line segment and $L_0$the distance between the starting and end points. The higher the value, the more the fracture deviates from a straight line.

Measurement of tortuosity were carried out on primary fractures only using the software Adobe Illustrator CC 2018. The fracture path was traced and the length of each straight line

segment added together to derive the total length of the fracture path, which was then divided by the length of the straight line between the start and end point of the fracture (thickness of the cylinder wall) to derive a value for the tortuosity of the fracture path. Here, tortuosity is used to compare the two dimensional length of fracture paths and as an indicator of the planarity of the fracture path. Further processing of the high resolution datasets was performed in Avizo™, a commercial 3D visualisation and analysis software developed by Thermo Fisher Scientific. The first step was to decrease the file size by cropping the dataset as much as possible, so that only the area containing the fracture remains. In order to do that efficiently, the coordinate system was transformed so that the fracture is located parallel to the x-axis. The extraction of the fracture from the dataset requires correct identification of intact rock and void space (fracture). Therefore, a grey-value analysis was carried out and Figure 3-25 displays the voxel count (pixel count) as a function of grey scale value. High grey scale values refer to lighter tones and therefore dense areas (intact rock) and low grey scale values refer to darker tones and therefore less dense areas (fracture).

For all scans, shale and sandstone samples, the grey-value diagram shows two distinct peaks, which refer to void space and intact rock respectively. Any pixel with a grey scale value less than the first peak can be considered as fracture and any pixel with a grey scale value greater than the second peak is considered intact rock. The major challenge is determining, which pixels are void space and which are intact rock for grey values in-between these two peaks. Every effort was made to minimise human decision making in the segmentation process by using preferably automated algorithms, using the grey scale values from the grey value histogram (Figure 3-25). However, extraction of the fracture required some additional manual selection using the “magic wand” tool in Avizo. This tool allows to manually pick a voxel, i.e. the grey value of that particular voxel, and all directly connected voxels with grey values within a certain range of the picked grey value are automatically selected. Using this process, the fracture has been extracted from the dataset and a three-dimensional visualisation of the fracture only was possible. This allows for a better descriptive interpretation of the fracture morphology and comparison with other rock types. With the extracted fracture dataset, a thickness map has been calculated. The algorithm used calculates the distance between the centre skeleton of the volume and the point furthest away in a specified direction. As the fracture is parallel to the x-axis, the width of the fracture is represented by the y-direction, which was chosen for the calculation of the thickness (Figure 3-26). The fracture map can also be visualised as a 3D volume. An overview of the micro-CT image processing workflow is given in Figure 3-27.

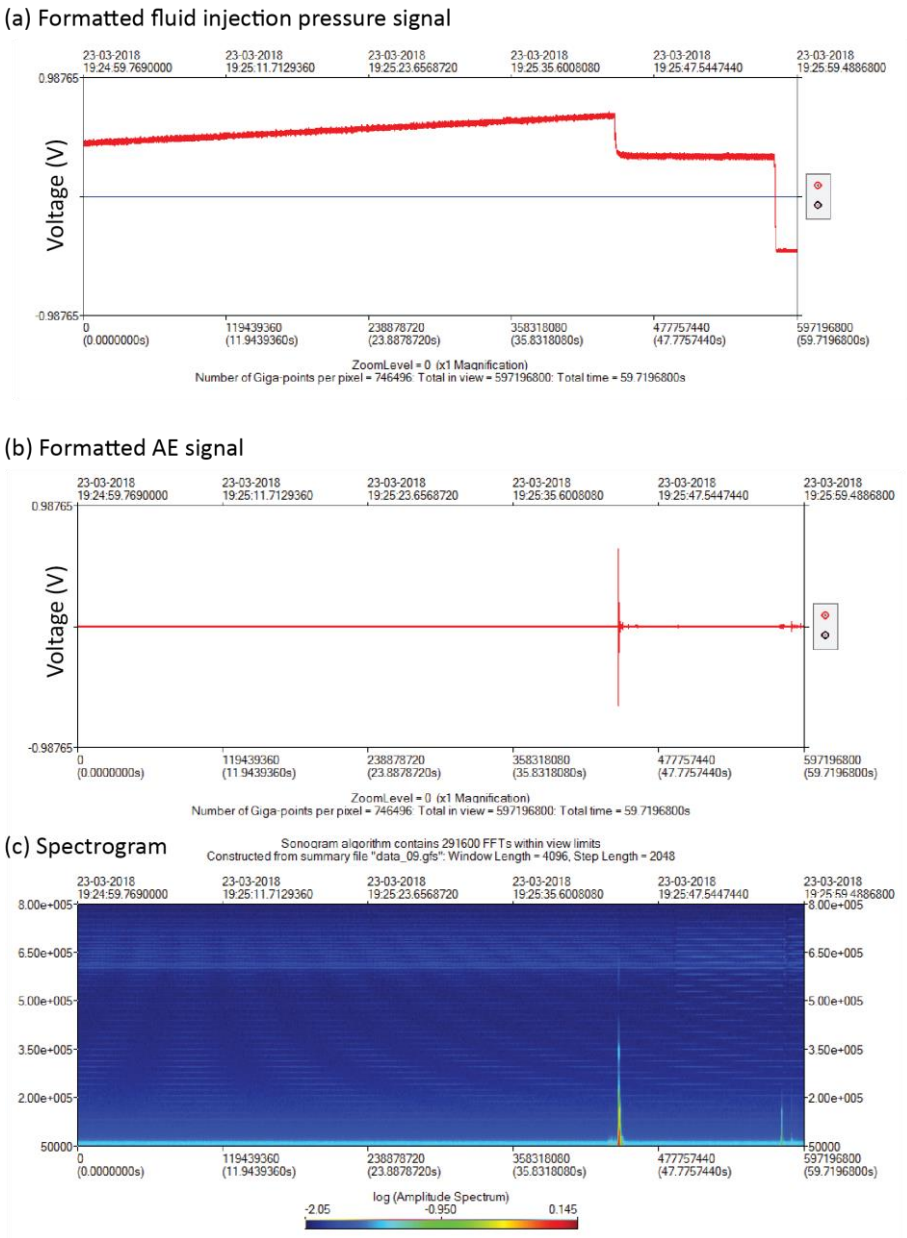

Figure 3-21: Screenshot of InSite-Lab showing formatted data; (a) fluid injection pressure and (b) AE signal.

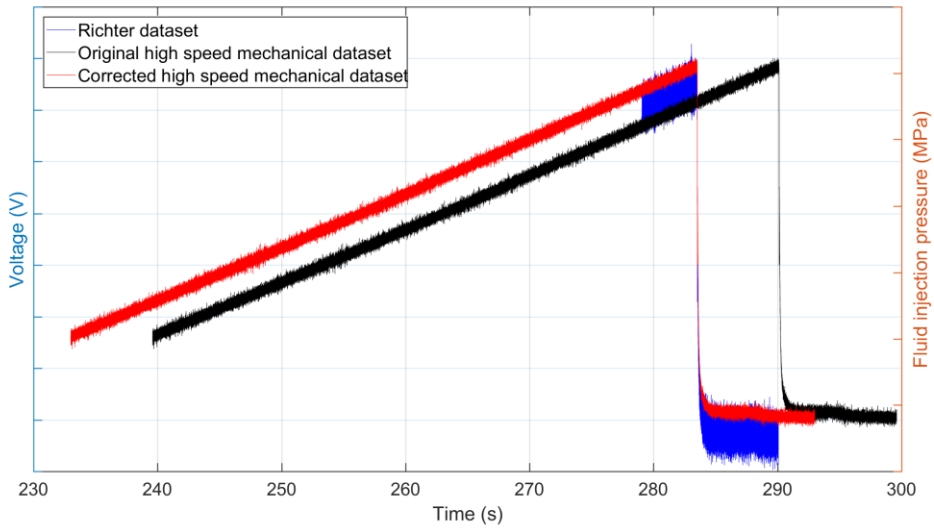

Figure 3-22: Time synchronisation diagram showing the fluid injection pressure recorded by the continuous streaming unit (blue line) and the high speed data logging system (black line – original time, orange line – corrected time).

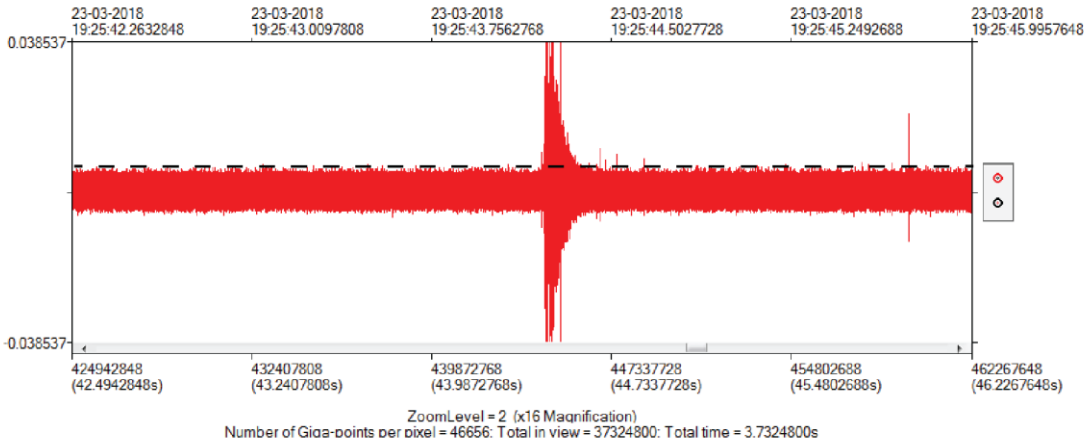

Figure 3-23: Screenshot of Insite-Lab showing a continuous 3.7s long waveform (red line) with the black dashed line marking the upper limit of the noise level of that signal.

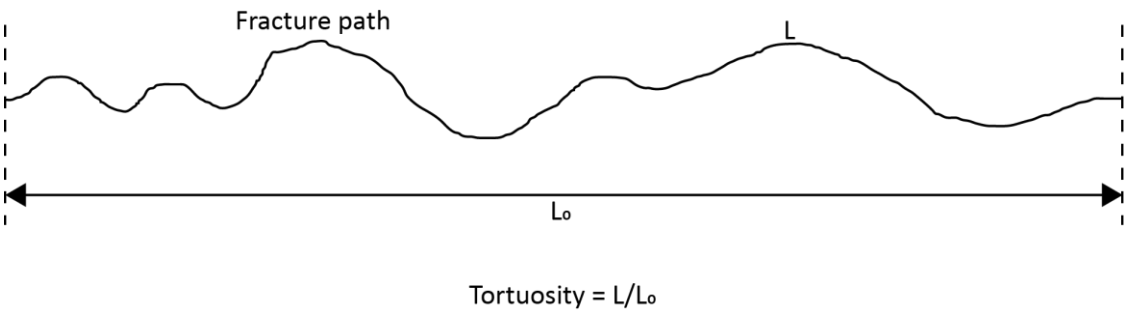

Figure 3-24: Schematic of the concept of tortuosity showing the two dimensional length of the fracture path.

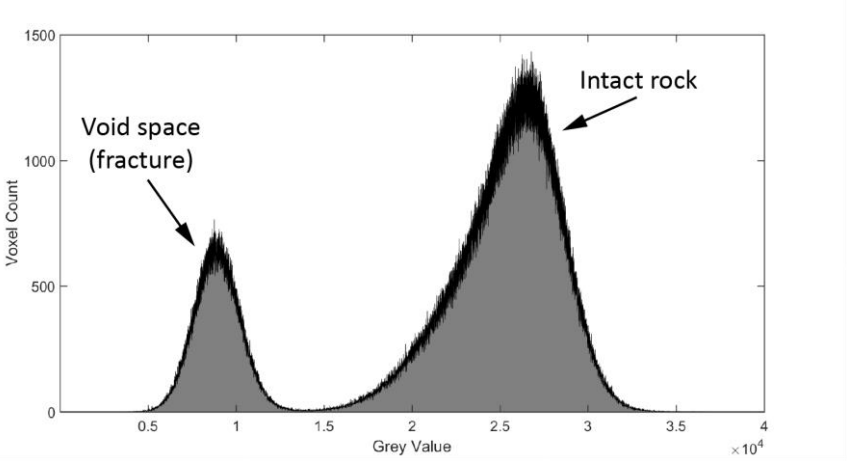

Figure 3-25: Example of a grey value histogram for Nash Point Shale micro-CT scan

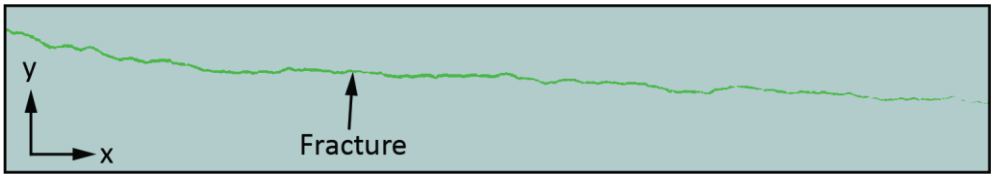

Figure 3-26: Example of extracted fracture from a Nash Point Shale sample

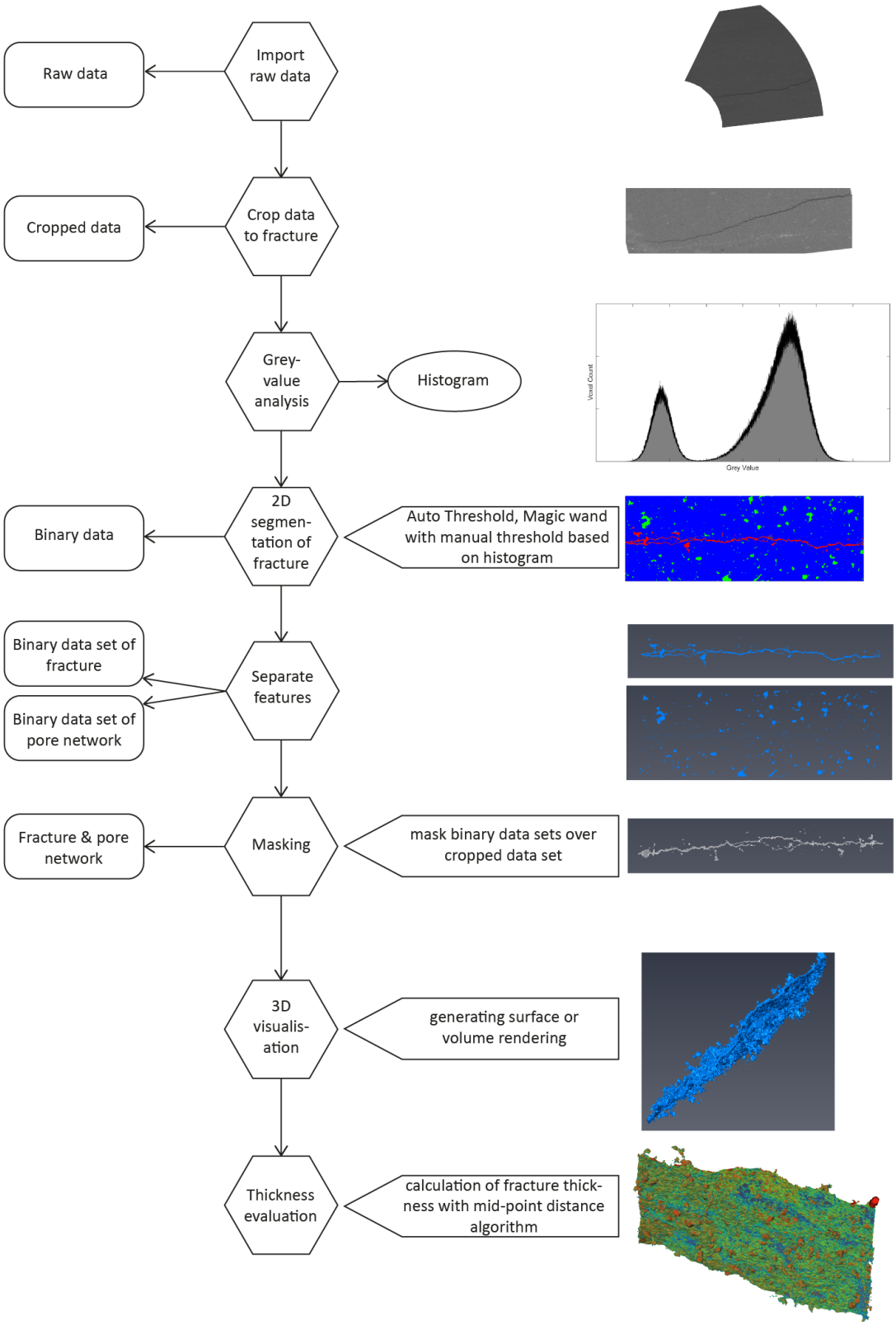

Figure 3-27: Workflow for X-ray CT data processing of high resolution images

3.6 Setup for permeability measurements after hydraulic fracturing

The existing hydraulic fracturing setup (Chapter 3.3) has been modified, to measure the permeability after hydraulic fracturing occurred using the steady-state-flow technique (Figure 3-28a). For the permeability experiments, we used a thick-walled hollow cylinder sample with an outer diameter of 36mm and an inner diameter of 10mm. The smaller outer diameter was necessary to create space inside the rubber jacket for a liner (Figure 3-28b), which was designed with a network of grooves (Figure 3-28 c). The liner transports the fluid, migrating through the newly developed fracture, to a modified sensor waveguide (Figure 3-28b), which plugs into the sensor ports of the rubber jacket. The modified waveguide includes a centre hole and is connected to a second pore water pump (Figure 3-28a), which receives the fluid that migrates through the fracture.

Initially, hydraulic fractures are generated using the same experimental procedure as described in Chapter 3.3. After the sample failed, a steady state flow is established with a differential fluid pressure inside the sample conduit and outside the sample to establish a hydraulic gradient. Two servo-controlled pumps independently supply high-pressure pore fluid (distilled water) to both, the inside and outside of the test sample. Each pump can be separated from the circuit by electronically operated valves, which enables the sample to be subjected to fluid flow through the fracture at a known hydraulic gradient. During the experiment, permeability was measured under changing effective pressure conditions up to 25 MPa via steady-state flow and Darcy's law. The average differential fluid pressure was kept constant at about 5MPa, whereas the axial and confining stresses were increased/decreased in increments of 3-5 MPa. After each change in external pressure, the pore-fluid system was allowed to equilibrate to the new pressure conditions and establish a new steady flow, which was assumed to be the case when volume in the upstream reservoir decreased at a similar flow rate as the downstream volume increased. This also confirmed that no leaks were in the system. A minimum of 2min is permitted to ensure stable flow rates and a steady-state flow through the sample before permeability measurements were taken over a duration of at least 3min. All mechanical/pressure data (axial stress, confining pressure, pore pressures and reservoir volumes) were recorded and logged continuously at 2s intervals. Volume changes in the upstream (internal) and downstream (outside the conduit) reservoir were used to calculate the volume flow rate at each confining pressure stage. For the calculation of the axial surface area of the fracture, a single rectangular fracture profile is assumed defined by the crack opening, which is derived from changes in the radial dimensions of the sample, and the length of the pressurised zone (19.2mm). By applying Darcy's Law, permeability is calculated directly from

the fluid flow rate, pressure gradient and the crack dimensions using the following expression (Jones and Meredith, 1998; Benson, 2004):

$$\kappa = \frac{Q}{A}\frac{\mu * L}{(P_u - P_d)} \qquad 3\text{-}3$$

where:
- κ = permeability (m^2),
- Q = volume flow rate (flow velocity) (m^3/s),
- A = axial surface area of the fracture (m^2),
- P_u = internal fluid pressure (Pa),
- P_d = conduit external fluid pressure (Pa),
- μ = fluid viscosity (Pa·s),
- L = length of fracture (m) (inner radius – outer radius).

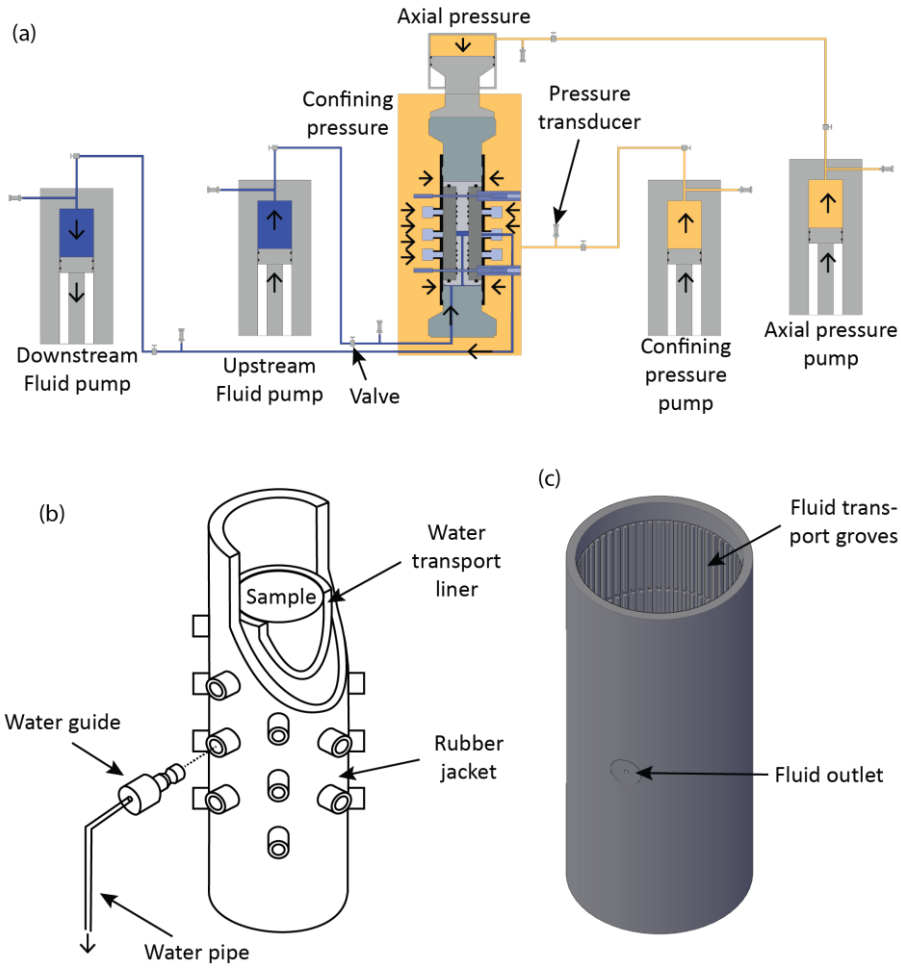

Figure 3-28: MHF permeability setup; (a) schematic of TRX setup for permeability measurements after hydraulic fracturing, (b) schematic of sample setup with water transport liner and rubber jacket and (c) 3D image of water transport liner.

4 Sample Material and Description

The rock types used in this study, a shale and a sandstone, were chosen because of their anisotropic character and low permeability, which are key characteristics for unconventional reservoirs. This chapter describes the petrography of the two rock types and their physical and baseline mechanical properties. Standard methodologies and tests, which are described below, have been used to determine the properties.

4.1 Petrography of sample material studied

4.1.1 Nash Point Shale

This shale was collected from the cliffs at Nash Point on the south coast of Wales (south-west of Cardiff) (Figure 4-1). Here, the cliffs consist of pale grey limestone beds (≈1m) of the Blue Lias formation, interbedded with argillaceous, calcareous shale and/or calcareous marl (Figure 4-2) (May and Hansom, 2003; Paul et al., 2008). The shale and marl beds are between one to tens of centimetres thick and the contacts are usually very sharp and planar (Figure 4-3). The deposits at Nash Point are organic-rich, argillaceous sediments deposited in a suboxic to anoxic marine environment and of Sinemurian and Hettangian (Lower Jurassic) age (190-200 ma) (Weedon, 1986; Arzani, 2004). The shale is light to dark grey and well laminated, and becomes fissile when weathered. Based on the location of sample collection, the shale is referred to as Nash Point Shale (NPS) in this thesis.

Micro fractures are observed to be predominantly parallel to the visible bedding orientation, most likely the opening of bedding planes due to stress relaxation. The shale consists predominantly of carbonates (≈63%, dominantly calcite and some dolomite), clay (≈23%) and silicates (≈14%, quartz, feldspar, plagioclase and minor contents of pyrite). The clay contents are dominantly illite (≈63%), illite-smectite (≈32%) and chlorite (≈5%). Thin section examination under an optical microscope showed a fabric that is characterised by a very fine grained (grains <2 µm in size) clay and organic-rich matrix with disseminated, isolated dominantly elongated calcite crystals (3 - 600µm in size), lithic fragments, predominantly subangular to rounded quartz and chlorite grains, and mica flakes (Figure 4-4). The microstructure can be described as homogenous, matrix dominated and without any visible layers of different mineralogy in the mm-cm scale. The well-defined micro lamination is shown by a strong preferred alignment of minerals (Figure 4-4a and b). Calcite veins are present within the shale at different scales. They are also clear in the cored samples, mostly sub-normal to normal (≈75-90°) to the bedding (Figure 4-5), but also under the microscope, where they are predominantly aligned with the preferred orientation of the minerals (Figure 4-4c and d). Furthermore, microscopic images

also showed carbonate rich areas, which contain less organic matter and appear lighter under plane polarised light (Figure 4-4e). These areas are dominated by inorganic materials and cemented by calcite (Arzani, 2004; Saif et al., 2017).

Additional detail was obtained using polished thin sections, examined using Scanning Electron Microscopy (SEM) to take Back Scatter Electron (BSE) and Secondary Electron (SE) photomicrographs. The BSE photomicrographs confirm the observed microstructure of a fine grained matrix where organic matter and pyrite are easily distinguished from the background, and where single quartz, mica, calcite and dolomite grains were also identified, embedded within the matrix (Figure 4-6). Again, no layering due to alternating mineralogy is visible. Organic matter is randomly distributed in randomly stretched patches with complex geometries, and is mostly non-porous in the investigated samples. Organic matter content ranges from 2-20% as identified in the low resolution BSE overview images (Figure 4-7). Pyrite grains are loosely packed, non-porous and have a framboidal structure and occur as single grains or in clusters (Figure 4-8). Secondary electron photomicrographs of fresh fractures in the shale show smooth fracture surfaces for fractures along the bedding and rough, ridged surfaces when fractured perpendicular to the bedding (Figure 4-9).

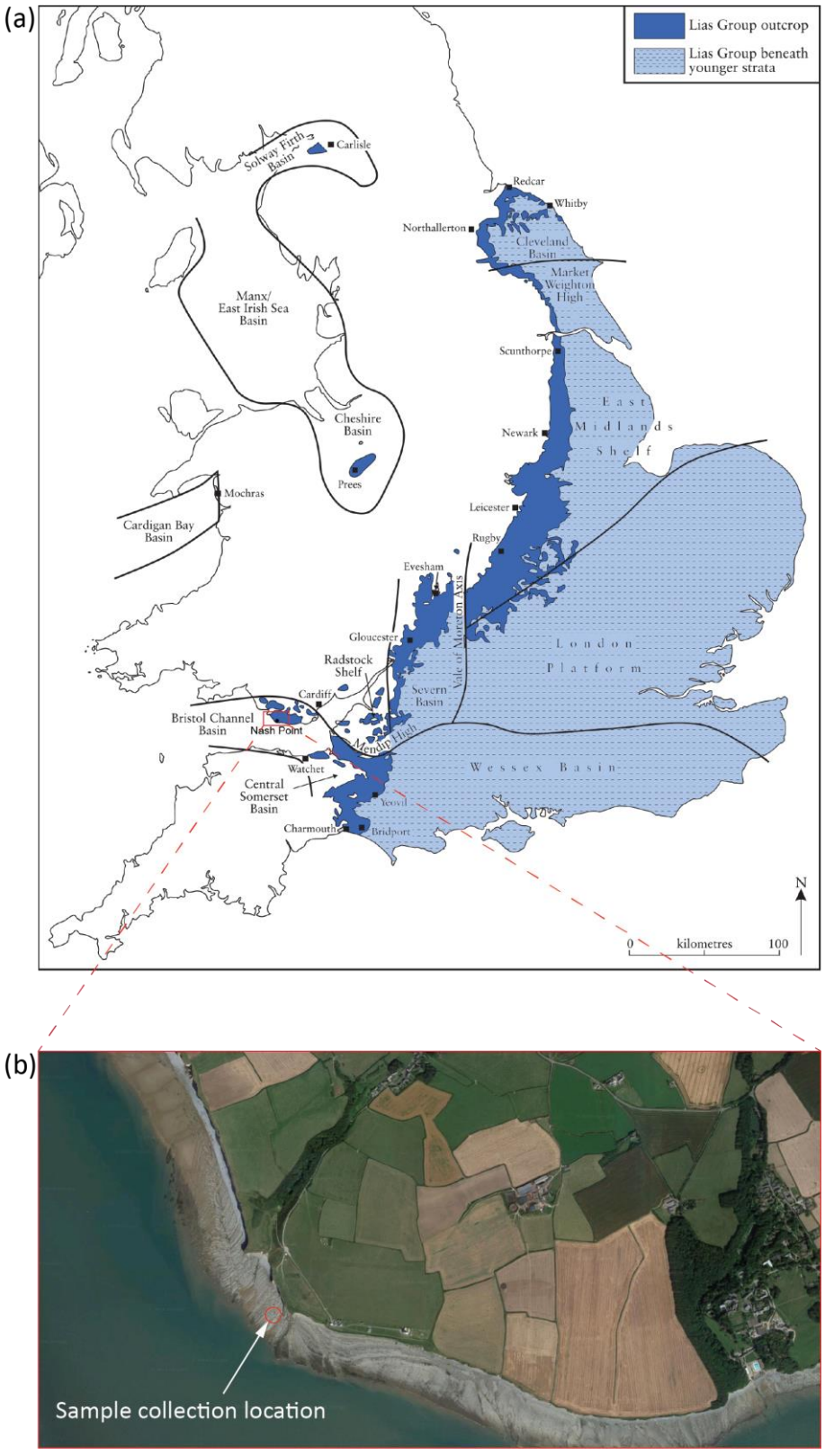

Figure 4-1: Location of sample collection; (a) Map of Lias Group outcrop in the UK (modified from Simms et al. (2004); (b) Birds-view image of Nash Point indicating location of sample collection (Google maps, 24/04/2018).

Figure 4-2: Picture of cliffs at Nash Point, South Wales. The picture shows the limestone sequence interbedded with shale and marl.

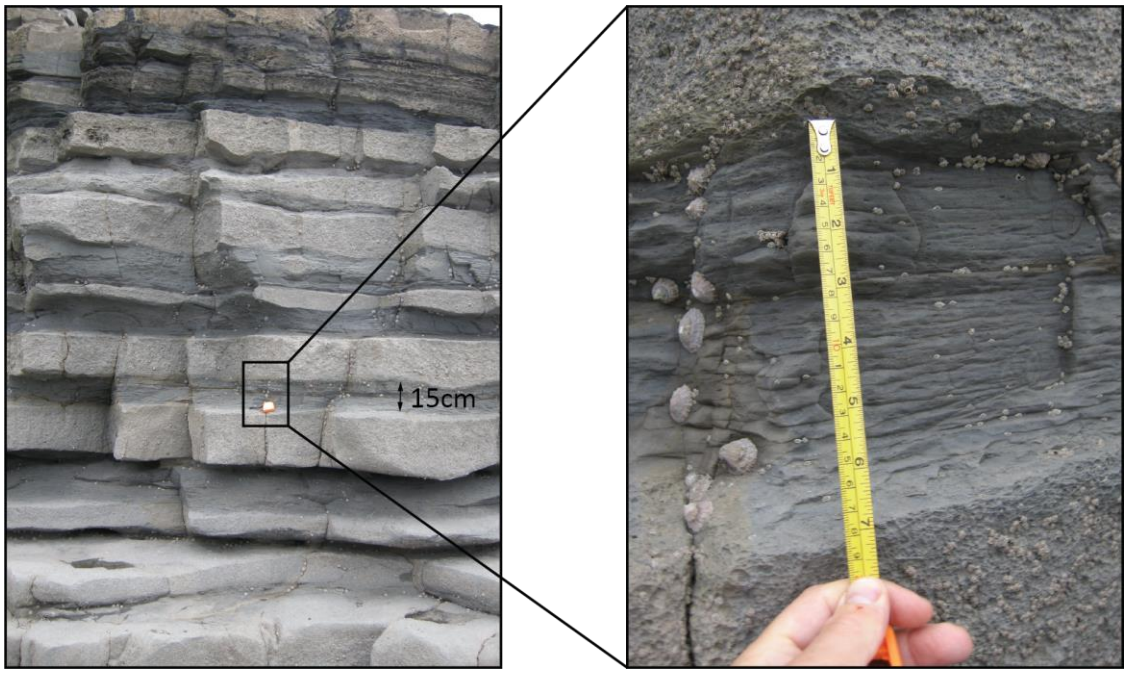

Figure 4-3: Sequence of alternating limestone and shale beds. Shale beds are between 10-30cm thick and more eroded inwards than the limestone. The horizontal bedding in the shale is clearly visible in the blow-up image.

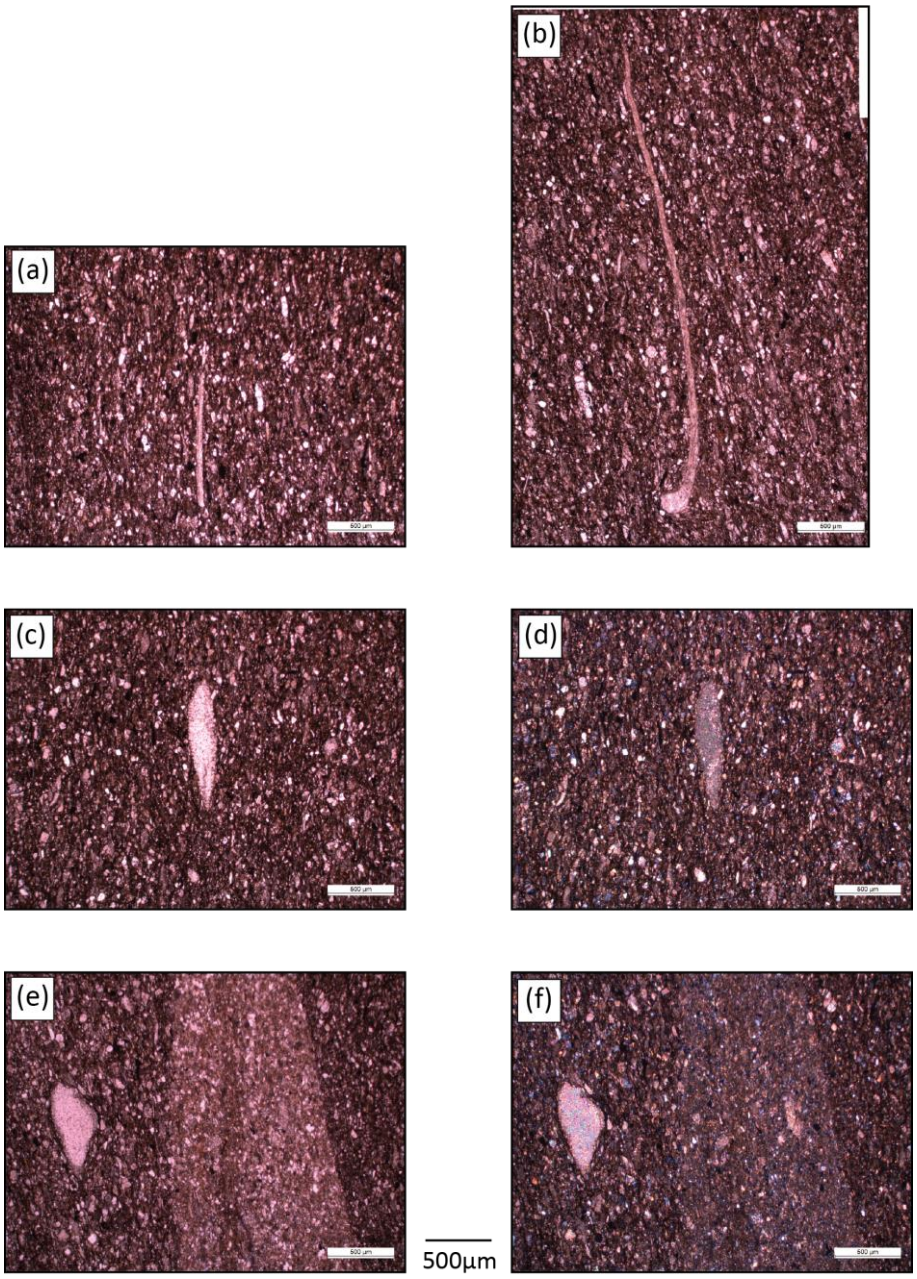

Figure 4-4: Photomicrographs of NPS showing the preferred alignment of minerals, calcite veins (a and b) and an elongated calcite grain (c - f). (a), (b), (c) and (e) are taken under plan-polarised light and (d) and (f) under cross-polarised light.

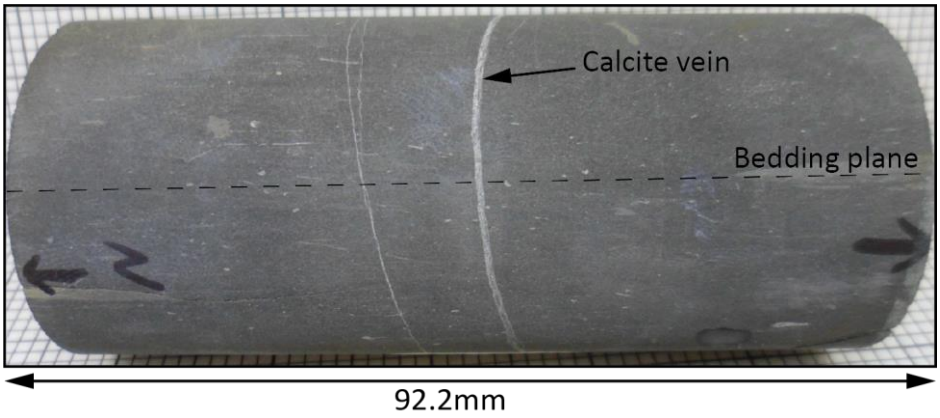

Figure 4-5: Cored Nash Point Shale sample showing a calcite vein at ≈90° to the bedding.

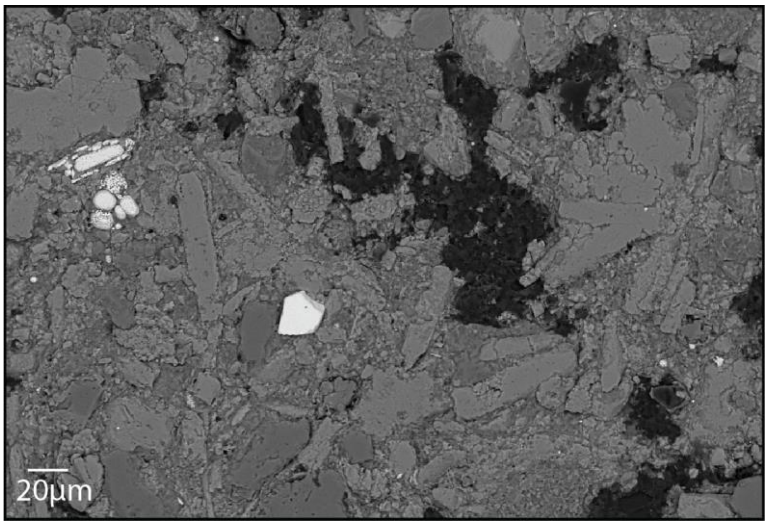

Figure 4-6: Back Scattered Electron Photomicrograph of NPS showing organic matter (black), pyrite (white) and different minerals (carbonates, quartz, feldspar and clay minerals) and clay matrix, which are represented by different shades of grey.

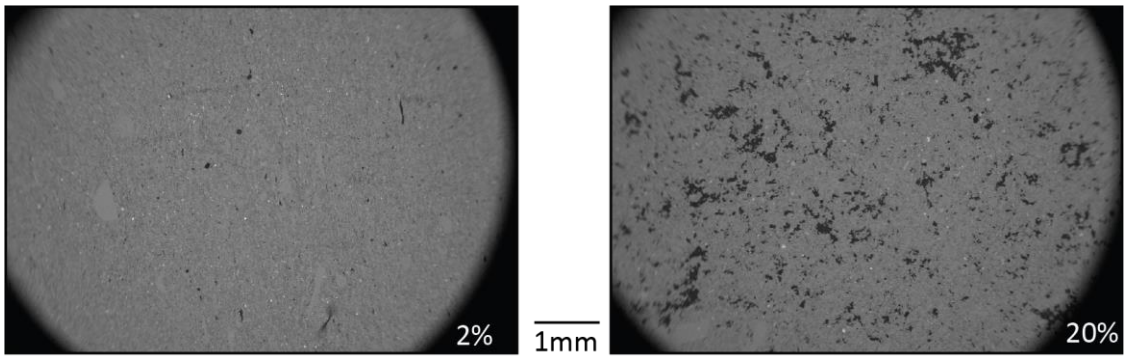

Figure 4-7: Low resolution Back Scattered Electron overview-photomicrographs of NPS showing organic matter content (black).

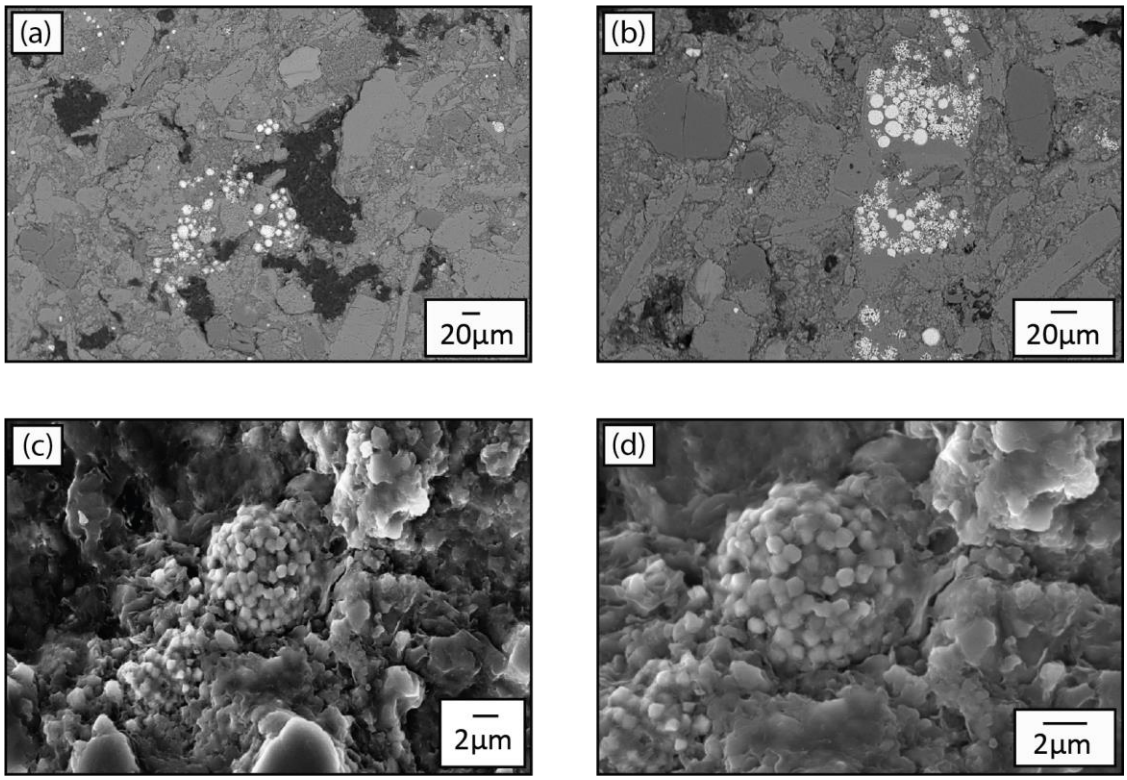

Figure 4-8: SEM Photomicrographs of pyrite grains; (a) and (b) are BSE images showing single grains and clusters, (c) and (d) are SEM images, revealing the framboidal structure of the pyrite in detail.

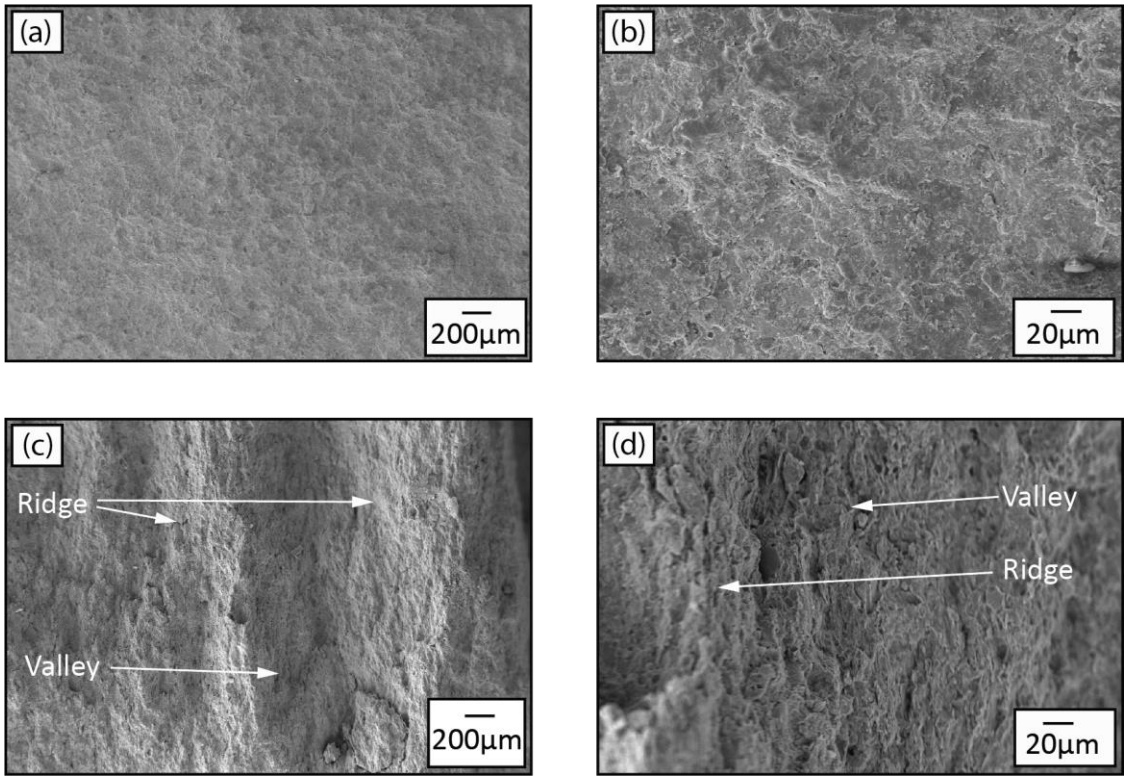

Figure 4-9: Secondary Electron Photomicrographs of fresh fractures in NPS; (a) and (b) along bedding, (c) and (d) perpendicular to bedding.

4.1.2 Crab Orchard Sandstone

Crab Orchard Sandstone (COS), from the Cumberland Plateau, Tennessee, USA, is a fine grained, crossbedded fluvial sandstone of Silurian age (419.2 – 443.8 ma). The grains range from subhedral to subrounded, are approx. 0.1-0.5mm in size and usually don't show any preferred alignment (Figure 4-10). The material exhibits mm scale cross-bedding that is clearly visible to the naked eye in hand specimen (Figure 4-11). Although this bedding orientation cannot be seen clearly using optical microscopy, Benson (2004) stated the presence of an alignment of mica flakes parallel to the bedding plane. The rock consists predominantly of quartz (>80%) and is cemented by phyllosilicates and sericitic clay (Benson et al., 2003, 2006), which makes it a sub-arkose according to Folk's classification (MacKenzie et al., 2017). The remaining material consist of orthoclase feldspar, which accounts for ≈10-12% and is variably altered to sericite, ≈5% clay minerals (Illite, kaolinite and chlorite) and minor contents of lithic grains, such as muscovite mica and calcite, which occasionally occur as a cement in conjunction with clays. SEM photomicrographs of fresh fractures (Figure 4-12) show a rough fracture surface with numerous 'pits' where quartz grains are plucked out of the matrix (Atkinson, 1979b).

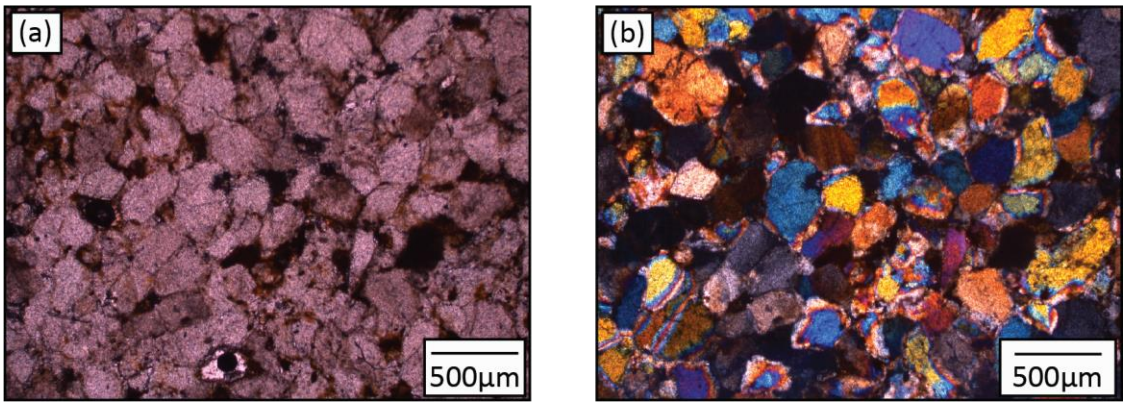

Figure 4-10: Photomicrographs of Crab Orchard Sandstone taken under plane-polarised (a) and cross-polarised (b) light.

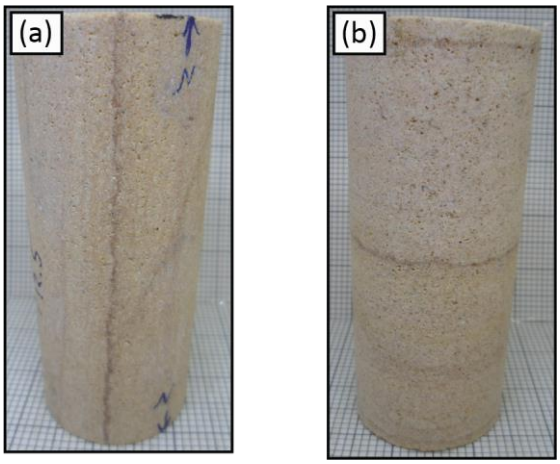

Figure 4-11: Pictures of Crab Orchard Sandstone samples showing the mm-scale cross bedding parallel (a) and normal (b) to the sample axis.

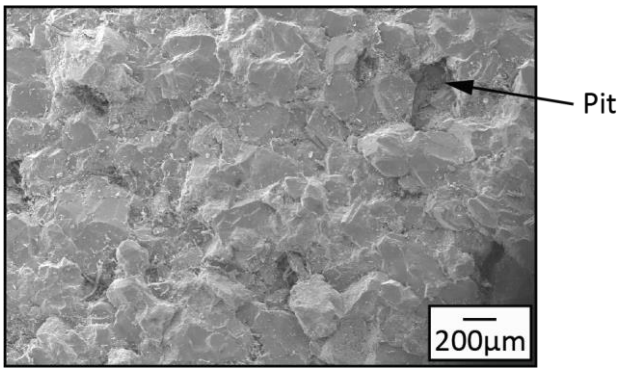

Figure 4-12: Secondary Electron Photomicrographs of a fresh fracture in COS.

4.2 Petrophysical measurements and characterisation

4.2.1 Experimental methods

Density and Porosity

Material density and porosity (ϕ) have been determined according to the ISRM Suggested Methods for determining porosity and density (Ulusay, 2014). Material dry density (ρ_b) was calculated from the mass of the oven-dried sample (M_d) and the defined bulk volume (V_b) of a cylindrical sample given by $V_b = L\frac{D}{2}\pi^2$ using sample diameter D and length L. The dimensions of the sample are averages from several (minimum 7) calliper measurements on each core. Using these densities, according to the Suggested Methods (Ulusay, 2014) the porosity is defined as:

$$\phi = \frac{M_{sat} - M_d}{V_b}\frac{1}{\rho_w}x100 \qquad 4\text{-}1$$

with ρ_w being the density of water, M_{sat} the mass of the saturated sample, M_d the mass of the oven-dried sample and V_b the bulk volume.

Elastic wave velocity

Acoustic wave velocity testing is a non-destructive testing technique based on the propagation velocities of elastic waves in the material. Here it is used to characterise the elastic and anisotropic properties of the materials. Two types of acoustic waves are distinguished, compressional and shear waves. Compressional waves are characterised by particle movement parallel to propagation direction, whereas shear waves exhibit particle transversal movement perpendicular to propagation direction. Compressional wave velocities were measured to verify the anisotropic character of the starting (as-collected) material and to determine the orientation of the bedding in the case it was not clearly visible. The elastic wave data were taken under ambient laboratory conditions on dry core samples with a diameter of 40mm and a length of between 40 and 60mm. The sample was clamped between two ultrasonic sensors (Panametrics V103 for P-wave and V153 for S-wave) (Figure 4-13). The transmitting sensor is excited by an ultrasonic generator (JSR Ultrasonics DPR300) supplying a 450V inverse spike and generating a P or S mechanical signal. The mechanical pulse is received by a second identical piezo transducer, which converts the wave into an electrical signal. The signal is then pre-amplified and displayed on a digital oscilloscope, which is time-synchronised to the input pulse. This allows the time-of-flight to be determined and the elastic wave velocity computed from the distance travelled (Birch, 1960). To minimize scattering effects, we used transducers with a central frequency of 1 MHz. P-wave velocities were measured across the diameter as a

function of azimuth every 10˚ around the cylindrical samples using the time-of-flight method (Jones and Meredith, 1998; Benson et al., 2003). The wave velocity was calculated from the length of the travel path (sample diameter) and the travel time of the acoustic wave, corrected for travel through the transducer end caps, via:

$$V_P = \frac{D}{t_P} \qquad 4\text{-}2$$

where D = sample diameter (mm)

t_P = P-wave travel time

V_P = compressional elastic wave velocity.

Permeability

The permeability of rock is a key physical property, describing the ability of pore fluid to move within a rock mass (Guéguen and Palciauskas, 1994). Permeability is one of the more time-consuming rock properties to measure and there are three commonly employed measurement techniques: (1) steady-state-flow method, (2) pulse decay or transient pulse method (Brace et al., 1968; Walder and Nur, 1986) and (3) oscillating pore pressure method (Kranz et al., 1990; Fischer, 1992; McKernan et al., 2017). The steady-state-flow technique is a simple method and does not require complicated interpretations. However, when working with fine-grained rocks, where permeability may be very low, it can be very difficult and time consuming to establish steady-state-flow conditions, and the two other techniques are preferred, using a gas as the fluid. The steady-state-flow method applies a constant pressure gradient under steady-state flowing conditions. The relationship is defined by Darcy's law, a mathematical statement describing fluid flow properties through a porous medium that incorporates:

- a pressure gradient is required for fluid flow to occur and the flow direction is from high pressure towards low pressure,
- the volume flow rate (discharge rate or flow velocity) is directly proportional to the pressure gradient.

However, Darcy's law is only valid for slow, viscous flow with a low volume flow rate typically <1m/s (Guéguen and Palciauskas, 1994). Faster fluid flows become turbulent and the law breaks down. Darcy's law is defined via (Boulin et al., 2012):

$$q = -\frac{\kappa}{\mu}\Delta P \qquad 4\text{-}3$$

where: q = Fluid flux (Darcy's velocity) (m/s)

κ = Permeability (m^2),

μ = fluid viscosity (Pa·s),

ΔP = Pressure gradient (Pa/m).

Here, the fluid flux (q) is the fluid volume which passes through the surface area of the sample over time, and is often referred to as Darcy's velocity. It is defined as the quotient of volume flow rate (Q) and the surface area of the sample. Rearranging equation 4-3 for permeability, κ, and substituting ($P_u - P_d$) for the differential pressure (ΔP), where P_u is the upstream pressure and P_d the downstream pressure, and with sample length L, the following is obtained:

$$\kappa = \frac{Q}{A}\frac{\mu * L}{(P_u - P_d)} \qquad 4\text{-}4$$

where: κ = Permeability (m^2),

Q = Volume flow rate (flow velocity)(m^3/s),

A = Surface area of the sample (m^2),

P_u = upstream Pressure (Pa),

P_d = downstream Pressure (Pa),

μ = fluid viscosity (Pa·s),

L = sample length (m).

The steady-state-flow method was applied to determine the permeability of the Crab Orchard Sandstone. Samples were first vacuum saturated with distilled water for a minimum of 24hrs. The permeability experiments were performed using a triaxial deformation cell operating in hydrostatic mode (Figure 4-14 a). The sample is separated from the confining oil through an impermeable rubber jacket (Sammonds, 1999). Two servo-controlled pumps independently supply high-pressure pore fluid (distilled water) to establish the constant differential pore pressure across the sample length. The effective pressure is given by the effective pressure law $P_{eff} = P_c - \alpha_{eff} * P_p$, with $\alpha_{eff} = 1$ (Keaney et al., 2004). Full saturation was assumed once the downstream pore fluid pump started receiving pore fluid at an equal rate to the injection pore fluid pump. Fluid flow through the sample, from the upstream to the downstream reservoir, was directly measured via the reservoir volume change as a function of time (Figure 4-14b), giving the volume flow rate (Q) directly. If the slopes of reservoir volume change are equal with opposite sign, the permeability can be calculated. Unequal slopes indicate compaction or a leak in the system (Jones and Meredith, 1998). For the permeability

measurements cylindrical samples of length L and diameter D are used, so that the surface area is given as $A = \pi\frac{D^2}{4}$. By applying Darcy's Law, permeability is calculated directly from the volume flow rate, pressure gradient and the sample dimensions using the following expression:

$$k = \frac{4 * \frac{dV}{dt} * \mu * L}{\pi * D^2 * (P_u - P_d)} \qquad 4\text{-}5$$

where:
- κ = Permeability (m^2),
- $\frac{dV}{dt}$ = Volume flow rate (Q) (m^3/s),
- A = Surface area of the sample (m^2),
- P_u = upstream Pressure (Pa),
- P_d = downstream Pressure (Pa),
- μ = fluid viscosity (Pa·s),
- L = sample length (m),
- D = sample diameter (m).

For low permeability rock types, it is difficult to achieve steady-state flow in a reasonable time frame. Hence, permeability measurements for the Nash Point Shale were conducted at the University of Manchester using the oscillating pore pressure method and gas as flowing fluid (Rutter et al., 2013; McKernan et al., 2017). For our measurements, Argon was used as fluid medium, silicon oil as confining medium and the cylindrical sample was sealed between two platens using heat shrink tubing and connected to an upstream and downstream reservoir (Figure 4-15a). The upstream pressure oscillates in a sinusoidal pattern with a fixed frequency around a mean value. As a result, the downstream pressure maintains the same period as the upstream signal, but is amplitude-attenuated and phase-shifted (Figure 4-15b) (Kranz et al., 1990; McKernan et al., 2017). By measuring the steady-state pressure amplitude ratio between the upstream and the downstream reservoirs, and the phase shift combined with the knowledge of fluid and system parameters, the permeability can be calculated. For reliable measurements both pressure amplitude and oscillation frequency must be adjusted for the rock tested (Kranz et al., 1990). Several phenomena are associated with using gas as flow medium, which may cause deviations from Darcy's law and corrections are necessary to determine the permeability. Klinkenberg (1941) showed that the measured permeability of a sample varies with the molecular weight of the gas and the applied pressure due to gas slippage. This non-Darcy effect is exhibited as a non-laminar flow in porous media, occurring when the average rock pore throat radius is similar to the mean free path of the gas molecules,

causing the velocity of individual gas molecules to accelerate at the contact with the rock surface (Rushing et al., 2004). Klinkenberg determined that gas permeability approaches a limiting value at an infinite mean flowing pressure. This limiting permeability value is often referred to as Klinkenberg-corrected permeability and relates liquid permeability to gas permeability (Rushing et al., 2004) by

$$\kappa_L = \kappa_\infty (1 + \frac{b_s}{P_{mean}}) \qquad 4\text{-}6$$

where: κ_L = liquid permeability,

κ_∞ = Klinkenberg-corrected permeability (at infinite mean pressure),

b_s = gas slippage factor,

P_{mean} = mean core pressure.

Anisotropy

Rock properties and their behaviour is also strongly influenced by anisotropy present in the rock mass (or sample): either inherent to the rock type or induced due to the stress state. A medium is characterised as anisotropic when its properties change with measurement direction (Amadei, 1982). The influence of anisotropy can be seen for elastic wave velocities, fluid permeability and anisotropy on strength and deformational responses (Jones and Meredith, 1998; Sayers, 1999; Gehne and Benson, 2017), but can also effect engineering applications (Schormair et al., 2006). For elastic wave velocity and permeability this refers to the wave velocity and magnitude of fluid flow respectively as a function of the migration direction through the sample with respect to layering (e.g. Benson et al., 2006). Alternatively, anisotropy may be generated by small scale heterogeneities (Meyer, 2002), as shown by Jones and Meredith (1998) and Sayers (1999) in shales, and by Meyer (2002) and Gehne and Benson (2017) in sandstones. Studies have also reported large variations in the mechanical properties depending on the bedding orientation (e.g. Nasseri et al., 2003; Bidgoli and Jing, 2014; Rybacki et al., 2015; Gehne and Benson, 2017). Here, anisotropies were typically determined by testing samples in both directions, parallel and normal to bedding. Using the measured peak values from both directions, the bulk anisotropy can been calculated with the general formula $Ax = 100\ \% * ((Xmax - Xmin)/Xmean)$ where Ax is the anisotropy parameter and X is the experimentally measured value (Benson, 2004; Benson et al., 2005).

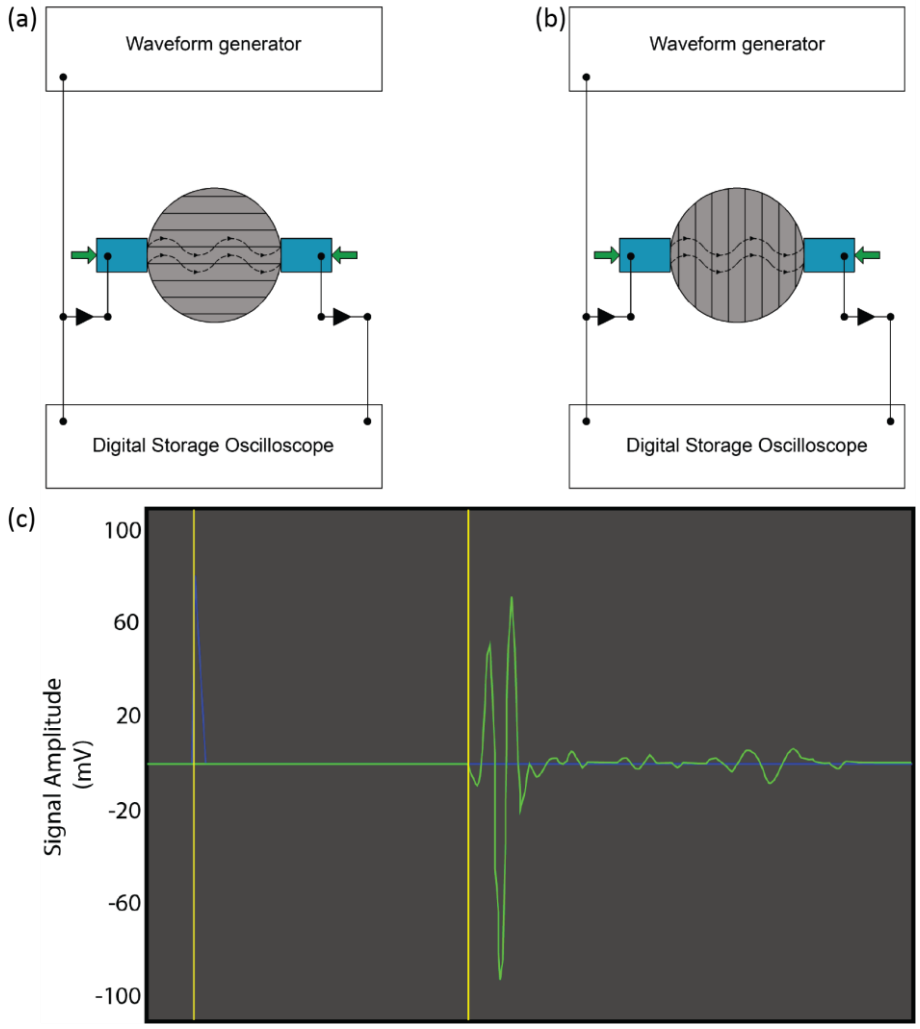

Figure 4-13: Schematic of setup for elastic velocity measurements; The sample is rotated in 10° increments about its axis, allowing wave velocities to be calculated as a function of azimuth. (a) Wave propagation parallel to bedding; (b) wave propagation normal to bedding; black arrows and black dashed line indicating travel direction of signal; green arrows indicate applied radial force on sensors to improve sensor-rock surface contact; (c) schematic of typical measurement on oscilloscope.

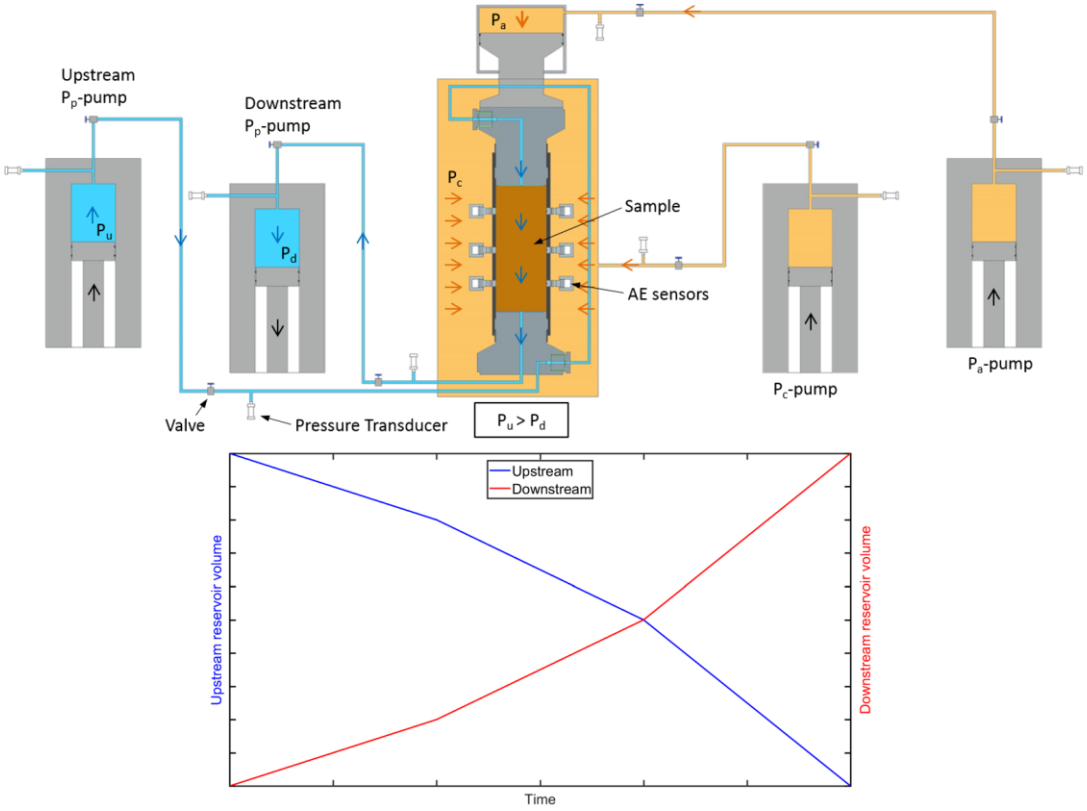

Figure 4-14: Steady-state method for permeability measurements; (a) Schematic diagram of triaxial deformation cell used for steady-state permeability measurements, upstream reservoir pressure (P_u), downstream reservoir pressure (P_d), axial pressure (P_a), and confining pressure (P_c); (b) Reservoir volume change with time.

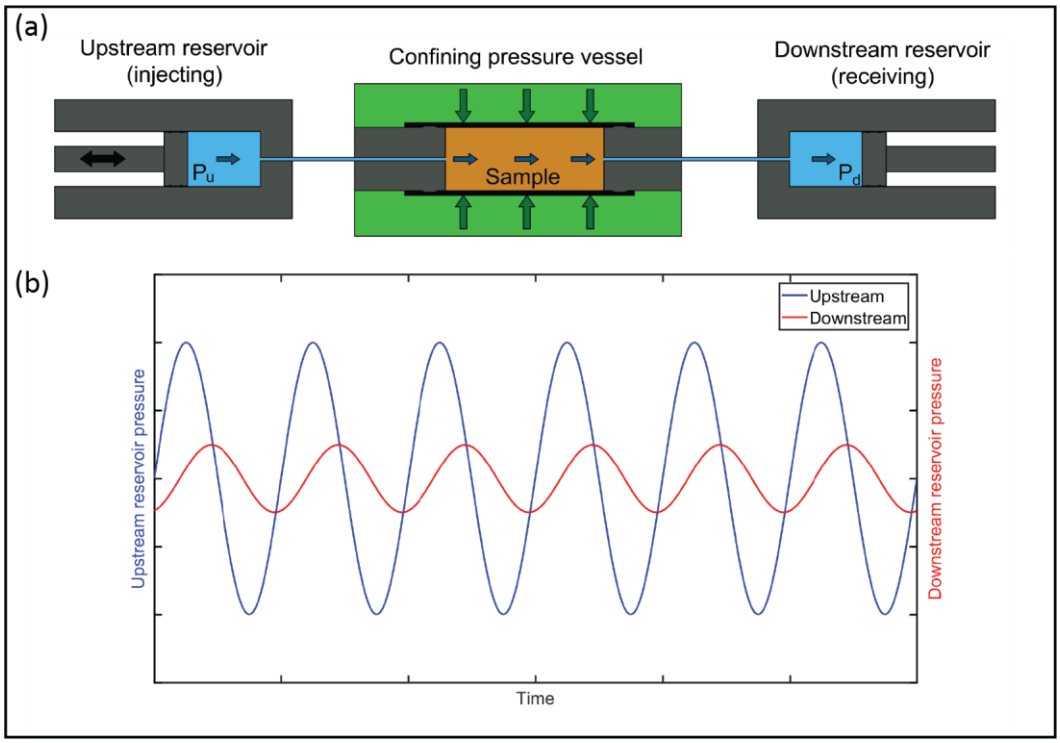

Figure 4-15: Schematic of oscillation method for permeability measurements; (a) Schematic of measurement setup for the permeability oscillation method, upstream reservoir pressure (P_u), downstream reservoir pressure (P_d), dark green arrows indicate the confining pressure; (b) Oscillation of upstream and downstream reservoir pressure with time. The downstream pressure maintains the same period as the upstream signal, but is amplitude-attenuated and phase-shifted.

4.2.2 Petrophysical properties of Nash Point Shale and Crab Orchard Sandstone

To further characterise both rock types, basic physical properties (grain density, porosity, elastic wave velocity and permeability) were determined according to the methods above. The shale has an average grain density of 2.64g/cm^3 and an average total porosity of 6.31% (Table 4-1). Compressional wave velocities were measured across the diameter of three samples, in each of two directions with respect to the anisotropy plane, every 10 degrees. Velocity data for Nash Point Shale are presented in Figure 4-16 (for dry samples). A significant P-wave variation with azimuth is seen for NPSx (bedding parallel to coring axis), whereas only small velocity variations have been measured for NPSz (bedding normal to coring axis). For both directions, a velocity minimum is seen at ≈90° and ≈270°, and velocity maxima at ≈0° and ≈180°. The velocity maxima coincides with the orientation of bedding planes, which have been marked on the sample before coring. The apparent anisotropy is highest (approximately 56%) when the sample is cored in the x-direction (Figure 4-13) leading to the bedding rotating around the x-axis. When the sample rotates around the z-axis, waves always travel sub-parallel to the bedding plane, resulting in only small velocity variations and hence a smaller apparent anisotropy of approximately 3%. It is inferred that the maximum anisotropy for NPS is at 56% due to this effect. Compressional wave velocities were used to distinguish between the shale,

the marl and the limestone. This is important, as visual inspection between these lithologies was often challenging, and so elastic wave velocity was deployed as a key tool. The marl and the limestone show a much lower anisotropy, ≈10% and ≈1% respectively, compared to the shale (≈56%) allowing positive identification. Permeability was measured at hydrostatic pressure conditions (Chapter 4.2.1) with increasing and decreasing effective pressure (confining pressure P_c – pore pressure P_p) over the range 5MPa to 50MPa (Figure 4-17). Significant differences in the permeability parallel and perpendicular to inherent bedding are evident with gas permeability measurements of 10^{-18} m^2 parallel and 10^{-20} m^2 normal to bedding, yielding a permeability anisotropy of ≈200%. However, both flow directions show a similar response to changing external pressure conditions with permeability decreasing with increasing effective pressure and subsequently increasing when effective pressure is reduced, most likely due to the closure and re-opening of pores and cracks. Permeability does recover to an extent, but it does not reach its original value indicating a permanent reduction of permeability.

The Crab Orchard Sandstone has an average grain density of 2.66g/cm^3 and an average total porosity of 7.1% (Table 4-1) (Gehne and Benson, 2017), which is characterised by pervasive networks of both angular pore space and a crack fabric: both are clearly seen in the scanning electron micrograph images (Figure 4-12). Wave velocity data for the Crab Orchard Sandstone is presented in Figure 4-18 for dry samples cored in x and z-directions. Like the shale, a clear P-wave variation with azimuth is seen for COSx (bedding parallel to coring axis), with the maximum velocity (3653 m/s) measured parallel to the cross-bedding and the minimum (2754 m/s) perpendicular to the cross-bedding. Again, the velocity variations for COSz (bedding normal to coring axis) are relative small, with a maxima of 3386m/s and a minima of 3302 m/s. Both, the velocity magnitude as well as the degree of anisotropy are lower compared to the shale. These data give the sandstone an average anisotropy of approximately 13% for COSx and 3% for COSz. Permeability was measured concomitantly at effective hydrostatic pressures over a range of 5 to 90 MPa (Chapter 4.2.1). This was repeated for four pressure cycles on cores with the flow direction parallel and normal to bedding to derive the anisotropy. A mean fluid pressure of around 5MPa was set and maintained and using a constant pressure gradient of 0.4-0.8 MPa across the sample. For both flow directions, permeability decreases with increasing effective pressure and increases when effective pressure is subsequently reduced (Figure 4-19). A further permeability reduction is induced by each subsequent pressure cycle. And, although permeability does recover to an extent, it does not reach its original value indicating a permanent reduction of permeability. While both flow directions show the same general behaviour, there are significant differences between the measurements for COSx and

COSz. The initial permeability parallel to bedding (k_x), with a value of $33x10^{-18}m^2$, is one order of magnitude higher than normal to bedding (k_z) ($2x10^{-18}$ m^2), a strong initial permeability anisotropy (A_k) of around 180%, similar to the Nash Point Shale. The effect of pressure on permeability suggest that the microstructure of COS consists mainly of low aspect ratio cracks that are cemented and elongated, and low aspect ratio pores. At higher pressures, the remaining equant (high aspect ratio) pore space then takes over (Gehne and Benson, 2017).

Table 4-1: Physical rock properties including bulk density and total porosity.

Rock type	**Grain density (ρ_s) (g/cm³)**		**Total porosity (ϕ_T) (%)**	
Nash Point Shale	2.64	±0.012	6.31	±0.75
Crab Orchard Sandstone	2.66	±0.001	7.09	±0.2

Table 4-2: Physical rock properties including elastic wave velocity and initial permeability.

Rock sample	**# of samples**	**Velocity (m/s)**			**Anisotropy parameter (%)**		
		Average	Std. Dev.	Range	Average	Std. Dev.	Range
COSx	3	3184	167	2849-3645	13.2	3.8	10-18
COSz	1	3335	27	3302-3386	3	N/A	N/A
NPSx	3	3539	681	2510-4613	55.8	3.5	53-60
NPSz	3	4662	56	4862-5047	3.3	0.7	2.6-3.9

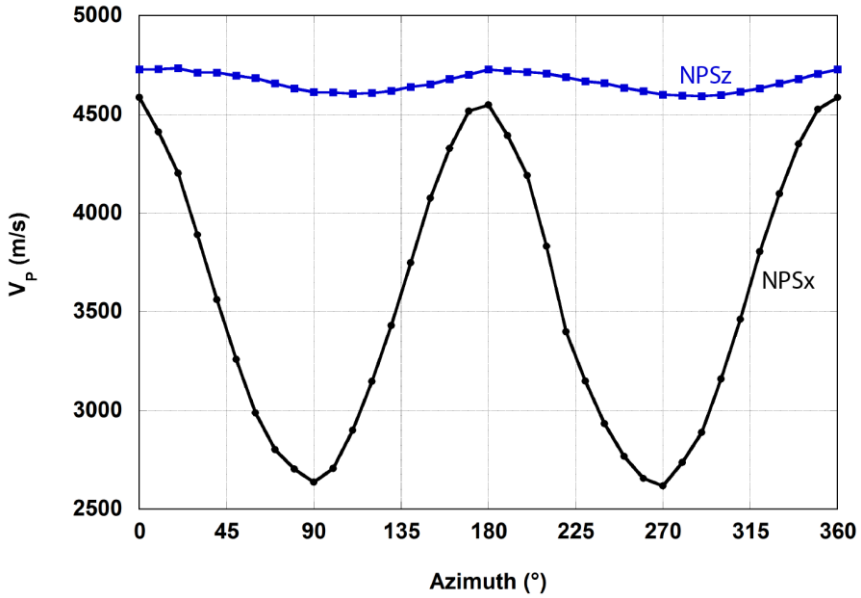

Figure 4-16: Nash Point Shale elastic wave velocities as a function of azimuth (dry samples); NPSx – cored parallel to bedding; NPSz – cored normal to bedding. The directional dependence of wave velocity indicates an anisotropic character of the shale.

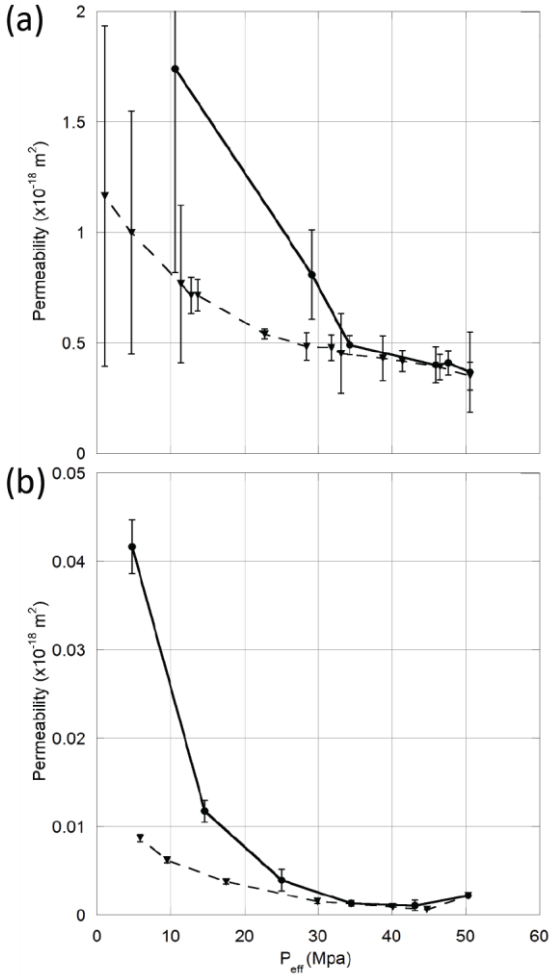

Figure 4-17: Permeability evolution for Nash Point Shale over an effective pressure range up to 50 MPa; (a) permeability parallel to bedding, (b) permeability perpendicular to bedding. Effective pressure increase is shown with solid lines, decrease with dotted lines.

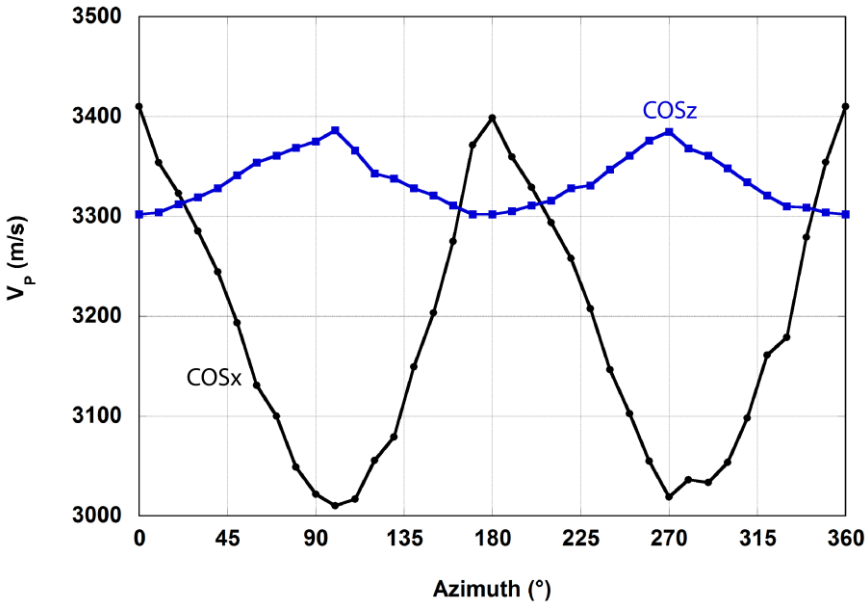

Figure 4-18: Crab Orchard Sandstone elastic wave velocities as a function of azimuth (dry samples). The directional dependence of wave velocity indicates an anisotropic character of the sandstone.

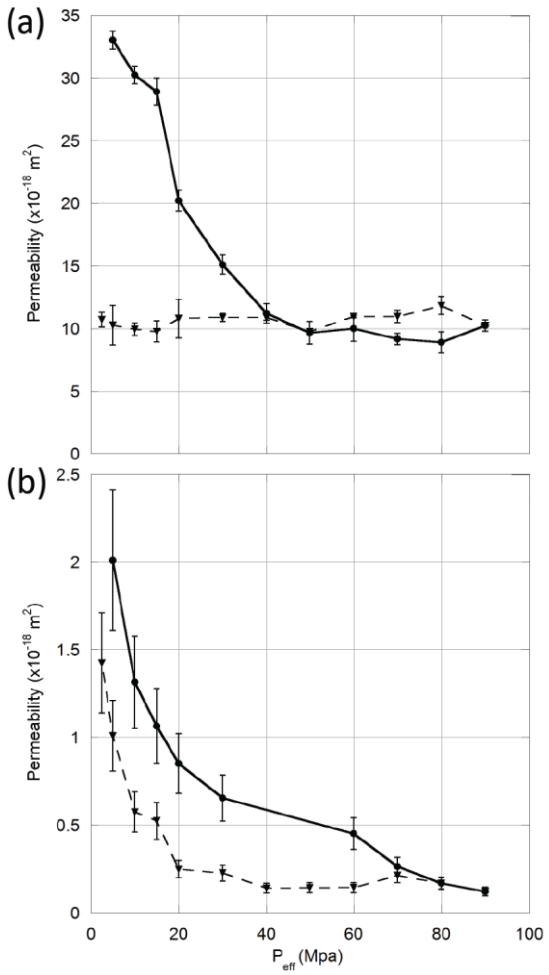

Figure 4-19: Permeability evolution for Crab Orchard Sandstone over an effective pressure range up to 90 MPa; (a) permeability parallel to bedding, (b) permeability perpendicular to bedding. Effective pressure increase is shown with solid lines, decrease with dotted lines (Gehne and Benson, 2017).

4.3 Mechanical properties

4.3.1 Experimental methods

Elastic wave velocity measurements showed that Nash Point shale is exceptionally anisotropic, even when compared with other shales, and this structural anisotropy is reflected in its mechanical properties as reported in detail below. Mechanical rock properties have been determined by a series of standard experiments including uniaxial compression tests, triaxial compression tests and tensile strength tests. The procedures for these test followed those set by the International Society of Rock Mechanics (Ulusay, 2014). Test specimens were drilled using a radial arm drilling machine and diamond drill bits followed by grinding of the end surfaces to achieve a good planarity of the surfaces and perpendicularity (±0.01mm) to the longitudinal axis. For uniaxial and triaxial tests, cores were prepared with a diameter of either 25 or 40mm and a length of approximately 2.5 times the diameter. Discs with a diameter of 40mm and thickness of approximately 20mm were used for the Brazilian disc tests (indirect tensile strength). To evaluate a potential directional strength dependence, samples were cored parallel and perpendicular to the inherent bedding for tensile, uniaxial and triaxial experiments.

The tensile strength was determined by Brazilian disk tests, an indirect tension test carried out at ambient pressure conditions (Ulusay, 2014). To apply an indirect tensional force, a rock disc is compressed diametrically between a set of jaws (Figure 4-20). The axial force is applied through a 600kN hydraulic press built into a stiff load frame. This setup allows for tensile stresses to be induced in the central region of the disc and perpendicular to the loading direction. The peak load P_P is recorded and together with the disc diameter D and the disc thickness t, the tensile strength σ_T can be calculated by (Ulusay, 2014):

$$\sigma_T = 0.636 \frac{P_P}{D * t} \qquad 4\text{-}7$$

Tensile strength was measured in all three principal fracture orientations relative to inherent bedding; Short-Transverse (S-T), Divider (Div) and Arrester (Arr) (Chong et al., 1987) (Figure 4-21). In the Short-Transverse orientation, the fracture plane and propagation direction are parallel to the bedding plane. In the Divider orientation, the fracture plane is normal to inherent bedding but propagates parallel to the inherent bedding planes, i.e. the fracture takes all bedding planes simultaneously. For the Arrester orientation, both the fracture plane and propagation direction are normal to the inherent bedding plane, taking one bedding plane at a time (Chandler et al., 2016). This allows for the evaluation of the rocks for strength

anisotropy, and serves as an important guideline value for the later experiments using pore fluid pressure to directly fracture rock, described in Chapter 3.3.

Uniaxial compression tests were utilised to determine the unconfined rock strength, Young's modulus and Poisson's ratio. Cylindrical specimens of both rocks with a diameter to length ratio of about 1:2.5 were longitudinally compressed between two loading platens by a 600kN hydraulic press (supplied by Instron, Figure 4-22). A load cell records the axially applied force, and external extensometers were used to measure axial and radial deformation. A chain was placed around the central part of the sample to measure the changes in the circumference (Fairhurst and Hudson, 1999). Additionally, the movement of the loading platens was also measured and recorded by the data logging software of the UCS machine. Corrections were applied before the test series to account for deformations of the loading frame and thus correct for machine stiffness. With knowledge of the peak load at failure, axial and radial deformation, sample dimensions, and axial and radial strain, the unconfined compressive strength and Poisson's ratio can be calculated using the following equations (Ulusay, 2014). The axial ε_a and radial strain ε_r are the ratios of the initial length L_0 and radius r_0 respectively to the change in these dimensions ΔL and Δr, taken at peak load, and are defined as follows:

$$\varepsilon_a = \frac{\Delta L}{L_0} \qquad 4\text{-}8$$

and

$$\varepsilon_r = \frac{\Delta r}{r_0} \qquad 4\text{-}9$$

The unconfined compressive stress σ_c is equal to the maximum axial load sustained by the sample and can be calculated by dividing the compressive peak load P_P by the initial cross-sectional area $A_0 = {r_0}^2\pi$. This is written as

$$\sigma_c = \frac{P_P}{{r_0}^2\pi} \qquad 4\text{-}10$$

Poisson's ratio υ describes the expansion in the direction perpendicular to the direction of compression and is defined as the ratio of radial strain to axial strain:

$$\nu = \frac{\varepsilon_r}{\varepsilon_a} \qquad (4\text{-}11)$$

The Young's modulus E is defined as the ratio of axial stress change to axial strain produced by the stress change (Ulusay, 2014) and is a measure of the stiffness of the rock. There are several methods to determine the Young's Modulus. In a large study with 531 compression tests, Malkowski and Ostrowski (2017) compared the three most widely used methods, which are also suggested by Ulusay (2014), for sandstones, mudstones, claystones and coal. They found that the average Young's modulus E_{ave}, given by the slope of the elastic part of the stress-strain curve gives the smallest variability in values and recommended that method. In this study, all three methods were used, with the same result as Malkowski and Ostrowski (2017). Therefore, the average Young's Modulus E_{ave} has been used in the following which is defined by:

$$\mathrm{E}_{ave} = \frac{\Delta\sigma}{\Delta\varepsilon_a} \qquad (4\text{-}12)$$

where: $\Delta\sigma$ is the change in axial stress and $\Delta\varepsilon_a$ is axial strain caused by the axial stress change (Ulusay, 2014).

Finally, conventional triaxial experiments measure the strength of the rock sample as a function of confining pressure. Similar to the uniaxial compressive tests, cylindrical samples are compressed along the longitudinal axis, but are confined radially by a confining pressure P_c, which is applied to the specimen's outer walls. The confining pressure is applied using a so-called Hoek-cell (Hoek and Franklin, 1967), a small pressure vessel, where oil is used to generate the confining pressure ($\sigma_H = \sigma_h$) and a rubber sleeve separates the sample from the confining medium. The sample is positioned inside the cell and at first, a hydrostatic pressure is established ($\sigma_V = \sigma_H = \sigma_h$). Then, the axial stress is increased until failure occurs, while the confining stress is kept constant. For efficiency reasons, multi failure state tests with a multi-stage procedure were performed. To achieve this, confining pressure was increased just before ultimate failure of the sample and the axial loading continued. Usually three failure stages were achieved for one specimen, and multiple failure stress values can be obtained to construct an empirical failure envelope. Peak axial stress and confining pressure are used to define the Mohr envelope, which is fitted using the least-square method (Lisle and Strom, 1982). From the envelope, the Mohr-Coulomb parameters internal friction angle ϕ_i and "apparent" cohesion C can be obtained (Ulusay, 2014) as:

$$\phi_i = arc\sin\frac{m-1}{m+1} \qquad 4\text{-}13$$

and

$$C = b\frac{1 - sin\phi_i}{2 * cos\phi_i} \qquad (4\text{-}14)$$

where m is the gradient of the failure envelope and b the intersect with the axial stress axis (y-axis).

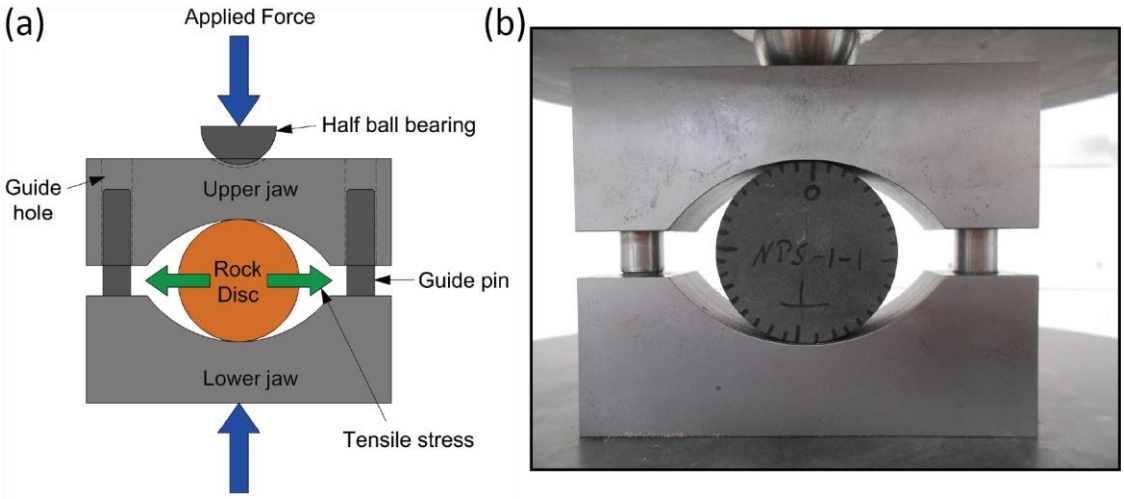

Figure 4-20: Brazilian Test setup (Indirect Tensile Strength); (a) Schematic of the setup and indicating direction of tensile stresses (green arrows) perpendicular to applied load; (b) Image of Brazil test of NPS.

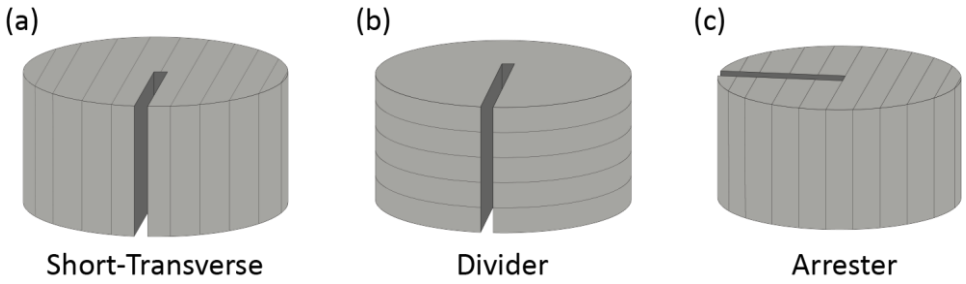

Figure 4-21: Principal fracture directions relative to inherent bedding; (a) Short-Transverse; (b) Divider; (c) Arrester. Figure modified after Chong et al. (1987).

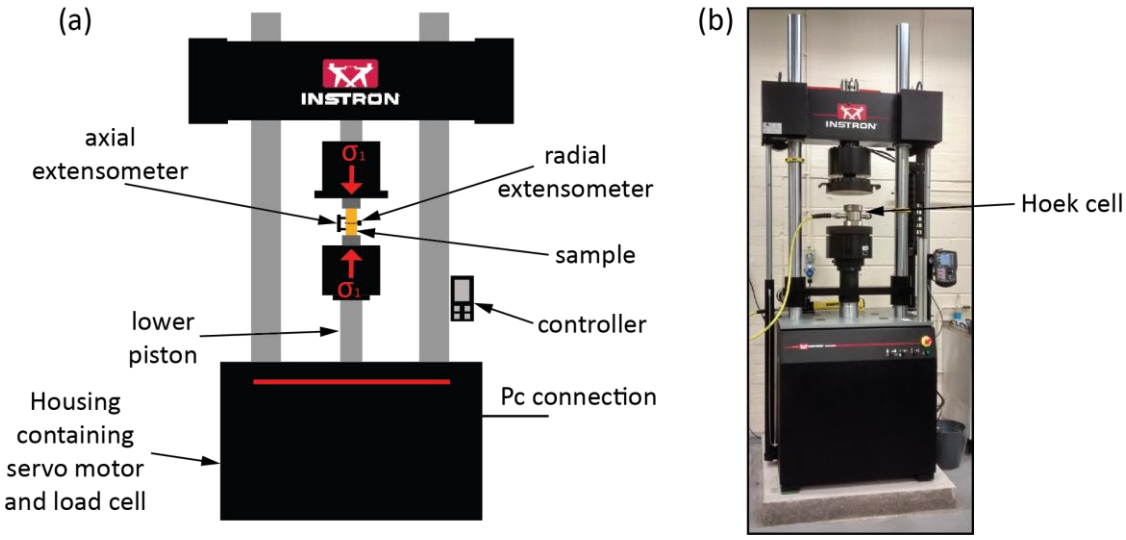

Figure 4-22: Uniaxial strength test apparatus (Instron); (a) Schematic of the UCS testing apparatus and indicating direction of applied compressional stress σ_1 (red arrows); (b) Image of UCS testing apparatus including Hoek cell. Lower piston moves upwards to increase the load.

4.3.2 Mechanical and physical rock properties of NPS and COS

Tensile strength

To characterise the mechanical behaviour of Nash Point Shale and Crab Orchard Sandstone, especially the effect of anisotropy, a series of standard laboratory test according to the methods described above were performed. Firstly, the tensile strength and the compressive strength was determined and assessed. As expected from previous analyses, both rock types show a directional strength dependence. The tensile strength has been measured in the three principal fracture directions relative to the bedding (Figure 4-21) (Chandler et al., 2016). The Divider orientation is the strongest for both rocks with an average value slightly higher for the sandstone compared to shale (COS = 9.8 MPa, Shale = 8.8 MPa). For the shale, S-T is the weakest direction, with much lower average values (4.7 MPa) compared to the Divider and Arrester orientation (8.8 MPa and 8.1 MPa respectively). This is not the case for the sandstone, where S-T and Arr have similar average values of 8.6 MPa and 8.4 MPa respectively. The shale and the sandstone therefore have a similar strength in the Arrester direction, but very different in the S-T, with the sandstone strength almost double compared to the shale. The data highlights the strength anisotropy of the two rock types and the difference in the influence of the bedding planes on the strength. In general, Nash Point Shale exhibits a wider range of measurements for all three fracture orientations suggesting a stronger effect of the bedding planes. The indirect tensile strength measurements show a very high tensile strength anisotropy (≈60%) for the shale, whereas COS has a much lower strength anisotropy of about 13%. These values are almost identically to the elastic wave velocity anisotropy.

The developed tensile fractures in the two rock types also highlight the different effect of the bedding planes (Figure 4-24). In the sandstone the bedding does not has a significant effect on

the fracture path, and all three directions show a similar fracture pattern: a main fracture parallel to the loading direction (Figure 4-24d-f). In contrast, the fracture advance direction in the shale is strongly influenced by the direction of the bedding relative to the loading direction. In the short-transverse direction, the fracture is parallel to the loading direction and planar (Figure 4-24a). The fracture in the divider orientation is sub-parallel to the loading direction, but curved (Figure 4-24b). Fracturing in the arrester direction produces a more complex structure with multiple fracture. A main fracture perpendicular to the bedding and multiple diversions along bedding planes (Figure 4-24c).

Uniaxial compressive strength

Directional dependence has also been noted in the compressional strength and the Young's Modulus for both rock types (Figure 4-25). Unconfined compressive strength values for Nash Point Shale range between 24 und 72MPa, with higher strengths normal to bedding, whereas the Young's modulus varies between 2 and 18 GPa, with the lower value for bedding normal compression. The same relationships, but with higher absolute values, can be seen for Crab Orchard Sandstone, with strength values between 88 and 182 MPa (higher strength for COSz) and Young's modulus raging between 17 and 28GPa (lower for COSz). For both parameters, NPS (UCS 103% and Young's Modulus 273%) exhibits a higher anisotropy compared to the sandstone, with 69% UCS anisotropy and 48% for Young's Modulus.

Table 4-3: UCS and Young's Modulus for NPS and COS

Rock type	Unconfined compressive strength			Young's Modulus		
	Average (MPa)	Std. Dev. (MPa)	Anisotropy (%)	Average (GPa)	Std. Dev. (GPa)	Anisotropy (%)
NPSx	36	9	103	8.8	4.7	273
NPSz	55	14		3	0.5	
COSx	123	22	69	23.1	3	48
COSz	153	21		20.1	2.1	

Nash point Shale samples compressed parallel to bedding failed by multiple axial splitting along bedding planes (Figure 4-26a), whereas when compressed normal to bedding, the sample failed by single axial splitting cutting across the bedding at ≈90° (Figure 4-26b). Conversely, Crab Orchard Sandstone, irrespective of bedding orientation, failed dominantly by single axial splitting with some secondary fractures in the same plane (Figure 4-26c & d). However, when bedding was parallel to compression direction the fracture developed mostly parallel or at a shallow angle (<10°) to the bedding, whereas the fracture developed at a larger angle (70-90°)

to the bedding when σ_1 was orientated perpendicular to the bedding. Irrespective of the failure mode, the shale generally deformed in a more “brittle” manner, with a sudden failure (Figure 4-27 top panel) compared to the sandstone, which exhibited a more ductile failure behaviour (Figure 4-27 bottom panel).

Triaxial compressive strength

Triaxial compressive strength increases approximately linearly for both rock types. As for the uniaxial data, higher absolute strength values were measured for the sandstone and with loading direction normal to bedding (Figure 4-28) compared to parallel to bedding. Figure 4-28 shows peak axial stress plotted against confining pressure, as well as Mohr-Coulomb failure envelopes (Lisle and Strom, 1982; Ulusay, 2014). This allows the internal friction angle and cohesion to be determined, listed in

Table 4-4. The fracture geometry of the two rock types developed under triaxial conditions and deformed parallel and normal to bedding is displayed in Figure 4-29. NPSx samples show a single fracture at ≈60° to the horizontal. A similar failure pattern was observed for NPSz samples with a fracture at ≈60°. However, almost all NPSz samples also showed an opening along a bedding plane. Given the orientation of σ_1, it is most likely an unloading fracture, where the damage occurred during the loading of the sample and during unloading the bedding plane started to open up. Crab Orchard Sandstone samples deformed parallel to bedding showed multiple fracture at ≈60° and ≈130°, crosscutting each other. In addition, COSz samples show both a primary fracture at ≈60° and a secondary fracture parallel to bedding.

Table 4-4: Mohr-Coulomb parameters for NPS and COS

Rock type	Cohesion (MPa)	Internal friction angle (°)
NPSx	17	33
NPSz	25	29
COSx	17	51
COSz	32	48

To summarise, Nash Point Shale and Crab Orchard Sandstone have different petrophysical and mechanical properties and show significant differences in the rock fabric in terms of matrix structure, grain alignment and grain size. Furthermore, petrophysical and mechanical properties vary considerably depending on the relative orientation of the induced signal, flow or imposed strain (deformation) with respect to the cross-bedding. The sandstone has a stronger tensile and compressive strength and a higher permeability by at least one to two

magnitudes, despite a similar porosity. However, the shale exhibits a much stronger directional dependence for all properties. Both rocks, however, are highly anisotropic, and therefore highly suitable for a laboratory study on such phenomena.

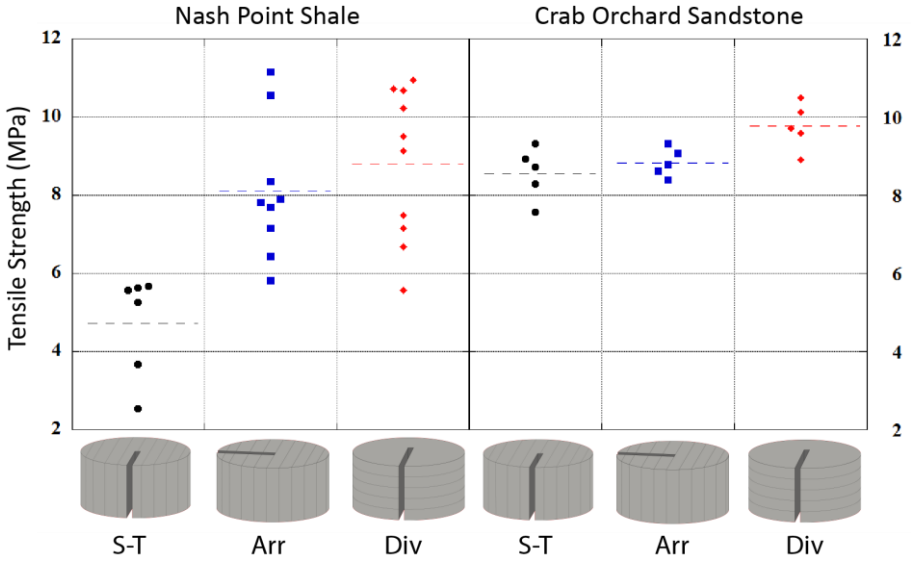

Figure 4-23: Tensile strength for Nash Point Shale and Crab Orchard Sandstone from Brazilian disk tests.

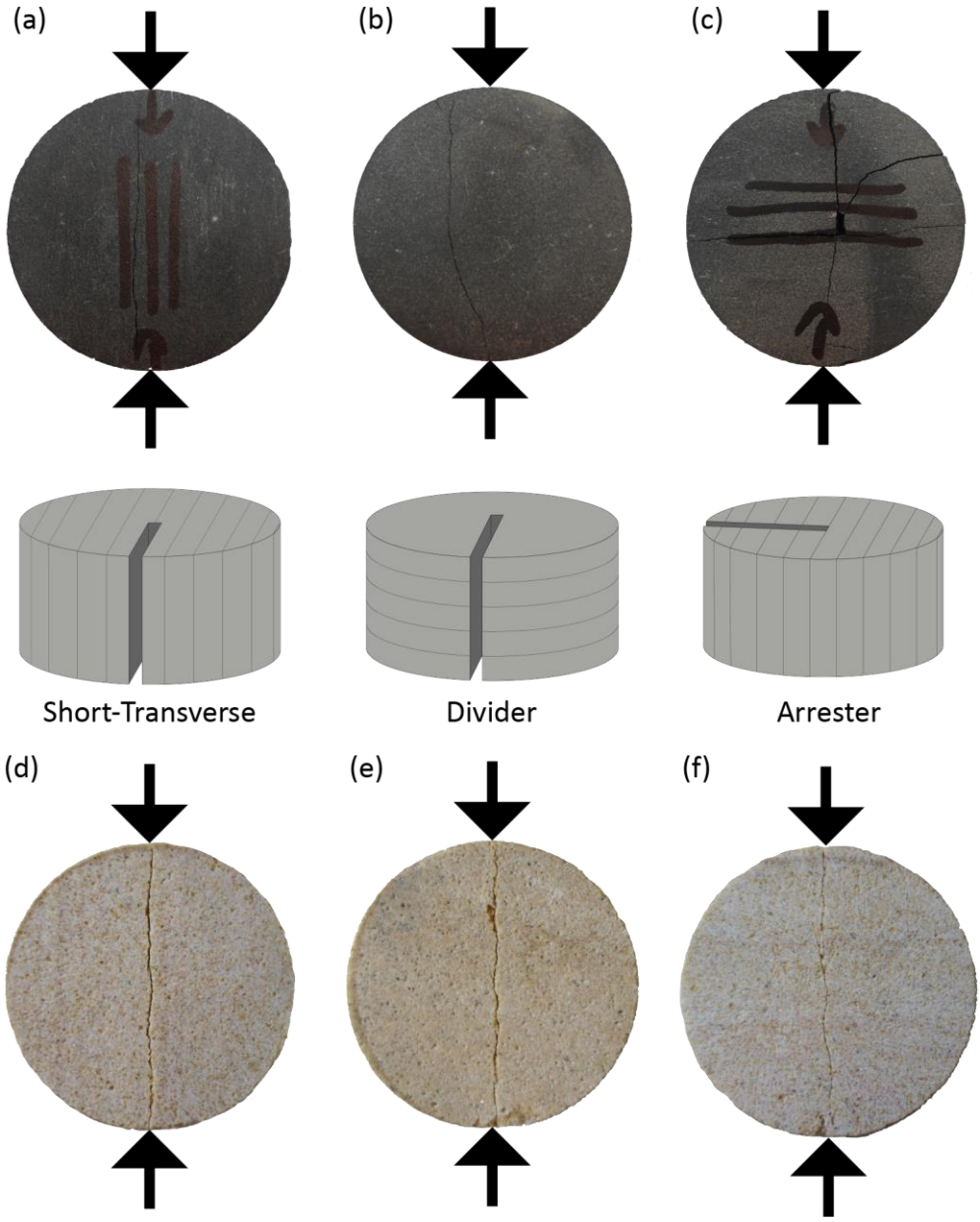

Figure 4-24: Brazilian test failure mechanism for NPS (a-c) and COS (d-f). (a & d) Short-Transverse, (b & e) Divider and (c & f) Arrester fracture orientation. Back arrows indicating loading direction.

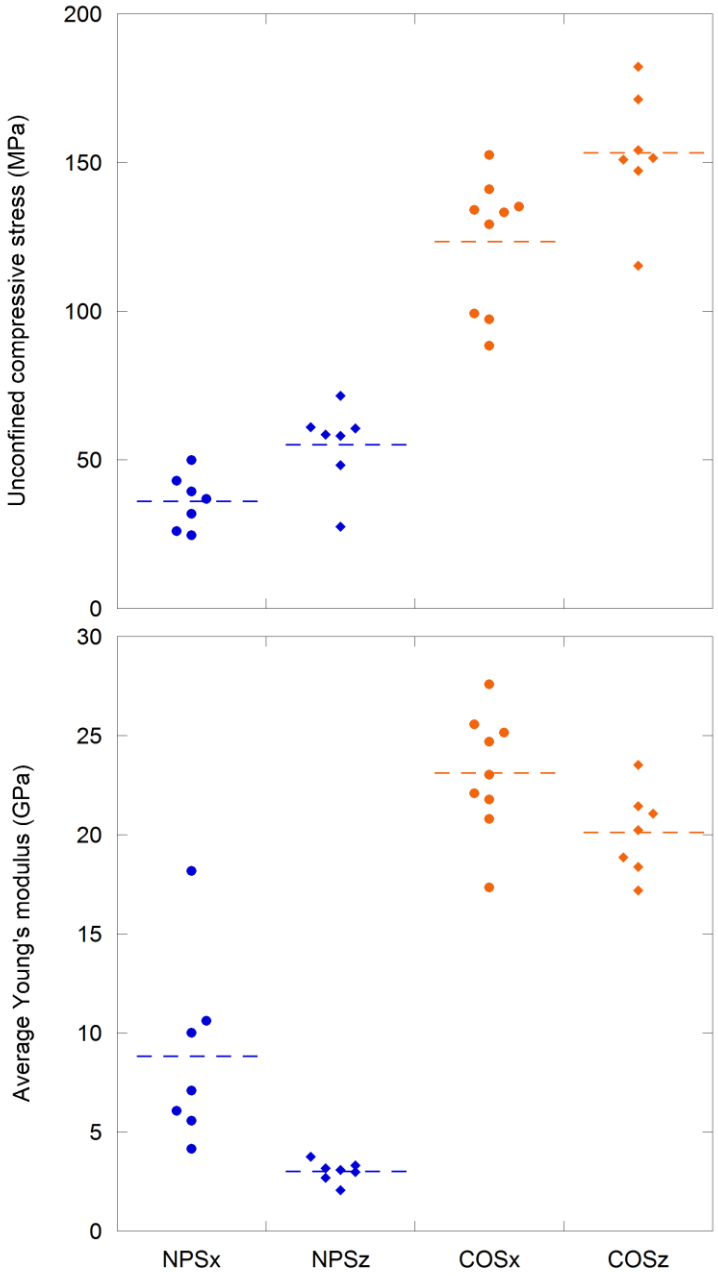

Figure 4-25: Results of unconfined compression tests for NSP and COS including (a) the unconfined compressive strength and (b) the average Young's modulus. Dashed horizontal line shows the average.

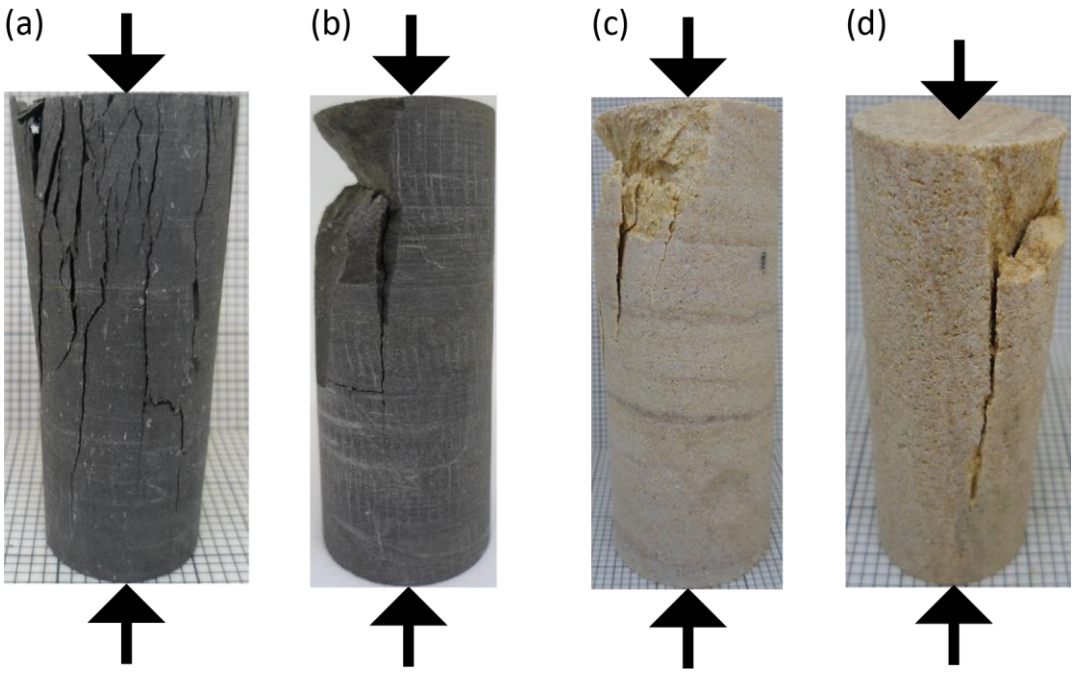

Figure 4-26: Uniaxial compression test failure mechanism for NPS (a & b) and COS (c & d); (a) & (c) are compressed parallel to bedding and (b) & (d) perpendicular to bedding. Black arrows indicating loading direction.

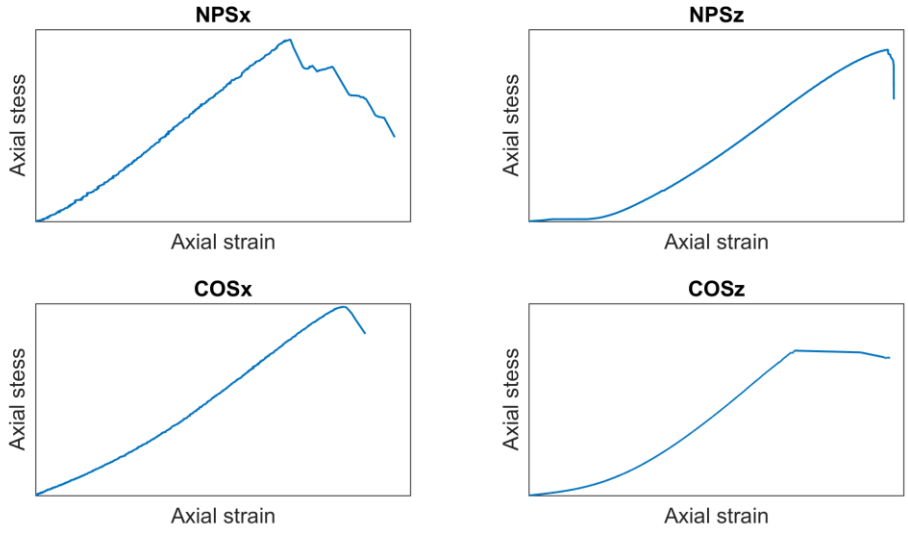

Figure 4-27: Failure behaviour during uniaxial compression tests for NPS and COS.

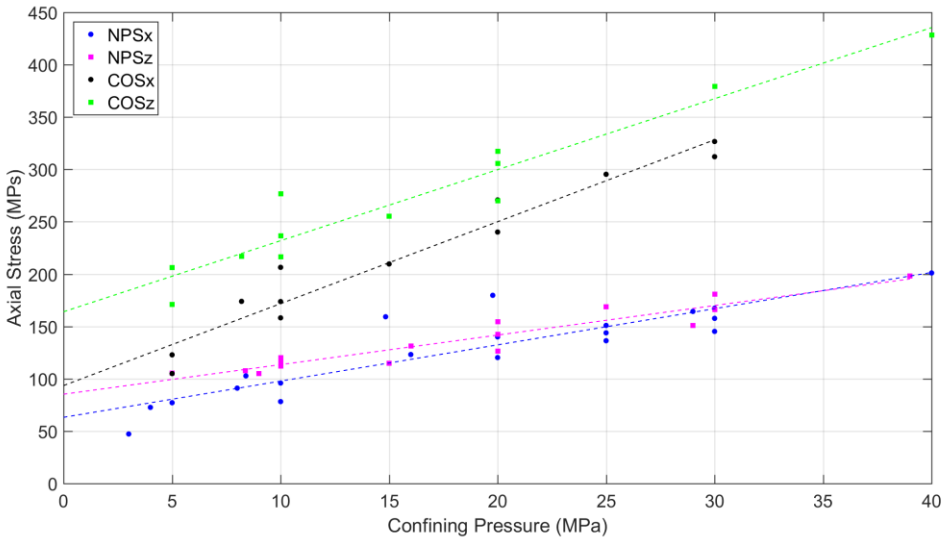

Figure 4-28: Results of triaxial compression tests for NPS and COS parallel and normal to bedding; dashed lines denote the Mohr-Coulomb failure envelopes determined according to Lisle and Strom (1982) and Ulusay (2014).

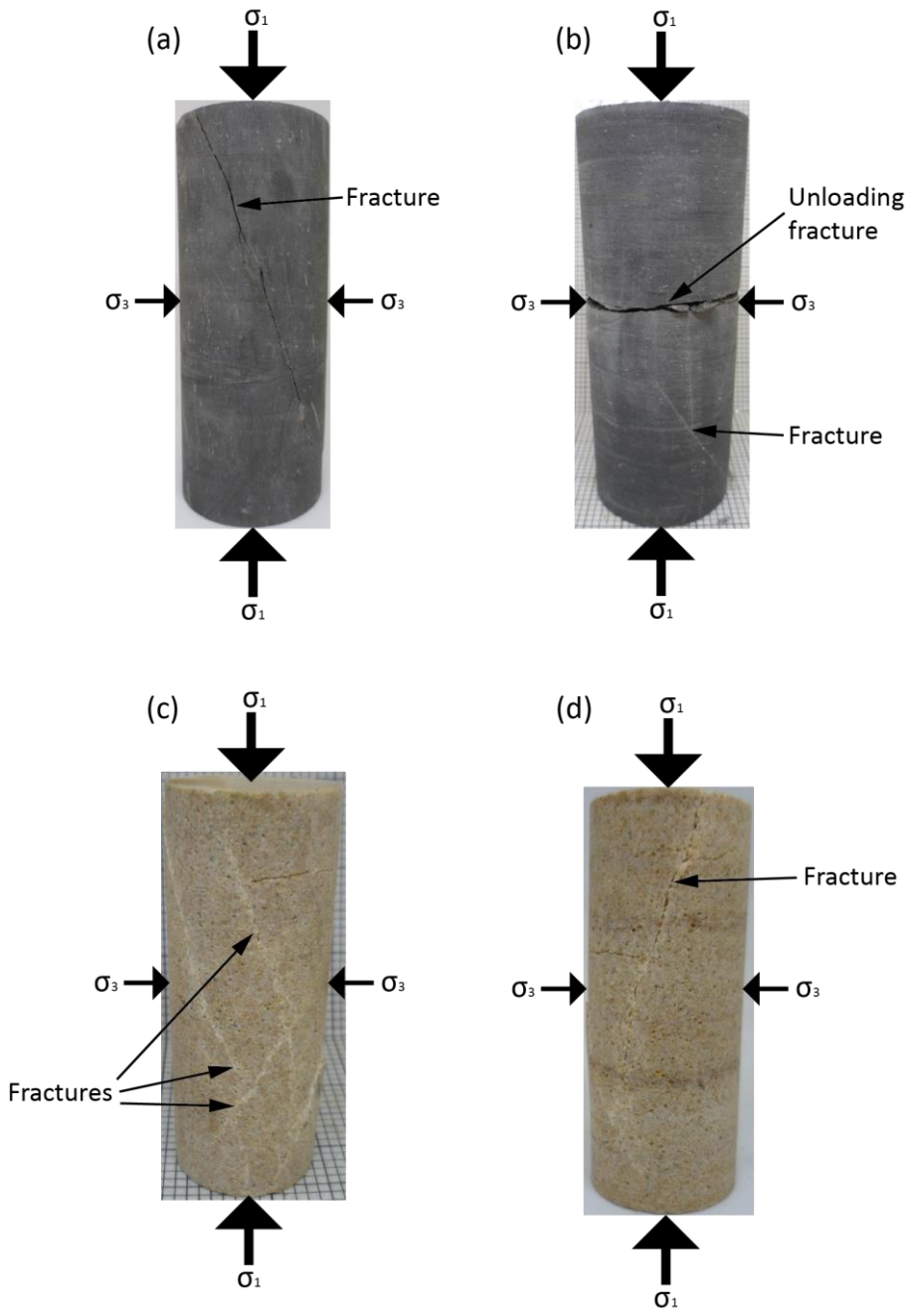

Figure 4-29: Triaxial compression test failure mechanism for NPS (a & b) and COS (c & d). (a) & (c) are compressed parallel to bedding and (b) & (d) perpendicular to bedding. Black arrows indicating principal stress directions. Confining pressure kept constant, while axial load was increased until failure occurred.

4.4 Nash Point Shale compared to unconventional resource lithologies

Unlike conventional reservoirs, "unconventional oil" reserves are contained within low permeability (<20 × 10^{-15} m^2) sedimentary rock lithologies such as shale and so-called tight (cemented) sandstone and carbonate rocks (Bennion et al., 1996). For this study, Crab Orchard Sandstone was used to represent a tight-sandstone and Nash Point Shale as an analogue for a typical shale reservoir, due to accessibility to and workability of this material. Whilst Nash Point Shale is not a pure shale petrologically, it does share many of the features of well-known gas-shales, which makes this rock a very suitable analogue. Figure 4-30 shows the mineralogical composition of several gas bearing shales, including Barnett Shale, Eagle Ford Shale, Marcellus Shale and Green River Shale from the USA and Bowland Shale, Whitby Mudstone and Nash Point Shale found in the UK.

Several studies (e.g. Amann et al., 2012; Sone and Zoback, 2013b; Rybacki et al., 2015) have shown that in shales, physical properties and fracture behaviour are often linked to the rock composition, especially clay content. Figure 4-30 shows that Nash Point Shale and in particular the Eagle Ford Shale formation (Texas, USA), which is a major unconventional oil and gas play, have similar mineralogical compositions. Both are carbonate rich and can be classified as calcareous mudstone or mudstone. Much like Nash Point shale, the mineral composition of Eagle Ford shale is dominated by calcite (≈50-60%) with lesser amounts of clay (20-30%) and quartz (5-10%) (Mullen, 2010), and it has a mean porosity of 7.5% (Chalmers and Bustin, 2017). In contrast, the Bowland Shale, Whitby Mudstone, Barnett Shale and Marcellus shale are more quartz rich and are better described as siliceous or argillaceous mudstones. However, the mechanical behaviour of rocks does not solely depend on the mineralogical composition. Further characteristics such as rock fabric, physical properties, and inherent anisotropy, is likely to significantly influence the rocks response to stress change and deformation. Therefore, further key petrophysical and geomechanical parameters of Nash Point Shale have been compared to the above mentioned shale gas lithologies (Table 4-5). Most of the results listed in Table 4-5 are compiled from the work of Weedon (1986); Arzani (2004); Bowker (2007); Loucks and Ruppel (2007); Bruner and Smosna (2011); Jarvie (2012a); Hobbs et al. (2012); Breyer et al. (2013); Harvey and Gray (2013); Mokhtari (2015); Rybacki et al. (2015); Houben et al. (2016); Schieber et al. (2016); Fauchille et al. (2017) and McKernan et al. (2017).

Table 4-5: Overview properties of gas bearing mudrocks

	Nash Point Shale	Bowland Shale	Whitby Mudstone	Eagle Ford Shale	Barnett Shale
Age	Early Jurassic	Mississippian	Early Jurassic	Upper Cretaceous	Mississippian
Basin	Bristol Channel Basin, South Wales	Bowland	Cleveland Basin	Eagle Ford/ Austin Chalk Trend	Fort Worth
Stratigraphy	Limestone interbedded with calcareous mudrock and marl beds	Siliceous mudrock interbedded with clastic and carbonate deposits	Bioturbated silt-bearing, clay-rich mudrock	Interbedded and organic-rich argillaceous and calcareous mudrock, and limestone	Laminated, organic-rich siliceous and argillaceous lime mudrock and skeletal, argillaceous lime packstone
Thickness (m)	Up to 100	100-500	15-80	45-90	30-220
Average Clay content	23	6	63	20	39
Average Carbonate content	63	21	8	59	14
Average Silicate content	14	74	27	21	45
TOC (%)	1-6	1-6	2-11	1-7	1-14
Gas - Porosity (%)	5-8	5-10	1-9	5-11	1-12
Permeability (m^2)	$10^{-18} – 10^{-20}$		$10^{-19} – 10^{-21}$	$10^{-19} – 10^{-20}$	10^{-20} - 10^{-22}

	Nash Point Shale	Bowland Shale	Whitby Mudstone	Eagle Ford Shale	Barnett Shale
Micro structure	fine grained clay and organic-rich matrix with disseminated, isolated calcite crystals and lithic fragments	Quartz and carbonate grains within laminated quartz-rich or calcite-rich, fine grained matrix	silt-sized grains interbedded in fine grained argillaceous matrix	silt-sized grains interbedded in fine grained, organic rich clayey and calcareous matrix	silt-sized detrital grains, biotic fragments, and solid organic materials in fine grained matrix
Anisotropy	Well-defined micro lamination with strong preferred alignment of minerals (V_P = 56%)	Laminated matrix structure (V_P = 13%)	Preferred alignment of clay minerals (V_P = up to 30%)	Pronounced anisotropic fabric with strong preferred mineral alignment	Preferred clay orientation
Young's modulus (GPa)	2-18	43-47*		2-50	10-80
UCS (MPa)	24-72	160-220*		130-170	36-106
ITS (MPa)	2-12	9-13*		1-3	4-19

* BWS samples from Outcrop in Peak District

Beside the similar mineralogy, petrographic images of Eagle Ford Shale samples (Sone and Zoback, 2013a) show a similar microstructure and matrix compared to NPS. Both shales rocks have an anisotropic fabric where bedding planes are defined by preferred orientations of matrix clay and alignment of elongated grains, as well as similar organic matter contents, porosities and permeabilities. According to Houben et al. (2016) and Sondergeld et al. (2010), Whitby Mudstone and Barnett shale also have a similar microstructure with silt-sized grains interbedded in a fine grained matrix with preferred alignment of clay minerals. Fauchille et al. (2017) described a dominantly laminated quartz-rich matrix in the Bowland Shale, with some areas showing a more calcite-rich matrix. Generally, all of the above shale rocks have similar TOC values, low porosities and very low permeabilities in the micro to nano-Darcy range. Nash point shale exhibits weaker compressional strength and stiffness compared to the other shale rocks, but has similar tensile fracture values. The strong effect of the inherent anisotropy, low permeability, and the similarities in mineralogy and petrophysical and mechanical properties to other gas shale rocks makes Nash Point Shale a suitable representative rock type to study the behaviour of unconventional (gas/oil shale) reservoir rocks during hydraulic fracturing.

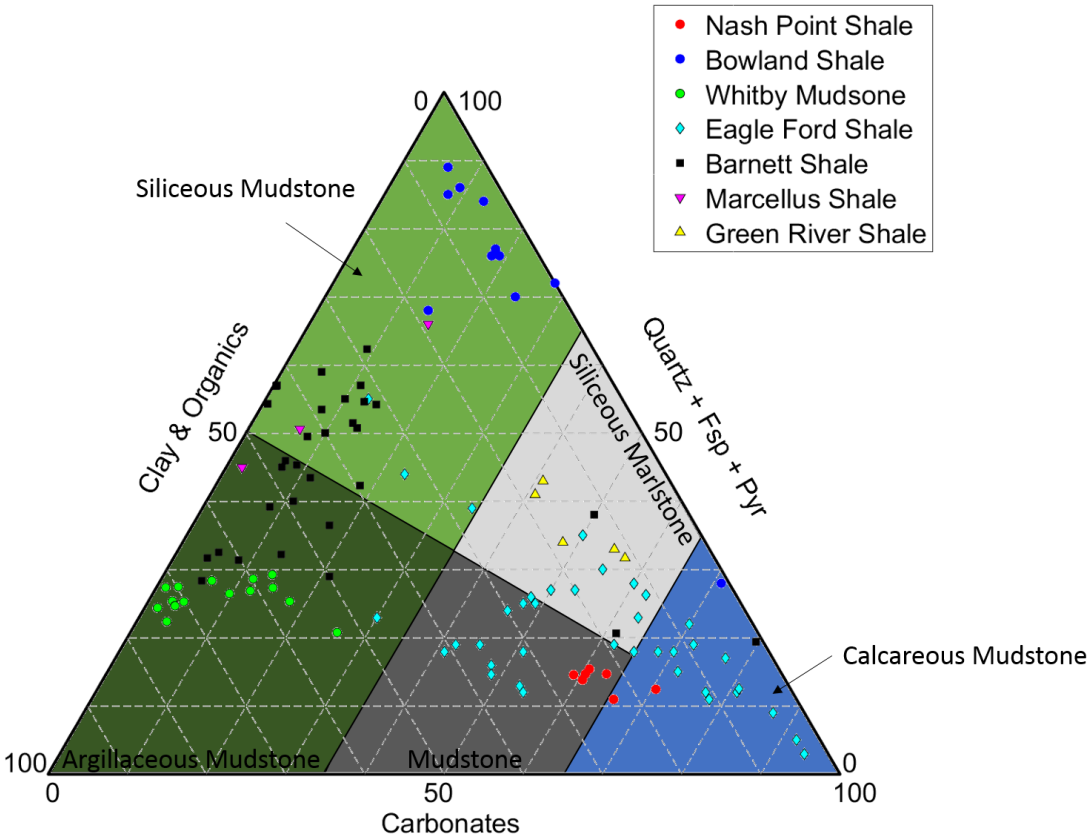

Figure 4-30: Comparison of mineralogical composition of several gas bearing shales. Nash Point, Bowland and Whitby are in the UK; the remainder are in the USA. Bowland shale data (Fauchille et al., 2017); Whitby data (Houben et al., 2016); US data (Lancaster et al., 1993; Vermylen, 2011; Vermylen and Zoback, 2011; Walls and Sinclair, 2011; Bowker, 2007; Chalmers et al., 2012; Ghanizadeh et al., 2013; Sone and Zoback, 2013a; Heller et al., 2014; Gasparik et al., 2014; Elston, 2014; Mokhtari, 2015; Rybacki et al., 2015; Enriquez Tenorio, 2016; Saif et al., 2017; Zhang et al., 2017); classification after Hennissen et al. (2017).

5 Hydraulic fracturing of shale and sandstone in the laboratory

5.1 Overview of hydraulic fracturing experiments

Hydraulic (tensile) fracturing is a complex process that is not fully understood, in particular the basic principles of injection pressure induced fracturing, and how this is modified by inherent anisotropy and the fabric of the rock matrix. Importantly, the process is then also modified by factors such as the external stress conditions (such as burial depth) as well as the presence of pore pressure. In this chapter, a detailed description of experimental results from laboratory hydraulic fracturing experiments (micro hydraulic fracturing) is presented. Data analysis focuses on the description of the fracture process, based on mechanical and seismic measurements, and the assessment of the developed fracture pattern. For this study, forty three hydraulic fracturing experiments were conducted using fluid overpressure to initiate hydraulic fracture (Chapter 3.3). The set of experiments included tests on two different rock types at different confining pressures, with different bedding orientations and using two different pressurisation fluids of different viscosity. The main focus of this study is on the behaviour of Nash Point Shale during hydraulic fracturing. However, a number of experiments using Crab Orchard Sandstone were initially conducted to better define experimental protocol and develop the setup, as it is easier to prepare samples but still exhibits a low permeability and high anisotropy. Furthermore, the sandstone also acts as a counterpoint to the fine grained NPS to investigate the effect of rock fabric and initial permeability on the fracturing process.

First, a summary of the results from all hydraulic fracturing experiments performed in this study is presented and summarised (Table 5-1), including the rock types, bedding orientation, experimental conditions, pressurising fluid and maximum fluid pressure. Afterwards, the recorded mechanical and seismic data as well as the source type mechanism of key experiments at different confining pressures, bedding orientations and rock types are described in detail. To evaluate reproducibility and the results, several experiments have been performed with Nash Point Shale samples parallel to bedding using the same or similar pressure conditions. Figure 5-1 shows the maximum recorded fluid pressure plotted against confining pressure for all experiments with the key experiments highlighted (red circles). It can be seen from the diagram that the maximum fluid pressure is relatively consistent and is not unduly influenced by the natural variability of rock material, especially in highly anisotropic shales. All experiments exhibit similar general mechanical characteristics of the fluid pressure evolution during the fracture process: a maximum fluid pressure is followed by a first gentle and then rapid fluid pressure decay. Shale samples also showed an oscillation phase before the final gradual pressure decay. The development of the final setup, including data recording and

time correlation, was an evolving process and several of the experiments in Table 5-1 are preliminary experiments (highlighted grey in Table 5-1). In general, the final setup was used for shale experiments with numbers above 94 and for sandstone above 63. Experiments for detailed analysis were then chosen based on dataset quality and in the following labelled according to the rock type, bedding orientation relative to the coring axis and σ_v, confining pressure and pressurisation fluid (Table 5-1 labels in brackets) for better readability (e.g. NPSx-15-w -> Nash Point Shale, parallel bedding, 15MPa confining pressure, pressurisation fluid water; COSz-2.2-oil -> Crab Orchard Sandstone, normal bedding, 2.2MPa confining pressure, pressurisation fluid oil). Additionally, the complexity of the fracture network has been examined through low resolution micro X-ray CT imaging (≈31µm) of the majority of tested samples. To evaluate the morphology of the developed hydraulic fractures in more detail, twelve samples (5x NPSx, 1xNPSz, 5x COSx, 1xCOSz) were then scanned at a high resolution (≈9µm) and studied under a Scanning Electron Microscopy and regular (white-light) microscopy.

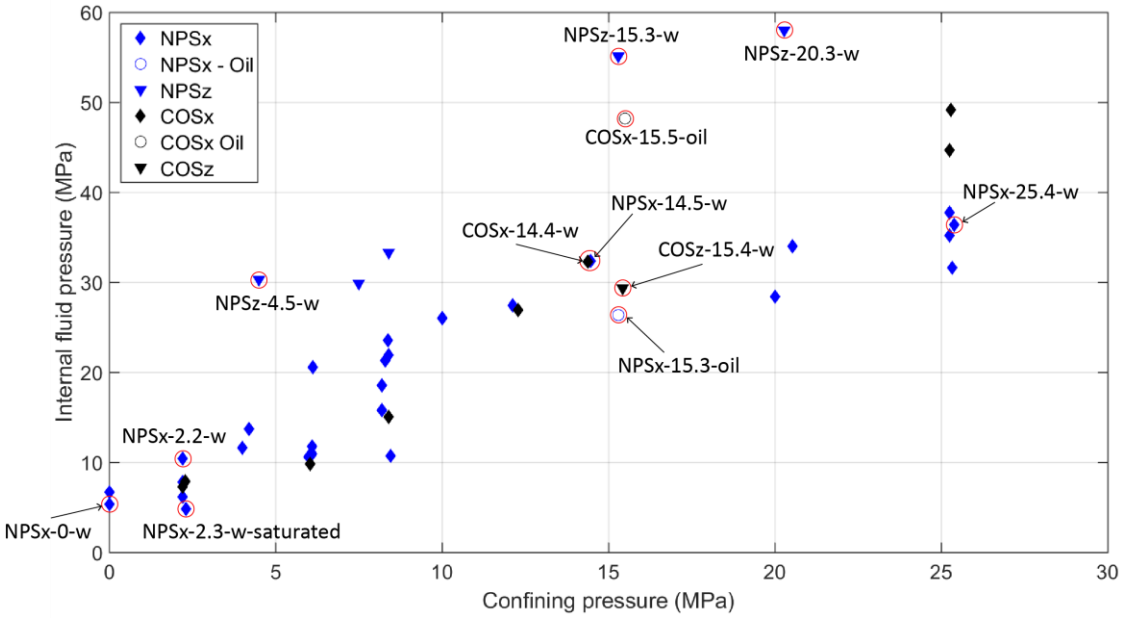

Figure 5-1: Maximum fluid pressure-confining pressure diagram of hydraulic fracturing experiments conducted within this study. Key experiments are highlighted with a red circle and labelled.

Table 5-1: Overview of micro hydraulic fracturing experiments ; experiments highlighted in bold writing are described in detail in this chapter, black labels indicate the use of the final setup and grey labels indicate preliminary experiments, labels in brackets are the labels used in the text of this thesis.

Sample	Bedding orientation	Max injection pressure (MPa)	Axial stress (MPa)	Confining pressure (MPa)	Flow rate (mL/min)	Pressurising fluid
NPSx-3-77	Parallel	6.7	7.9	0	1	water
NPSx-3-79 (NPSx-0-w)	**Parallel**	**5.35**	**5.4**	**0**	**1**	**water**
NPSx-3-66	Parallel	6.13	7.2	2.2	1	water
NPSx-3-89	Parallel	7.79	8.6	2.2	1	water
NPSx-3-97 (NPSx-2.2-w)	**Parallel**	**10.39**	**11.813**	**2.2**	**1**	**water**
NPSx-3-94 (NPSx-2.3-w-saturated)	**Parallel**	**4.83**	**5.99**	**2.3**	**1**	**water**
NPSx-3-85	Parallel	11.63	12.78	4	1	water
NPSx-3-57	Parallel	13.7	24.3	4.2	1	water
NPSx-3-82	Parallel	10.58	12.53	6	1	water
NPSx-3-83	Parallel	10.62	12.48	6	1	water
NPSx-3-92	Parallel	10.97	13.89	6.1	1	water
NPSx-3-104	Parallel	11.76	13.02	6.1	1	water
NPSx-3-47	Parallel	20.54	28.4	6.2	1	water
NPSx-3-49	Parallel	18.55	28.2	8.2	1	water
NPSx-3-70	parallel	15.81	16.8	8.2	2	water
NPSx-3-51	Parallel	21.3	28.5	8.3	1	water
NPSx-3-132-k	**Parallel**	**23.56**	**30.33**	**8.4**	**1**	**water**
NPSx-3-50	Parallel	21.94	28.4	8.4	1	water
NPSx-3-54	Parallel	10.7	49.9	8.5	1	water
NPSx-3-84	Parallel	25.98	39.8	10	1	water
NPSx-3-128	Parallel	27.45	32.344	12.1	1	water
NPSx-3-105 (NPSx-14.5-w)	**Parallel**	**32.34**	**34.96**	**14.5**	**1**	**water**
NPSx-3-88	Parallel	28.41	39.8	20	1	water

Sample	Bedding orientation	Max injection pressure (MPa)	Axial stress (MPa)	Confining pressure (MPa)	Flow rate (mL/min)	Pressurising fluid
NPSx-3-137	Parallel	34	40.34	20.53	1	water
NPSx-3-135	Parallel	37.72	48.97	25.3	1	water
NPSx-3-136	Parallel	35.16	52.74	25.3	1	water
NPSx-3-133	Parallel	31.63	37.45	25.3	1	water
NPSx-3-144 (NPSx-25.4-w)	**Parallel**	**36.35**	**42.42**	**25.4**	**1**	**water**
NPSx-3-146 (NPSx-15.3-oil)	**parallel**	**26.36**	**31.7**	**15.3**	**1**	**oil**
NPSz-3-139 (NPSz-4.5-w)	**Normal**	**30.29**	**35.76**	**4.5**	**1**	**water**
NPSz-3-56	Normal	29.87	33.55	7.5	1	water
NPSz-3-55	Normal	33.3	38.4	8.4	1	water
NPSz-3-131 (NPSz-15.3-w)	**Normal**	**55.11**	**61.67**	**15.3**	**1**	**water**
NPSz-3-138 (NPSz-20.3-w)	**Normal**	**57.98**	**64.29**	**20.3**	**1**	**water**
COSx-1-58	Parallel	7.3	9.3	2.2	5	water
COSx-1-62-k	Parallel	7.84	9.746	2.3	5	water
COSx-1-59	Parallel	9.78	18.1	6.1	5	water
COSx-1-60	Parallel	15.05	20.17	8.4	5	water
COSx-1-78	Parallel	26.88	32.06	12.3	5	water
COSx-1-63 (COSx-14.4-w)	**Parallel**	**32.3**	**44.9**	**14.4**	**5**	**water**
COSx-1-79	Parallel	44.69	52.88	25.25	5	water
COSx-1-81	Parallel	49.11	59.65	25.3	5	water
COSx-1-82 (COSx-15.5-oil)	**Parallel**	**48.17**	**66.57**	**15.5**	**5**	**oil**
COSz-1-80 (COSz-15.4-w)	**Normal**	**29.34**	**37.75**	**15.4**	**5**	**water**

5.2 Micro Hydraulic Fracturing of Nash Point Shale parallel to bedding

Information about the fluid-driven fracture process in shale was derived from a combination of fluid injection pressure, acoustic emission activity, and radial deformation measurements. Specifically, five key parameters are defined: (1) maximum fluid injection pressure (**$maxP_{inj}$**), (2) the onset of radial deformation (**rDef**), (3) the beginning of acoustic emission activity, which is defined as the onset of an exponential increase in the AE hit count rate (**AE_0**), (4) peak acoustic emission activity (**maxAE**) as well as (5) the point at which the fluid pressure starts to decrease rapidly (**P_{rd}**). Figures in this chapter show the time axis normalised (zeroed) to the time of maximum fluid injection pressure for ease of reading. In this section, the experimental results of hydraulic fracturing of Nash Point Shale is presented and analysed with bedding parallel to the sample axis (σ_v), denoted as NPSx, at confining pressures ranging from 0-25MPa, and using water as pressurisation fluid.

Hydraulic fracturing at medium confining pressure (14.5MPa) – NPSx-14.5-w

A benchmark experiment utilised NPS at a confining pressure of 14.5MPa, equating to approximately 600m depth of burial. Figure 5-2a shows a 0.9s time record illustrating internal fluid injection pressure (blue line), AE hit count rate (red dots) and radial deformation (green line), all recorded at a sampling frequency of 10kHz. The maximum fluid injection pressure ($maxP_{inj}$) of 32.36MPa predates the onset of radial deformation and increased AE activity commencing from 0.03s and 0.07s respectively. Interestingly, radial deformation onset is recorded prior to the beginning of seismic activity. However, AE activity occurs in two phases (Figure 5-2a), a “short” minor phase commencing at 0.07s that precedes the “main” phase of seismic activity that commences at 0.09s. A small decrease in P_{inj} (≈0.1MPa) at 0.075s can be linked to the initial short AE phase, as the peak coincides with the low point of the P_{inj} decrease (at 0.076s). A low frequency burst (100-200kHz) can be seen in Figure 5-2d at the same time (0.076s). The main phase of AE activity is linked to the first significant decrease in P_{inj} at 0.105s (Figure 5-2a). The trend in P_{inj} is easier to visualise if integrated with time to give a pressure rate, shown in Figure 5-2b. During that first significant pressure decrease, fluid pressure decay rate increases exponentially to a maximum of 625MPa/s. The peak AE rate occurs at the same time as the start of the rapid fluid pressure decay (0.105s, Figure 5-2a) and the onset of this main AE phase is characterised by an energy burst with a highly emergent to impulsive onset as seen in the continuous signal (Figure 5-2c). The respective spectrogram (Figure 5-2d) reveals two frequency components. While the most significant power lies in the range 100 to 300kHz, events appear rapidly with power in the 400kHz range. Afterwards, fluid pressure recovers briefly and oscillates for about 0.04s (Figure 5-2a), before the pressure continues to decrease at about 3.5MPa/s (Figure 5-2b), suggesting constant fluid pressure leakage through a fracture

that cannot be maintained by the constant (controlled) fluid injection rate used. Fracture opening, implied by the radial deformation data, increases rapidly between 0.1s and 0.15s before settling slightly (Figure 5-2a), exhibiting a number of 'breaks' in the deformation rate which coincide with either peaks or troughs in fluid pressure oscillation (black arrows). The AE activity peaks a second time with the first oscillation peak and then settles to a continuous (although scattered) level of 100 hits/ms for about 0.7s before decreasing to normal background level noise. The continuous seismic signal and spectrogram (Figure 5-2c and d) show a harmonic quasi-monochromatic coda in both frequency ranges 100-300kHz and at 400kHz. Source type (fault plane solution) analysis (Figure 5-3) show that during fracturing, tensile failure is dominant, but with also a significant element of shear failure.

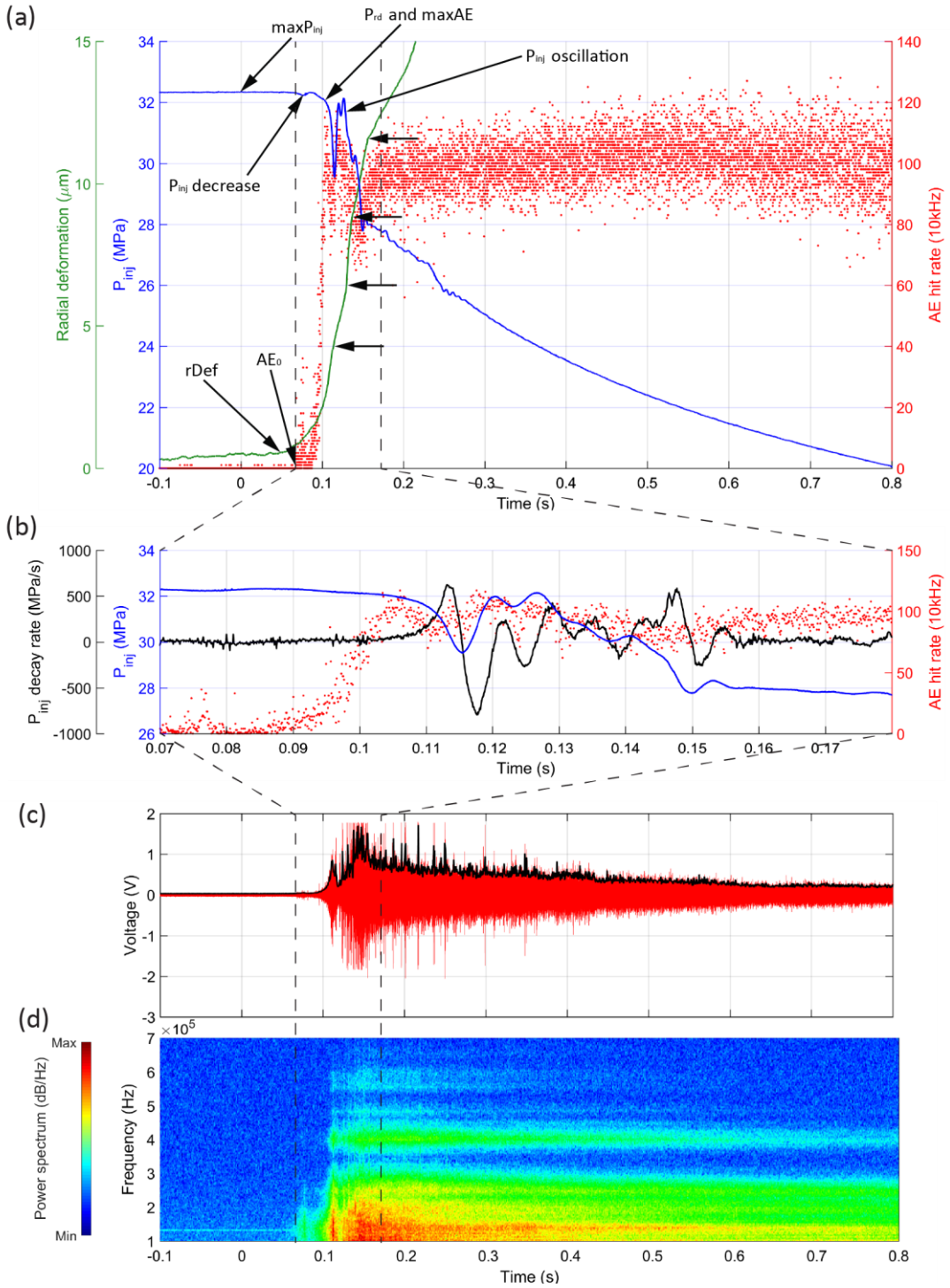

Figure 5-2: NPSx-14.5-w – Laboratory data from hydraulic fracturing simulation on NPS at 14.5MPa confining pressure and with bedding parallel to sample axis and σ_v; (a)Time-record of internal fluid injection pressure (blue line), radial deformation (green line) and AE hit counts (red dots), black horizontal arrows indicate change in radial deformation rate. (b) Fluid pressure decay rate (black line), fluid pressure (blue line) and AE hit count rate (red dots). (c) Snapshot of the continuous waveform (red line) including the signal envelope at the time of failure. (d) Respective spectrogram at the time of failure. The spectrogram data illustrates the frequency range exhibiting power (colour) with time. Time scales zeroed at maximum fluid injection pressure.

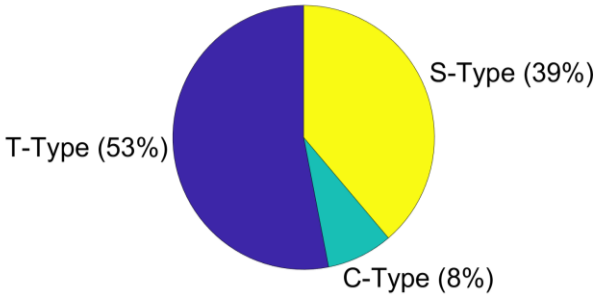

Figure 5-3: NPSx-14.5-w - Event type analysis results for hydraulic fracturing of NPSx at 14.5MPa confining pressure.

Hydraulic fracturing at low confining pressure (0-2MPa) – NPSx-0-w

At ambient pressure conditions, where AE records a far weaker signal, fluid injection pressure reached a maximum of only 5.4MPa before decreasing in a single phase (i.e. no oscillations) from approximately 0.08s (Figure 5-4a). This trend is mirrored in terms of radial strain with a small change seen at 0s (time of maxP_{inj}) before a significant increase at 0.08s is recorded. The pore fluid pressure decay rate remains steady (within the noise) at approximately 0.9MPa/s (Figure 5-4b), until 0.08s where it increases rapidly to a maximum of 302MPa/s at 0.09s before decreasing. The continuous waveform (Figure 5-4c) shows the weaker overall signal due to the lower confinement. Despite this, a number of short bursts occurring at the time of the onset of rapid fluid pressure decay are readily identified. The initial, very short, events (≈0.5ms) at 0.092 and 0.094s have an impulsive onset in the frequency range between 50-300kHz (Figure 5-4d). At about 0.11s, the decay rate steadies before falling to the low nominal value again after approximately 0.2s (Figure 5-4b). A second AE signal is detected during fluid pressure dissipation (Figure 5-4c) which is characterised by a more gradual onset, longer overall signal duration (0.097 to 0.12s), a gradual decreasing tail and a low amplitude. The spectrogram (Figure 5-4d) indicates that for the second long signal most of the energy is concentrated in a frequency range between 50-150kHz, with one very short spike dissipating energy over a range of 100-400kHz.

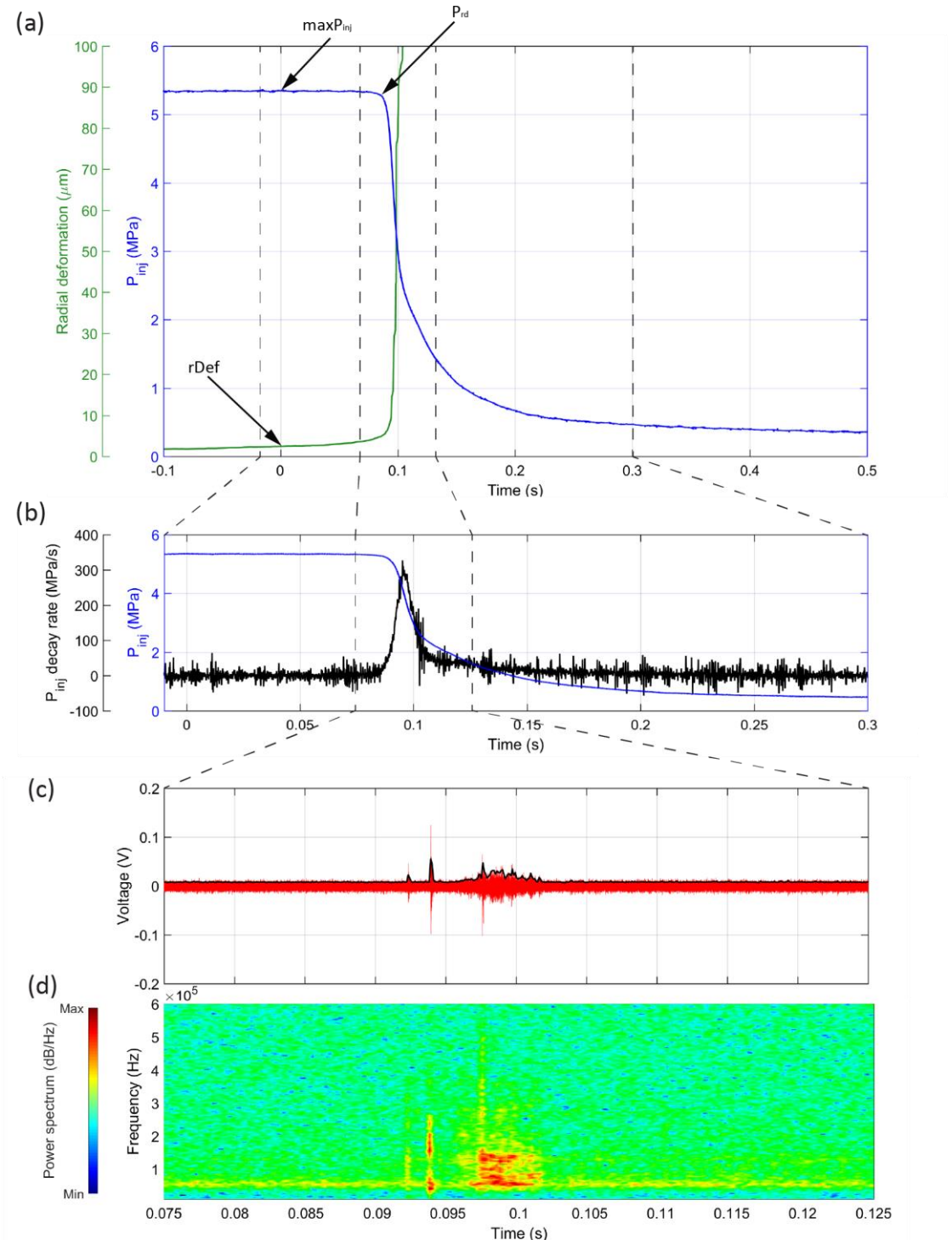

Figure 5-4: NPSx-0-w – Laboratory data from hydraulic fracturing simulation on NPS at ambient pressure and with bedding parallel to sample axis and σ_v; (a)Time-record of internal fluid injection pressure (blue line) and radial deformation (green line). (b) Fluid pressure decay rate (black line) and fluid pressure (blue line). (c) Snapshot of the continuous waveform (red line) including the signal envelope at the time of failure. (d) Respective spectrogram at the time of failure. The spectrogram data illustrates the frequency range exhibiting power (colour) with time. Time scales zeroed at maximum fluid injection pressure.

Hydraulic fracturing at low confining pressure (0-2MPa) –NPSx-2.2-w

Figure 5-5 shows the laboratory data for hydraulic fracturing at a confining pressure of 2.2MPa using water. A slight change in radial deformation is measured at the time of maximum fluid

pressure (10.4MPa) (Figure 5-5a); radial strain then increases with this trend accelerating at approximately 0.04s where P_{inj} starts to decrease markedly. Acoustic Emission activity also increases exponentially at around the same time (0.04s). Fluid pressure decay rate increases significantly at 0.035s (Figure 5-5b) from an average of less than 20MPa/s to a maximum of 720MPa/s at 0.043s followed by several oscillations with peak decay rates of approximately 390MPa/s. Also at 0.035s, radial deformation increases more significantly (Figure 5-5a), indicated by the break in slope of the radial deformation curve. Once the injection pressure has decreased to approximately 5MPa, the fluid pressure starts to oscillate for about 0.1s with a relative homogenous peak-to-peak amplitude behaviour. The AE activity follows the fluid pressure pattern (an oscillating pattern), but with a very small time offset (≈0.005s). The continuous signal in Figure 5-5c illustrates very well the series of short bursts during the fracturing, which have a low frequency and impulsive onset, and a short and fast decreasing tail. The most significant power is in the range 50-200 kHz (Figure 5-5d), but a higher frequency component occurs at 400 kHz. Whereas the lower frequency component is fairly continuous, it is notable that the high frequency components appear as shorter bursts or swarms. Following the oscillation, fluid pressure dissipates gradually from 0.15s and the radial strain increases significantly, signalling the end of the experiment at around 0.2s. Source type evaluation reveal that tensile and shear type events are dominant, likely due to the fracturing, with only a small percentage of compressional type events (Figure 5-6).

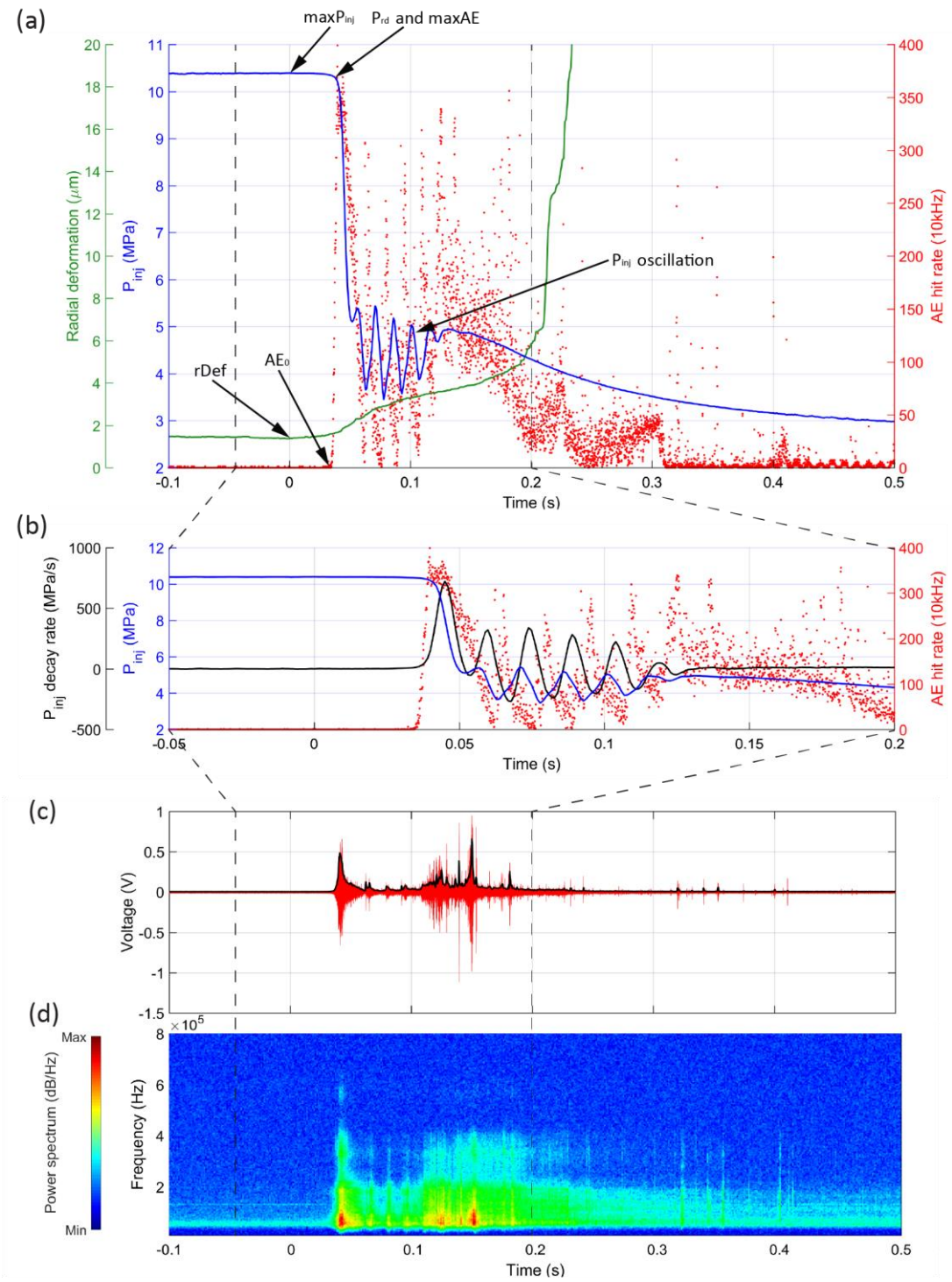

Figure 5-5: NPSx-2.2-w – Laboratory data from hydraulic fracturing simulation on NPS at 2.2MPa confining pressure and with bedding parallel to sample axis and σ_v; (a)Time-record of internal fluid injection pressure (blue line), radial deformation (green line) and AE hit counts (red dots). (b) Fluid pressure decay rate (black line), fluid pressure (blue line) and AE hit count rate (red dots). (c) Snapshot of the continuous waveform (red line) including the signal envelope at the time of failure. (d) Respective spectrogram at the time of failure. The spectrogram data illustrates the frequency range exhibiting power (colour) with time. Time scales zeroed at maximum fluid injection pressure.

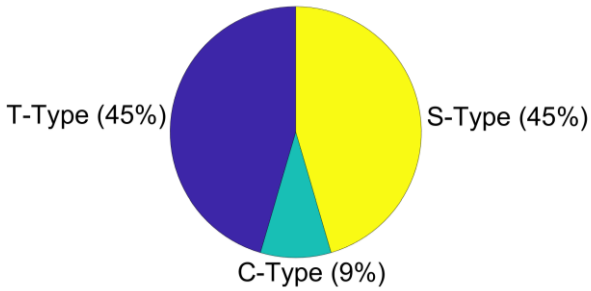

Figure 5-6: NPSx-2.2-w - Event type analysis results for hydraulic fracturing of NPSx at 2.2MPa confining pressure.

Hydraulic fracturing at high confining pressure (25.4MPa) – NPSx-25.4-w

Finally, hydraulic fractures were generated at a confining pressure of 25.4MPa, equivalent to about 1km depth. As expected, a higher fluid injection pressure was required to initiate hydraulic fractures, in this case 36.3MPa (Figure 5-7a). Shortly afterwards at approximately 0.045s, a small decrease in pressure injection is recorded accompanied by both a rapid increase in radial deformation from approximately 0.04s and a rapid increase in AE hit rate also from approximately 0.04s. Translating P_{inj} into decay rates (Figure 5-7b) reveals a phase of increased pressure decay 0.04-0.053s at approximately 50MPa/s. Fluid pressure then enters the main phase of rapid pressure decrease at 0.053s (Figure 5-7a) with a maximum decay rate of 1000Mpa/s. This significant pressure decrease to 30.3MPa coincides with the first AE peak activity and the continuous AE signal (Figure 5-7c) exhibits a sharp event at that time. The fluid pressure exhibits a single oscillation and recovers to 32.5MPa (at 0.065s) before finally entering a period of gradual pressure decay after 0.07s, where pressure decay re-stabilises at approximately 55 MPa/s. The rebound in fluid pressure is also seen in AE activity with a short time offset (Figure 5-7c). Each change in fluid pressure decay rate was associated with a slight change in the radial deformation curve, which stabilised at 46µm. The spectrogram (Figure 5-7e) shows an emergent onset with a harmonic coda with the most significant power occurring at approximately 100-200kHz that decreases in amplitude by 0.15s. A second higher frequency (but lower power) component occurs at 400kHz and also disappears gradually by approximately 0.15s. During the fracturing, tensile type events dominated (57%), but AE events also showed shear (32%) and compressional character (11%), as shown in Figure 5-8.

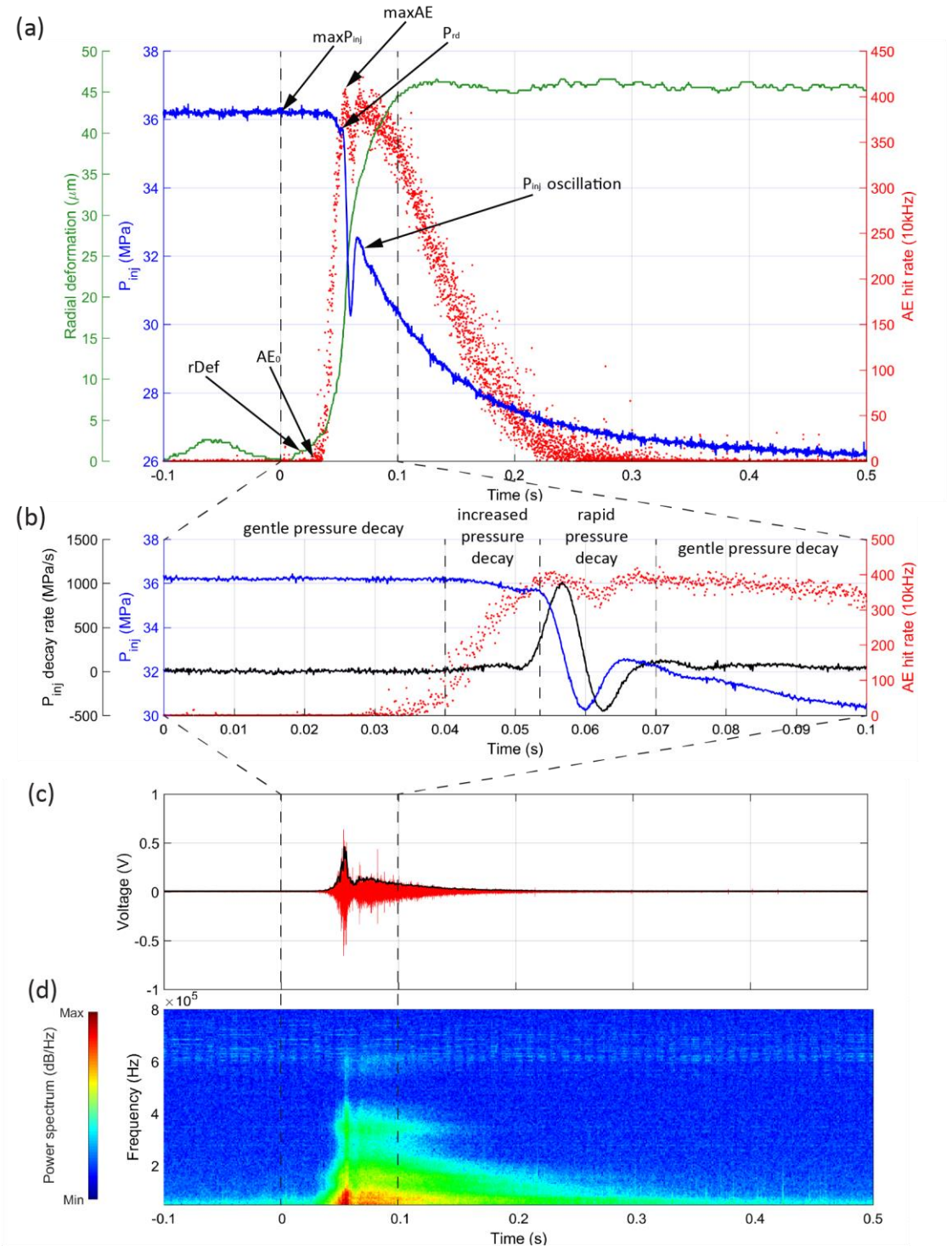

Figure 5-7: NPSx-25.4-w – Laboratory data from hydraulic fracturing simulation on NPS at 25.4MPa confining pressure and with bedding parallel to sample axis and σ_v; (a)Time-record of internal fluid injection pressure (blue line), radial deformation (green line) and AE hit counts (red dots). (b) Fluid pressure decay rate (black line), fluid pressure (blue line) and AE hit count rate (red dots). (c) Snapshot of the continuous waveform (red line) including the signal envelope at the time of failure. (d) Respective spectrogram at the time of failure. The spectrogram data illustrates the frequency range exhibiting power (colour) with time. Time scales zeroed at maximum fluid injection pressure.

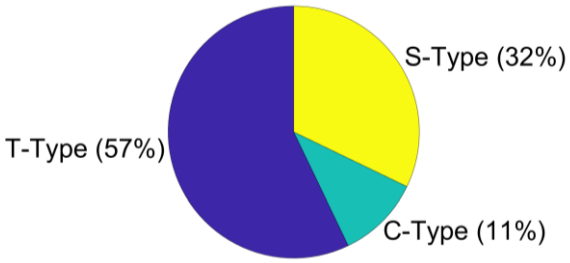

Figure 5-8: NPSx-25.4-w - Event type analysis results for hydraulic fracturing of NPSx at 25.4MPa confining pressure.

Hydraulic fracturing with saturated sample – NPSx-2.3-w-saturated

All experiments analysed so far have been oven-dried prior to the experiment. To check for any effects of longer-term fluid infiltration, a sample saturated in water using the vacuum immersion method (7 days) was also tested for comparison at a confining pressure of 2.3MPa. Figure 5-9 shows a 0.6s time record of the data. In general, the key features are the same as for initially dry samples as previously shown in Figure 5-5, but without the distinctive oscillations. Maximum fluid pressure (4.83MPa) predates the onset of radial deformation and seismic activity, both occurring at approximately 0.025s. Shortly after at 0.03s, fluid pressure decay rate starts to increase rather gentle at an average of 0.3MPa/s (Figure 5-9b), but then increases from 0.06s to peak at 0.08s (22 MPa/s) and 0.12s (34MPa/s). Peaks in the acoustic emission, although difficult to positively identify, at 0.06s and 0.08s approximately correspond with the onset of increased pressure decay rate at 0.06s and the first decay rate peak at 0.08s. The continuous signal (Figure 5-9d) is weak, and characterised by a gentle onset and small weak coda. The spectrogram (Figure 5-9e) shows a low frequency content between 50-100kHz containing the most significant power.

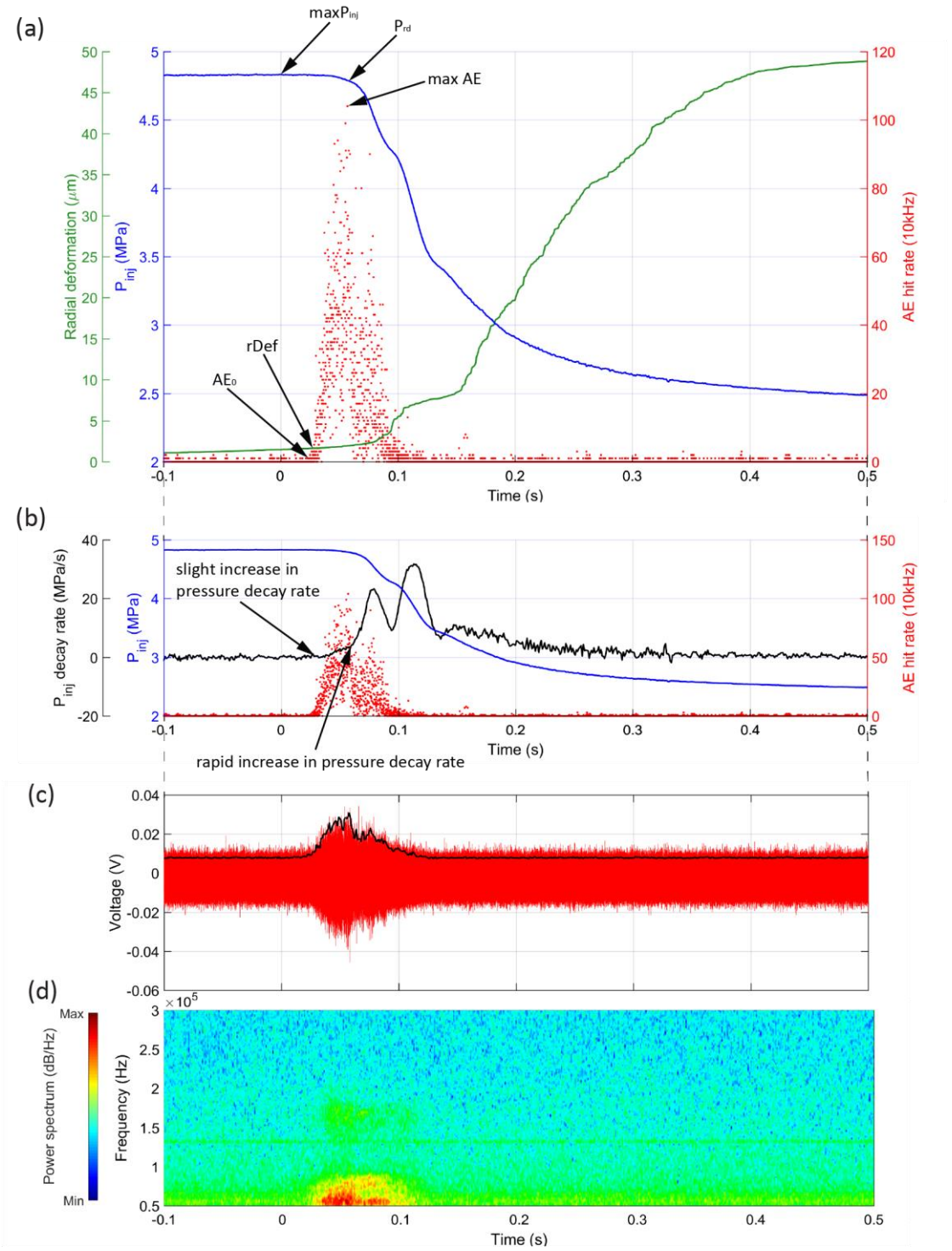

Figure 5-9: NPSx-2.3-w-saturated – Laboratory data from hydraulic fracturing simulation on NPS at 2.3MPa confining pressure, saturated and with bedding parallel to sample axis and σ_v; (a)Time-record of internal fluid injection pressure (blue line), radial deformation (green line) and AE hit counts (red dots). (b) Fluid pressure decay rate (black line), fluid pressure (blue line) and AE hit count rate (red dots). (c) Snapshot of the continuous waveform (red line) including the signal envelope at the time of failure. (d) Respective spectrogram at the time of failure. The spectrogram data illustrates the frequency range exhibiting power (colour) with time. Time scales zeroed at maximum fluid injection pressure.

5.3 Micro Hydraulic Fracturing of Nash Point Shale normal to bedding

Following the fracturing parallel to bedding, a series of experiments are presented, describing hydraulic fracture of Nash Point Shale with bedding normal to the sample axis and σ_v (denoted as NPSz), at confining pressures in the range from 5-20MPa and using water as pressurisation fluid. With the central conduit orientated normal to σ_v, radial fractures are forced to cross several bedding planes as they propagate. Experiments where conducted at different confining pressures (Table 5-1), but only the results from tests at 4.5MPa, 15.3MPa and 20.3MPa are described in detail here. All following experiments were initially dry.

Hydraulic fracturing at low confining pressure (4.5MPa) – NPSz-4.5-w

Figure 5-10a shows a 0.6s time record of data obtained at 4.5MPa confining pressure, recording a maxP_{inj} of 30.3MPa, which coincides with changes in radial deformation. Shortly afterwards at 0.004s, acoustic emission activity starts to increase exponentially and exhibits a first AE peak at 0.007s (Figure 5-10b). At that time, fluid pressure starts to decrease gradually (Figure 5-10b) until 0.01s, when fluid pressure decay rate increases rapidly (maximum 3980MPa/s) at approximately the same time as peak AE activity (0.01s, main AE peak). The onset of AE activity can be seen in the continuous AE signal (Figure 5-10c) as a single impulsive onset with a long harmonic quasi-monochromatic tail. The most significant power is in the range 100-400 kHz (Figure 5-10d), but higher frequency components occur at 600 kHz, fading out earlier (at 0.2s) compared to lower frequencies with decrease in amplitude by 0.3s (for approximately 300 kHz) and 0.4s (for 100kHz). After the first significant pressure drop to 17.1MPa (Figure 5-10a), the fluid pressure oscillates for a short time, before decreasing gradually (average ≈14MPa/s) to confining pressure level. Seismic activity plateaus for 0.1s before it also gradually decreases to the normal background noise level (at 0.5s). Radial deformation increased gradually during the fracture and plateaued at approximately 0.06s until approximately 0.15s, where deformation increases exponentially.

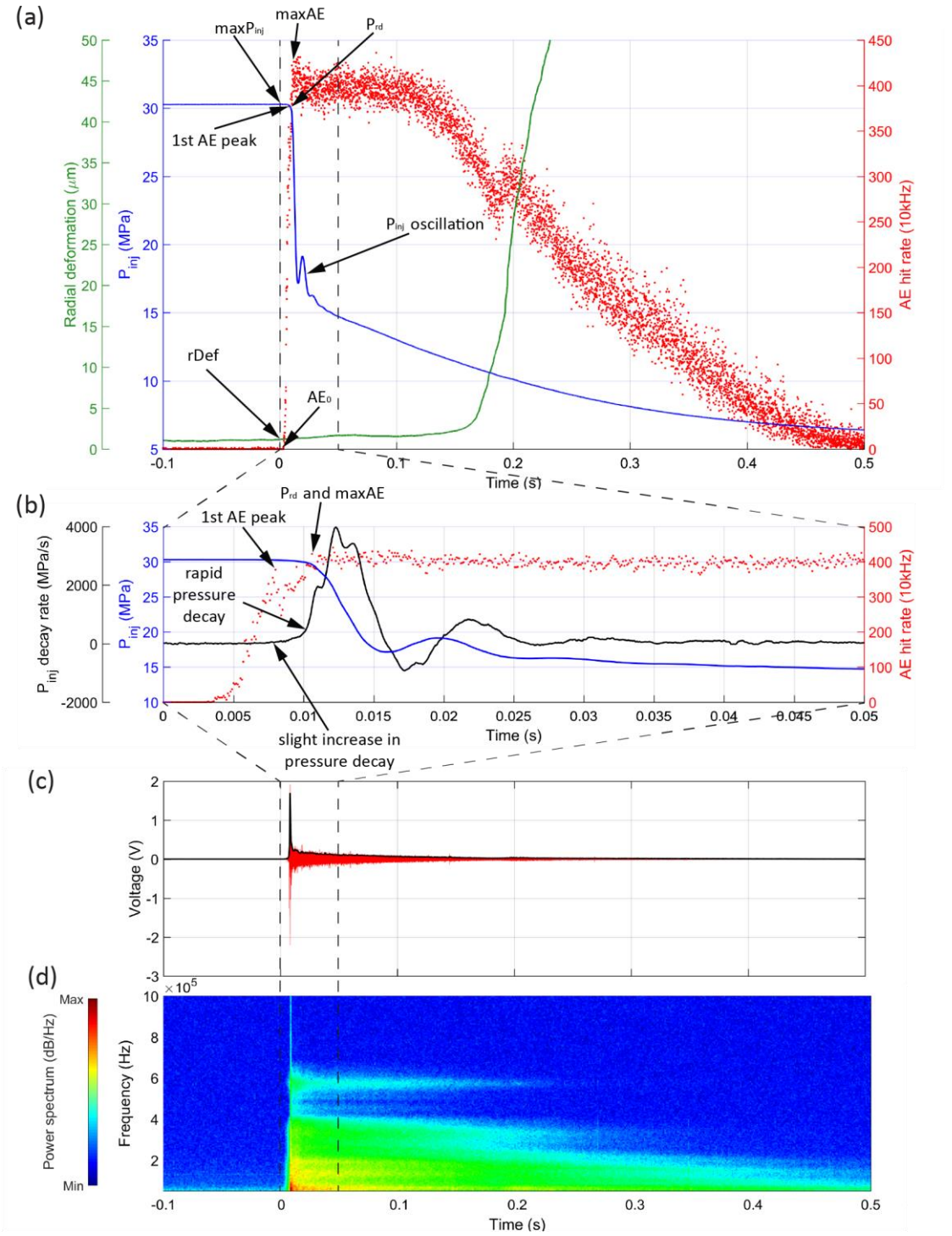

Figure 5-10: NPSz-4.5-w – Laboratory data from hydraulic fracturing simulation on NPS at 4.5MPa confining pressure and with bedding normal to sample axis and σ_v; (a)Time-record of internal fluid injection pressure (blue line), radial deformation (green line) and AE hit counts (red dots). (b) Fluid pressure decay rate (black line), fluid pressure (blue line) and AE hit count rate (red dots). (c) Snapshot of the continuous waveform (red line) including the signal envelope at the time of failure. (d) Respective spectrogram at the time of failure. The spectrogram data illustrates the frequency range exhibiting power (colour) with time. Time scales zeroed at maximum fluid injection pressure.

Hydraulic fracturing at medium confining pressure (15.3MPa) - NPSz-15.3-w

The hydraulic fracturing of Nash Point shale normal to bedding at medium confining pressure showed a different behaviour prior to the main hydraulic fracturing event, which is visualized in a 8s long time record in Figure 5-11a. With increasing confining pressure, a higher $maxP_{inj}$ of 50.11MPa was recorded, but in this case $maxP_{inj}$ occurred 6.17s prior to the significant fluid pressure decrease, a much longer delay than observed in previous experiments. At the time of maximum fluid pressure, a very slightly increased seismic activity was recorded. However, during the following steady pressure decay for about 6s, two phases of increased acoustic activity (at 4.4s and 4.95s) with low frequency events (50-200kHz, Figure 5-11b) occur. The first AE phase coincide with a very small radial deformation at 4.4s and a slight increase in the decay rate (average decay rate of 0.04MPa/s to 0.7MPa/s). Despite these differences, the mechanical characteristics during the fracturing process are similar: a rapid fluid pressure decay, followed by an oscillation phase before a steady pressure decay. Figure 5-12a shows a zoom in on the data of the main fracturing event. The third and "main" phase of acoustic activity starts at about 5.8s (Figure 5-12a), shortly after the onset of radial deformation (5.78s). The peak activity (Figure 5-12a) coincides with a significant increase in radial deformation and a decrease in fluid pressure (at 6.14s). Coinciding with a further increase in both radial deformation rate as well as AE hit rate, the pressure decay rate starts to increase significantly at approximately 6.17s, reaching a maximum of 5712MPa/s (Figure 5-12b). During this phase, AE events show the most significant power in the range 100 to 300kHz, but a higher frequency component occurring also at 400 kHz (Figure 5-12d). The continuous signal (Figure 5-12c) has a gradual emerging onset, a sharp peak event and a harmonic monochromatic long tail. At about 30MPa, P_{inj} rebounds to approximately 34MPa, before the fluid pressure gradually decreases to confining pressure. Source type analysis of the extracted AE events revealed that tensile type failure was the dominant mechanism (48%) during fracturing. Shear failure types accounted for 38% and compressive type failure for 14% (Figure 5-13).

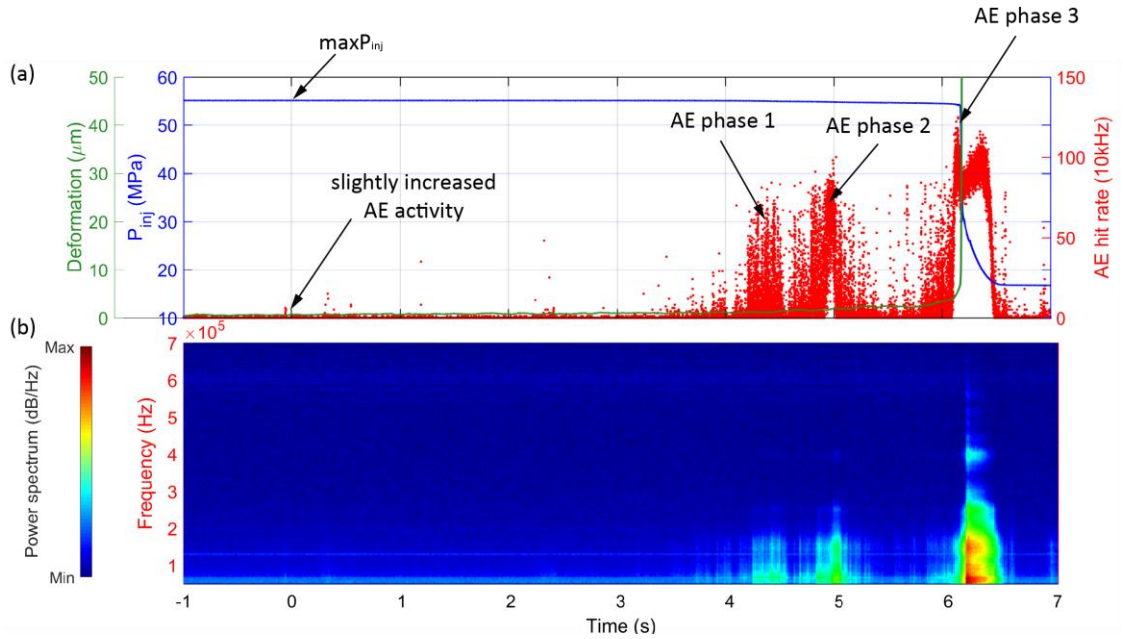

Figure 5-11: NPSz-15.3-w – (a) 8s time-record of internal fluid injection pressure (blue line), radial deformation (green line) and AE hit counts (red dots) for hydraulic fracturing simulations at 15.3MPa confining pressure of NPS with bedding normal to sample axis and σ_v and (b) a snapshot of the respective spectrogram. Time scales zeroed at maximum fluid injection pressure.

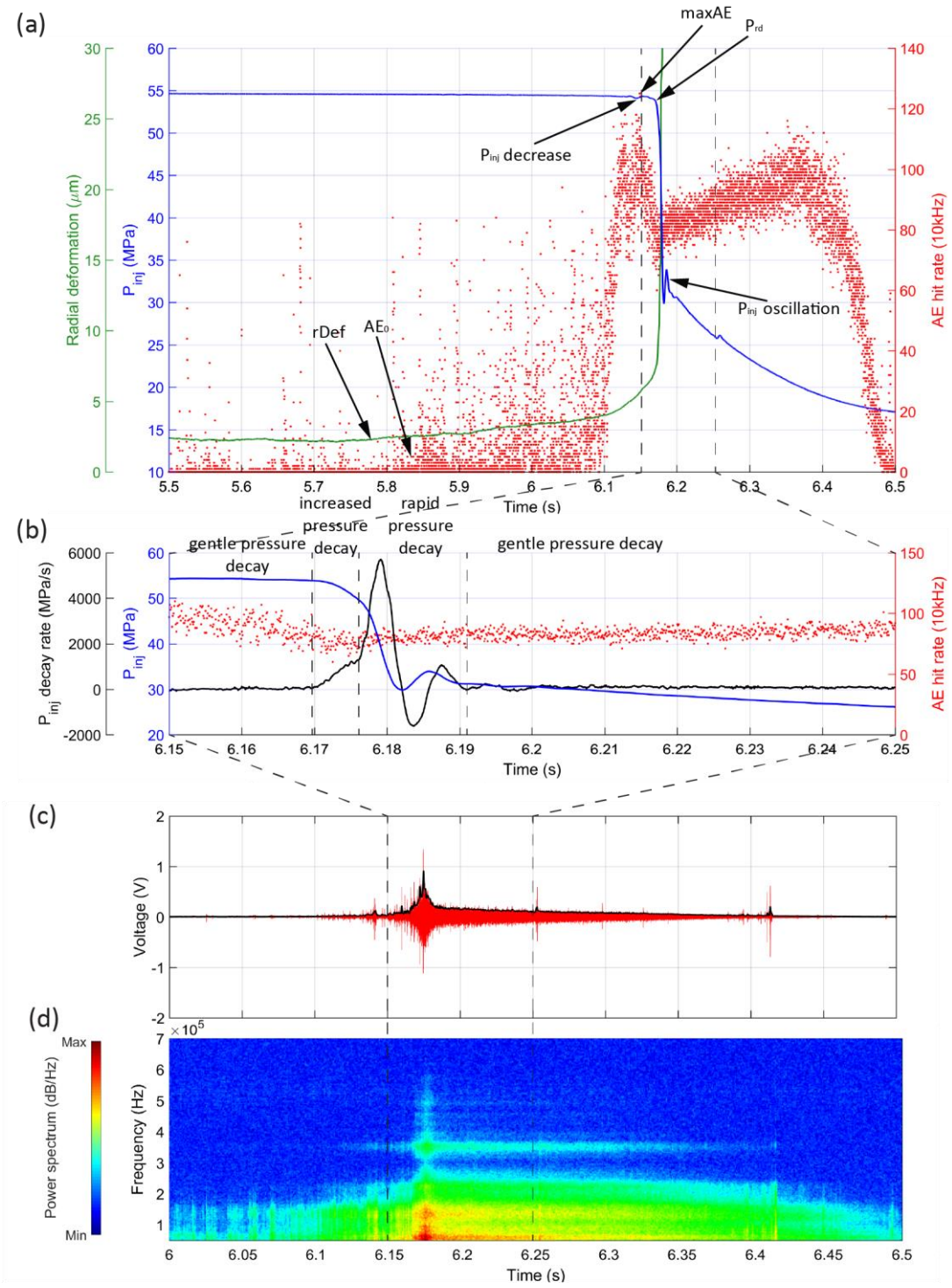

Figure 5-12: NPSz-15.3-w – Laboratory data at time of failure (zoom in from Figure 5-11) from hydraulic fracturing simulation on NPS at 4.5MPa confining pressure and with bedding normal to sample axis and σ_v; (a)Time-record of internal fluid injection pressure (blue line), radial deformation (green line) and AE hit counts (red dots). (b) Fluid pressure decay rate (black line), fluid pressure (blue line) and AE hit count rate (red dots). (c) Snapshot of the continuous waveform (red line) including the signal envelope at the time of failure. (d) Respective spectrogram at the time of failure. The spectrogram data illustrates the frequency range exhibiting power (colour) with time. Time scales zeroed at maximum fluid injection pressure.

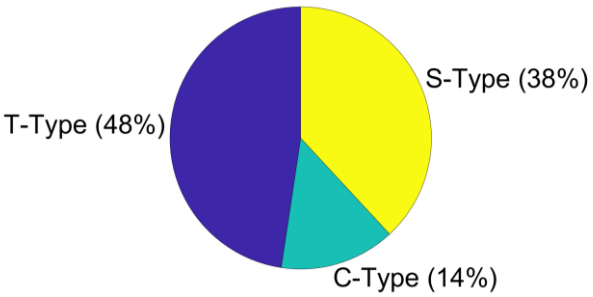

Figure 5-13: NPSz-15.3-w - Event type analysis results for hydraulic fracturing of NPSz at 15.3MPa confining pressure

Hydraulic fracturing at high confining pressure (20.3MPa) - NPSz-20.3-w

Figure 5-14a shows data from 20.3MPa confining pressure, where P_{inj} reached a maximum of 58MPa. Just prior to maxP_{inj}, radial deformation was first detected at -0.01s. At 0.02s, a small decrease in P_{inj} is observed before the onset of rapid fluid pressure decay at 0.032s. The initial decrease in fluid pressure is associated with a first phase of increased seismic activity commencing at 0.01s (Figure 5-14a) which shows the main power distribution in a low frequency range 50-200kHz (Figure 5-14d). A second AE swarm starts soon after at 0.025s and increases exponentially. Peak AE activity coincides with the increase in pressure decay rate (Figure 5-14b) and an increase in radial deformation rate at 0.032s. During the rapid fluid pressure decay, decay rates increase to a maximum of 7292MPa/s. The continuous AE waveform (Figure 5-14c) indicates a fast emergent to impulsive onset with a sharp peak event and three frequency components; the most significant power lies in the range 50-200kHz and two higher frequency components occur at 400kHz and 600kHz (Figure 5-14d). A single P_{inj} oscillation is recorded after the rapid pressure decay (Figure 5-14a), increasing again to 42.5MPa. At approximately 0.12s, a change in the fluid pressure curve is detected, which coincides with another sharp increase in radial deformation and a halt in AE hit rate decrease. The following plateau in the AE rate matches the plateau in the radial deformation curve, both lasting from approximately 0.13-0.21s. Afterwards, AE activity decreases rapidly (at 0.21s) and radial deformation increases significantly (at 0.21s and 0.025s), indicating the end of the experiment. The AE waveform has a harmonic monochromatic long tail (Figure 5-14c), which has an oscillating amplitude and lasts for the entire fluid dissipation. All three frequency components gradually disappear with higher frequency components first at 0.2s (600kHz) and 0.25s (400kHz) compared to the low frequency events which last until 0.35s (Figure 5-14d). Tensile type events dominated the fracturing process accounting for 50%, whereas 31% were of shear mode and 19% of compressional type (Figure 5-15).

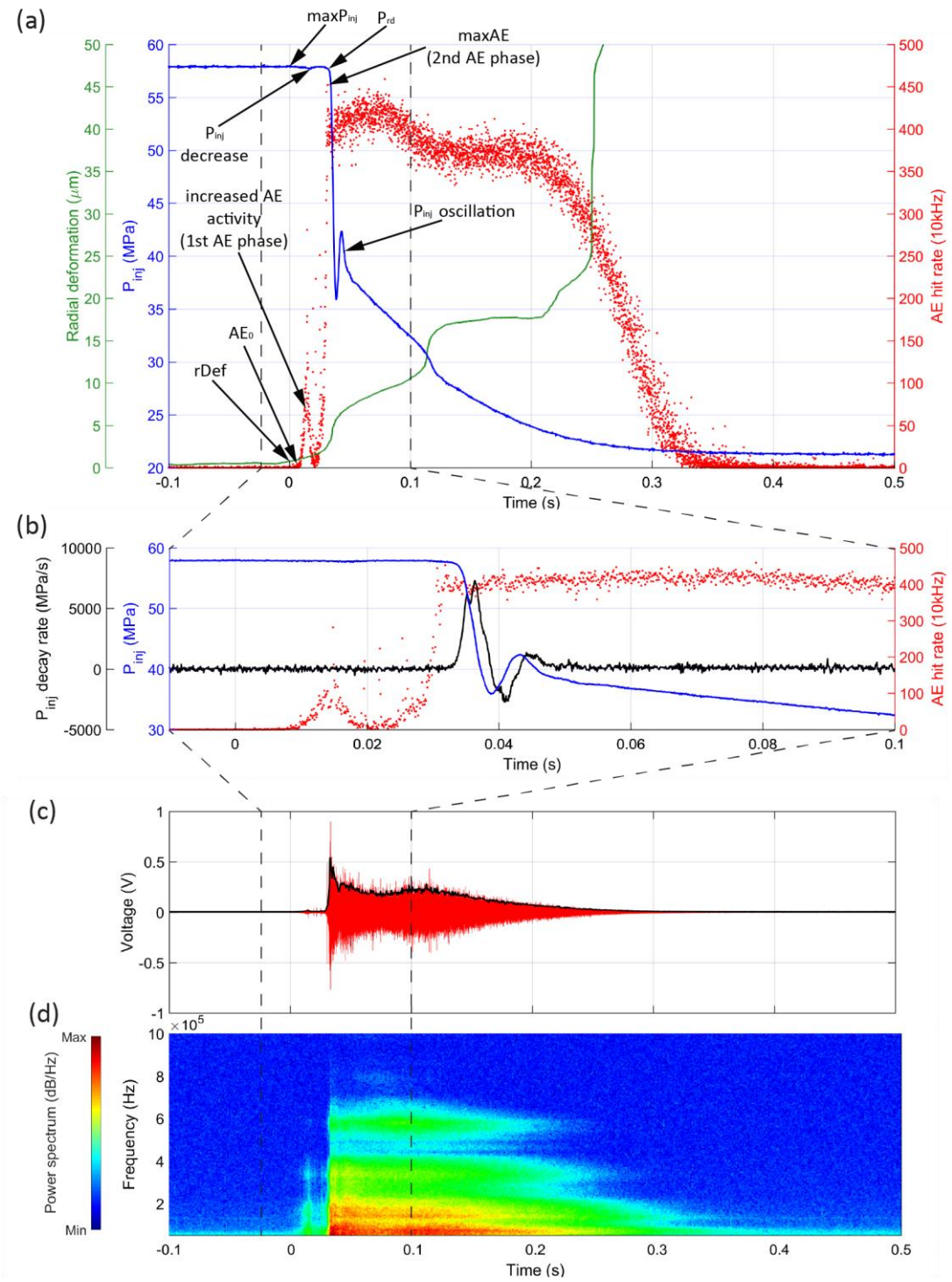

Figure 5-14: NPSz-20.3-w – Laboratory data from hydraulic fracturing simulation on NPS at 4.5MPa confining pressure and with bedding normal to sample axis and σ_v; (a)Time-record of internal fluid injection pressure (blue line), radial deformation (green line) and AE hit counts (red dots). (b) Fluid pressure decay rate (black line), fluid pressure (blue line) and AE hit count rate (red dots). (c) Snapshot of the continuous waveform (red line) including the signal envelope at the time of failure. (d) Respective spectrogram at the time of failure. The spectrogram data illustrates the frequency range exhibiting power (colour) with time. Time scales zeroed at maximum fluid injection pressure.

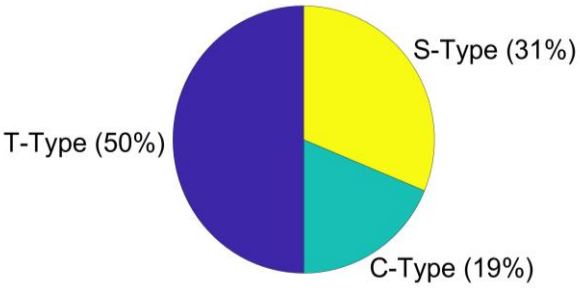

Figure 5-15: NPSz-20.3-w - Event type analysis results for hydraulic fracturing of NPSz at 20.3MPa confining pressure

5.4 Micro Hydraulic Fracturing of Crab Orchard Sandstone

As a counterpoint to the low permeability and fine grained Nash Point Shale, hydraulic fracturing experiments at a confining pressure of approximately 15MPa were carried out using Crab Orchard Sandstone samples with bedding both parallel (COSx) and normal (COSz) to σ_v.

Hydraulic fracturing parallel to bedding at medium confining pressure (14.4MPa) - COSx-14.4-w

Figure 5-16 shows the data for hydraulic fracturing with bedding parallel to σ_v and at a confining pressure of 14.4MPa. The onset of radial deformation and the onset of increased AE activity occur simultaneously with maxP_{inj} (32.3MPa) at 0s (Figure 5-16a). This is followed by a period of 0.05s, where P_{inj} gradually decreases, radial deformation gradually increases and AE hit rate increases exponentially. The AE waveform shows a low frequency (100-150kHz) emergent onset (Figure 5-16d) during that time period. At 0.05s, AE activity peaks (Figure 5-16a) and fluid pressure decay rate increases significantly up to a maximum of 93MPa/s (Figure 5-16b). Radial deformation also increases more significantly now. During that main fracturing event, the continuous signal (Figure 5-16c) shows multiple peaks and most energy is contained between two bands of 100-300 kHz and 400-450kHz (Figure 5-16d). Afterwards at 0.1s, fluid pressure decay enters a smooth and gradual decrease and radial deformation reaches a plateau just under 4 μm (Figure 5-16a). During the time of constant radial deformation, AE rate also stabilises at a level of 95 khits/s and higher frequency events (400-450kHz) rapidly dying out to leave a pervasive low frequency (100-250kHz) component (Figure 5-16d). At 0.195s, radially deformation finally accelerates to sample failure and AE activity decreases in a manner analogous to P_{Einj} (Figure 5-16a). The AE waveform exhibits a long harmonic, monochromatic coda in the frequency range 100-200kHz (Figure 5-16d). The results of the source type analysis are presented in Figure 5-17. During the main fracturing event, shear type failure is dominant (52%), but with also a significant part of the events being of compressional type (40%). Only a small percentage (8%) are tensile failures.

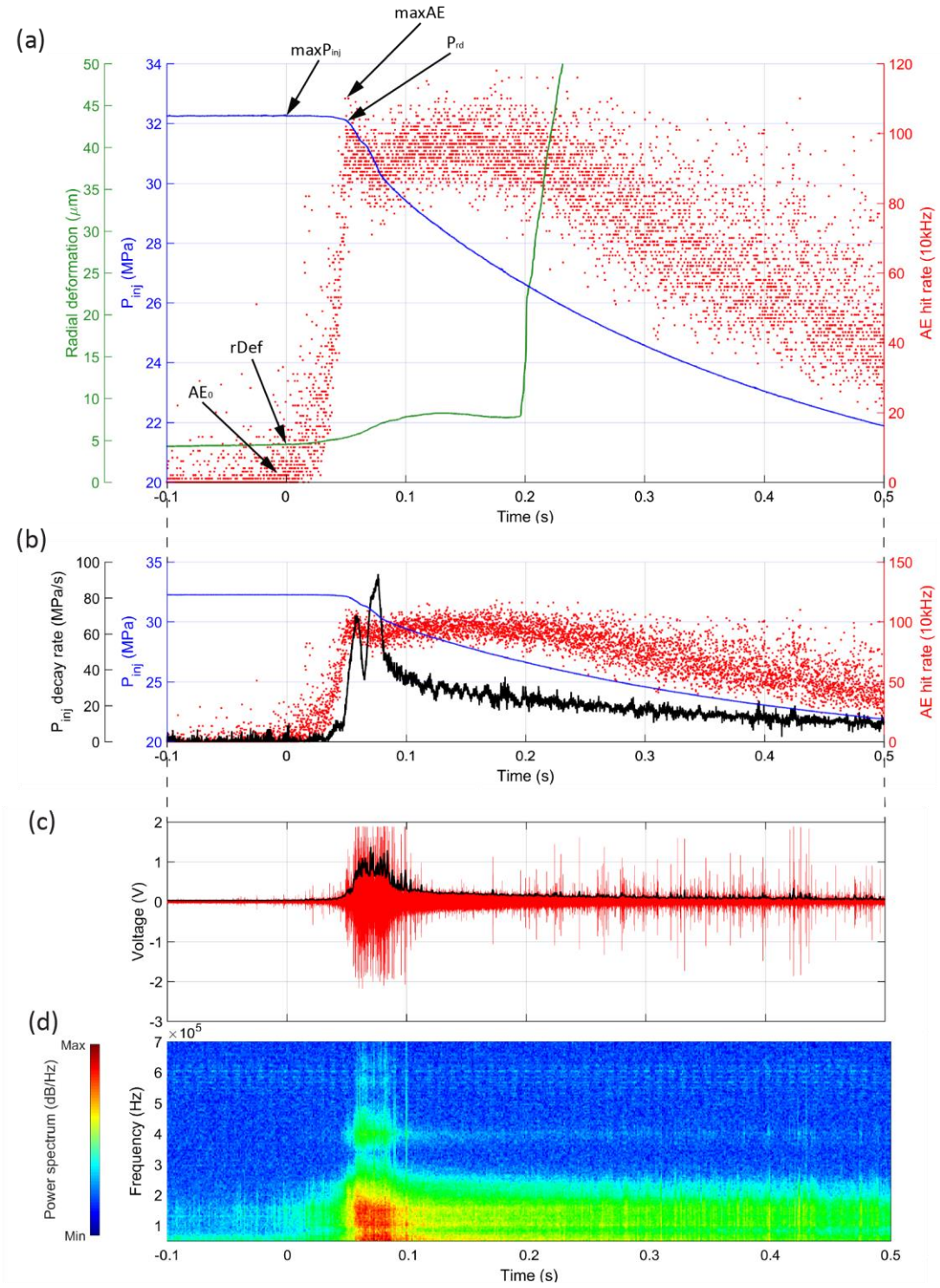

Figure 5-16: COSx-14.4-w – Laboratory data from hydraulic fracturing simulation on COS at 14.4MPa confining pressure and with bedding parallel to sample axis and σ_v; (a)Time-record of internal fluid injection pressure (blue line), radial deformation (green line) and AE hit counts (red dots). (b) Fluid pressure decay rate (black line), fluid pressure (blue line) and AE hit count rate (red dots). (c) Snapshot of the continuous waveform (red line) including the signal envelope at the time of failure. (d) Respective spectrogram at the time of failure. The spectrogram data illustrates the frequency range exhibiting power (colour) with time. Time scales zeroed at maximum fluid injection pressure.

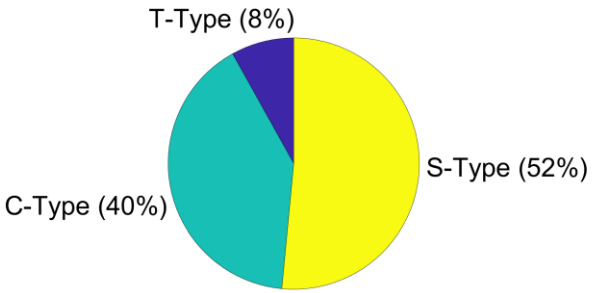

Figure 5-17: COSx-14.4-w - Event type analysis results for hydraulic fracturing of COSx at 14.4MPa confining pressure

Hydraulic fracturing normal to bedding at medium confining pressure (15.4MPa) - COSz-15.4-w

Hydraulic fracturing normal to bedding (at 15.4MPa confining pressure) (Figure 5-18) shows a similar mechanical behaviour to the previous example parallel to bedding (Figure 5-16). During the experiment, a maximum fluid pressure of 29.3MPa was reached with an initial increase in AE and radial deformation occurring at about the same time (Figure 5-18a). For the following 0.17s, fluid pressure decreases gradually and radial deformation as well as AE hit rate increase exponentially. At approximately 0.17s, fluid pressure decay rate (Figure 5-18b) increases significantly that coincides with the peak AE rate and a linear increase of radial deformation. Fluid pressure decay rate (Figure 5-18b) reaches a maximum of 150MPa/s and afterwards follows a general trend similar to the main P_{inj} decrease, but with a few oscillations at 0.21 and 0.22s corresponding to variations in the P_{inj}-time curve. The decrease in AE hit rate plateaus shortly at 400 khits/s at approximately the same time (0.18s) as elevated P_{inj} decay rate before the hit rate decreases to normal background level noise (at 0.45s). The continuous waveform and the spectrogram for the time of failure in Figure 5-18c and d show a gradual emerging onset and a coda of similar shape. The most significant energy occurs at a frequency range between 50-400 kHz during the fracturing process with a higher frequency component at 600kHz. Similar to fracturing parallel to bedding, shear type events also dominate (59%) during hydraulic fracturing normal to bedding, with only 26% compressional type events and 16% of tensional character (Figure 5-19).

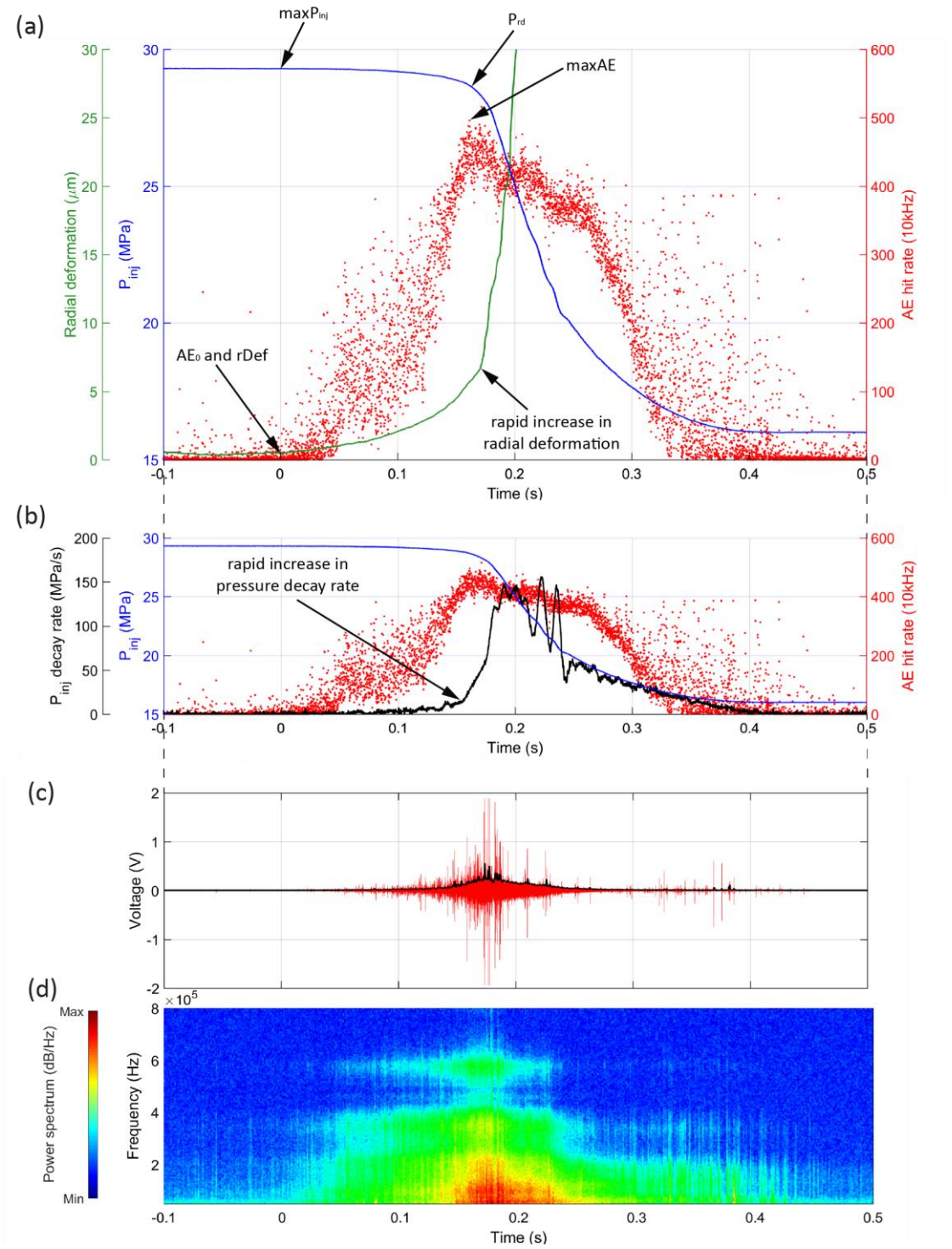

Figure 5-18: COSz-15.4-w – Laboratory data from hydraulic fracturing simulation on COS at 14.4MPa confining pressure and with bedding normal to sample axis and σ_v; (a)Time-record of internal fluid injection pressure (blue line), radial deformation (green line) and AE hit counts (red dots). (b) Fluid pressure decay rate (black line), fluid pressure (blue line) and AE hit count rate (red dots). (c) Snapshot of the continuous waveform (red line) including the signal envelope at the time of failure. (d) Respective spectrogram at the time of failure. The spectrogram data illustrates the frequency range exhibiting power (colour) with time. Time scales zeroed at maximum fluid injection pressure.

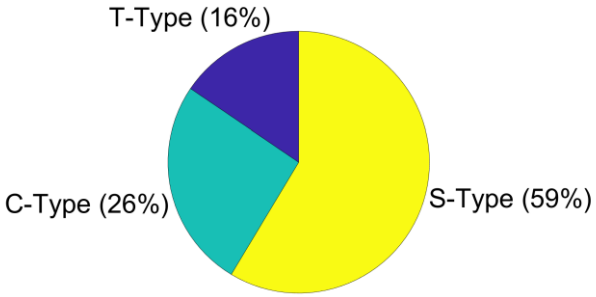

Figure 5-19: COSz-15.4-w - Event type analysis results for hydraulic fracturing of COSz at 15.4MPa confining pressure

5.5 Morphology of hydraulic fractures in shale and sandstone

Micro X-ray Computed Tomography (micro-CT) scans at low (31µm) and high resolution (9µm), combined with SEM and white-light microscope imaging were used for a detailed evaluation of the developed fracture network and fracture morphology. Low resolution micro-CT scans were used for a descriptive evaluation of the developed fracture network in terms of the complexity of the developed fracture network (single or multiple fracture network), the location of the fracture relative to bedding, and the aperture. To analyse the morphology of the developed fractures, higher resolution micro-CT was then performed, using sub-sections of the fractured rock shell. Figure 5-20 shows the samples, which have been scanned (red and green circles) and an overview of the developed fracture patterns is given in Table 5-2, including a brief description of the fracture network pattern, average tortuosity and aperture.

Table 5-2: Overview of fracture morphology of shale and sandstone samples (only micro X-ray CT scanned samples) – water as pressurised fluid; bold labels in brackets are the labels used in the text of this thesis.

Sample	Bedding	Max P_{inj} (MPa)	Pc (MPa)	Aperture (µm)	Average Tortuosity	Fracture network description (qualitative)	Fracture orientation relative to bedding
NPSx-3-79 **(NPSx-0-w)**	Parallel	5.17	0	<30-60		two primary fractures, radial opposite directions, planar to slightly curved, few parallel secondary fractures	parallel and sub-parallel (30-45degrees)
NPSx-3-66	Parallel	6.13	2.2	20-45	1.03	two primary fractures, radial opposite directions, planar to slightly curved	parallel
NPSx-3-97 **(NPSx-2.2-w)**	Parallel	10.13	2.2	<30-60		two primary fractures, radial opposite directions, planar to slightly curved, few parallel secondary fractures	parallel
NPSx-3-94	Parallel	4.75	2.3	<30-60		single, planar fractures, curved in some areas	parallel
NPSx-3-57	Parallel	13.7	4.2	<30-60		planar to slightly curved main fracture with parallel secondary fracture (splitting)	parallel
NPSx-3-83	Parallel	10.62	6	<30-60		single, planar to slightly curved fracture with some parallel secondary fractures	parallel
NPSx-3-104	Parallel	11.76	6.1	20-60	1.03	slightly curved fracture with parallel and sub-parallel secondary fractures	parallel
NPSx-3-70	parallel	15.81	8.2	<30-60		single, planar fracture, with few parallel secondary fractures in some areas	parallel
NPSx-3-128	Parallel	27.45	12.1	<30-60		planar to slightly curved single fracture	parallel

Sample	Bedding	Max P_{inj} (MPa)	Pc (MPa)	Aperture (μm)	Average Tortuosity	Fracture network description (qualitative)	Fracture orientation relative to bedding
NPSx-3-105 **(NPSx-14.5-w)**	Parallel	32.36	14.5	20-60	1.02	slightly curved primary fracture with sub-parallel secondary fractures near BH wall	sub-parallel (10-20degrees)
NPSx-3-137	Parallel	34.0	20.5	<30-60		single, planar fracture	parallel
NPSx-3-135	Parallel	37.72	25.3	<30-60		single, planar fracture with sub-parallel secondary fractures near BH wall	parallel
NPSx-3-136	Parallel	35.16	25.3	<30-60		single, planar fracture	parallel
NPSx-3-133	Parallel	31.63	25.3	<30-60		single, planar fracture	parallel
NPSx-3-144 **(NPSx-25.4-w)**	Parallel	36.04	25.4	<30-60	1.01	single, planar fracture	parallel
NPSz-3-139 **(NPSz-4.5-w)**	Normal	30.06	4.5	<30-60		one primary planar fracture	N/A
NPSz-3-56	Normal	29.9	7.5	<30-60		one primary planar fracture, with a few sub-parallel secondary fractures near the BH wall	N/A
NPSz-3-131 **(NPSz-15.3-w)**	Normal	54.9	15.3	25-120	1.03-1.05	multiple, planar fractures	N/A
NPSz-3-138 **(NPSz-20.3-w)**	Normal	57.8	20.3	<30-60		one primary planar fracture, with a few perpendicular secondary fractures near the BH wall	N/A
COSx-1-58	Parallel	7.3	2.2	20-40	1.2	one tortuous, wavy main fracture with small parallel to sub-parallel secondary fractures, pre-existing pores connected	sub-parallel (about 30 degrees)

Sample	Bedding	Max P_{inj} (MPa)	Pc (MPa)	Aperture (µm)	Average Tortuosity	Fracture network description (qualitative)	Fracture orientation relative to bedding
COSx-1-59	Parallel	9.78	6.1	10-30	1.16	one tortuous, wavy main fracture with small parallel to sub-parallel secondary fractures, pre-existing pores connected	parallel
COSx-1-78	Parallel	26.88	12.3	10-30	1.11	one tortuous, curved main fracture with few small parallel to sub-parallel secondary fractures, pre-existing pores connected	sub-parallel (about 30 degrees)
COSx-1-63 (COSx-14.4-w)	Parallel	31.98	14.4	<30-50		one tortuous, wavy main fracture with small parallel to sub-parallel secondary fractures, pre-existing pores connected	parallel
COSx-1-79	Parallel	44.69	25.3	<30-50		one tortuous, curved main fracture, pre-existing pores connected	parallel
COSx-1-81	Parallel	49.11	25.3	<30-50		one tortuous, curved main fracture, pre-existing pores connected	parallel
COSz-1-80 (COSz-15.4-w)	Normal	29.05	15.4	25-50	1.11	one main tortuous and curved fracture, with some parallel secondary fractures, pre-existing pores connected	N/A

For the shale as well as the sandstone, and both orientations, fractures were observed to have formed along the axis of the sample, parallel to σ_v (Figure 5-21).

In Nash Point Shale, hydraulic fracturing produced primarily a homogenous fracture network with one or two primary fractures independently from the bedding orientation (Figure 5-22 and Figure 5-23). Nash Point Shale samples with the bedding orientated parallel to the sample axis (parallel bedding) always showed fractures parallel (e.g. Figure 5-22a-c and e) or sub-parallel (e.g. Figure 5-22d) to the inherent bedding. The bedding orientation was indicated by elongated grains present within the rock matrix visible in micro-CT images (Figure 5-24).

Hydraulic fractures in NPS showed a homogenous fracture geometry and fractures mainly restricted to one plane (Figure 5-25). The aperture in shale samples ranges from 20 to 60µm (Table 5-2, measurement limited to the resolution of the scan) and is relatively uniform along the radial fracture path from the conduit to the edge of the sample (Figure 5-26). The width of the fracture only varies slightly (Figure 5-26) as the fracture width is dominantly represented by one colour (turquoise) in the thickness map and only in a few areas increases slightly (to light green). The average tortuosity of hydraulic fractures in shale over the tested pressure range is shown in Figure 5-27 and ranges from 1.01 to 1.03 for fractures parallel to bedding (Figure 5-27a). The low values show that fractures in Nash Point Shale do not deviate much from a straight line and can therefore be characterised as planar.

Fracture geometry is often linked to the rock fabric and SEM images reveal that hydraulic fractures in the shale propagate primarily through the fine grained rock matrix (Figure 5-28a) and along grain boundaries (Figure 5-28b, c, e and f) or frequently bifurcated when encountering larger grains or lithic fragments. On a micro scale, SEM imaging showed occasional fracture process zones with increased micro-fracture density (Figure 5-28d).

At lower confining pressures, two radial fractures propagated in diametrically opposed directions from the central borehole parallel to bedding, seen at zero and 2MPa confining pressure (Figure 5-22a and b). At higher confining pressures (Figure 5-22d-f), samples only developed one planar fracture parallel to bedding. The change with confining pressure can also be seen in the fracture geometry and secondary fracturing. Samples fractured at lower confining pressures tend to have a slightly higher tortuosity (Figure 5-27) with 1.03 for 2.2MPa and 6.1MPa compared to 1.01 for 25.4MPa confining pressure and develop a more complex fracture network with a higher degree of secondary fracturing and bifurcation. Figure 5-29 shows the fracture orientation and fracture pattern over the length of a NPS sample with

parallel bedding and fractured at a confining pressure of 6.1MPa. The fracture developed parallel to σ_v along the sample axis (Figure 5-29b) over the entire length of the sample (Figure 5-29b). No significant offsets or changes in fracture direction are observed in the xz-plane (Figure 5-29b), and a relative homogenous fracture developed over the sample length with occasional bifurcation occurring. At the top and bottom of the sample, the fracture appears to be more homogenous and planar as seen in Figure 5-29c-1 and Figure 5-29c-4 with less secondary fracturing and branching. Whereas in the centre of the sample, the area where the sample is pressurised, fractures seem to be more curved overall and a more complex fracture network developed with several fracture segments and more bifurcation. In contrast, Figure 5-30 shows the fracture geometry for the central section of a sample fractured at 25.4MPa parallel to bedding. The fracture can be described as homogenous and planar with a very low tortuosity (1.01). Almost no secondary fracturing or bifurcation was observed. Figure 5-31 shows a 3D volume of a hydraulic fracture in Nash Point Shale generated at high confining pressure with an overall homogenous geometry and planar morphology.

Despite cutting across many bedding planes, fractures in shale samples with the bedding normal to σ_v show a similar fracture pattern compared to fracturing parallel to bedding. Samples dominantly showed a homogenous fracture network with one primary fracture (Figure 5-23a, b and d) across the length of the sample and an average aperture between 25-60µm (Table 5-2). Bifurcation and secondary fractures parallel and perpendicular to the primary fracture are frequent features. However, micro CT imaging revealed a complex fracture network with multiple primary fractures and secondary micro fractures for sample NPSz-15.3-w (Figure 5-23c). Two areas with hydraulic fractures developed on opposite sides of the conduit. The fracture network extended over the entire sample length, but showed varying degrees of complexity. The complexity varies from top to bottom and was highest in the middle section of the sample, where the pressurised chamber was located (Figure 5-32 – slice 2 and 3). This area shows an extensive damage zone in between the primary fractures (Figure 5-32 – zoom 1 and zoom 2) with many small micro fractures in between and in close proximity, which are dominantly parallel to sub-parallel to the large fractures. However, some fractures are also noticed which are sub-perpendicular to the primary fractures. Fracture aperture along the radial fracture path is relatively uniform between 25 and 70µm. The top and bottom part of the sample shows a simple fracture network, with two relatively planar fractures (Figure 5-32 – slice 1 and 4). Despite the complexity of the fracture network, the tortuosity of primary fractures is still low ranging between 1.03 and 1.05 (Figure 5-27b).

In contrast to the fine grained matrix of the shale, the characteristics of hydrofractures in the coarser grained sandstone have been investigated. All micro-CT scanned sandstone samples, independently of confining pressure and bedding orientation showed one major fracture (Figure 5-33) with similar fracture morphologies and damage zones extending over about half of the sample length, not reaching either the top or bottom of the sample. In samples with parallel bedding, fractures developed parallel to bedding (Figure 5-33a-c).

The geometries of the fractures are curved and wavy (Figure 5-34), with tortuosity values between 1.11 and 1.16 (Figure 5-35), which are lower in samples tested at higher confining pressures. Fracture propagation involves intergranular (between grains - fracture grows along the grain boundaries) (Figure 5-36a and b) as well as transgranular (through grains) fracture propagation (Figure 5-36c and d). The intergranular crack propagation depends on grain-bond strength and develops a diffuse fracture geometry that strays significantly from a straight plane as can be seen in the high-resolution micro-CT images and the SEM images of the fracture (Figure 5-34) and the tortuosity lines (Figure 5-35). The high-resolution images also show that fractures in the sandstone connecting pre-existing pores along the fracture path, which is particularly well observed in the cross section of the fracture in Figure 5-34d. This gives the fracture an overall more complex morphology as seen in the 3D-volume of a hydraulic fracture in Crab Orchard Sandstone (Figure 5-37).

Figure 5-38a shows the aperture along the radial fracture path. The aperture varies between 20 and 70µm and becomes thinner towards the edge of the sample. The bright yellow areas indicate large local thicknesses due to the cross cutting of pores (Figure 5-38a). The three dimensional view of the fracture in Figure 5-38b also shows the variations in aperture with the dark blue areas indicating thin areas and orange representing connected pores. Microscale kinks, bends, fracture branching, sharp diversions and arrested fracture ends are visible along the fracture path (Figure 5-39), adding to the fracture complexity.

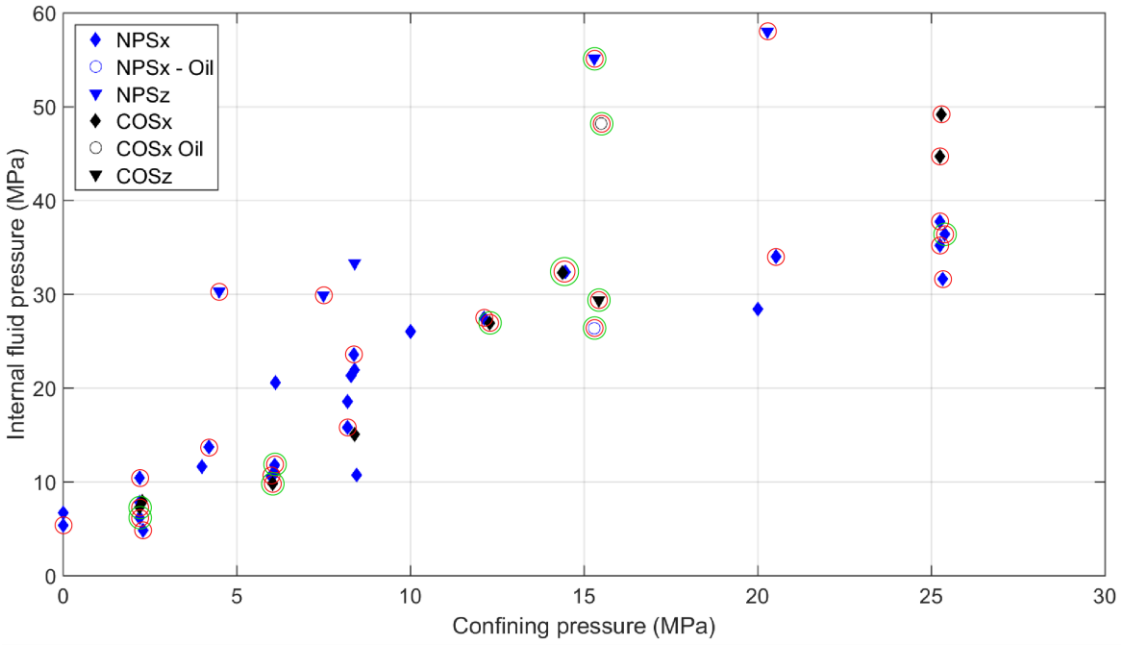

Figure 5-20: Overview plot of X-ray CT scanned samples. Low resolution scans are highlighted with a red circle and high resolution scans with green circles.

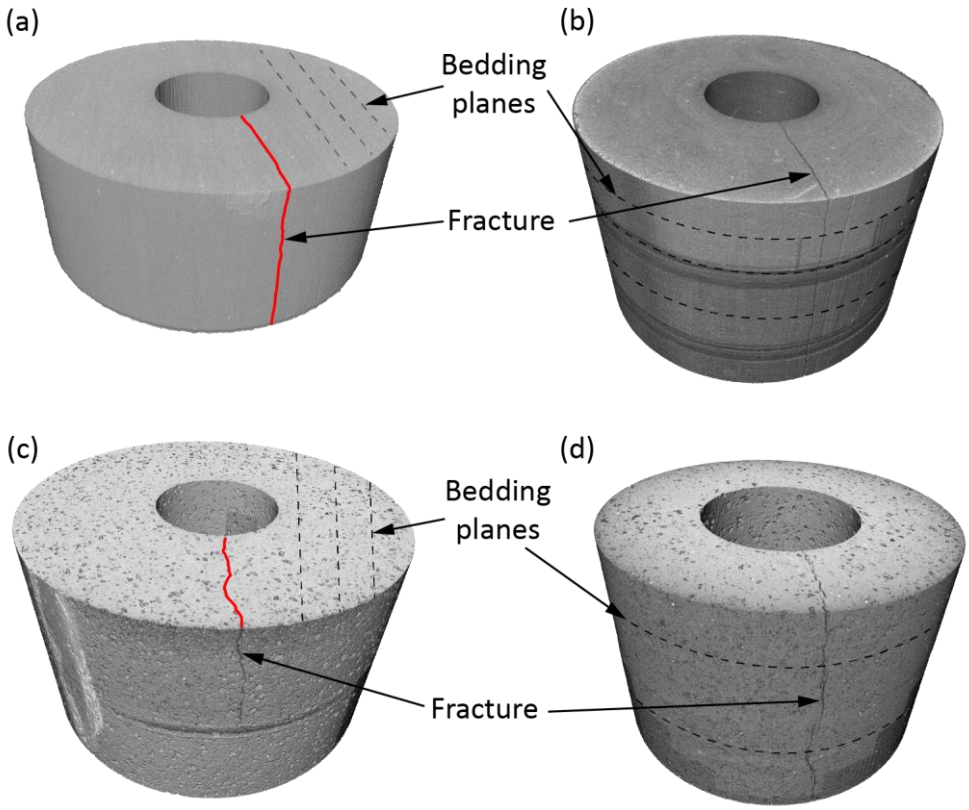

Figure 5-21: Fracture orientation in Nash Point Shale and Crab Orchard Sandstone relative to sample geometry, stress field and bedding orientation; (a) NPS parallel bedding, (b) NPS normal bedding, (c) COS parallel bedding, and (d) COS normal bedding.

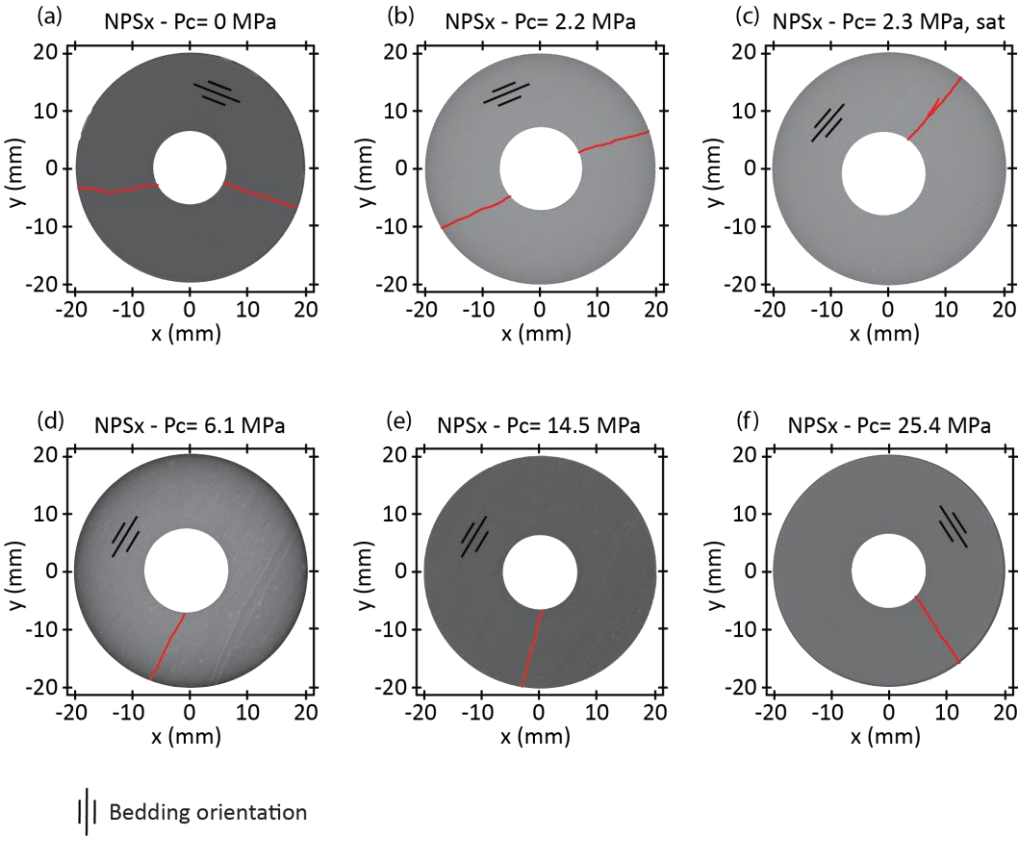

Figure 5-22: Micro X-ray CT images indicating the fracture network developed in Nash Point Shale parallel to bedding; NPSx - fracture parallel to bedding.

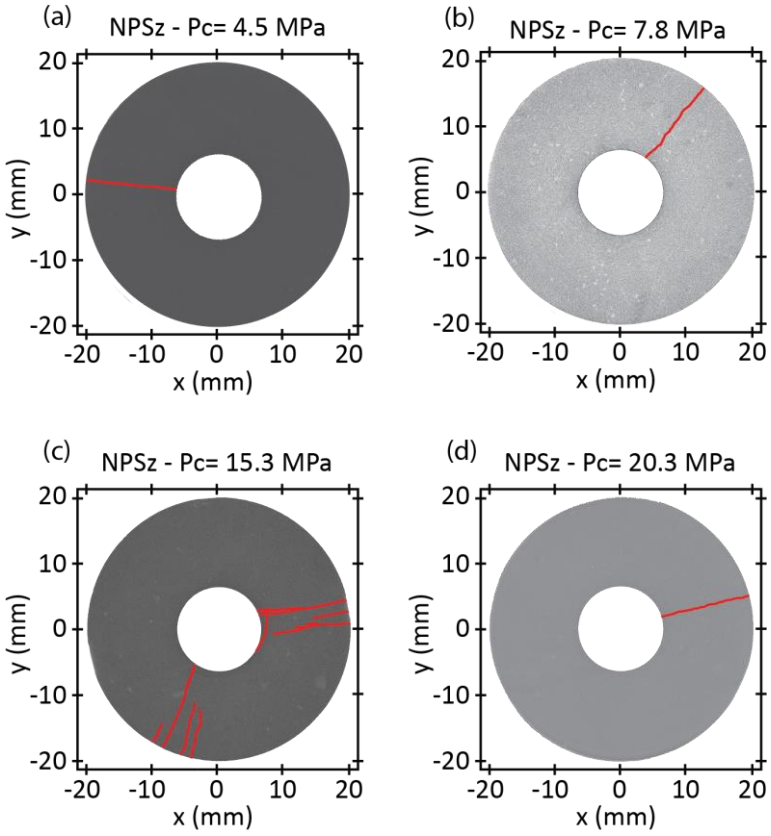

Figure 5-23: Micro X-ray CT images indicating the fracture network developed in Nash Point Shale normal to bedding; NPSz - fracture normal to bedding.

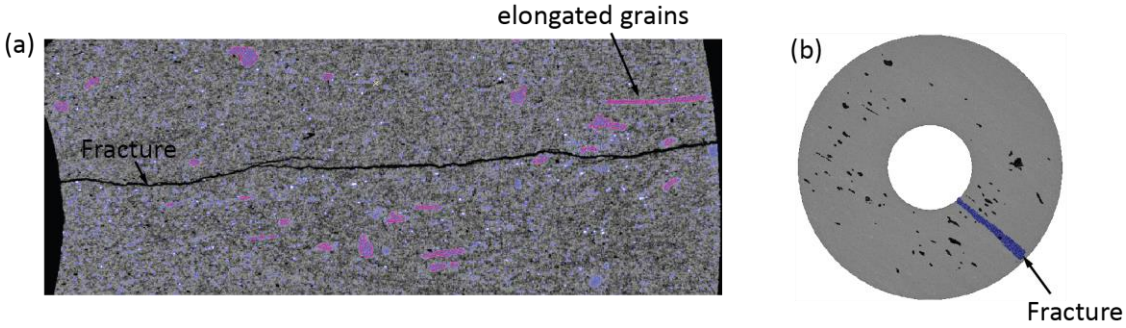

Figure 5-24: Determination of bedding orientation in NPS in micro X-ray CT images; (a) in raw image and (b) after segmentation.

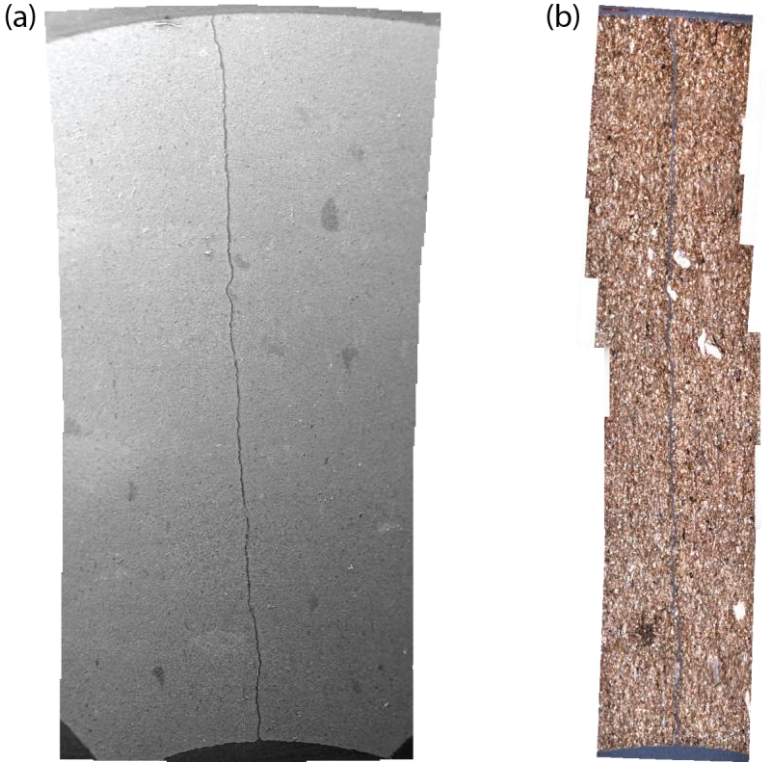

Figure 5-25: Photomicrographs of typical hydraulic fracture developed in NPSx; (a) SEM and (b) microscope thin section.

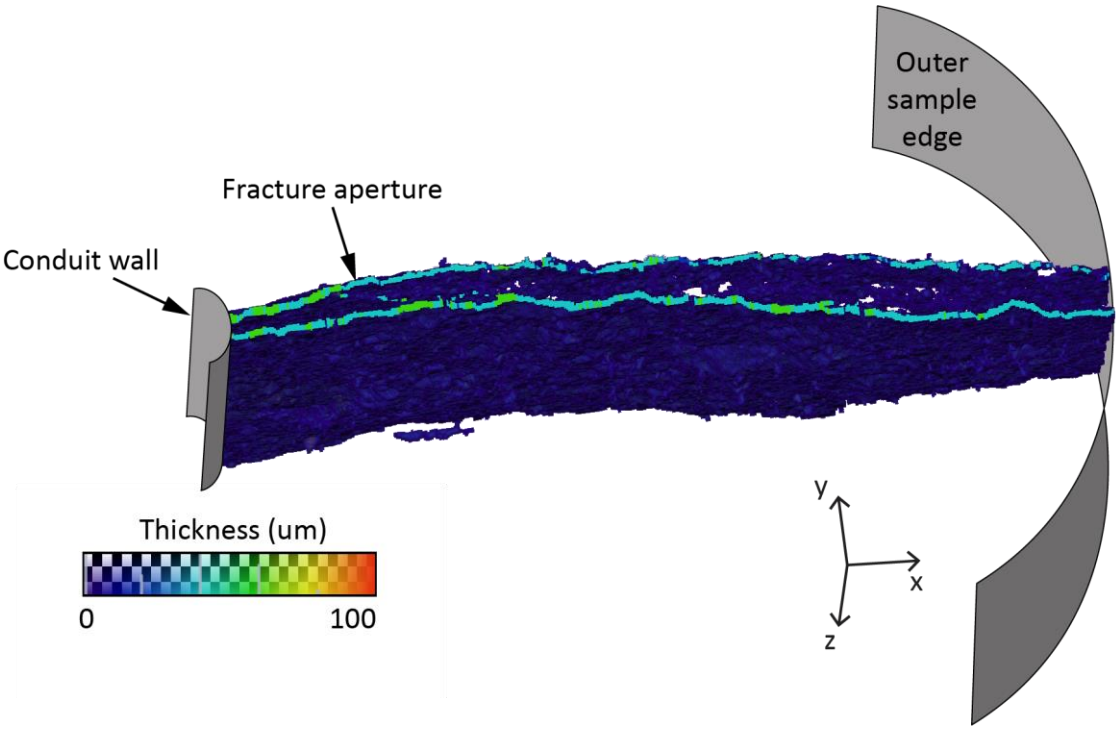

Figure 5-26: Thickness map of a hydraulic fracture in Nash Point Shale parallel to bedding (NPSx-14.5-w). Slice along the xy-plane through the fracture to show the fracture aperture.

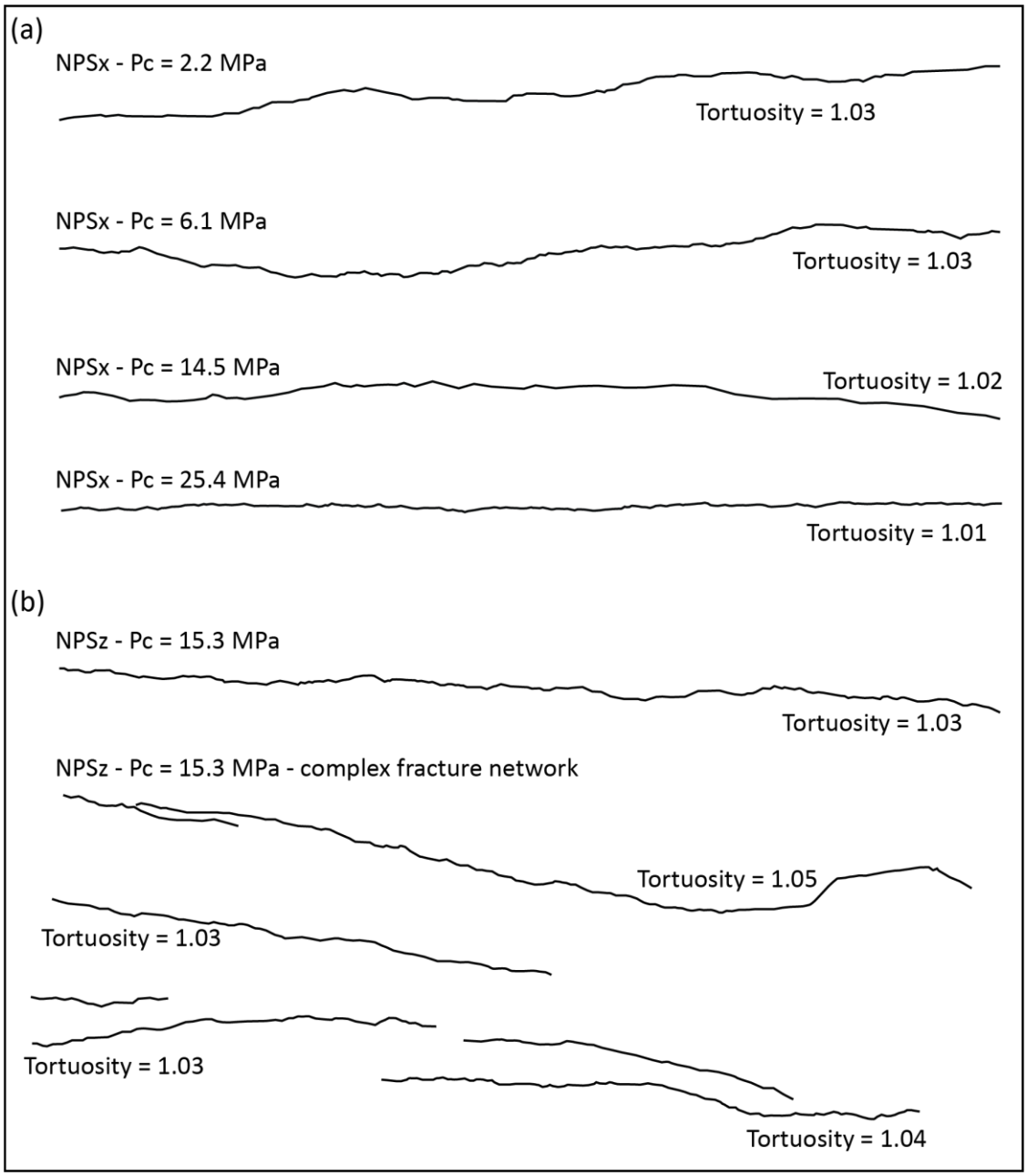

Figure 5-27: Tortuosity lines for NPS samples; (a) fracture parallel to bedding and (b) fracture normal to bedding.

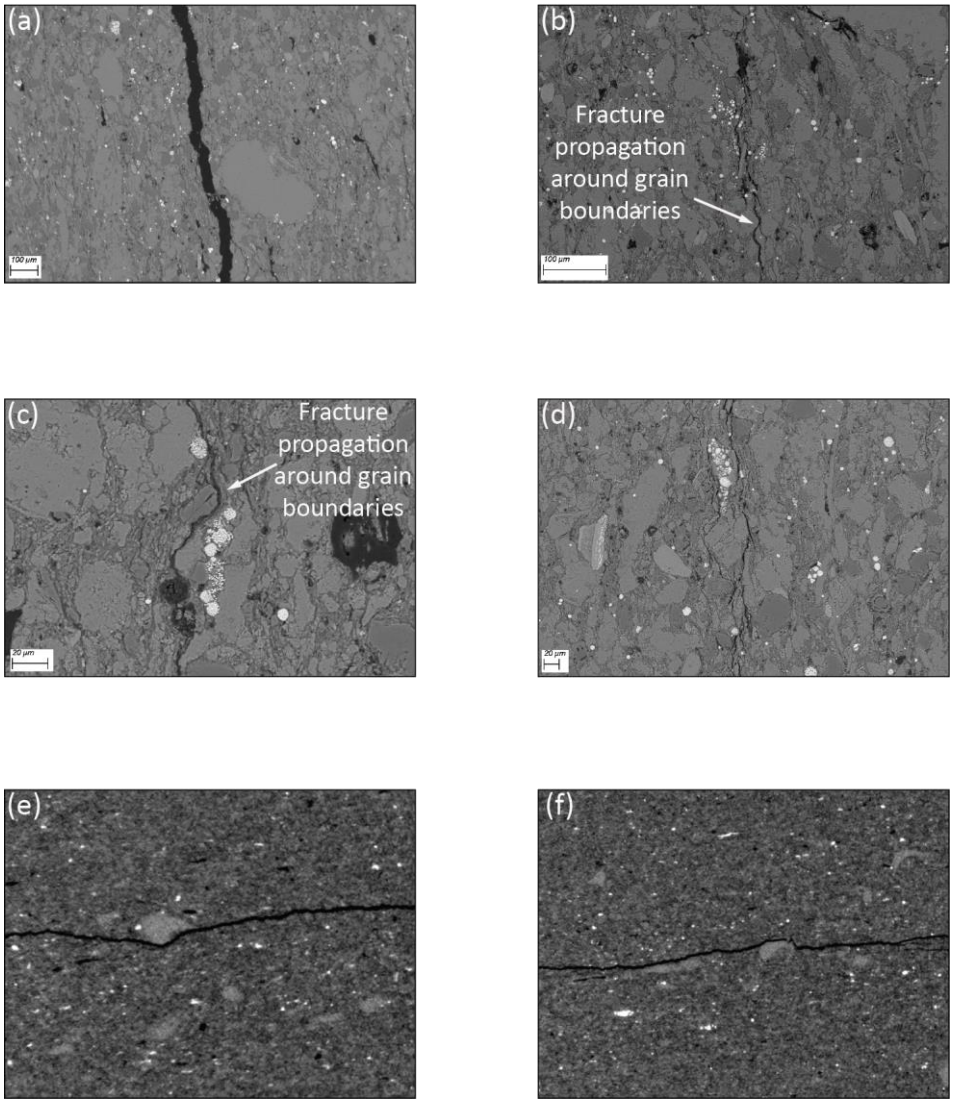

Figure 5-28: SEM-Photomicrographs of NPS showing (a) fracture propagation through the fine grained matrix, (b) and (c) fracture propagation along grain boundaries (intergranular) and (d) area of increased crack density; (e) and (f) X-ray CT-Photomicrographs showing fracture propagation along grain boundaries (intergranular).

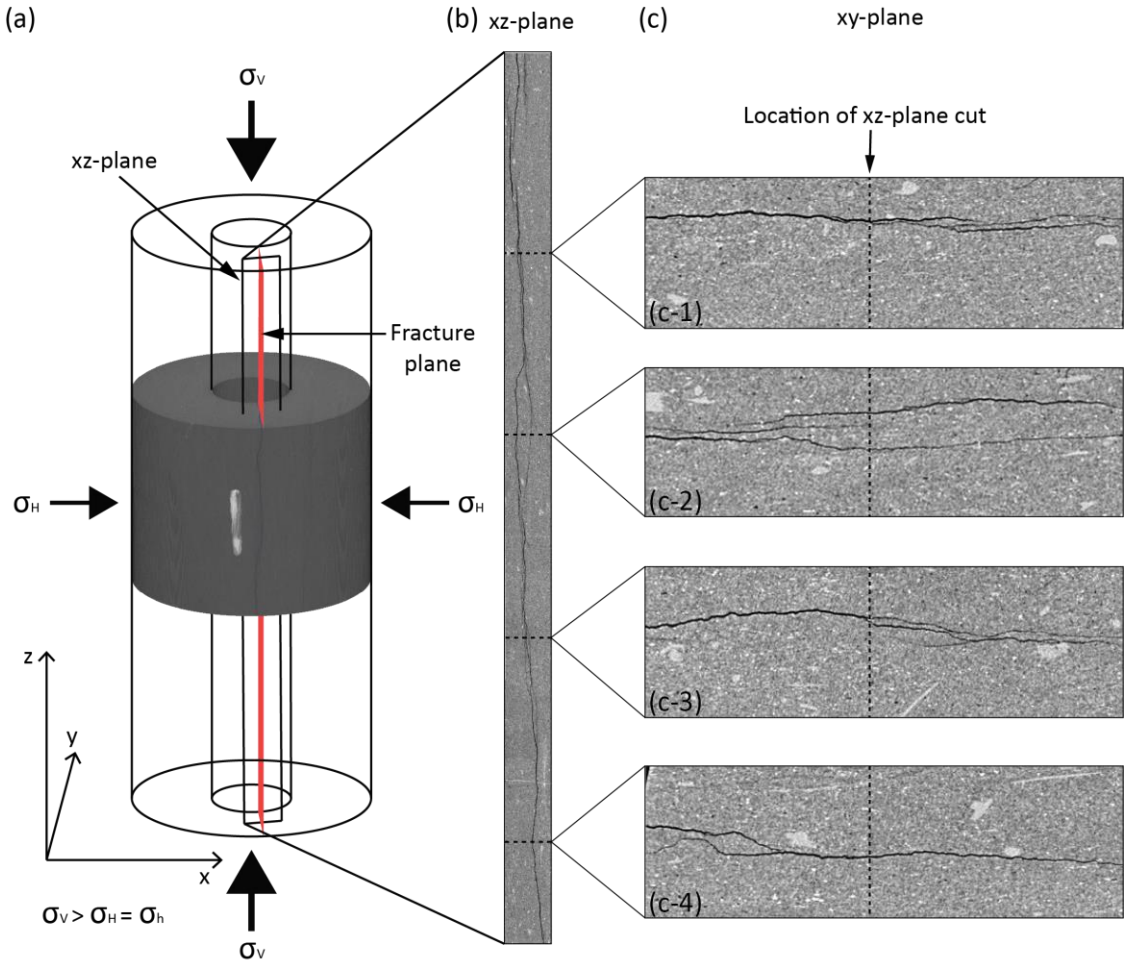

Figure 5-29: Fracture orientation and geometry in Nash Point Shale parallel bedding at 6.1MPa confining pressure (not to scale); (a) orientation of fracture plane relative to sample geometry and stress field, (b) axial fracture geometry (xz-plane), (c) radial fracture geometry (xy-plane) at different points over the length of the sample.

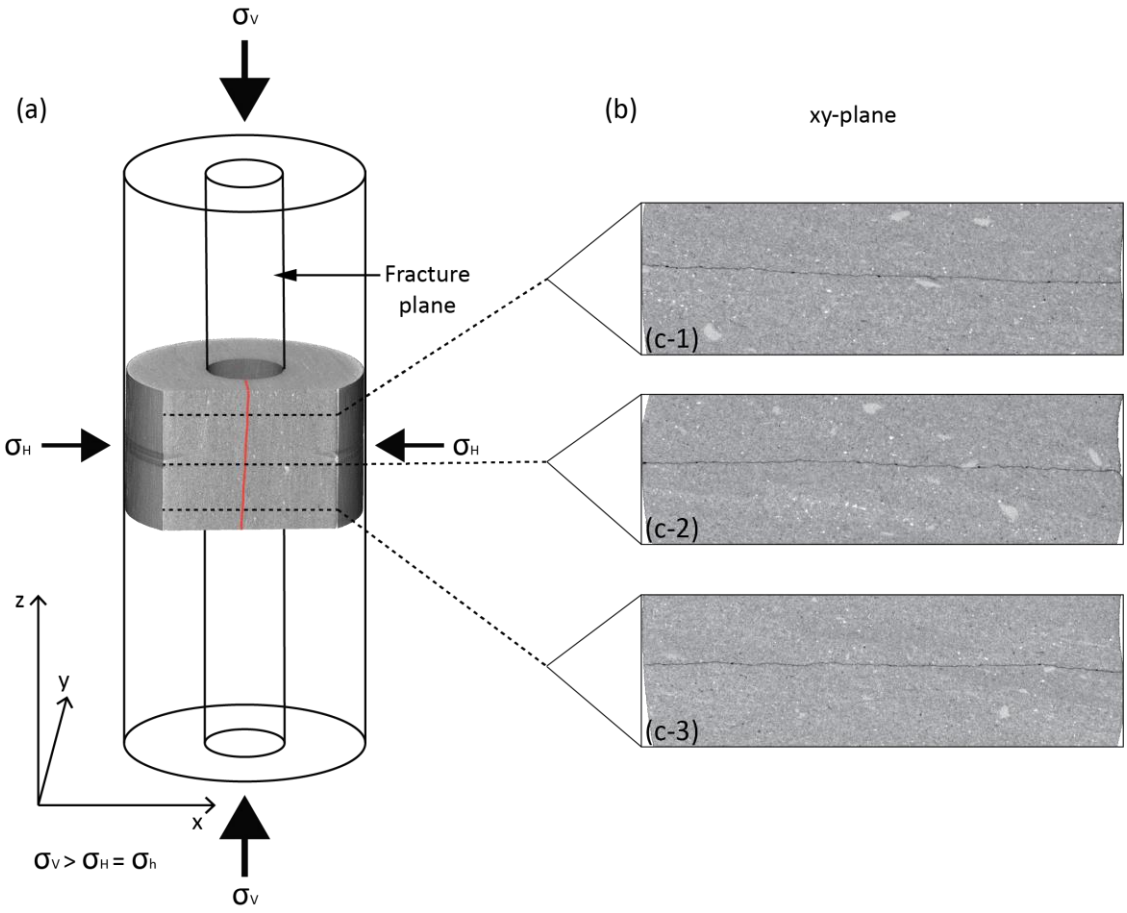

Figure 5-30: Fracture geometry in Nash Point Shale parallel bedding at 25.4MPa confining pressure (not to scale); (a) orientation of fracture relative to sample geometry and stress field, (b) radial fracture geometry (xy-plane).

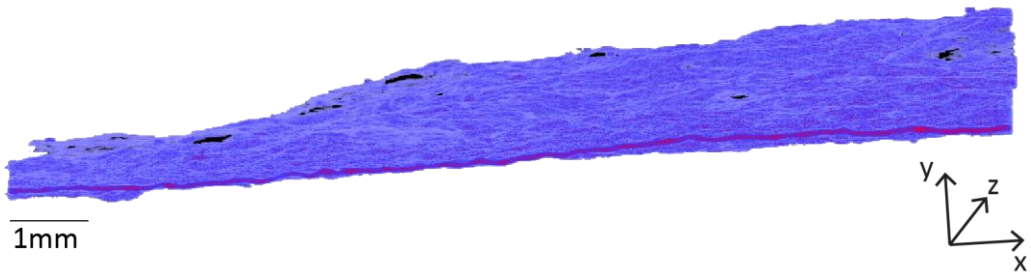

Figure 5-31: 3D – Volume of a hydrofracture in Nash Point Shale generated at high confining pressure (25MPa) showing a planar and homogenous morphology.

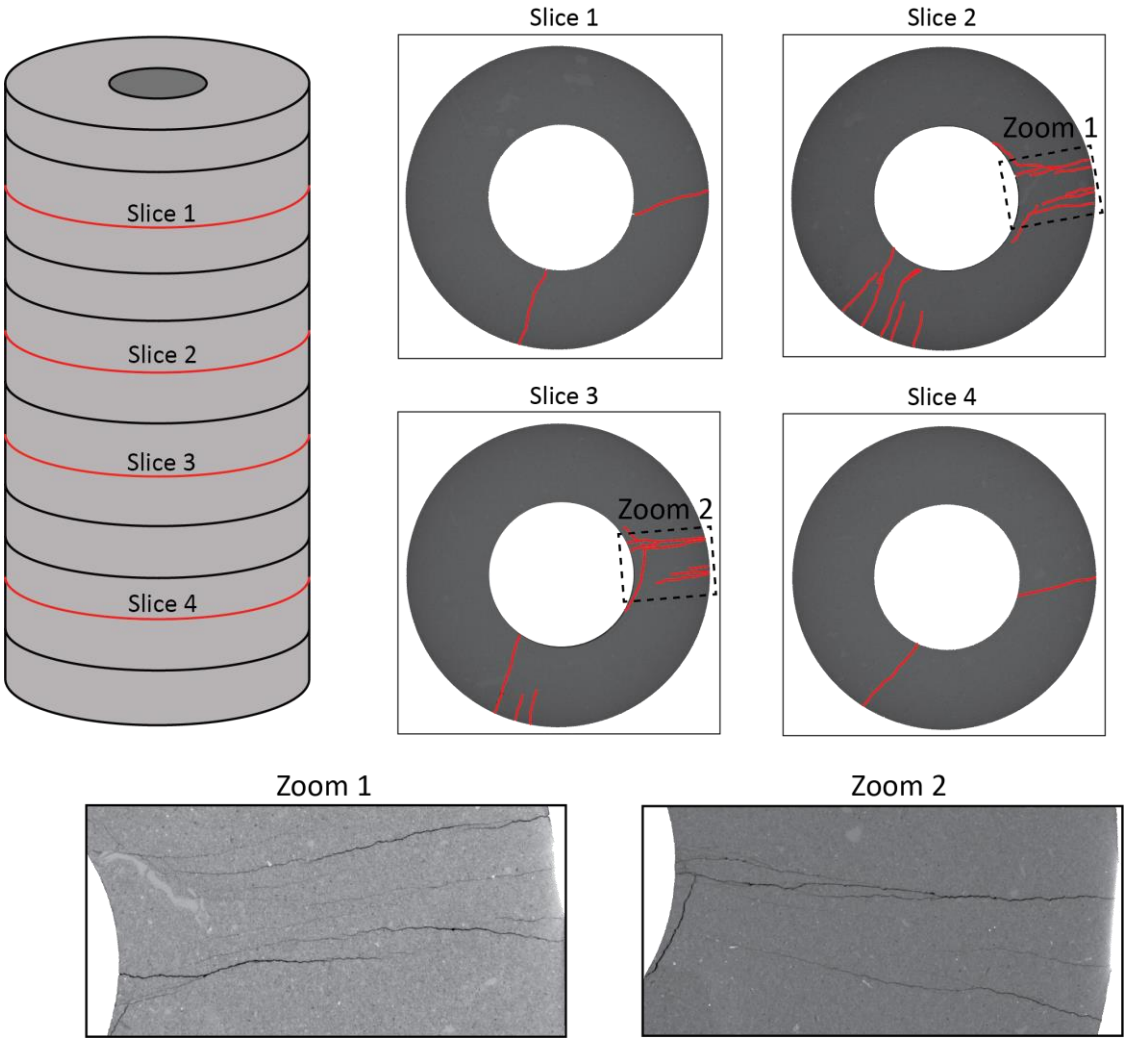

Figure 5-32: Fracture network complexity of sample NPSz-15.3-w

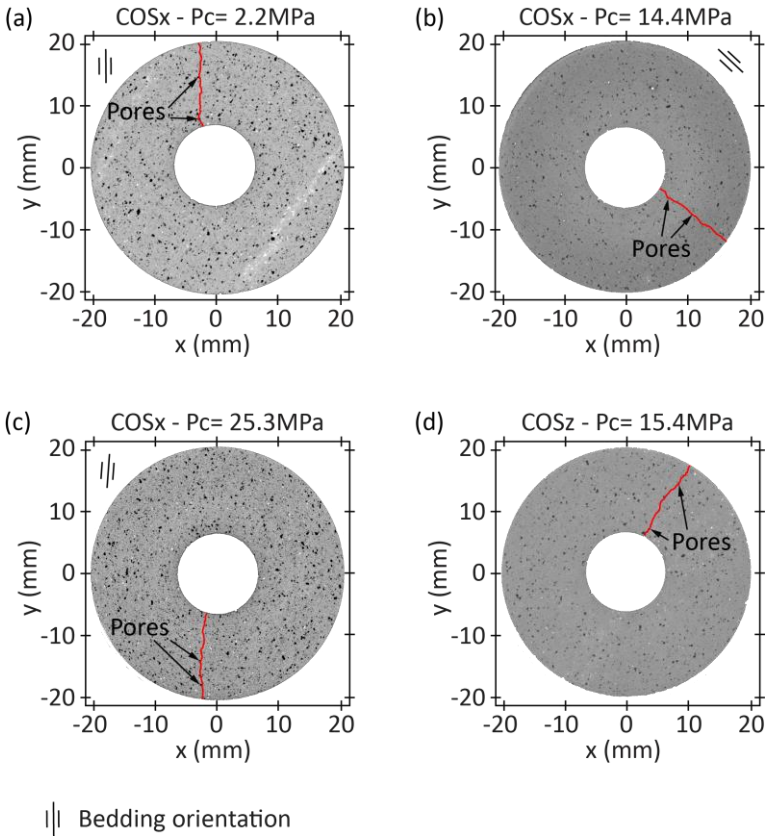

Figure 5-33: X-ray CT images indicating the fracture network developed in COS parallel and normal to bedding at confining pressures of 14.4MPa and 15.4MPa respectively.

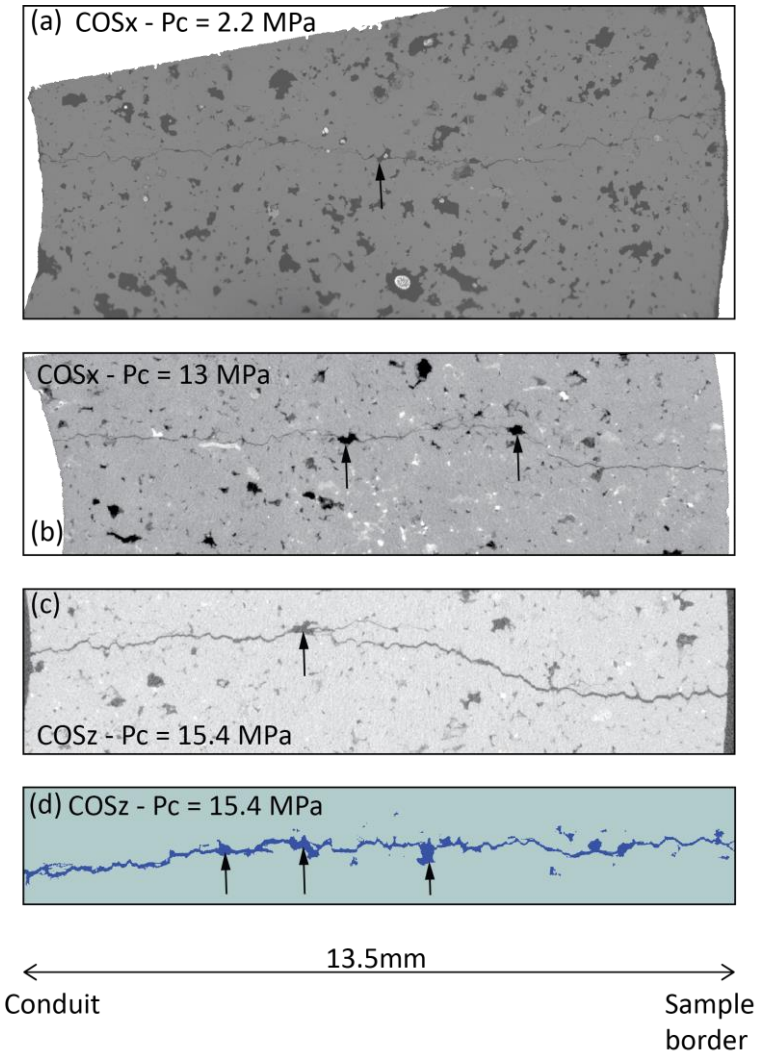

Figure 5-34: High resolution images showing the fracture geometry in COS parallel and normal to bedding; black arrows indicating pre-existing pore spaces.

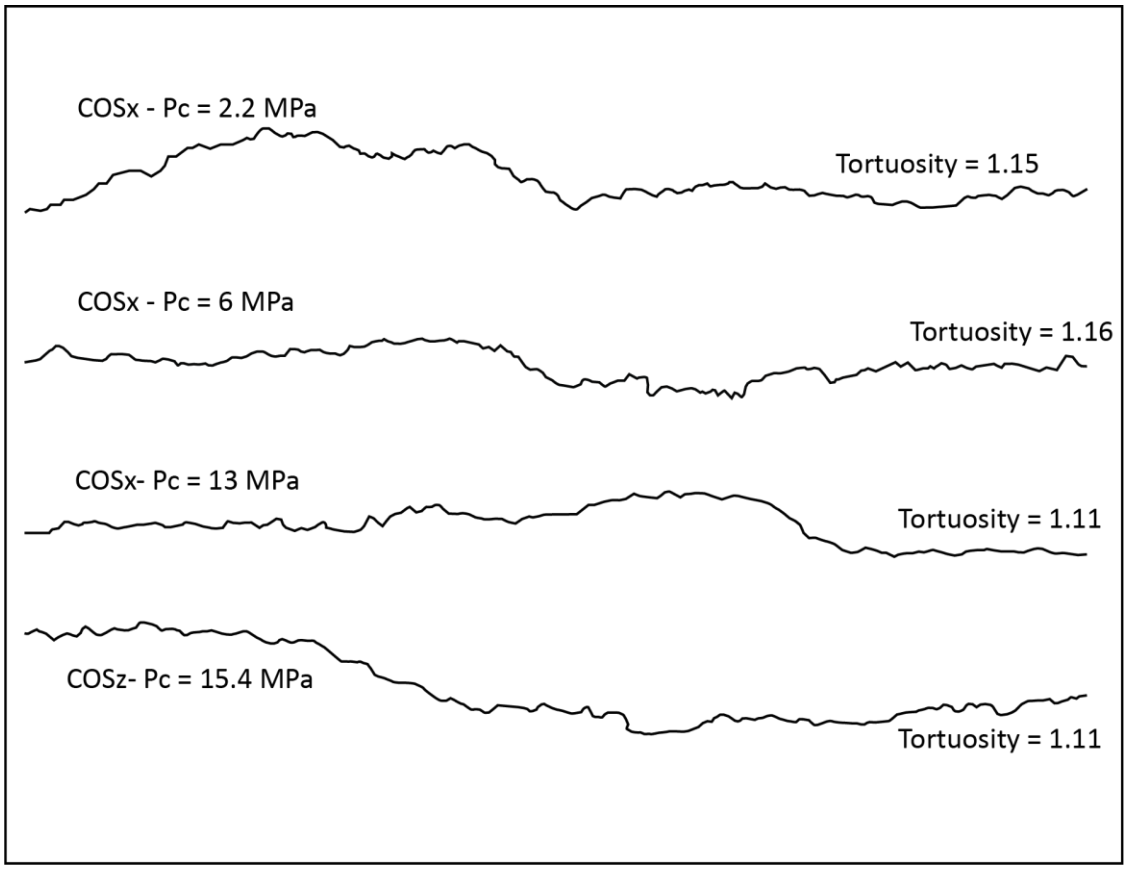

Figure 5-35: Tortuosity lines for four COS samples; COSx - fracture parallel to bedding, COSz - fracture normal to bedding.

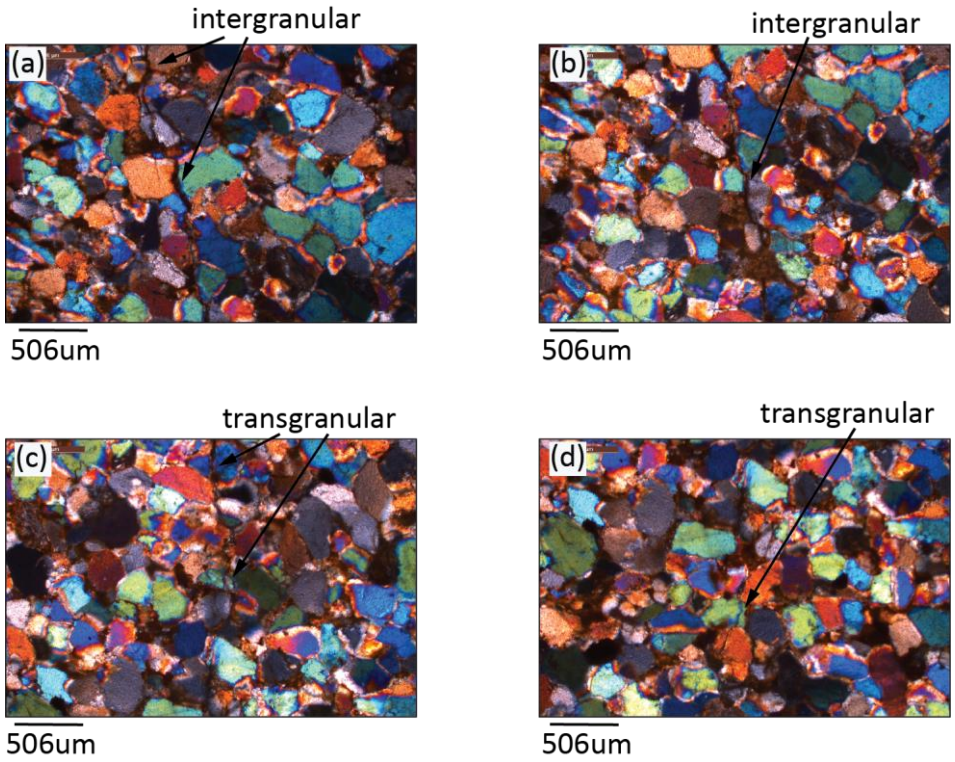

Figure 5-36: Thin section photomicrographs of COS showing intergranular (a) and (b) and transgranular fracture propagation (c) and (d).

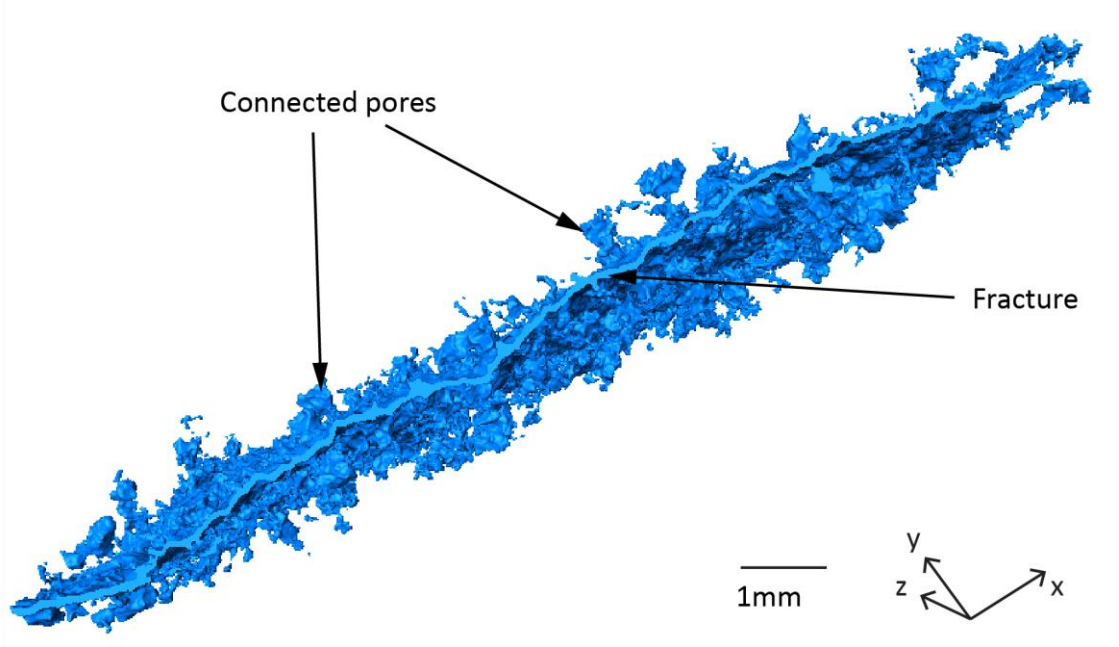

Figure 5-37: 3D volume of a hydraulic fracture generated in Crab Orchard Sandstone normal to bedding at 15.4MPa confining pressure using water as pressurisation fluid.

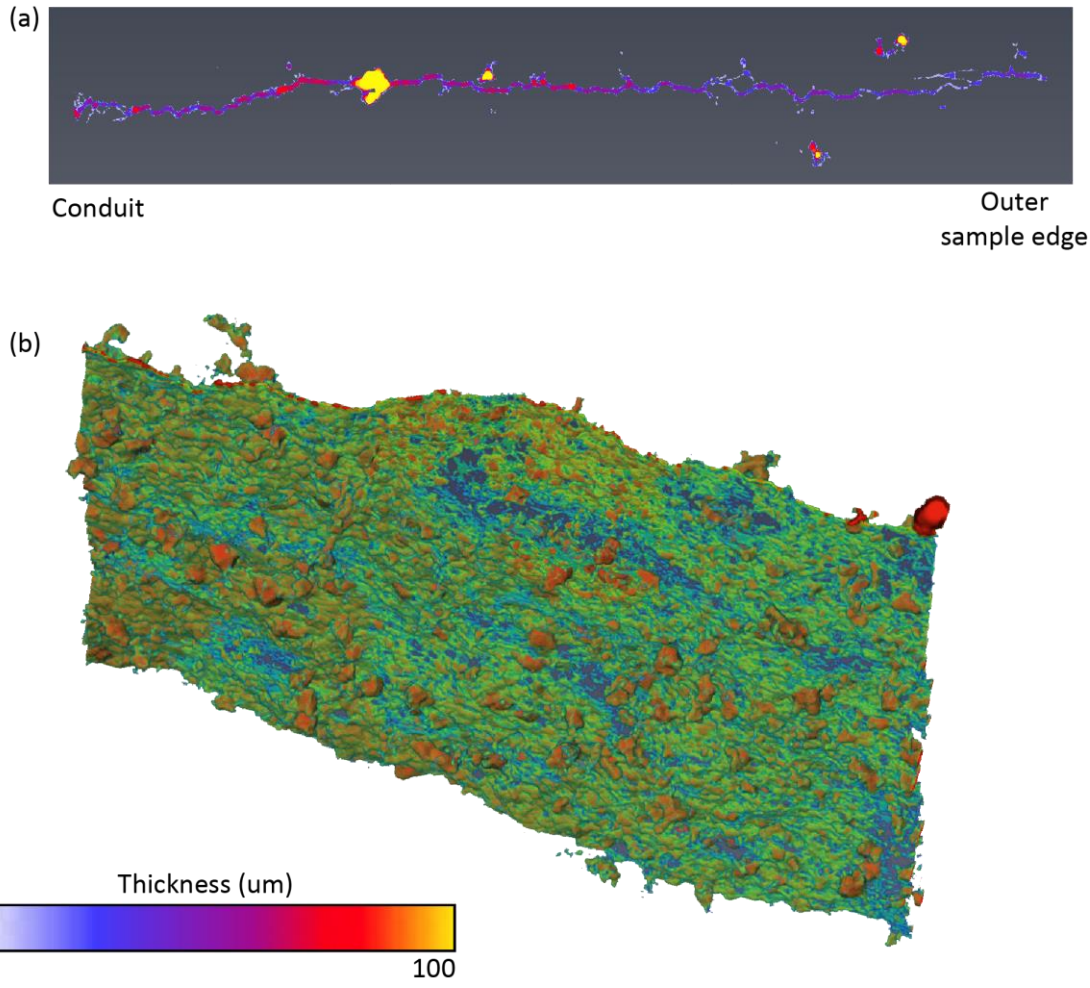

Figure 5-38: Thickness map of a hydraulic fracture in Crab Orchard Sandstone parallel to bedding; (a) 2D thickness map and (b) normalised 3D-thickness map where red is the maximum thickness and blue the minimum.

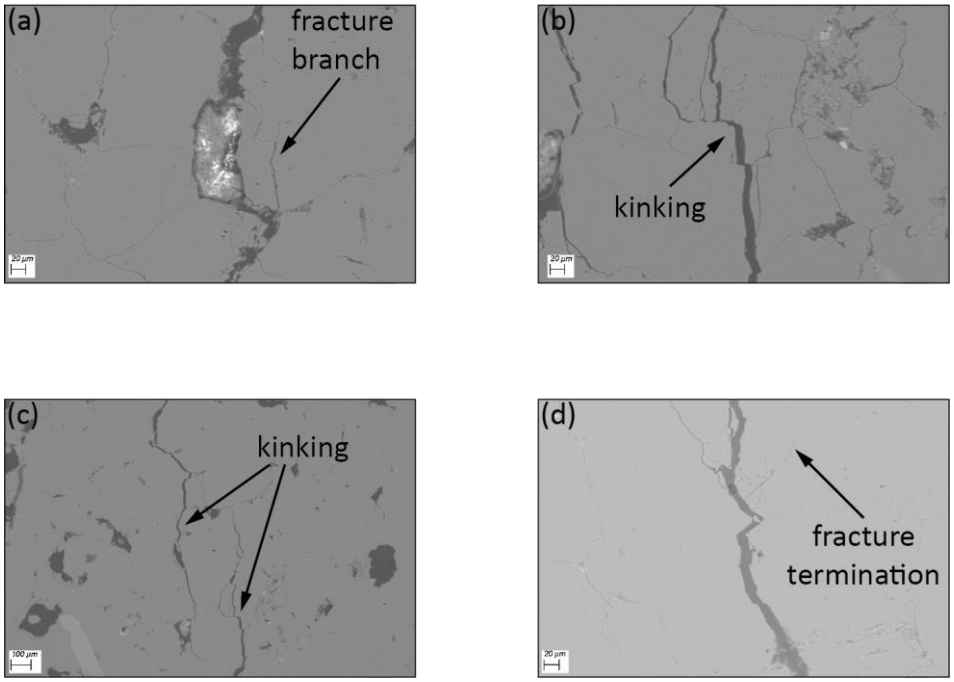

Figure 5-39: SEM Photomicrographs of COS showing (a) branching, (b) and (c) kinking and (d) fracture termination along the fracture path.

5.6 Micro Hydraulic Fracturing with oil as pressurising medium

A second set of experiments has been carried out using a silicone oil as pressurising fluid, which has a higher viscosity (55 mm^2/s) compared to water (1.0034 mm^2/s). The silicon oil was used to fracture one sample of each rock type with the conduit parallel to bedding at medium confining pressure (≈15.4MPa). For the oil driven fracturing experiments, a slight modification of the apparatus was required to use oil as pressurising medium. A fluid separator was added to the fluid circuit as described in detail in Chapter 3.2.3.

Hydraulic fracturing of Nash Point Shale at medium confining pressure - NPSx-15.3-oil

A 0.6s long time record of the data from the oil-driven fracturing of Nash Point Shale, including internal fluid injection pressure (blue line) and AE hit count rate (red dots), is presented in Figure 5-40. A maximum fluid injection pressure of 26.35MPa was recorded. At the same time, a first phase of increased AE activity occurred (Figure 5-40a), with the onset just prior to maxP_{inj} and peak AE rate shortly after maxP_{inj}. The continuous signal (Figure 5-40c) and the spectrogram (Figure 5-40d) show a low frequency seismic burst (50-200kHz), with an impulsive onset and a very short coda. Afterwards, P_{inj} decreased first gradually (average ≈2.3MPa/s) until about 0.04s, at which time a second AE phase starts (Figure 5-40a) and the pressure decay rate starts to increase (Figure 5-40b). At approximately 0.07s the third and main AE phase starts and increases exponentially. The peak AE rate at 0.09s (Figure 5-40a) coincides with a significant increase of the pressure decay rate (Figure 5-40b), which reaches a maximum of 21MPa/s. During the main fracturing event, a series of low frequency seismic bursts (50-200kHz) with impulsive onsets and a very short coda (Figure 5-40 c and d) have been recorded. The end of increased seismic activity at approximately 0.26s (Figure 5-40a) coincides with a change in pressure decay rate (Figure 5-40b) and P_{inj} gradually dissipated afterwards from 23.3MPa to the confining pressure level. During the hydraulic fracturing of shale using silicone oil, the fracture type analysis shows a similar distribution compared to water induced fracturing. Tensile type (44%) and shear type events (38%) are dominant and 18% of the events are of compressional character (Figure 5-41). The sample fractured with a single tensile fracture (Figure 5-42a) parallel to bedding. The fracture has a homogenous (Figure 5-42b) and planar (tortuosity 1.01) (Figure 5-42c) morphology and the aperture ranges between 36-45µm along the radial fracture path.

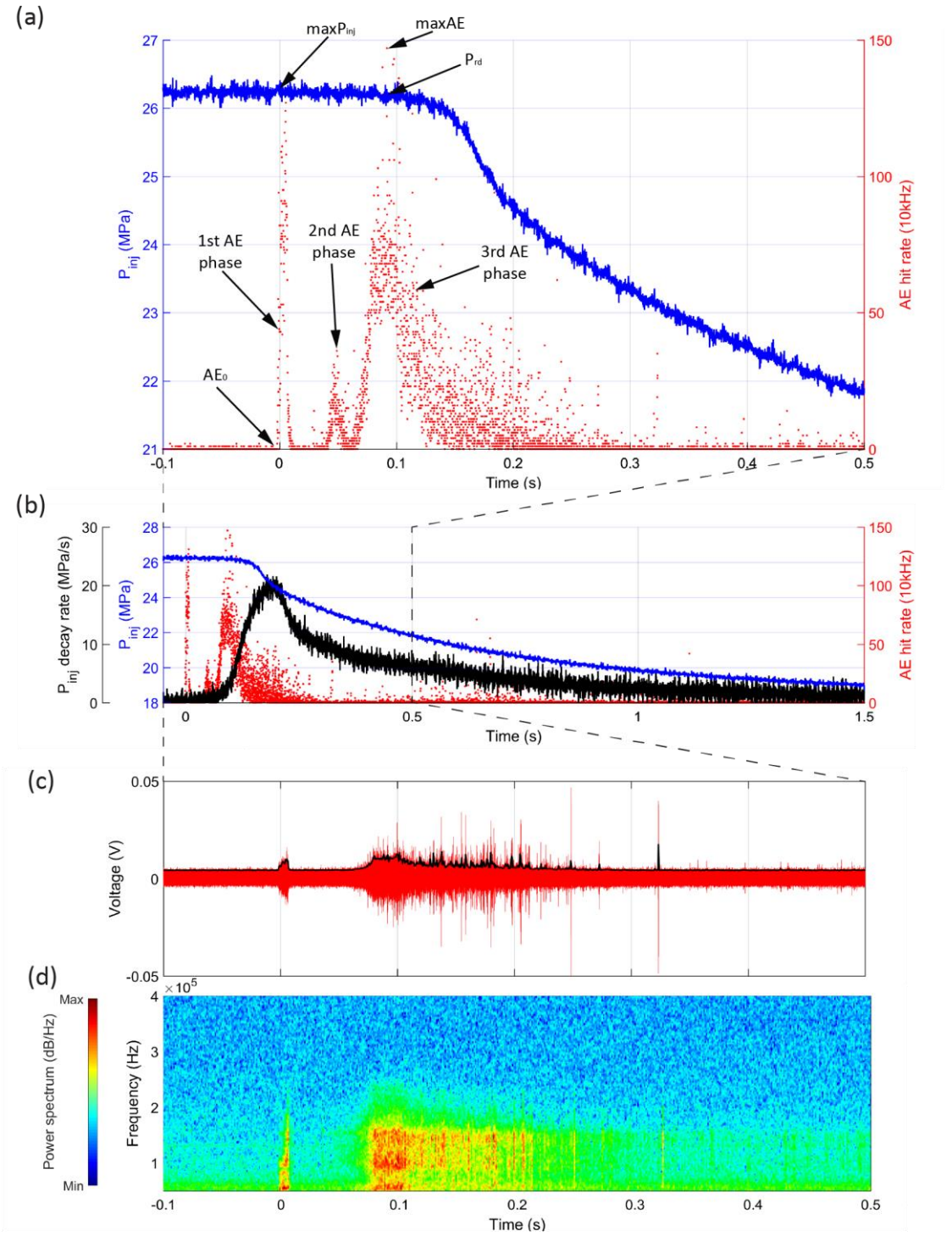

Figure 5-40: NPSx-15.3-oil – Laboratory data from hydraulic fracturing simulation on NPS at 15.3MPa confining pressure, bedding parallel to sample axis and σ_v and using silicone oil as pressurising fluid; (a)Time-record of internal fluid injection pressure (blue line) and AE hit counts (red dots). (b) Fluid pressure decay rate (black line), fluid pressure (blue line) and AE hit count rate (red dots). (c) Snapshot of the continuous waveform (red line) including the signal envelope at the time of failure. (d) Respective spectrogram at the time of failure. The spectrogram data illustrates the frequency range exhibiting power (colour) with time. Time scales zeroed at maximum fluid injection pressure.

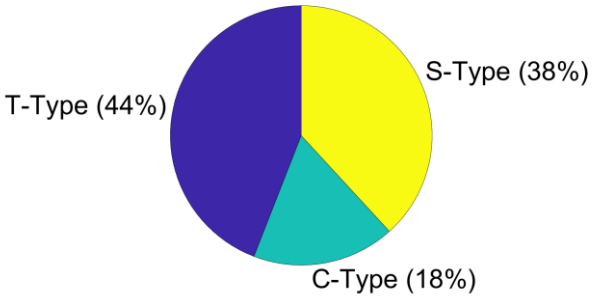

Figure 5-41: NPSx-15.3-oil - Event type analysis results for hydraulic fracturing of NPSx at 15.3MPa confining pressure using oil as pressurisation medium.

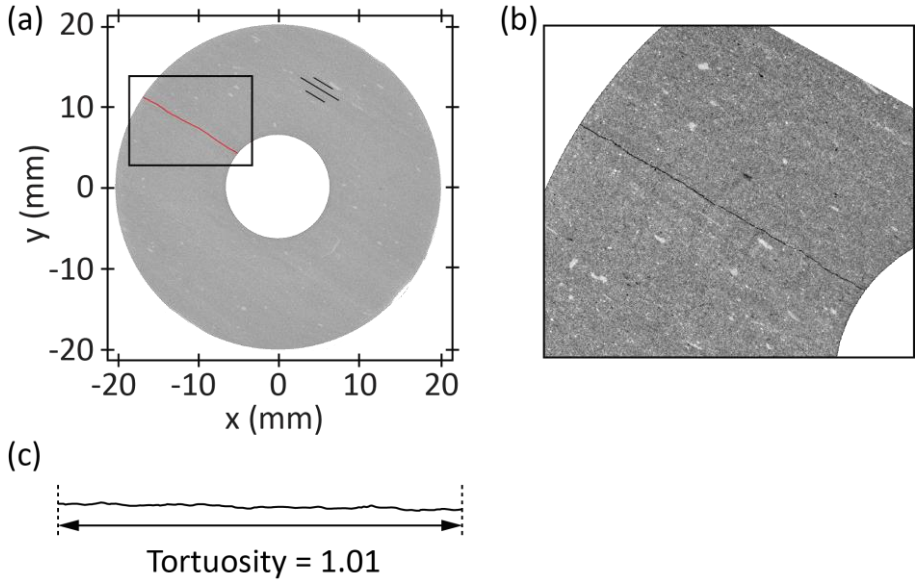

Figure 5-42: NPSx-15.3-oil - Fracture network and morphology of NPSx fractured with silicone oil as pressurising fluid; (a) micro X-ray CT image (resolution 31µm) showing the evolved fracture network (black rectangle marks area of high resolution scan), (b) high resolution scan of fracture (resolution 9µm), and (c) tortuosity of the fracture path.

Hydraulic fracturing of Crab Orchard Sandstone at medium confining pressure - COSx-15.5-oil

The higher viscosity silicone oil was also used to generate hydraulic fractures in Crab Orchard Sandstone parallel to bedding. The data is shown in Figure 5-43 as a 2s time record to visualize the mechanical and seismic responses. A maximum fluid injection pressure of 48.2MPa is reached during the experiment. Increased acoustic activity starts immediately before the maximum fluid pressure and increases exponentially to a maximum at 0.17s, which coincided with an increase in pressure decay rate (Figure 5-43b) from an average of 1.3 to a maximum of 34MPa/s. Radial deformation starts to increase at the same time (0.17s) and increases linearly shortly afterwards at approximately 0.19s (Figure 5-43a). The continuous waveform (Figure 5-43c) as well as the spectrogram (Figure 5-43d) reveal a series of low frequency seismic bursts (100-200kHz) during the fracturing process, which have an impulsive onset and a very short

coda. A higher frequency component is present at 600kHz at the time of peak AE activity. Fluid pressure decreases more rapidly until approximately 0.65s (Figure 5-43b), which coincides with the end of increases AE activity, before a more gradual exponential decay takes the pressure down to the confining pressure level (Figure 5-43a). Acoustic emission activity decreases at a similar rate as the fluid pressure (Figure 5-43a) and mimics the oscillating pattern of the pressure decay rate (Figure 5-43b and c). During the hydraulic fracturing of the sandstone, shear type (49%) and compressional type (37%) events dominated with tensile type events accounting for 14% (Figure 5-44). During the hydraulic fracturing, one primary radial fracture developed parallel to bedding (Figure 5-45a). Pre-existing pores are connected along the fracture paths (Figure 5-45c), which exhibits a low tortuosity (1.06, Figure 5-45b) and can therefore be descripted as planar. However, secondary fracturing was observed (Figure 5-45d) parallel to the primary fracture. The aperture ranges between 54-72µm along the radial fracture path, not including the width of connected pore spaces.

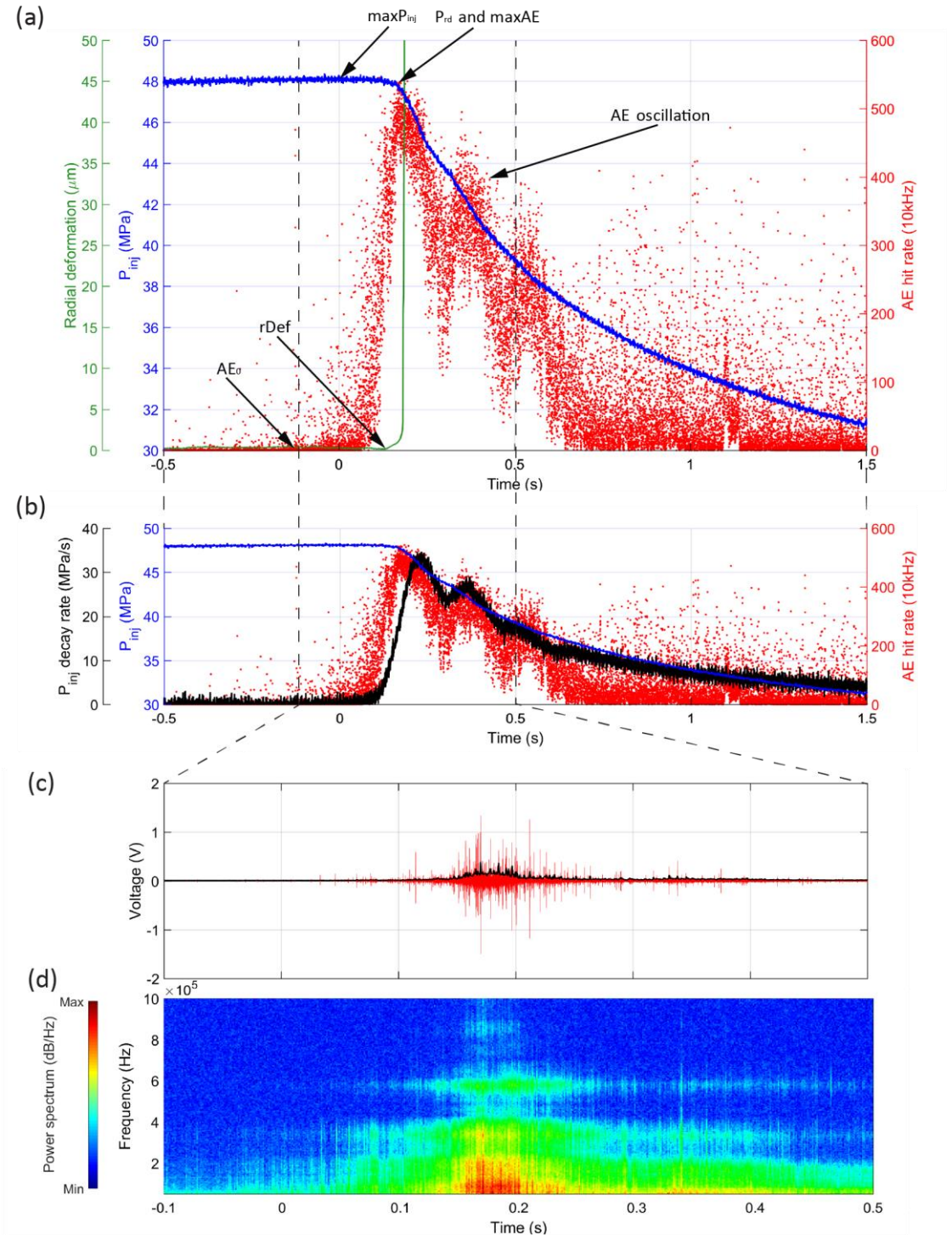

Figure 5-43: COSx-15.5-oil – *Laboratory data from hydraulic fracturing simulation on COS at 15.5MPa confining pressure, bedding parallel to sample axis and* σ_v *and using silicone oil as pressurising fluid; (a)Time-record of internal fluid injection pressure (blue line), radial deformation (green line) and AE hit counts (red dots). (b) Fluid pressure decay rate (black line), fluid pressure (blue line) and AE hit count rate (red dots). (c) Snapshot of the continuous waveform (red line) including the signal envelope at the time of failure. (d) Respective spectrogram at the time of failure. The spectrogram data illustrates the frequency range exhibiting power (colour) with time. Time scales zeroed at maximum fluid injection pressure.*

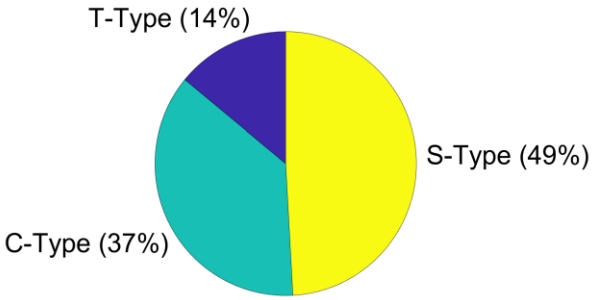

Figure 5-44: COSx-15.5-oil - *Event type analysis results for hydraulic fracturing of COSx at 15.5MPa confining pressure using oil as pressurisation medium.*

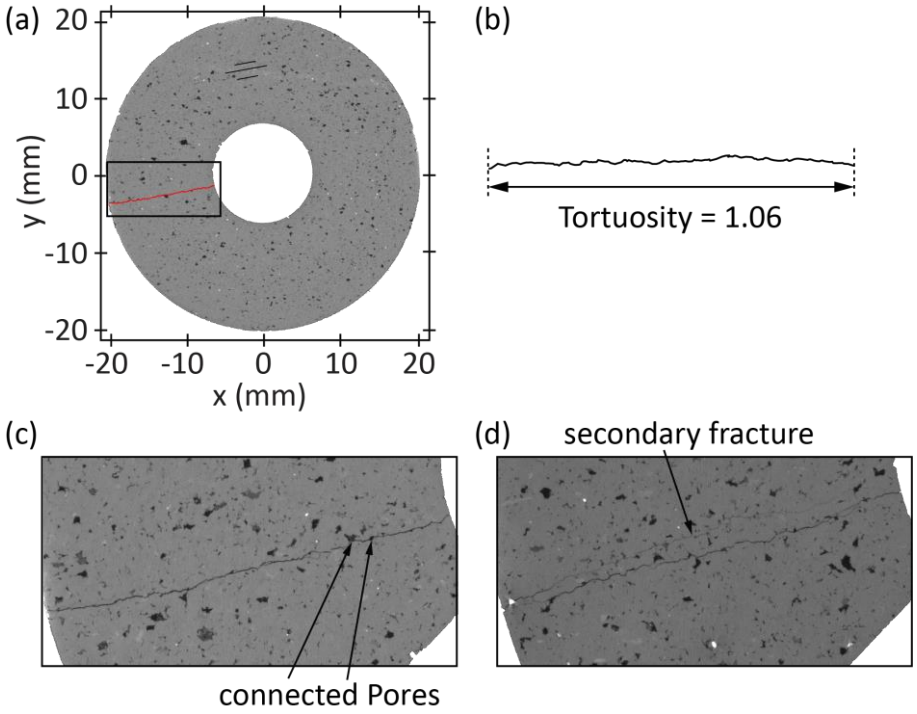

Figure 5-45: COSx-15.5-oil - *Fracture network and morphology of COSx fractured with silicone oil as pressurising fluid; (a) micro X-ray CT image (resolution 31µm) showing the evolved fracture network (black rectangle marks area of high resolution scan), (b) tortuosity of the primary fracture path, (c) and (d) high resolution scans of fracture (resolution 9µm) from different heights of the sample.*

5.7 Permeability measurements after hydraulic fracturing

The main aim of hydraulic fracturing is to enhance extraction and flow rates from unconventional hydrocarbon reservoirs through the generation of hydraulic fractures, which are critical for an economical extraction of oil and gas. Many studies modelled the enhanced permeability achieved through hydraulic fracturing, but to date not many attempts have been made to measure permeability enhancement in laboratory experiments. The final experiment was designed to measure permeability directly after hydraulically fracturing of the sample. This has the advantage that the permeability enhancement can be measured "in-situ" without any changes to the fracture geometry or morphology and the effect of confining pressure can be investigated. This is important to understand the permeability increase in field operations but also for the calibration of numerical models. A modified sample setup was used for the permeability experiments as explained in Chapter 3.6.

Initially, the sample was hydraulically fractured using the same protocol as used for all experiments, which is described in Chapter 3.3. The experimental data of the fracturing phase is presented in Figure 5-46. Four sharp fluid pressure decreases can be seen at approximately 450s, 520s, 590s and the final one at approximately 605s. The pressure decreases coincide with spikes in the radial deformation time-curve, which increase with every successive step up to a maximum of just under 180µm at the final pressure decrease. Afterwards, radial deformation decreases again and stabilised at ≈20µm.

The second part of the experiment involved the measurement of fracture permeability at various effective pressures over a range from 2.5MPa to 20MPa. After fracture, a steady state flow was established with a differential fluid pressure inside the sample conduit and outside the sample. Volume changes in the upstream (internal) and downstream (outside the conduit) reservoir (Figure 5-47 – upper panel) were used to calculate the volume flow rate at each pressure stage, which are plotted in Figure 5-48.

For the calculation of the surface area of the fracture, a single rectangular fracture profile is assumed defined by the crack opening, which is derived from changes in the radial dimensions of the sample, and the length of the pressurised zone (19.2mm). After fracture initiation at 8.4MPa confining pressure, a radial deformation of ≈20µm (Figure 5-46) has been measured which equates to a permeability of $1.9 \times 10^{-15} m^2$ (≈1.9mD) at this pressure stage. To account for the crack closure with increasing confining pressure, an approximate for the relative crack closure was derived from the radial deformation measurements recorded during the experiment (Figure 5-49). An approximate crack opening for each pressure step (Table 5-3) has

then been calculated from the relative crack closure using an initial fracture opening of 20µm, which was measured at the end of fracturing (Figure 5-46). The evolution of permeability is shown in Figure 5-50 as a function of effective pressure and also given in Table 5-3. Fracture permeability decreases with increasing pressure and even when confining pressure decreases again, the permeability did only recover slightly. At an effective pressure of approximately 14MPa, the gradient of decreasing permeability changes and permeability decreases less with increasing effective pressure.

Table 5-3: Results of permeability measurements after hydraulic fracturing of Nash Point Shale; P_c – confining pressure, P_{eff} – effective pressure.

Phase	Absolute crack aperture (µm)	Cross sectional area (m^3)	P_{eff} (MPa)	P_c (MPa)	Permeability (m^2)
1	20.0	3.84E-07	2.5	8.4	1.9E-15
2	19.6	3.76E-07	4.4	10.3	1.8E-15
3	18.7	3.60E-07	6.4	12.3	1.4E-15
4	16.0	3.06E-07	9.2	15.1	1.2E-15
5	14.9	2.86E-07	12.1	18.0	7.6E-16
6	14.4	2.76E-07	14.2	20.1	4.3E-16
7	13.2	2.53E-07	19.1	25.0	2.5E-16
8	13.6	2.60E-07	9.2	15.1	2.0E-16
9	14.2	2.73E-07	2.3	8.2	2.4E-16

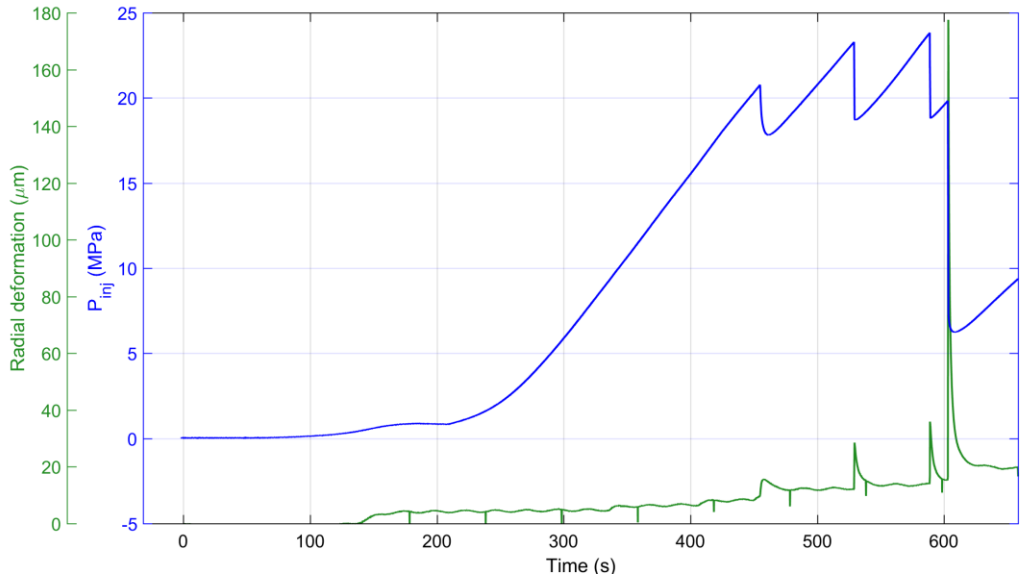

Figure 5-46: Experimental data record for the hydraulic fracturing of Nash Point Shale parallel to bedding at 8.4MPa confining pressure.

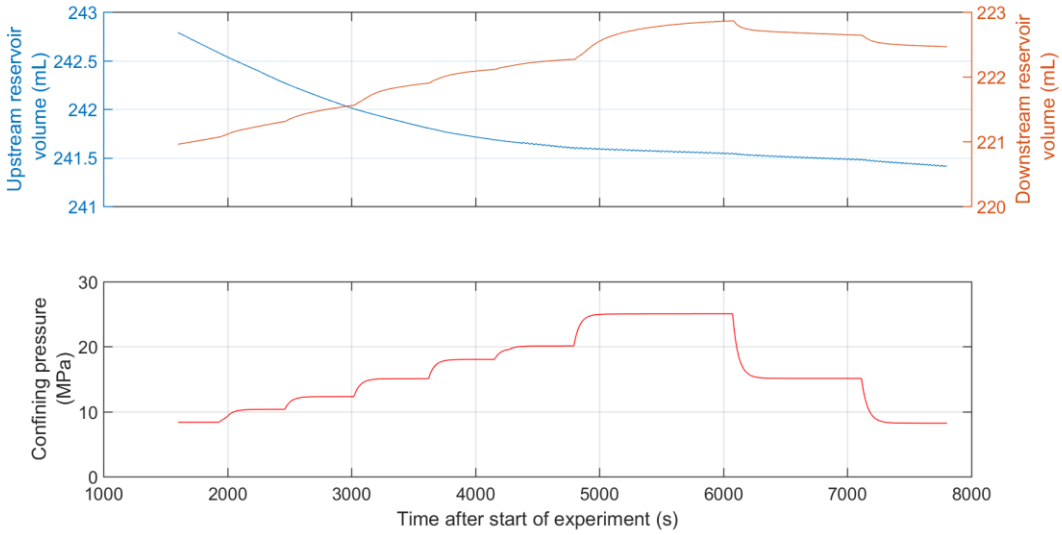

Figure 5-47: Reservoir volume change and confining pressure over time during the permeability measurements

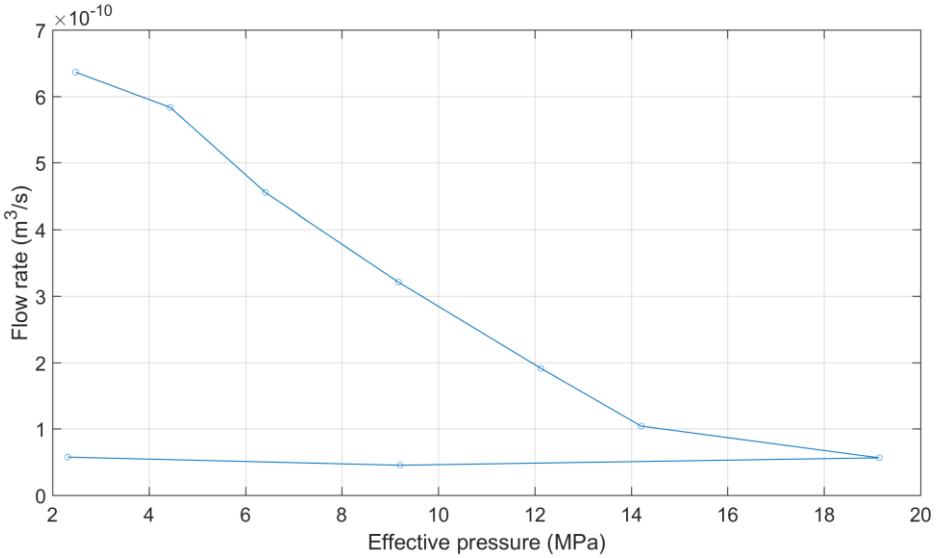

Figure 5-48: Flow rate vs effective pressure diagram

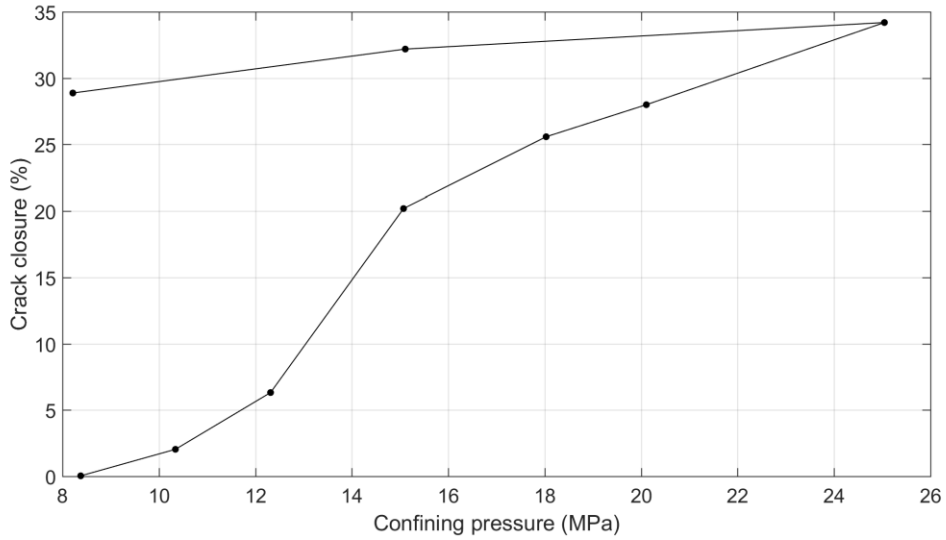

Figure 5-49: Relative closure of fracture aperture as function of confining pressure

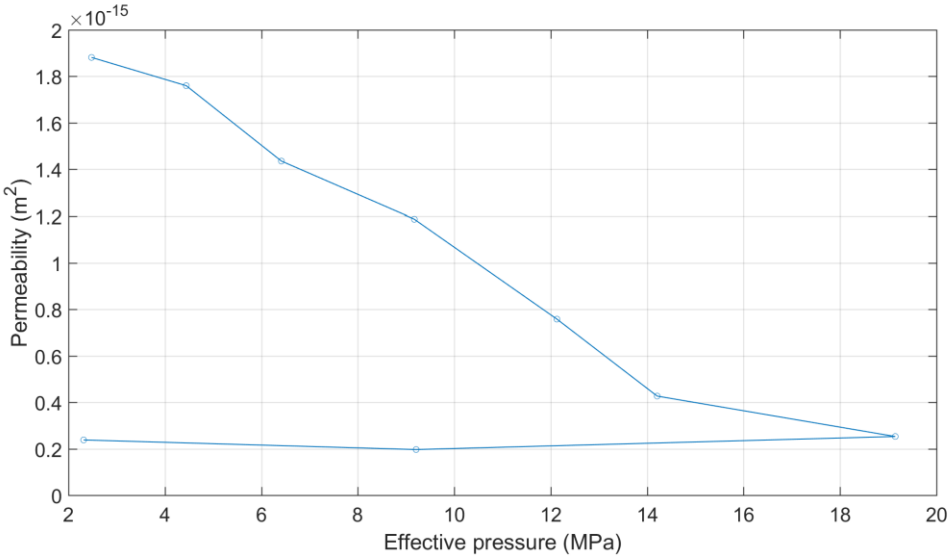

Figure 5-50: Permeability vs effective pressure diagram

6 Discussion

In the following discussion, the failure process during hydraulic fracturing of Nash Point Shale is analysed and evaluated in detail. First, the mechanics of tensile fracturing via purely mechanical-driven (Brazilian test) and fluid-driven fracturing are compared and discussed together with the effect of anisotropy on the fracturing process. Secondly, the coupled fluid-rock mechanics of fluid-driven fracture propagation are discussed including an interpretation and correlation of the mechanical as well as seismic measurements and the seismo-mechanical relationship. Thirdly, the effects of rock fabric and initial permeability on hydraulic fracturing and fracture geometries are interpreted together with the permeability enhancement in NPS through hydraulic fracturing. This evaluation is followed by a comparison of common hydraulic fracturing models with experimental data from this study. Finally, the data from this study is evaluated for the potential to derive fracture toughness for the tensile fracture mode at elevated pressures by using fluid pressure measurements and AE energy calculations.

6.1. Decoding the mechanics of fluid-driven fracturing and the role of anisotropy

Hydraulic fracturing generates tensile fractures using a pressurised fluid. To achieve this, fluid is injected into a central conduit at a rate sufficient to generate sufficient overpressure to exceed the tensile strength of the rock. The fracture then extends by continuing to pump fluid into the conduit. This general setup applies equally as described in laboratory studies (this work) or as seen in field approaches (e.g. Haimson and Fairhurst, 1969b; Zoback et al., 1977; Gandossi, 2013).

Purely mechanical-driven (ITS) and fluid-driven fracturing

When comparing tensile strength values determined by indirect tensile strength tests (Brazilian tests) and thick-walled cylinder tests at ambient pressure conditions (Figure 6-1a), the latter method (green dots) provides slightly higher values, but within reasonable range. The maximum fluid pressure recorded during hydraulic fracturing simulations may be related to the tensile strength of the rock. However, to understand the implications of the fluid on the fracturing process, a brief evaluation of the purely mechanically-driven tensile fracturing combined with the seismic signature is appropriate. To achieve this, AE activity and applied load were recorded concomitantly and at a high sampling rate during a standard “Brazilian” test (indirect tensile test) in the short-transverse direction (parallel to bedding). The data from the Brazilian test (Appendix A.7) showed that sample breakdown occurs instantaneously at the same time as the onset of exponential AE hit rate increase, which indicates fracture initiation. This is in contrast to the fluid-driven fracturing, where a notable time delay is measured

between fracture initiation in Nash Point Shale and sample breakdown as recorded via the AE signal. This suggests a difference in fracture initiation and initial facture propagation mechanism between purely mechanical (Brazilian-disc) and fluid-driven (hydraulic-fracture) processes. During the Brazilian tests, unstable fracture propagation occurs immediately, advancing the fracture to the edge of the sample, whereas hydraulic fracturing shows an initially slow fracture advance. The AE data provide additional support for the difference in underlying fracture mechanisms (Figure 6-1). For the mechanical-driven fracturing (Figure 6-1c), very pronounced, short bursts of AE are recorded over a range of frequencies up to 1MHz, although with a band of power concentrated at 100-400kHz initially, and then a second band of power centred at 600kHz later in the experiment. Conversely, for the fluid-driven fracturing (Figure 6-1b), the power lies at much lower frequencies of just 100-200kHz. The difference in frequency spectrum indicates fluid interaction, as lower frequencies are often associated with fluid movement or hybrid rock/fluid flow (e.g. Benson et al., 2008).

Decoding hydraulic fracturing: maximum fluid pressure, fracture initiation pressure and breakdown pressure

Two common assumptions concerning the initiation and propagation of hydraulic fractures in rocks are, (1) that fracture initiation and sample breakdown (strength failure) occur simultaneously at maximum fluid pressure and, (2) that due to the large stress concentration at the tip of the fracture, once the sum of tensile strength and pressure normal to the fracture are exceeded, the fracture continues to propagate in an unstable manner. However, from the data reported in this study, it is clear that the picture is more complex, and that these assumptions may not be true. Both Nash Point Shale and Crab Orchard Sandstone exhibit a significant time delay between maximum fluid injection pressure, fracture initiation and the physical breakdown of the sample. A good proxy for fracture initiation is the onset of acoustic emission hit rate (e.g. Zoback et al., 1977). This is verified via Brazilian disk tests where the applied load decreases at the moment of elevated AE activity. In all experiments, peak AE rate, and rapid decay of fluid pressure, were good indicators for the physical breakdown of the sample, and is further supported by radial deformation, which increases significantly at approximately the same time. To fully analyse the progressive failure during hydraulic fracturing, different stages of the fracturing process are distinguished. Following Bieniawski (1967a), a distinction is first made between fracture initiation as a local failure process where a pre-existing crack starts to extend (Griffith concept), and fracture propagation as a global failure process, where fracture grows subsequent to initiation in either a stable or unstable manner. Specifically, three key types of pressures are identified here to describe the hydraulic fracturing process: (1) maximum fluid injection pressure, the maximum pressure recorded

during the fluid pressurisation, (2) fracture initiation pressure, where a small initial defect develops, and (3) breakdown/failure pressure, where the sample physically fails. An overview of these parameters for the experiments conducted here is given in Appendix A.8. All three pressures increase with increasing confining pressure (shown for the $maxP_{inj}$ in Figure 5-1), but are also influenced by the inherent anisotropy.

The effects of anisotropy on the hydraulic fracturing process in Nash Point Shale

In contrast to samples with parallel bedding, where hydraulic fractures developed in the Short-Transverse direction (Figure 5-21), hydraulic fracturing experiments with the central conduit orientated normal to σ_v, forces fractures to propagate in the Divider and the Arrester orientations (Figure 5-21), assuming that fractures initiate in the pressurised, central, part of the sample and propagate radially and axially. Radial fracture propagation occurs normal to the bedding orientation, taking several bedding planes at the same time (Divider orientation, Figure 4-21). However, the fracture also advances normal to the bedding orientation when propagating vertically but this time taking one bedding plane at a time (Arrester orientation, Figure 4-21). In the case of a penny-shape fracture, these two processes will occur simultaneously and the strength of the rock would most likely be a combination of the two fracture orientations.

The hydro-mechanical characteristics of the fracture process are similar for both normal and parallel bedding: a rapid fluid pressure decay, indicated by maximum AE rate and change in fluid pressure decay rate, followed by an oscillation phase. However, a significantly higher fluid pressure is required to initiate hydraulic fracture normal to bedding. Fracture initiation now depends on the strength of the rock material rather than the bonding strength between the bedding planes and therefore would require significantly higher fluid pressures to initiate fracture. The difference in breakdown pressures for the two fracture orientations, Short-Transverse and Divider, maintains a ratio of approximately 1.7 with increasing confining pressure (Figure 6-2). The same effect of increased tensile strength due to anisotropy has been seen in the Brazilian disk experiments with no confining pressure (Figure 6-1a), where a similar strength ratio for the two fracture orientations was calculated (average ratio 1.9). This suggests that the influence of anisotropy does not change with increasing pressures, and even at very high pressures, anisotropy will partly control fracture initiation. Higher absolute fluid pressures are likely the cause for the higher pressure decay rates recorded in experiments with normal bedding, compared to shale experiments with parallel bedding. Similarly, faster peak decay rates and decreasing decay lengths were also observed with increasing confining pressures for shale samples of both bedding orientations. The higher fluid pressures force the fracture open

more rapidly and allowing for faster flow rates and equally a faster pressure release. This also shows in the fewer fracture stages in shale samples with normal bedding (e.g. Figure 5-10) and with increasing confining pressure.

Samples with normal bedding showed a plateau in the radial deformation, commencing at the end of the oscillation. This suggests a change in fracture propagation orientation from radially to axially. First, the fracture propagates dominantly radially by following the shortest stress path. Once the radial fracture reaches the edge of the sample, fracture propagation continuous vertically but changing from a propagation in the Divider orientation to propagation in the Arrester orientation. In summary, anisotropy results in higher breakdown pressures, different fracture propagation orientation relative to bedding, higher fluid pressure decay rates and a faster decay process as well as fewer discrete fracture propagation steps and less deformation of the sample prior to fracture initiation.

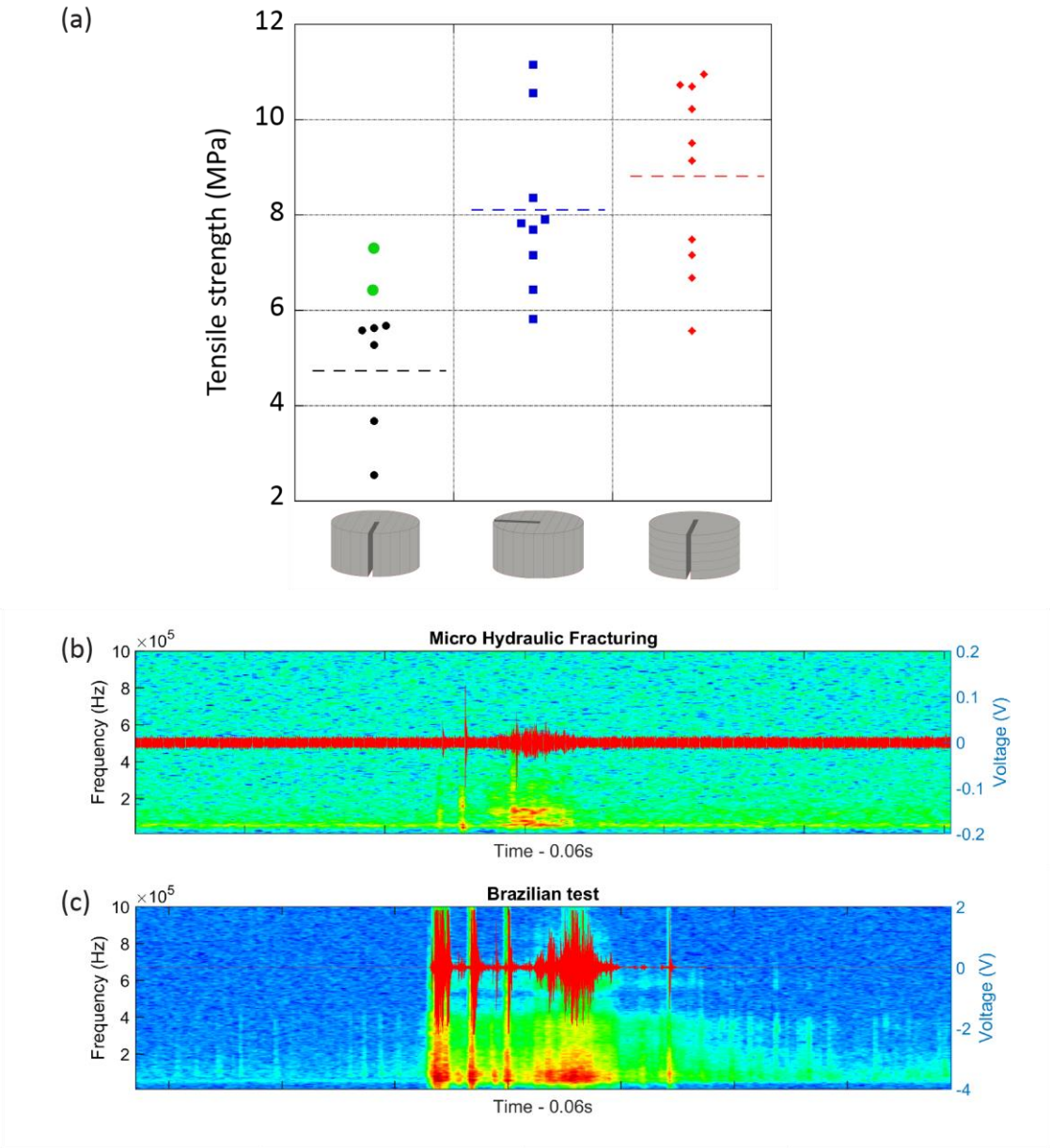

Figure 6-1: Comparison ITS and MHF ; (a) Tensile strength of Nash Point Shale determined via indirect tensile strength and thick walled cylinder tests (green dots), Continuous signal and spectrogram for (b) fluid-driven tensile fracturing at ambient pressure conditions and (c) indirect tensile strength test (Brazilian test) at ambient pressure conditions.

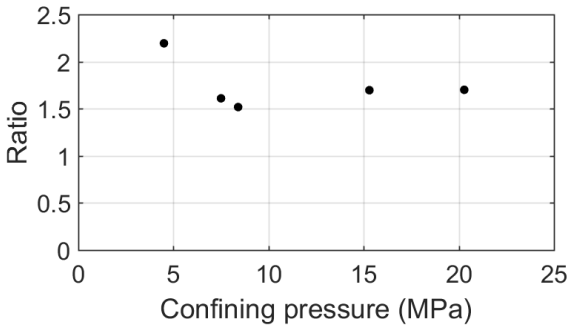

Figure 6-2: Breakdown pressure ratio Divider / Short-Transverse as function of confining pressure

6.2. The role of fluids in promoting hydraulic fracture extension

Interpretation based on fluid injection pressure and AE hit rate

All shale experiments, independently of anisotropy orientation or confining pressure showed similar mechanical characteristics in terms of the initial fracture process and followed the same fracturing sequence. In general, the maximum fluid injection pressure is seen to predate fracture initiation, which is followed by an almost instantaneous pressure drop associated with unstable fracture propagation. After the initial pressure decrease, an oscillation phase of the fluid pressure is usually observed before fluid pressure gradually decreases to the level of the confining pressure. The time delay between maximum fluid injection pressure and fracture initiation may indicate an elastic or plastic behaviour of the shale sample, a hypothesis supported by the relatively gradual change in radial deformation at the time of maximum fluid injection pressure. A similar response in thin walled granite cylinders was observed by Schmitt and Zoback (1989), who reported an increasing compliance with increasing fluid injection pressure prior to failure which they attributed to dilatant effects, which result in a non-linear strain response of the sample prior to failure. Dilatancy prior to fracture initiation has also been suggested to result in an increased permeability of the plastic deformation zone near the conduit wall (Figure 6-3) (Schmitt and Zoback, 1993). This is important as increased permeability is likely to induce compressive stresses due to the fluid infiltration acting to delay further fracturing in a negative feedback loop (Li et al., 2016).

The phase from fracture initiation to sample breakdown (e.g. Figure 5-2a) is most likely characterised by a stable crack propagation, as little or insufficient fluid pressure is available along the fracture surfaces to initiate unstable fracture. However, the decreasing fluid injection pressure combined with the observation of low frequency seismic activity (e.g. Figure 5-2a) suggest that fluid flow occurs within the fracture allowing pressure to build up. At the time of rapid fluid pressure decay, sufficient fluid pressure has built up over the fracture length, increasing the stress concentration at the fracture tip and ultimately initiating unstable crack propagation. This is accompanied by fracture opening that in turn allows for an almost instantaneous release of fluid pressure. Evidence for the unstable fracture propagation are the high pressure decay rates (625-1012MPa/s for parallel bedding and 3979-7292MPa/s for normal bedding), which are proportional to fluid flow velocities according to Bernoulli's principal, suggesting that a critical fracture velocity, crack length and energy release (Figure 2-4) is exceeded for unstable fracture propagation to occur. The time delay between fracture initiation and sample failure may be linked to the time taken for the pressure to build up within the fracture, and in turn to reach the critical energy release for the transition from stable to unstable fracture propagation. In such a scenario the delay is related to the developing fracture

geometry and complexity of the fracture network. Smooth, planar fractures are likely to allow faster fluid flow and pressure build up, reducing the delay time. Such a model would explain the longer delay seen in sample NPSz-15.3-w (2.9s compared to 0.02s for 'simple' fracture networks), in which a complex fracture network with multiple fractures developed. A difference in the time delay is also observed between Nash Point Shale (average delay 0.02s) and Crab Orchard Sandstone (average delay 0.14s), most likely due to the higher fracture path tortuosity in the sandstone. In addition, Schmitt and Zoback (1993) and Li et al. (2016) both recorded fluid pressure decreases before failure as seen in the shale (average 0.4MPa) and sandstone (average 0.4MPa) experiments. An alternative explanation for the time delay between fracture initiation and sample breakdown, and these small reductions in fluid injection pressure prior to unstable fracture propagation, is likely to be related to increasing permeability near the conduit wall caused by dilatancy of the rock (Figure 6-3). Assuming that pore pressure recharge cannot keep up with fluid injection pressure increase, pressure gradients would lead to fluid infiltration into the rock mass during pressurisation. The fluid infiltration produces a compressive circumferential stress near the inner wall (Schmitt and Zoback, 1992) that temporarily limits the rate of fracture (Boone et al., 1991; Schmitt and Zoback, 1993) and delays the onset of unstable fracture propagation.

After unstable fracture propagation, the majority of experiments (e.g. Figure 5-5) show a oscillating pattern in both fluid injection pressure and AE hit rate (with a small time offset), and both follow an increasing (but step-wise) radial deformation. Taking the NPS data, the oscillation of the fluid pressure suggests an incremental crack growth, where the peak of each oscillation is the required pressure to re-start crack propagation. Further support for the incremental crack propagation was previously demonstrated by Vinciguerra et al. (2004), who hydraulically fractured Darley Dale Sandstone using an internal jacket to prevent fluid flow into the fracture. Despite no fluid infiltration, they also reported an incremental fracture progression indicated by two distinct phases of AE activity and event locations over time. The AE pattern, which mimics the fluid injection pressure proves a seismo-mechanical link and that seismic activity is directly related and controlled by the pressurised fluid. The halt in propagation and hence the fluid oscillation is most likely caused by a pressure decrease within the fracture, resulting in a reduction of stress intensity at the fracture tip. This result is important as stress intensity should increase as the fracture extends when fluid pressure is acting along the entire length of the fracture (Figure 6-4 case 1). However, if the fluid pressure does **not** act along the entire fracture, but is only acting on a small section of the fracture, the stress intensity at the fracture tip decreases with crack length as seen in Figure 6-4 (case 2), and an initially unstable fracture growth becomes stable (Zoback and Pollard, 1978). This is the

case in NPS, where unstable fracture propagation in the shale reflects the scenario whereby fluid demand within the fracture is higher than fluid supply (e.g. Whittaker et al., 1992; Detournay and Carbonell, 1997), resulting in a fluid pressure decrease in the fracture similar to the “lined” experiments of Vinciguerra et al. (2004). This further supports the conclusion that fluid pressure is only applied to a small section of the crack, which reduces the stress intensity at the crack tip with increasing crack length and ultimately causing the halt in propagation once stress intensity decreases below the critical stress intensity. Continued growth therefore requires an increasing fluid pressure over the entire length of the fracture to exceed the required stress concentration at the crack tip (Zoback et al., 1977; Detournay and Carbonell, 1997). Figure 6-5 illustrates a typical joint fluid-mechanical-AE interpretation during a representative experiment (in this case NPSx-25.4-w as seen in Figure 5-7) and a conceptual model of the incremental fracture propagation is shown in Figure 6-6. Shortly after the maximum fluid injection pressure is achieved, AE hit rate starts to increase, which indicates fracture initiation. Following this point, fluid pressure and AE hit rate decrease during the initial quasi-stable fracture propagation. At some point, fluid pressure within the fracture reaches a critical pressure to propagate the crack under unstable conditions (Figure 6-6a) at which point AE activity peaks (Figure 6-5). However, fluid flow is not sufficient to maintain the pressure due to high fracturing speeds during unstable fracture propagation, which results in a pressure decrease near the fracture tip (Figure 6-6b), a decline in AE activity (Figure 6-5), and eventually a halt of fracture propagation. As the injection flow rate has not been changed, eventually, the fluid pressure inside the fracture is re-established and the stress concentration at the fracture tip induces a new fracture propagation sequence. This cycle may be repeated several times during the entire hydraulic fracturing process until the fracture reaches the outer edge of the sample as seen for sample NPSx-2.2-w (Figure 5-5).

This model is supported by the trend in the radial deformation, with initially only a small radial deformation recorded, followed by incremental increases at the same time as the peak in fluid pressure decay rate and AE activity. Finally, when the fracture reaches the outer edge of the sample, fluid pressure dissipates in a steady manner (essentially, a through-going ‘leak’ at this point) until it reaches confining pressure. During this phase, increased AE hit rate is recorded, likely to be related to the fracture extension in a vertical sense as shown by post-experiment analyses. Another source for the elevated AE hit rate is the fast (turbulent) fluid flow through the fracture as local pockets of turbulence generate rock-fluid coupling resulting in AE events.

Seismic signal interpretation during hydraulic fracturing

Using Figure 5-5 (NPSx-2.2-w) as an example, AE rate builds rapidly during fracture events and remains high; this may be interpreted as the initial fracturing of fresh rock in tension, followed by an induced low frequency tremor driven by rapid fluid movement through the newly established crack. Sonogram data from the hydraulic fracturing experiments at medium and high confining pressure support this, showing a seismic signal with an impulsive to rapid emergent onset and a long harmonic, quasi-monochromatic coda. These seismic signatures of the shale during the fracturing process have very similar characteristics compared to so-called hybrid events (e.g. Benson et al., 2010; Harrington and Benson, 2011), often recorded during magmatic and/or hydrothermal fluid injection beneath volcanoes driven by pressure disturbances associated with fluid flow (Kumagai and Chouet, 2000). This interpretation is also consistent with studies to directly induce fluid flow in volcanic rocks (e.g. Benson et al., 2014; Fazio et al., 2017). Finally, this view is further supported by the measured, high, fluid decay rates present through the fracture. At higher confining pressures, seismicity associated with rock/fluid coupling becomes dominant, signifying that seismicity generated by hybrid rock/fluid flow overprints fresh fracture events and significant fluid movement occurs within the fracture. Spectrogram data from shale experiments also reveal that the most significant power lies in the range 100 to 300 kHz and the low frequency component lasts for the entire fracturing process (e.g. Figure 5-2, NPSx-14.5-w). This further supports the previous interpretation as low frequencies that are often associated with fluid movement or hybrid rock/fluid flow (Benson et al., 2008). Similar hybrid and long-period seismic events have been reported during field scale hydraulic fracturing. Waveform data from fracking operations in the Barnett field, US, show a qualitatively similar overall signature (Das and Zoback, 2013) to AE data generated from experiments with conduits normal to bedding, with a short gradual build up and a short tail (Figure 6-7). During hydraulic fracturing experiments at Fenton Hill, New Mexico (Bame and Fehler, 1986; Ferrazzini et al., 1990) and at Montney, B.C., Canada (Eaton et al., 2013), similar hydraulic long-period events have also been recorded. This evidence provides not only clues as to the field-fracture direction, but adds confidence that laboratory data can be scaled to larger processes.

Source type (Tensile, Shear or Compression) analysis using first motion polarity of the waveform across the eleven channels revealed that tensile type events are dominant during the hydraulic fracturing of Nash Point Shale (Figure 6-8), as intuitively expected. This is consistent with post-test observations and micro-CT data. No obvious relative displacement, and a clear aperture between both fracture sides also indicate a dominant tensile fracture regime. However, at low confining pressures, tensile and shear events occur in almost equal

numbers, whereas with increasing confining pressure, tensile type events become more dominant. This is likely due to the higher level of micro fracturing at lower confining pressures, which tend to propagate at a shallow angle to the bedding. These data are consistent with observations by Chen et al. (2015), who identified such effects and demonstrated that shear type events were associated with fractures inclined towards the primary fracture direction.

Effect of viscosity on the mechanics of hydraulic fracturing

When comparing hydraulic fracturing using fluids with different viscosities, it becomes evident that hydraulic fracturing is dominantly controlled by coupled fluid-rock mechanics. The difference in viscosity allows for different degrees in fluid-rock interaction in terms of fluid infiltration into the rock matrix and fluid flow into the fracture. Due to the low permeability of both rock types and the high viscosity of the silicone oil, it was assumed that no fluid infiltration into the rock matrix would occur during pressurisation, with zero initial pore pressure. While breakdown pressures for NPS are similar for both water and silicone oil (32.36 and 26.36 respectively, Figure 5-1), COS oil-driven fracturing reached a significantly higher maximum fluid pressure (48.2MPa) compared to water-driven fracturing (32.3MPa) (Figure 5-1). Assuming that water infiltrates the sandstone more easily and faster than the silicone oil, the difference in breakdown pressures supports the previous interpretation that built-up pore pressures within the sandstone reduce the stress required to fail in tension resulting in premature failure of the sample. As there is no significant breakdown pressure difference in NPS, it can be assumed that pore pressures during the hydraulic fracturing with water at low to medium confining pressure are not sufficient within the shale samples to initiate pre-mature failure. Another indicator for the different fracture dynamic between oil and water-driven fracturing in NPS is the less instantaneous and slower pressure decay (pressure decay rate 21MPa/s (Figure 5-40b) compared to 625MPa/s (Figure 5-2b)) and the lack of an oscillation phase of the fluid pressure and AE activity (Figure 5-40a). The difference in the mechanical and seismic behaviour suggests that oil-driven fracture propagation in NPS is likely to be stable rather than unstable, as stress intensities, fracture propagation velocities and crack length required for the transition from stable to unstable fracture propagation are likely to have not been achieved. This interpretation is supported by observations of Zoback and Pollard (1978), who demonstrated that crack tip stress intensity depends on fluid viscosity and crack length. Accordingly, stress intensities at the crack tip reduce with increasing viscosity for constant crack lengths and increasing viscosities therefore prolong stable fracture propagation (Zoback and Pollard, 1978; Whittaker et al., 1992; Molenda et al., 2015). Here, the finite wall thickness has most likely contributed to the restriction of unstable fracture propagation, which might have been attained with increasing fracture length in samples with larger wall thicknesses. Further

evidence for the different fracture dynamics when using different viscosity fluids can be seen in the seismic signature. While the water-driven fracturing shows an impulsive emergent onset and a long harmonic, quasi-monochromatic coda (Figure 5-2), oil-driven fracturing exhibits impulsive seismic bursts (Figure 5-40), which indicates no or much less hybrid rock/fluid flow. This observation provides further support that fluid flow into the fracture is restricted due to the thin fracture aperture and high fluid viscosity, which results in lower stress intensities at the fracture tip and prevents unstable fracture propagation.

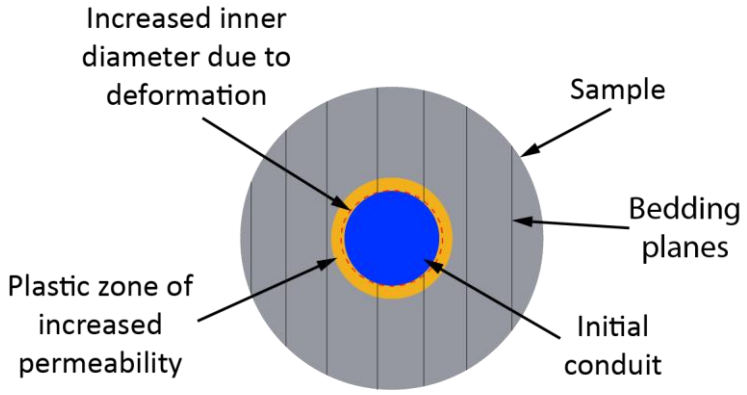

Figure 6-3: Schematic showing deformed conduit and plastic deformation zone with increased permeability. Larger deformation of conduit diameter normal to bedding planes.

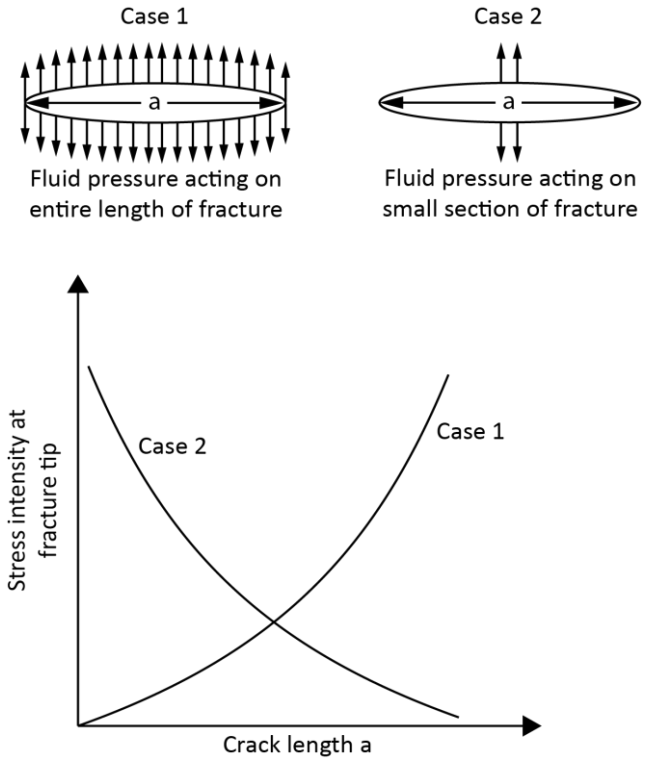

Figure 6-4: Schematic of fracture intensity dependence on crack length for cracks under internal fluid pressure acting over small section and entire length of crack. Figure modified from Zoback and Pollard (1978).

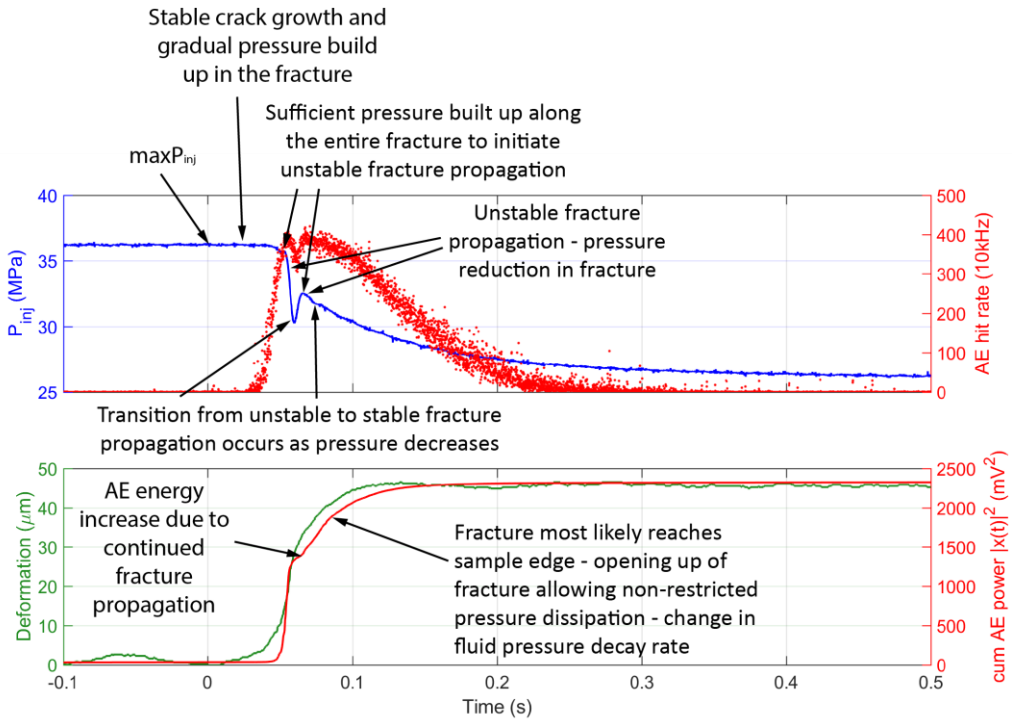

Figure 6-5: Interpretation of hydraulic fracturing process based on mechanical and seismic data (NPSx-25.4-w).

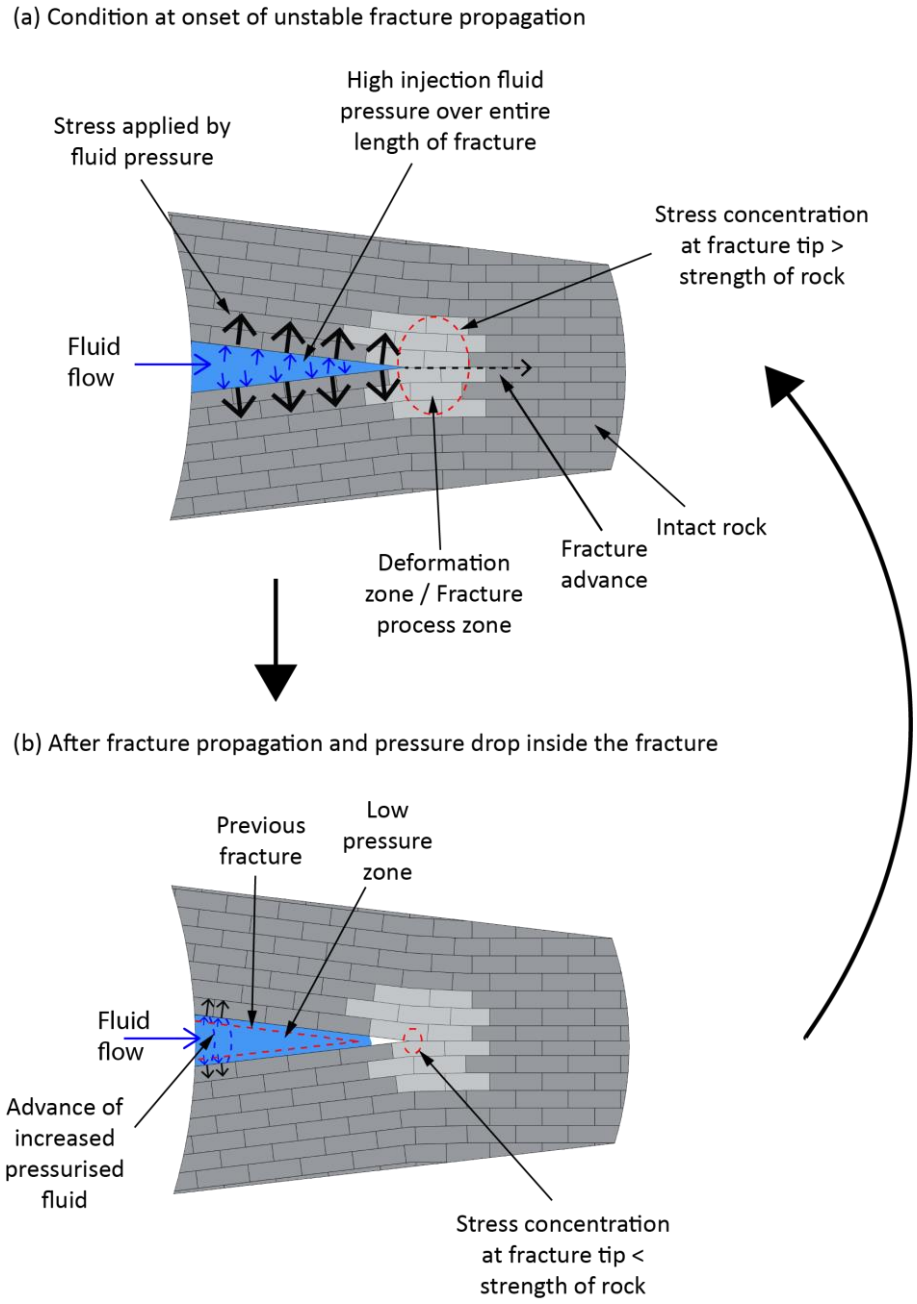

Figure 6-6: Conceptual model of incremental fracture propagation during hydraulic fracturing experiments with Nash Point Shale; (a) sufficient fluid pressure has built up along the entire length of the sample (blue arrows indicating fluid pressure and black arrows indicate stress applied on fracture walls) to generate the required stress at the fracture tip (large red ellipse at fracture tip) for unstable fracture propagation to occur with the result of fracture advance (dashed black arrow), (b) that increases the fracture volume and leads to a pressure drop inside the fracture (low pressure zone) as fluid flow cannot maintain the pressure, reducing the stress at the fracture tip and ultimately bringing the fracture advance to a temporary halt. Fluid inflow continues and pressure inside the fracture starts to build up again until condition (a) is reached. This cycle occurs multiple times during hydraulic fracturing experiments with Nash Point Shale.

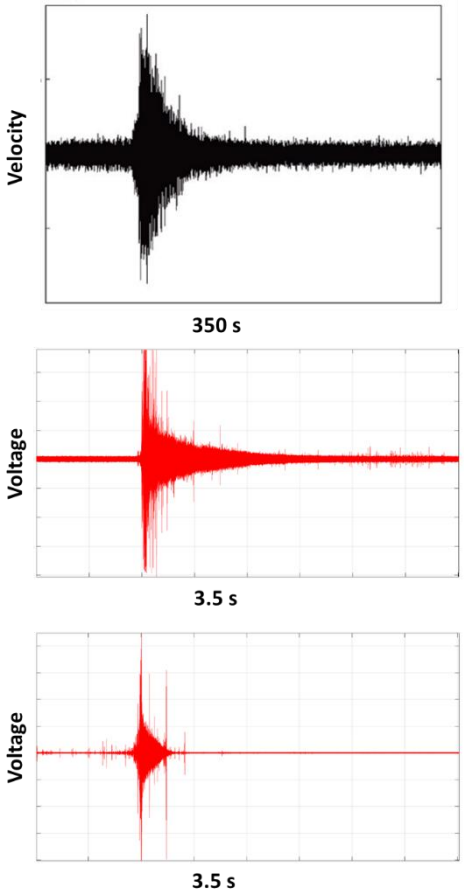

Figure 6-7: Qualitative comparison of field and laboratory seismic data; (a) Long-period events recorded during the treatment of a well in the Barnett play (Das and Zoback, 2013); (b) Events recorded during a laboratory hydraulic fracturing simulation in NPS at 15MPa confining pressure parallel to bedding; (c) Events recorded during a laboratory hydraulic fracturing simulation in NPS at 15MPa confining pressure normal to bedding. All three data sets show the main energy activity at low frequencies.

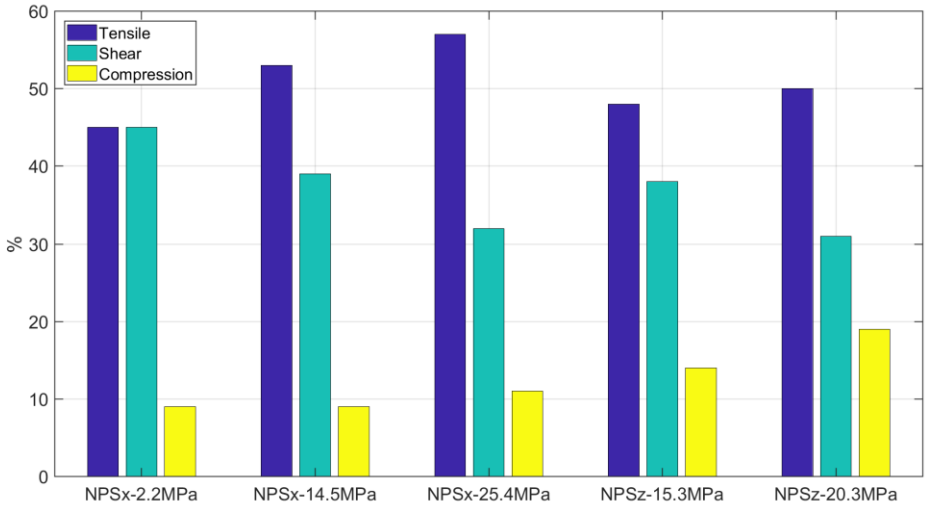

Figure 6-8: Overview AE source types during hydraulic fracturing of Nash Point Shale; data sets shown for parallel bedding (NPSx) and normal bedding (NPSz) at different confining pressures.

6.3. *Fracture geometries in low porosity sedimentary rock: effects of rock fabric on hydraulic fracturing and permeability enhancement*

The ultimate aim of hydraulic fracturing is to enhance extraction and flow rates from unconventional hydrocarbon reservoirs through the generation of hydraulic fractures. This new fracture conductivity, defined as the product of fracture permeability and fracture aperture, is a key indicator to evaluate the effectiveness of fracturing and plays a significant role in the evaluation of long term production of shale wells (Tan et al., 2018). However, fracture permeability depends on many factors like fracture compressibility, fracture roughness and fracture surface offset as well as effective stress and rock strength (Kassis and Sondergeld, 2010; Guo et al., 2013; Tan et al., 2018). Thus, it is important to understand the controls on fracture geometries and the ability to capture the evolution of hydraulic fracture conductivity under known laboratory conditions can provide key findings for reliable well performance analysis and optimizing fracturing design.

In tests with NPS parallel to bedding, the orientation of the new fractures, and therefore the new/enhanced permeability, is generally controlled by the orientations of the bedding planes which provide planes of weakness. Most of the specimens failed by axial splitting and generated more or less planar axial fractures parallel or sub-parallel to bedding planes (Short-Transverse orientation). In shale, fracture behaviour is often linked to rock composition, especially clay content. However, micro-CT data suggest a more likely relationship between ductility and the rock fabric, particularly the bedding planes. The bedding anisotropy can be described as rigid ‘sheets’ or ‘blocks’ glued together with a ductile material (Figure 6-9 a) so that sheets can move apart elastically. This means that fractures developing parallel to the inherent bedding rely dominantly on the strength of the bedding and follow these planes of weakness, only diverting when encountering lithic fragments (Figure 6-9a). The required stress for tensile failure is reduced due to elastic deformation in the deformation zone (Figure 6-9b and c), which likely promotes further fracture advance along the bedding plane.

In samples tested at low confining pressure, two fractures usually propagated from the conduit in diametrically opposite directions, whereas at higher pressures only a single fracture developed. Furthermore, it appears that the degree of micro fracturing decreases with increasing pressures, but the geometry and roughness of the primary fracture seems not to be influenced by the pressure, as no significant systematic differences were observed. Hydraulic fractures propagating normal to bedding showed a similar geometry, but with slightly more tortuous fracture geometries (Figure 5-27). Fractures normal to bedding interact with bedding planes to drive shear displacement on these bedding planes (Rutter and Mecklenburgh, 2017),

which can result in a more tortuous fracture path or a more complex fracture network as seen for sample NPSz-15.3-w (Figure 5-32). These observations suggest that confining pressure and the orientation of bedding planes have an influence on the developed fracture network and fracture geometry. This effect of the bedding planes on the fracture network is also seen in the fracture patterns observed during Brazilian tests on NPS (Figure 4-24). In addition, at higher confining pressures, the number of fracture propagation stages decreased, which is also likely to be associated with the fracture geometry. Micro-CT image analysis showed that with increasing confining pressure the number of primary fractures and the degree of micro fracturing decreased, which concentrated most of the fluid pressure on a smaller fracture volume resulting in a more localised fracture propagation.

Conversely, experiments using COS illustrate the effect of a different rock fabric in terms of grain size and matrix, as well as the influence of initial permeability. This is despite the fact that this rock has a similar porosity and a high inherent anisotropy. Despite a much higher tensile strength of the sandstone (8.6 MPa compared to 4.7 MPa in the NPS), hydraulic fractures initiate at similar pressure as NPS and are not significantly affected by bedding orientation (17.9 MPa parallel and 13.9 MPa normal to bedding). The relatively low breakdown pressures are a result of reduced tensile strength of the rock, via a combination of deformation and built-up pore pressures (Figure 6-9e and f). Depending on the baseline (pre-fracture) permeability, pore pressure is built up faster and over a more extensive area ahead of the fracture in COS due to a slightly higher permeability, resulting in lower fracture initiation pressures. Similar fracture initiation pressures for both bedding orientations suggest that fracture initiation in the Crab Orchard Sandstone is less influenced by bedding planes and their orientation. In addition, the onset of fracture in the COS appears to occur at a similar time as maximum fluid injection pressure and in combination with radial deformation, which also starts to change at the time of maximum fluid pressure, indicates little or no deformation occuring prior to fracture initiation. This suggests a more brittle behaviour in Crab Orchard Sandstone as compared to Nash Point Shale. COS exhibits a different fracture dynamic than seen in NPS. The longer delays between fracture initiation and sample breakdown seen in the sandstone experiments compared to shale indicate a prolonged subcritical and stable crack development, prior to unstable fracture propagation. Subsequently, the connecting of pre-existing pores along the fracture path in the sandstone effectively enlarges the fracture aperture (Zoback et al., 1977) allowing for the pore fluid supply to keep up with the fluid demand in the fracture. This results in a much smaller pressure decrease compared to NPS, promoting fracture propagation to the edge of the sample without the oscillatory behaviour seen in the NPS where fracture advance outpaced the fluid.

Additionally, the COS experiments showed that the fracture mechanism is also effected by the rock fabric and inherent permeability. Whereas in the shale, tensile type events dominate, the hydraulic fracturing of COS is dominated by shear and compressional events and only a minor part is of tensile character (Figure 6-10). This agrees with observations from hydraulic fracturing field operations in tight sandstone, where shear type failure events dominated during fracturing (Warpinski et al., 2004; Dusseault, 2013). The shear and compression type events are likely to occur on the fracture flanks resulting from increased pore pressures and fluid infiltration, whereas tensile type events are generated at the fracture tip, due to the tensile stresses ahead of the fracture tip. Increased pore pressures along the fracture walls aid stick-slip shearing, which generate microseismic acoustic emissions (Dusseault, 2013).

The fracture pathway in COS is significantly influenced by the rock fabric and discontinuities (Figure 6-9d). Here, induced fractures take the path of least resistance along grain boundaries and through pre-existing pores, and are apparently not influenced by bedding planes and their orientation. This is likely also due to the cementation in the sandstone, which is not present in the shale. The higher tortuosity (Figure 5-35) of hydrofractures in the sandstone results from the correlation of grains and pre-existing pores in the sandstone. These heterogeneities may modify the stress field near the crack tip and affect the propagation direction, forcing the fracture to divert and develop a diffuse fracture geometry that strays significantly from a straight plane. In all samples, one radial fracture developed with a complex network of micro fractures, adding to the complexity of the fracture network on a micro scale and the surface area of the fracture. These observations suggest that hydraulic fracturing in COS is controlled by the initial permeability, and at a micro-scale by grain-bond strength and grain-cement boundaries (Figure 6-9d). However, at the macro-scale the bedding planes still influence the overall propagation direction of the fracture as they tended to propagate parallel to the bedding (with deviations).

Permeability of Nash Point Shale after hydraulic fracturing: new data

To directly measure the fluid flow properties of the newly developed fracture (permeability), a novel protocol was employed described in Chapter 3.6 to measure *in-situ* flow rate as a function of confining pressure. At an effective pressure of 2.5MPa a permeability of $1.9x10^{-15}m^2$ (≈2mD) has been determined (Figure 5-50), which is equivalent to a crack aperture of approximately ≈20µm. This is again consistent with post-test measurements using micro-CT. Compared to initial permeability data on fresh (non-fractured) intact Nash Point Shale samples of the order $10^{-18}m^2$, this represents an enhancement of three orders of magnitude. This is consistent with permeability increases measured in other studies (Bernier et al., 2007; Guo et al., 2013). To account for measurement errors and elastic effects, permeability values have

been calculated for a range of initial crack apertures (Figure 6-11), covering the range of apertures observed during this study (10-60µm), and using the fluid flow data measured by the voluometer system. However, this range of apertures does not significantly change the overall trend of magnitude of the equivalent permeability, which ranges from 0.6 to $3.8x10^{-15}m^2$ and is within the same order of magnitude. Over an effective pressure range from 2MPa to 19MPa, permeability decreases by one order of magnitude, highlighting the pressure dependency of fracture permeability which ultimately controls the performance of the stimulation and demonstrates the importance of proppants for an economical flow rate. Fracture permeability decreases quickly under increasing pressure because of two factors: decreasing aperture and increasing resistance to flow through the fracture (Walsh, 1981).

Resistance to flow through the fracture may be attributed to a range of factors such as viscous drag of the fluid in the narrow openings between the two fracture surfaces, and by the tortuosity of the flow path. In addition, under increasing confining pressure, the aperture decreases and the resistance to flow increases due to the smaller cross-sectional area, but also because the number of points and the area of contact between asperities of the opposing fracture surfaces increases, which leads to an increase in flow resistance due to the longer and more tortuous fluid path (Kranz et al., 1979). This is seen here (Figure 5-50 and Figure 6-11) at approximately 14MPa effective pressure where the trend in the permeability decrease changes abruptly, likely due to asperities. At low confining pressures, the contact area is relatively small and allows for a relatively fast fracture closure. With increasing contact area, fracture closure is increasingly inhibited by asperities that acts to decrease the closure rate. This is consistent with the observation by Kassis and Sondergeld (2010) that fracture offset is equally as effective in maintaining fracture permeability as proppants. Upon release of confining pressure, fracture permeability only recovers slightly, leaving a permanent reduction of permeability. This phenomena is known as hysteresis, a permanent reduction in permeability due to high stresses, and has also been observed in the laboratory by Kranz et al. (1979) in granite and by Gehne and Benson (2017) in Crab Orchard Sandstone (Figure 4-19) as part of this study. Fracture permeability depends on many factors such as the net stress on the fracture, fracture compressibility, the degree of secondary mineralization within the fractures, fracture roughness and fracture surface offset (Aguilera, 2006). This data shows the evolution of hydraulic fracture conductivity under known laboratory conditions, which provides a good understanding of the enhanced permeability after fracturing for a specific reservoir rock.

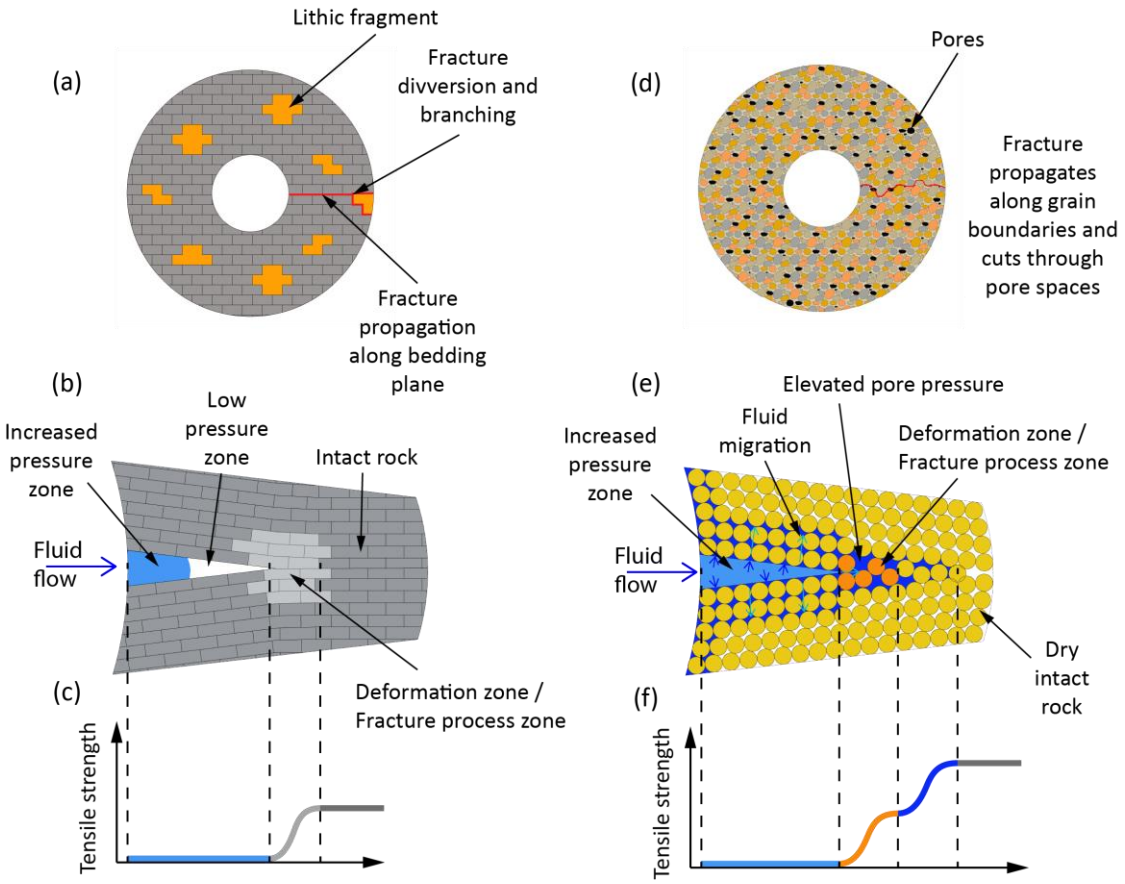

Figure 6-9: Conceptual model showing the interaction of rock fabric and inherent bedding planes on the fracture path and fracture network; (a) NPSx - Fracture develops along bedding plane but diverts or bifurcates when encountering lithic fragments in the path, (b) NPSx - Schematic diagram of an HF-induced tensile fracture propagation showing no pressure and deformation zone, (c) NPSx - Tensile strength; (d) COSx – Fracture path depending on rock fabric, developing along grain boundaries and through cement, (e) COSx - Schematic diagram of an HF-induced tensile fracture propagation showing zone of increased pore pressure due to fluid migration and (f) COSx - Tensile strength.

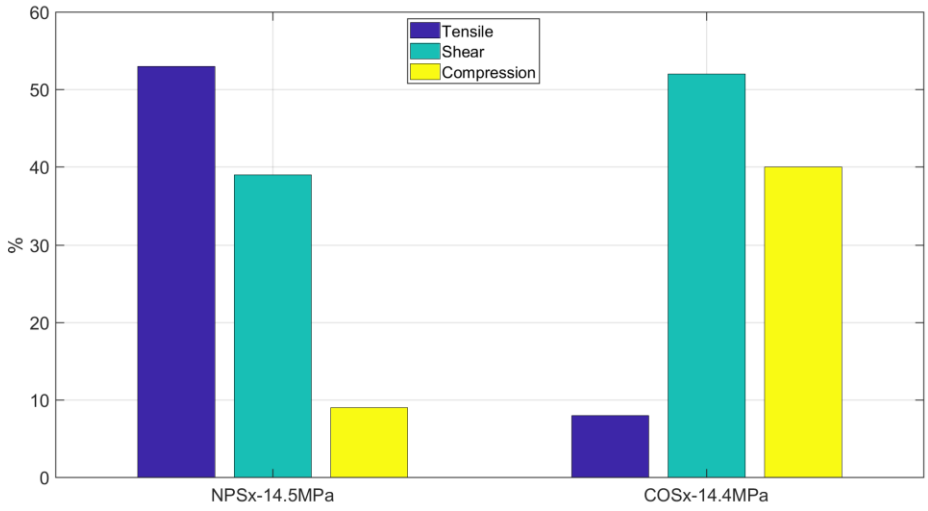

Figure 6-10: Overview AE source types during hydraulic fracturing of Nash Point Shale and Crab Orchard Sandstone (both parallel bedding).

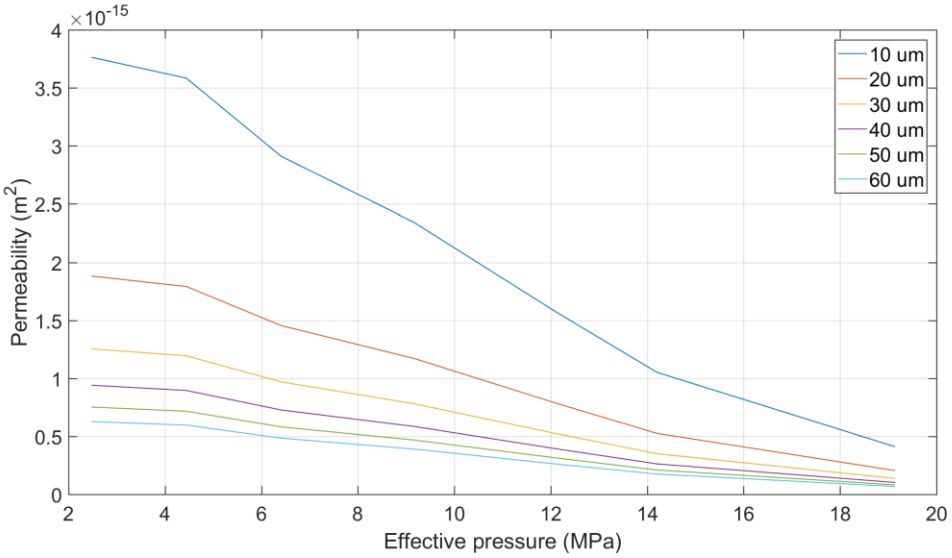

Figure 6-11: Permeability after hydraulic fracturing treatment vs effective pressure for a range of initial apertures between 10 to 60µm.

6.5. Hydraulic fracturing criteria applied to experimental data

The maximum fluid injection pressures at failure across all experiments are plotted as a function of confining pressure in Figure 5-1. For both rock types and bedding orientations, a common trend is evident. Namely, a general trend of increasing pressure of specimen breakdown with increasing confining pressure with the highest values determined for NPS with the bedding normal to the coring axis. This relationship between breakdown pressure and confining pressure has been shown by many studies, often using a linear approximation (Hubbert and Willis, 1957; Haimson and Fairhurst, 1969b; Brenne et al., 2014). However, the laboratory data here suggest a more complex variation, at least in the case of NPS. For shale samples with the bedding parallel to the coring axis, breakdown pressures as a function of confining pressures ranging from 0-25MPa are shown in Figure 6-12. A break in slope is evident at approximately 15 MPa which becomes more apparent when plotting the internal fluid overpressure ($P_{Einj}=P_{inj} - P_c$) against confining pressure (Figure 6-13). These data suggest that hydraulic fracturing behaviour of NPSx can be described as a two stage process with a peak breakdown pressure at 15MPa. At lower confining pressures, the required fluid pressure increases faster with increasing pressures (gradient ≈ 1.9) compared to higher confining pressures above 15MPa (gradient ≈-0.3), suggesting two competing processes which define the overall response. The positive regression intercepts with the breakdown pressure axis at about 3.5MPa, reflecting breakdown pressures without any confining pressure and corresponds to an apparent tensile strength of the rock of 4.3MPa. This is well within the range of tensile strength values of the rock (Figure 6-1) and confirms the validation of the relationship.

The interpretation of breakdown pressures has been the subject of many discussions, which lead to the development of several breakdown criteria for fluid-driven fracturing, including the linear-elastic (LE) model proposed by Hubbert and Willis (1957) (equation 2-30), the poro-elastic (PE) model from Haimson and Fairhurst (1967) (equation 2-32), and the fracture mechanics based (FM) model proposed by Abou-Sayed et al. (1978) (equation 2-33). These failure criteria are often used to predict the critical fluid injection pressure to initiate hydraulic fracturing. Here, these models are applied to understand and explain the behaviour of the rocks during hydraulic fracturing, especially the non-linear behaviour of the shale. First, the linear-elastic and poro-elastic models are applied, which are based on the tensile strength of the material. Since pore pressures inside the specimen are unknown, the two limiting cases of zero pore pressure (black dashed line) and a pore pressure equal to injection pressure (red dashed line), i.e. the specimen breakdown pressure, are considered. Further input parameters are the average Brazilian disk tensile strength and the Poisson's ratio. The Biot's coefficient

α=0.5 is used as an estimate for the shale. Rock properties used for the models are summarised in Table 6-1.

Table 6-1: Properties of Nash Point Shale and Crab Orchard Sandstone

Property	NPSx	NPSz	COSx
Static Poisson's Ratio	0.39 (Forbes Inskip et al., 2018)	0.06 (Forbes Inskip et al., 2018)	0.31
K_{IC} (MPa.m$^{1/2}$)	0.24 (Forbes Inskip et al., 2018)	0.71 (Forbes Inskip et al., 2018)	0.45 (Atkinson, 1979b)
Average tensile strength (MPa)	4.73	8.82	8.57
Biot's poroelastic parameter α	0.5	0.5	0.75 (Atkinson, 1979b)

Figure 6-14 shows the comparison of the experimentally determined maximum fluid injection pressures and predicted breakdown pressures using the linear-elastic (left panel) and poro-elastic models (right panel) for Nash Point Shale parallel bedding. The experimental results plot dominantly in-between the limiting cases (zero pore pressure and pore pressure = P_{inj}) in the Hubbert & Willis (linear-elastic) model (Figure 6-14, left). The poro-elastic model (Figure 6-14, right) underestimates the breakdown pressure for both pore pressure scenarios. For confining pressures below 15MPa, the linear-elastic impermeable scenario seems to be the better correlation, which has a similar gradient as determined for Nash Point Shale data over that pressure range (2 and 1.9 respectively). The fact that the apparent tensile strength (intercepts of fitted curve Figure 6-12) is in agreement with strength values derived from Brazilian tests (no fluid) further supports the assumption of no sufficient fluid infiltration. However, some minor fluid infiltration might occur, but without a significant effect on the strength of the rock. At higher confining pressures, the experimental data diverts from the impermeable scenario. This suggests, that at higher confining pressures, significant fluid infiltration into the shale matrix occurs and poro-elastic effects influence the fracture process. The increased fluid infiltration could either be a function of the time the fluid pressure is applied to the conduit wall or the magnitude of the injection fluid pressure, meaning that fluid infiltration commences at a sufficient differential pressure between fluid pressure in the conduit and pore pressure in the rock matrix. The data for Nash Point Shale parallel bedding indicate that the linear-elastic theory (Chapter 0) is valid for lower confining pressures, but poro-elastic effects need to be considered for higher confining pressures.

The experimental data for NPS normal bedding indicates a more linear increase in the tested confining pressure range compared to NPSx. But not enough experiments were conducted for NPSz to confidently evaluate the maxP_{inj}-P_c relationship and more experiments are required. However, both pressure prediction models (zero pore pressure) underestimate the required fluid injection pressure (Figure 6-15), which demonstrates that rock properties such as anisotropy also need to be considered in the failure model for hydraulic fracturing.

Confining pressure has a linear influence on the specimen breakdown pressures for Crab Orchard Sandstone in the pressure range 0-25MPa with a gradient of about 1.8 (Figure 6-16). The linear function intercepts with the breakdown pressure axis at about 2.8MPa, which corresponds to an apparent tensile strength of the sandstone of 3.4MPa. This is much lower than the average tensile strength of the sandstone (8.6MPa) derived from Brazilian disk experiments (Figure 4-23). Figure 6-17 shows the comparison of the experimentally determined and predicted breakdown pressures using the linear-elastic and poro-elastic models for Crab Orchard Sandstone parallel bedding. Considering the linear-elastic model (Figure 6-17, left panel), the data plots within the two pore pressure scenarios. The poro-elastic model (Figure 6-17, right panel) underestimates the injection pressure at higher confining pressures, but at pressures below 10MPa, the experimental data plots within the two limiting cases. The linear-elastic model yields a better prediction of breakdown pressure for Crab Orchard Sandstone, but pore pressure needs to be considered to account for the higher permeability of the sandstone (compared to the shale). Figure 6-18 shows the linear-elastic model for Crab Orchard Sandstone for a range of pore pressures and it can be seen that pore pressures approximately between 5 and 15 MPa have been present inducing early hydraulic fracturing in the Crab Orchard Sandstone according to the linear-elastic model. From the comparison of the experimental and modelled data it can be inferred that pore pressures build up within the sandstone during pressurisation, but not to the same level as P_{inj}, which would require a much higher permeability. The pore pressures reduce the effective stress and hence causing premature fracture initiation, explaining the discrepancy to the impermeable scenario and the low apparent tensile strength (intercepts of fitted curve Figure 6-16) compared to the tensile strength derived from Brazilian tests (no fluid) (Figure 4-23). However, the data suggest that the continuum elastic theory (Chapter 0) is valid over the tested pressure range for Crab Orchard Sandstone parallel bedding.

Predicted breakdown pressures have also been calculated using the fracture mechanics approach to explain the non-linear behaviour of Nash Point Shale parallel bedding. These models include the fracture toughness of the rock material (K_{IC}) and an initial flaw length (a_0) measured from the conduit wall, where fracture initiation behaviour is controlled not by the

typical but the maximum length of initial fractures connected to the conduit. Under isostatic conditions ($\sigma_{hmin} = \sigma_{Hmax} = P_c$) and the assumption that a_0 << r_i, the fracture mechanics model (equation 2-33) (Abou-Sayed et al., 1978) can be written as

$$P_b = P_c + \frac{K_{IC}}{1.2 * \sqrt{\pi a_0}} \qquad 6\text{-}1$$

where P_b is the breakdown pressure and P_c confining pressure. The average Mode I fracture toughness for the Nash Point Shale Short-Transverse direction is 0.24MPa.m$^{1/2}$ (Forbes Inskip et al., 2018). The initial length of pre-existing flaws is considered as an unknown variable. Thus, the curves are given for a range of initial fracture length a_0 in Figure 6-19a. The experimental data for Nash Point Shale plots in the range of initial fracture length from 0.05mm to slightly more than 1mm (Figure 6-19a), which seems reasonable considering the very fine grain size of the shale. Figure 6-19b plots the required breakdown pressure as a function of the initial flaw length a_0 for a range of confining pressures. Indicative initial flaw length were calculated for the experimental results as confining pressure and the critical fluid pressure is known and also plotted in Figure 6-19b. From the experimental data it can be seen that with increasing injection and confining pressure, the critical flaw length reduces. For most of the experiments, the critical flaw size lies between 0.05 and 0.5mm, which could be taken as the material specific initial flaw length for Nash Point Shale parallel bedding. It seems that the initial flaw size a_0 decreases with increasing injection and confining pressure, but shows a clear break at about 15MPa. Therefore, fracture mechanics do not give a clear explanation for the non-linear behaviour of the shale. This is another indicator that at this point (≈15MPa), an additional parameter starts to influence fracture initiation significantly and further supports the previous interpretation of an increasing effect of fluid infiltration and pore pressures. The fracture mechanics model has also been compared with experimental data from Crab Orchard Sandstone samples with parallel bedding (Figure 6-20). The experimental data plots between initial flaw lengths of 0.08 to 1.7mm (Figure 6-20a), which is longer than the calculated lengths in the shale. This is reasonable as the sandstone also has a larger average grain size. The required initial flaw size decreases with increasing confining pressure and no break has been observed (Figure 6-20b).

Comparing the results of all the three models (linear-elastic, poro-elastic and fracture mechanics), the linear-elastic model provides the best fit to the experimental data. However, pore pressures need to be considered to derive reasonable breakdown pressure predictions

and these pore pressures need to be a function of the initial permeability of the rock as well as confining pressure.

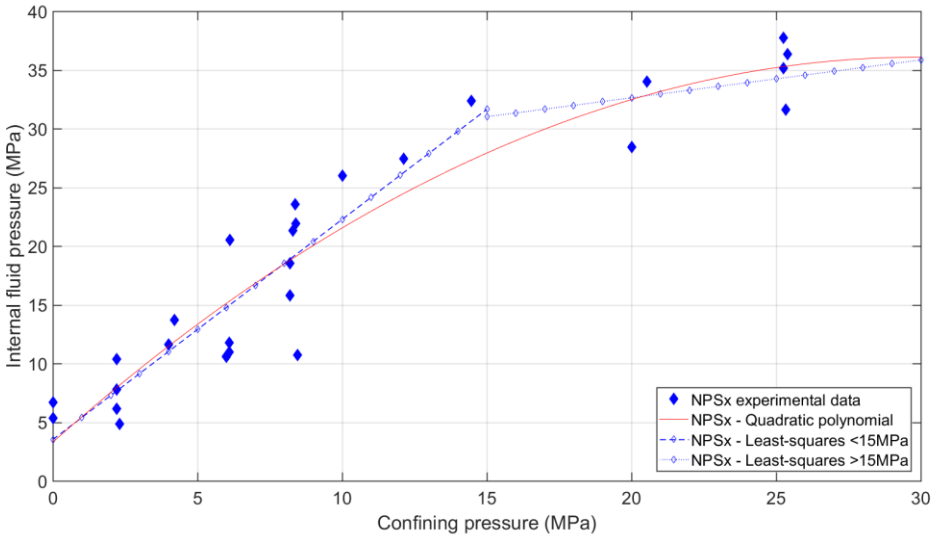

*Figure 6-12: NPSx – Maximum fluid **injection pressure** vs confining pressure including least-squares fit and quadratic polynomial fit curves.*

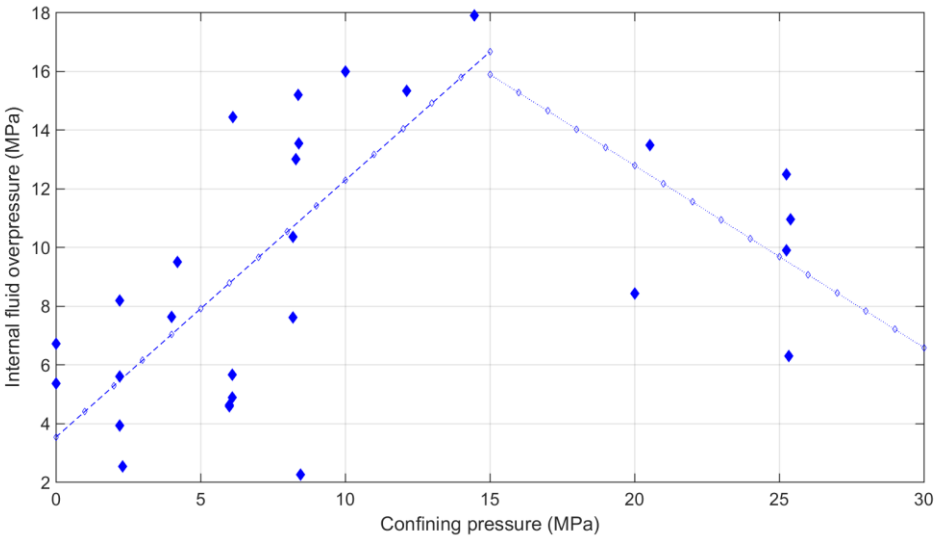

*Figure 6-13: NPSx – Maximum fluid **overpressure** vs confining pressure including least-squares fit curves for <15MPa and >15MPa confining pressure.*

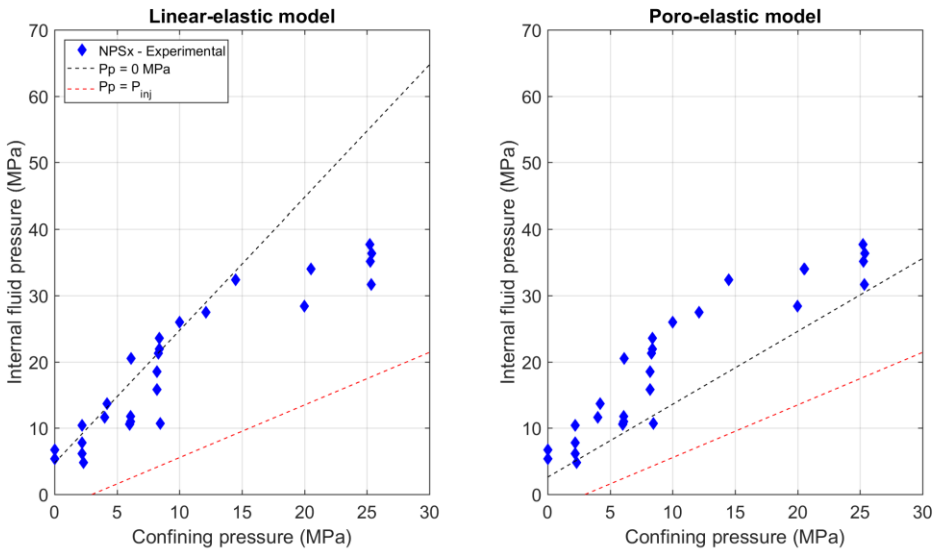

Figure 6-14: NPSx – Comparison of maximum fluid injection pressures determined from hydraulic fracturing experiments and breakdown pressures calculated with the linear-elastic (equation 2-30) (left) and poro-elastic model (equation 2-32) (right). Pore pressure inside the rock matrix was assumed to be zero (black dashed line) and equal to the injection pressure (red dashed line).

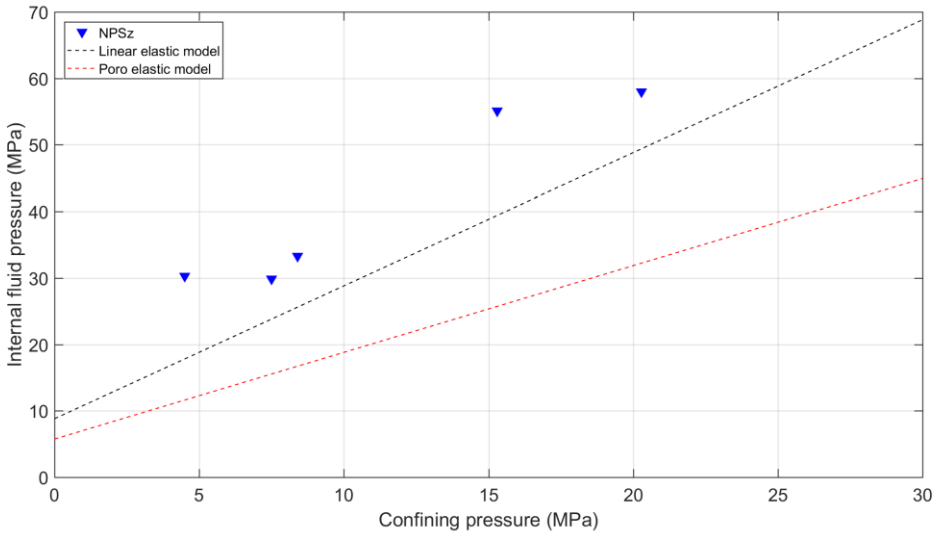

Figure 6-15: NPSz – Comparison of maximum fluid injection pressures determined from hydraulic fracturing experiments and breakdown pressures calculated with the linear-elastic (equation 2-30) and poro-elastic (equation 2-32) model. Pore pressure inside the rock matrix was assumed to be zero.

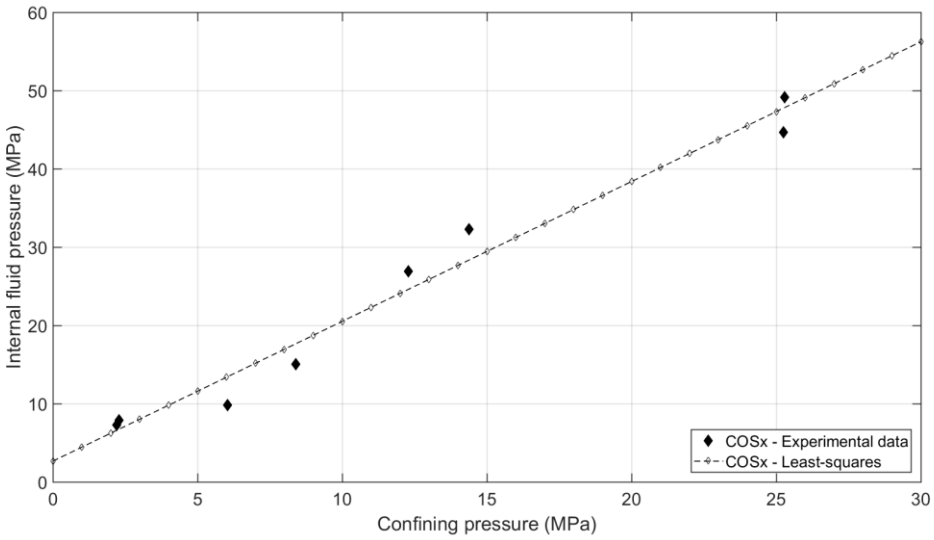

Figure 6-16: COSx – Maximum fluid injection pressures vs confining pressures with a linear relationship for the Crab Orchard Sandstone parallel bedding.

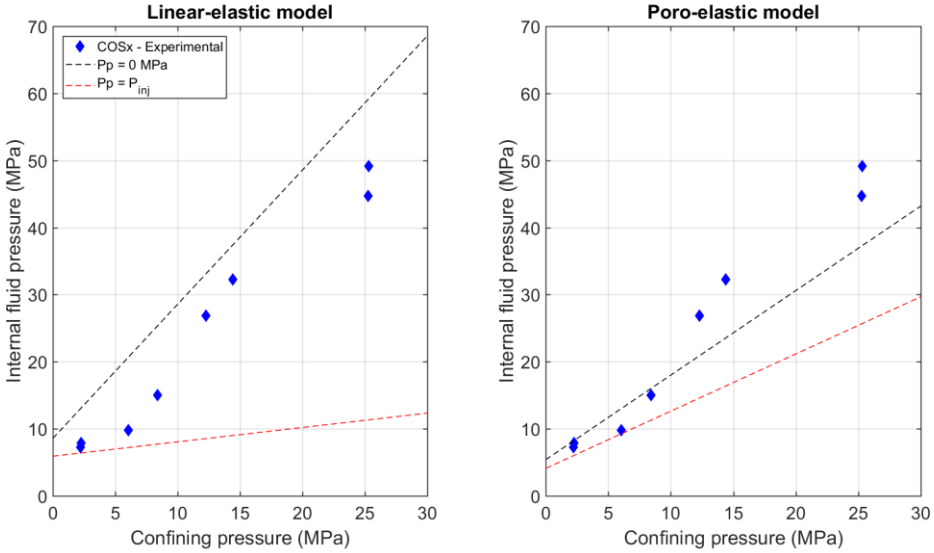

Figure 6-17: COSx – Comparison of maximum fluid injection pressures determined from hydraulic fracturing experiments and breakdown pressures calculated with the linear-elastic (equation 2-30) (left) and poro-elastic model (equation 2-32) (right). Pore pressure inside the rock matrix was assumed to be zero (black dashed line) and equal to the injection pressure (red dashed line).

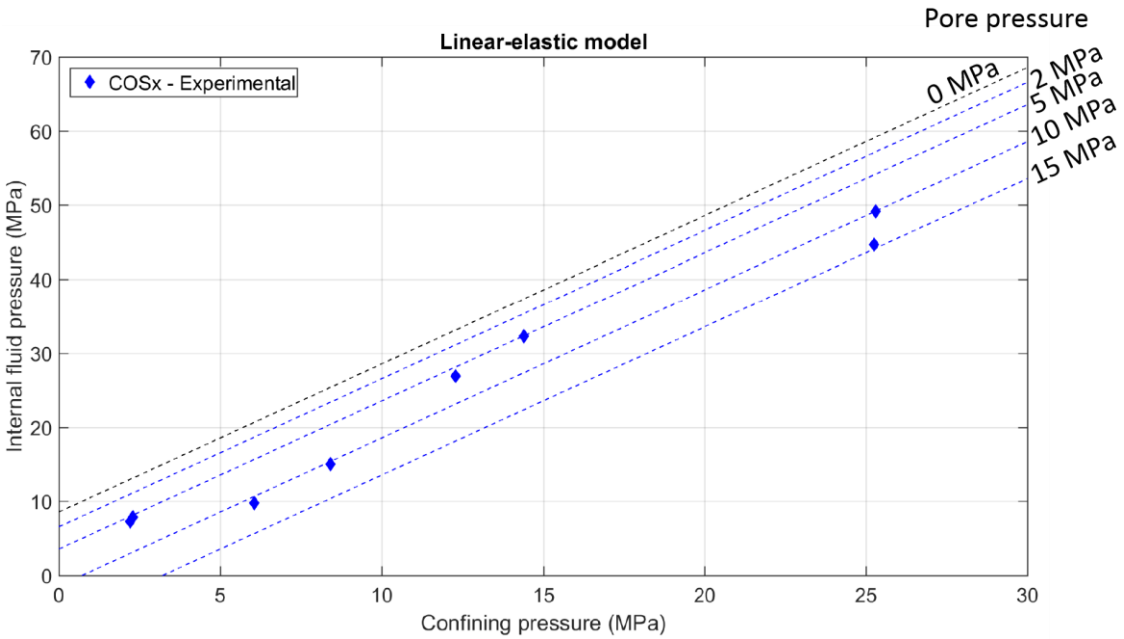

Figure 6-18: COSx – Linear-elastic model for Crab Orchard Sandstone for a range of pore pressures.

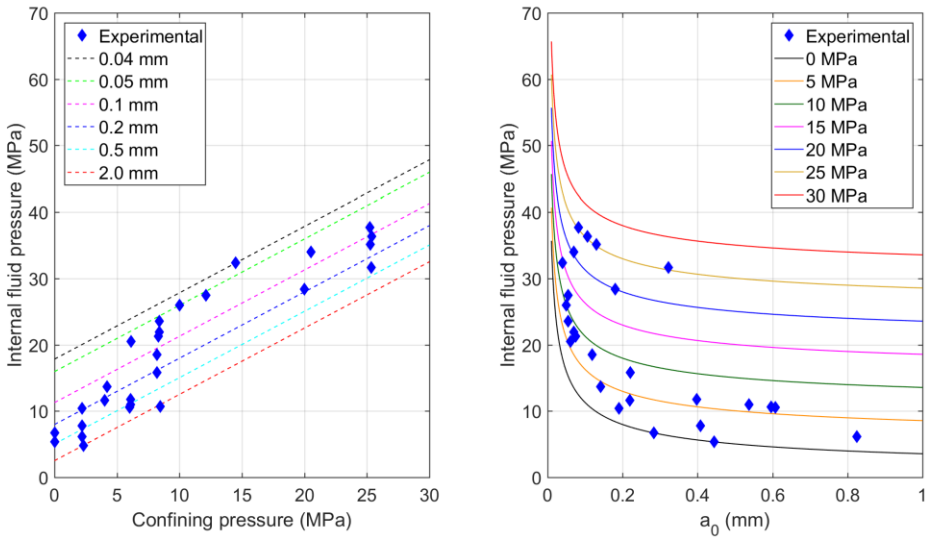

Figure 6-19: Comparison between experimental data from hydraulic fracturing experiments of Nash Point Shale parallel bedding and predictions from fracture mechanics model (Abou-Sayed, 1978). (left) The model results are plotted for a range of initial fracture length a_0 (0.04-2mm) and the fracture toughness KIC was determined in semi-circular bend tests (Forbes Inskip et al., 2018); (right) Critical fluid injection pressures for fracture propagation as a function of initial flaw length a_0. The model results are plotted for a range of confining pressures (0-30MPa). Initial flaw sizes were calculated for the experimental results and also plotted.

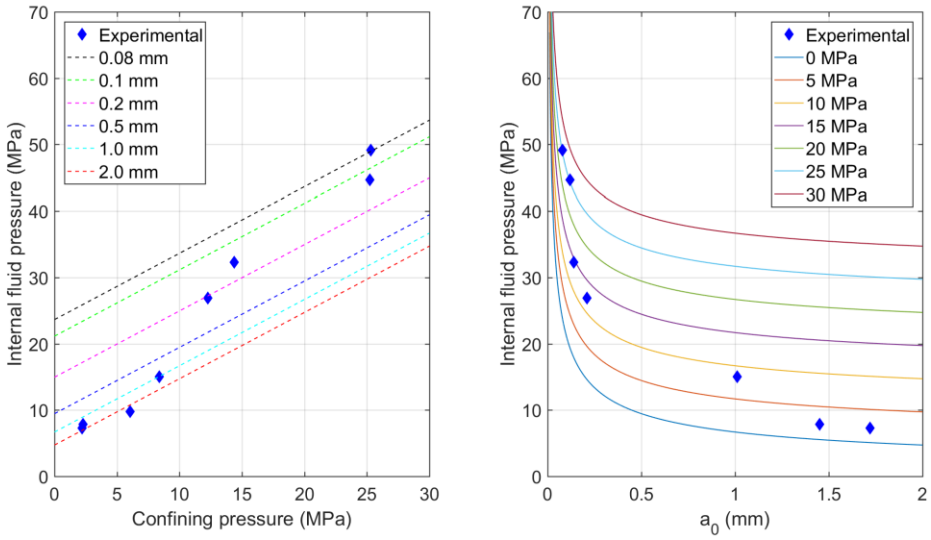

Figure 6-20: Comparison between experimental data from hydraulic fracturing experiments of Crab Orchard Sandstone parallel bedding and predictions from fracture mechanics model (Abou-Sayed et al., 1978). (left) The model results are plotted for a range of initial fracture length a_0 (0.08-2mm) and the fracture toughness K_{IC} was determined in double torsion experiments (Atkinson, 1979b); (right) Critical fluid injection pressures for fracture propagation as a function of initial flaw length a_0. The model results are plotted for a range of confining pressures (0-30MPa). Initial flaw sizes were calculated for the experimental results and also plotted.

6.6. Fracture toughness at elevated pressures for Nash Point Shale

From the interpretation of the different models, it became apparent that the continuum models based on the tensile strength of the rock material yield good predictions of the breakdown pressure for the shale. This suggests that the fracture initiation pressure can be associated with the tensile strength of the rock at elevated pressures. The fracture toughness on the other hand is more likely represented by the observed oscillation of the fluid pressure during the shale experiments and the oscillation peaks could be interpreted as the effective fracture toughness of Nash Point Shale at elevated pressures.

Based on these finding, a new approach is applied to analyse fracture toughness of the shale at elevated pressures using the pressures of the oscillation peaks and the total AE energy as an indicator for fracture advance. Accurate AE event localisation would be the obvious choice to determine the initial fracture length at each oscillation peak to calculate fracture toughness. Unfortunately, it was not possible within this study to accurately locate AE events. Therefore, a different approach has been used to approximate fracture advance at each propagation stage, based on the assumption that fracture advance is proportional to the released AE energy. The concept is illustrated in Figure 6-21. The fluid injection pressure at each oscillation peak is assumed to represent the required pressure acting over the entire length of the crack to further advance the existing crack, whereas the troughs of the oscillation indicate the point of halt of fracture propagation. Only peaks associated with recognisable changes in AE energy rate and /or AE hit rate were considered. The initial flaw length, before the first fracture advance is calculated using the fracture mechanics based model (Abou-Sayed et al., 1978) (Figure 6-19).

The total crack length (measured from the conduit wall) for each successive fracture advance is inferred from the total AE energy released under the assumption that fracture advance is proportional to the released total AE energy. The cumulated AE energy at the oscillation trough relative to the total released energy when the fracture reaches the outer edge of the sample is therefore used to determine the fracture length at this point via the following relationship:

$$\frac{cumulative\ AE\ energy\ at\ oscillation\ trough}{Total\ cumulative\ AE\ energy} = \frac{a_0}{(r_o - r_i)} \qquad 6\text{-}2$$

where a_0 is the fracture length at the start of each fracture advance (measured from the conduit wall) and r_o and r_i are the outer and inner radius of the sample. The initial AE energy is equal to the energy at fracture initiation. The point where the fracture reaches the sample edge is derived by a combined interpretation of fluid injection pressure, radial deformation, AE

activity, and AE energy over time. Often a combination of change in fluid pressure decay, AE hit rate change and/or a decrease of the total AE energy curve increase allows for a reasonable estimate of the end of fracture propagation. Micro-CT images showed dominantly planar and single fractures for the shale, which allows for the assumption that fracture propagation occurs radially along a vertical plane. An *effective* fracture toughness (eK_{IC}) can be calculated using equation 2-33, which rearranged for eK_{IC} gives:

$$eK_{IC} = \left(P_{inj} - P_c\right) * \left(F\left(\frac{a_0}{r_i}\right) * \sqrt{\pi * a_0}\right) \qquad 6\text{-}3$$

where P_{inj} is the fluid injection pressure, P_c the confining pressure and a_0 the length of the initial crack.

Samples with normal bedding showed fewer oscillations compared to samples with parallel bedding. This could be due to a higher apparent stiffness in normal bedding samples. Effective fracture toughness has been determined for several experiments in both bedding directions (S-T and Div) to evaluate the effect of elevated confining pressure. The detailed analyses including labelled diagrams as well as overview tables stating fracture propagation pressure, fracture length and effective fracture toughness for each fracture advance stage can be found in Appendix A.9. Comparing the values of the Short-Transverse orientation (parallel bedding) and Divider orientation (normal bedding), it shows that the Divider values are about two to three times higher (Figure 6-22). This is a similar ratio as seen for ambient fracture toughness as well as tensile strength values and breakdown pressures (Figure 6-2) comparing the two fracture orientations.

Effective K_{IC} – values determined here and the increase with increasing confining pressure (below 15MPa) are slightly higher compared to fracture toughness values determined in other experimental studies (Abou-Sayed, 1978; Winter, 1983; Stoeckhert et al., 2016) for sandstone, limestone and slate. However, fracture toughness values obtained from field hydraulic fracturing operations are orders of magnitudes higher than those experimentally derived (Thallak et al., 1993). These differences are associated with the higher complexity of the process in the field induced by fluid flow into the fracture and the rock matrix. Thallak et al. (1993) suggested that the fluid flow into the fracture and the rock matrix factors dominate the hydrofracture performance. Therefore, eK_{IC}-values obtained here reflect the complexity of the fracturing process including fluid flow through the fracture and into the rock matrix. Effective fracture toughness results for Nash Point Shale show a positive linear relationship (Figure 6-22)

between fracture toughness and confining pressure for confining pressures below 15MPa, which has also been demonstrated for sandstone and limestone (Abou-Sayed, 1978; Winter, 1983), and shows the pressure dependency of the fracture toughness. However, at confining pressures above 15MPa, a negative relationship has been observed between fracture toughness and confining pressure. This indicates that the effective fracture toughness at elevated confining pressures is influenced by built-up pore pressures in the same way as the tensile strength of the rock. Therefore, sufficient pore pressures inside the rock matrix reduce the fracture toughness of the rock and hence promote fracture propagation. Support for this interpretation is provided by Nie et al. (2017), who demonstrated that fracture toughness of water-saturated sandstones was reduced by 30-50% compared to dry samples.

Furthermore, the fracture advance is also proportional to the absolute difference of consecutive oscillation peaks. Sequential oscillation peaks of similar magnitude indicate a short fracture advance whereas large differences indicate a longer fracture advance. However, it seems that the effective fracture toughness values calculated here are a reasonable estimate of the fracture toughness of Nash Point Shale at elevated pressures. The linear relationship between effective fracture toughness and fluid overpressure could be used to predict more reliable breakdown pressures for field operations as current hydraulic fracture criteria often underestimate the breakdown pressures seen in the field.

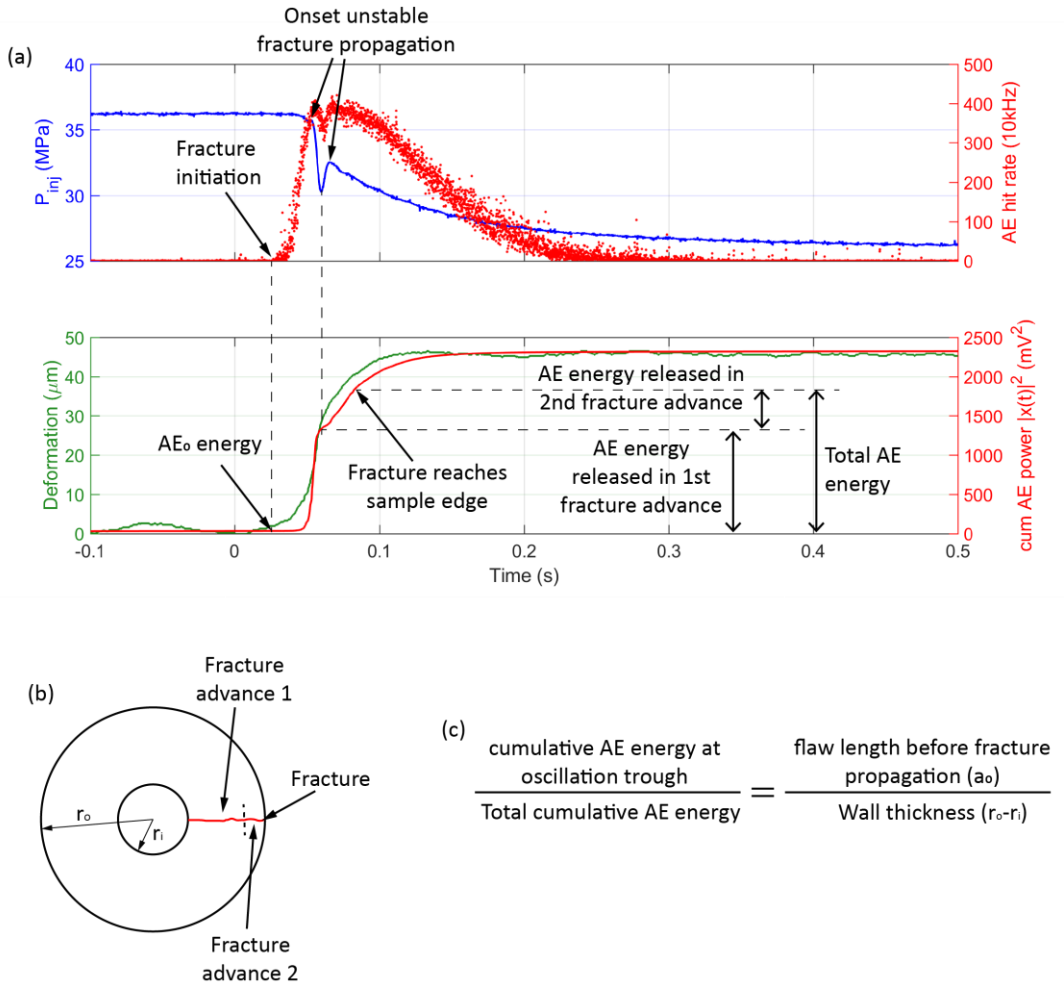

Figure 6-21: Concept of effective fracture toughness calculation from thick walled cylinder experiments at elevated pressures in Nash Point Shale; (a) experimental data and interpretation, (b) sample geometry and fracturing stages and (c) relationship AE energy and fracture length.

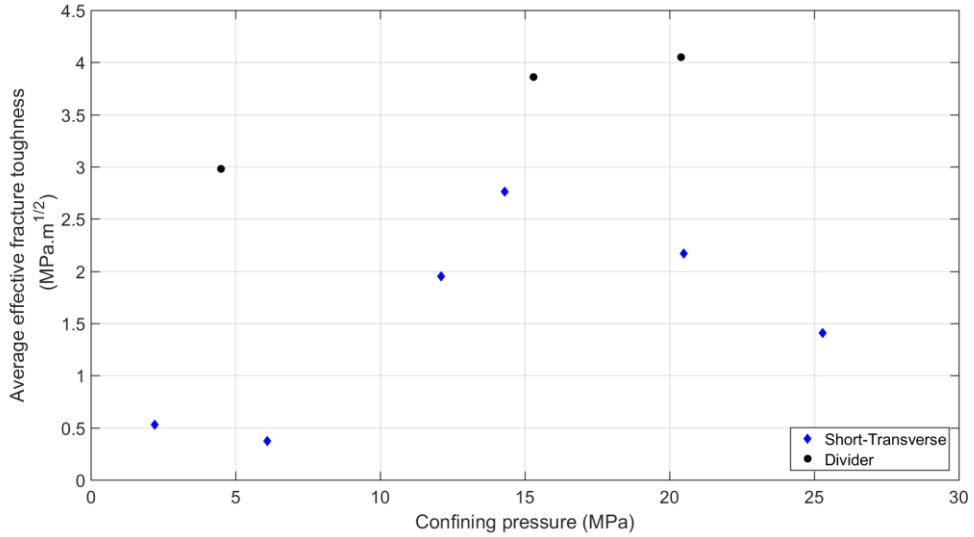

Figure 6-22: Effective fracture toughness vs confining pressure for Short-Transverse and Divider orientation.

7 Conclusions

This study presents a new laboratory-based investigation into the fluid-mechanical process of hydraulic fracturing, exploring the coupled effects of inherent anisotropy, rock fabric and initial permeability of the rock on tensile fracture initiation, propagation and geometry.

To achieve this, a comprehensive suite of laboratory controlled experiments have been designed and conducted to initiate and propagate tensile fractures from the centre of a thick-walled cylinder via direct fluid pressurisation. This pioneering setup allows for direct rock-fluid contact so that the fluid is free to enter the rock matrix as well as evolving the fracture network. The complexity and speed of the fracturing process have been addressed by simultaneously measuring radial deformation, fluid injection pressure and microseismicity at a high resolution. To investigate the effect of the inherent anisotropy and rock fabric, a highly anisotropic, low permeability shale and an anisotropic, tight sandstone have been compared. Experiments conducted with the sample axis and vertical stress (σ_v) both parallel and normal to the bedding plane are presented.

Fundamental differences between the purely mechanical and the fluid-driven tensile fracture process have been identified in the mechanics of the fracturing process, with additional evidence provided from the micro-seismic response using the embedded AE network. Specifically, whereas a purely mechanical process is characterised by a rapid response followed by an immediate unstable fracture propagation accompanied by short-duration high frequency bursts of AE, the fluid-driven fracture process shows an extended stable fracture advance with more AE power lying at lower frequencies. Both differences are evidence for the coupled fluid-rock mechanics during hydraulic fracturing.

From the laboratory evidence, it is concluded that anisotropy exerts a significant control on fracture characteristics and the pressures required to achieve failure. In general, the hydro-mechanical characteristics of the fracture process in Nash Point Shale are similar for both normal and parallel bedding: maximum fluid injection pressure is followed by a rapid fluid pressure decay and an oscillation phase. However, when testing samples with normal bedding orientation, significantly higher fluid pressures were required to initiate hydraulic fracture normal to bedding. With increasing confining pressure the ratio of the required fluid pressure between Short-Transverse and Divider orientation did not change over the tested pressure range, suggesting that the effect of anisotropy does not diminishes at elevated pressures. From radial deformation behaviour and AE activity in samples with normal bedding, it may additionally be concluded that once the fracture reaches the outer sample edge (radially,

divider orientation), propagation still continues in the vertically sense, but in the arrester orientation.

The high sampling-rate recording of mechanical and strain data combined with the time synchronisation to the AE data to a high accuracy revealed, for the first time, the underlying sequence of events during hydraulic fracturing at a high resolution. This distinguishes distinctive fracture stages by linking AE and mechanical behaviour to the ensuing fracture networks. These sequential fracturing steps are: (i) maximum fluid pressure, (ii) a short period of 'plastic' deformation, (iii) fracture initiation, (iv) stable fracture propagation, (v) sample breakdown and finally (vi) unstable fracture propagation. Maximum fluid injection pressure is followed by a period of plastic deformation resulting in a subtle pressure decrease prior to fracture initiation. Fracture initiation then occurs a short time prior to the physical (macro scale) breakdown of the sample as a consequence of initially stable fracture growth. Here it is concluded that the delay in unstable fracturing is related to fracture geometry and complexity of the fracture network as experiments with more complex fracture geometries showed longer delay phases. Once sufficient pressure has built up inside the fracture, fracture propagation evolves from a stable to an unstable regime, marking the breakdown of the sample. This is important, as these new data provide an alternative view to the widely applied assumption that both events occur at maximum fluid pressure. These observations show that AE activity, fluid injection rates, and deformation are key indicators for imminent breakdown in anisotropic sedimentary rocks subjected to elevated fluid pressures.

The oscillation of the fluid pressure and AE hit rate provide additional evidence for an incremental crack propagation in NPS, with an alternation between stable and unstable fracture propagation. The halt in propagation and hence the fluid oscillation is most likely caused by a sudden pressure decrease within the fracture, resulting in a decreasing stress intensity at the fracture tip and ultimately the halt of fracture advance. The understanding of the progressive failure process of hydraulic fracturing combined with the measurement of these real-world parameters, seismic activity, fluid injection pressure and deformation, could allow engineers to better control and monitor hydraulic fracturing, potentially a critical first step towards a more controlled approach to reservoir stimulation in an effort to reduce risks and increase controllability.

AE hit rate imitates fluid pressure behaviour over time, illustrating the link between micro-seismic activity and the pressurised fluid flow either into the rock or fracture, and the mechanical response of the sample due to that fluid movement. The seismo-mechanical

relationship during hydraulic fracturing shows that AE activity (or microseismic field monitoring) can generate a useful geophysical picture of the evolving tensile fracture nucleation in anisotropic rocks. Laboratory experiments generate data that helps to develop our understanding of fracking in the field, and how seismicity can be used to better understand the process remotely. Spectrogram data from hydraulic fracturing experiments of NPS are consistent with an impulsive (rapid) emergent onset and a long harmonic, quasi-monochromatic coda leading to the conclusion that the newly established crack gives way to rock/fluid coupling driven by rapid fluid movement, overprinting fresh fracture events. This is supported by similar long-period events recorded during hydraulic fracturing experiments in the Barnett field, US (Das and Zoback, 2013), at Fenton Hill, New Mexico (Bame and Fehler, 1986; Ferrazzini et al., 1990) and at Montney, B.C., Canada (Eaton et al., 2013). Seismic activity of hydraulic fracturing provides an opportunity to calibrate laboratory experiments to field operations, further helping operators to understand the fracturing process and the driving forces during hydraulic fracturing.

Crab Orchard Sandstone was used as a counterpoint to the fine grained NPS. A comparison of the results shows that rock fabric and initial permeability have a significant effect on the fracturing process. Despite a higher tensile strength of the sandstone, hydraulic fractures initiate at similar pressure as NPS and are not significantly affected by bedding orientation. The relatively low breakdown pressures are a result of reduced tensile strength of the rock via a combination of deformation and the build-up of pore pressures due to increased fluid infiltration as a consequence of the higher permeability of the sandstone. Furthermore, the characteristic oscillation phase as seen in shale experiments is absent in the sandstone. It is concluded that the connecting of pre-existing pores along the fracture path in the sandstone effectively enlarges the fracture aperture (Zoback et al., 1977) allowing for the pore fluid supply to keep up with the fluid demand in the fracture and preventing a pressure decrease within the fracture. This promotes fracture propagation to the edge of the sample without the oscillatory behaviour seen in the NPS experiments where fracture outpaced the fluid. This is further supported by analysis of the dominant failure mechanism of the AE. In the shale, tensile type events dominate whereas during the hydraulic fracturing of COS shear and compressional events dominate with only a minor part being tensile in character.

Independent of rock type or bedding orientation, hydraulic fractures always developed axially and therefore parallel to σ_v. This shows that fracture orientation is primarily controlled by the external stress conditions. However, the data also demonstrates that rock anisotropy, permeability and rock fabric are critical in governing fracture initiation, propagation, fracture

geometry and fracture network complexity. In the case of NPS with bedding oriented parallel to σ_v, the dominant control are the bedding planes themselves, which provide planes of weakness, and fractures only diverting when encountering lithic fragments. Hydraulic fractures propagating normal to bedding showed a similar fracture network, but with slightly more tortuous fracture geometries as shear displacements along bedding planes occur more frequently. In contrast to the shale, fracture geometry in the sandstone is significantly influenced by the rock fabric, as fractures grow along grain boundaries and through pre-existing pores, which results in more tortuous fracture paths compared to NPS.

Permeability enhancement through the newly developed fracture was directly measured using a novel protocol. Compared to initial permeability data on fresh (non-fractured) intact Nash Point Shale samples, an enhancement of three orders of magnitude has been achieved by hydraulic fracturing. Over a range from 2MPa to 19MPa, permeability decreases by one order of magnitude, highlighting the pressure dependency of fracture permeability which ultimate controls the performance of the stimulation. This data provides a new understanding of the enhanced permeability after fracturing for a specific reservoir rock (NPS) and therefore can aid in reliable well performance analysis and fracturing design by testing parameters such as fluid type and viscosity, pressurisation rate and proppant type and volume, to investigate their effect on the resulting new permeability.

For both rock types and in the case of the shale for both bedding orientations, breakdown pressures increase with increasing confining pressure. Similar to other rock types, Crab Orchard Sandstone shows a linear relationship between breakdown pressure and confining pressure. However, Nash Point Shale parallel bedding does exhibits a non-linear relationship between breakdown pressure and confining pressure, with a clear break at approximately 15MPa. Here, three different models are used to predict hydraulic fracturing breakdown pressures and are compared with experimental hydraulic fracturing results. The linear-elastic model (equation 2-30) (Hubbert and Willis, 1957), where the calculated breakdown pressure is a function of far-field stresses, tensile rock strength and pore pressure, yields the best fit for both rock types parallel to bedding. In the case of NPS, the experimentally determined breakdown pressures divert from the linear model at pressures above 15 MPa. Above 15MPa confining pressure, laboratory breakdown pressures are lower compared to the model and it is concluded that at this point built-up pore pressure starts to influence the fracturing process significantly. This conclusion is further reinforced due to the good fit between laboratory data and the linear-elastic model for Crab Orchard Sandstone in which pore pressure plays a more significant part due to its higher permeability.

Finally, this study concludes that the hydraulic fracturing process is intertwined with not just the macro-scale tensile strength of the rock, but also the fracture toughness (K_{IC}). To understand this, a new approach has been applied to derive the effective fracture toughness (mode I) at elevated pressures which accounts for a number of influencing factors like the initial crack length, fluid infiltration and fluid flow as well as the present stress-field. For Nash Point Shale parallel to bedding, it is here shown that tensile strength controls fracture initiation, whereas tensile (mode I) fracture toughness controls fracture propagation. When calculated via the oscillation of the fluid pressure and AE activity a picture of incremental fracture propagation is derived that is related to the fracture toughness of the rock. The initial increase with increasing confining pressure demonstrates the pressure dependency of fracture toughness in Nash Point Shale. However, from the eK_{IC}-data it is furthermore concluded that fracture toughness is also influenced by pore pressures. If sufficient pore pressures built-up inside the rock matrix, the effective fracture toughness is reduced and fracture propagation is promoted. This understanding of the dependency of hydraulic fracturing on tensile strength and fracture toughness of the rock but also pore pressures and initial rock permeability will help to predict more reliable breakdown pressures for field operations as current hydraulic fracture criteria often underestimate breakdown pressures seen in the field.

This study shows how induced seismicity could become a powerful tool to define the timing of fracture generation and fracture orientation relative to bedding orientation. A good proxy for fracture initiation is the onset of acoustic emission hit rate and in all experiments, peak AE activity and rapid decay of fluid pressure were good indicators for the physical breakdown of the sample. The forecast becomes even more reliable when using a combination of seismic activity, fluid injection rates and deformation (or strain) as indicators for imminent breakdown. By creating a detailed mechanical and geophysical image of tensile fracture nucleation and growth in anisotropic rocks, this data advances our understanding of fracking in the field, and investigates how mechanical data and seismicity can be used to better understand and monitor hydraulic fracturing remotely. Such a system not only could become a prediction/forecasting tool, but also a means to control the fracking process to prevent avoidable seismic events and fracture extend beyond the targeted lithology. These observations are important for hydraulic fracturing applications in the field, e.g. oil and gas extraction, and the understanding of the fundamental fracture properties of low permeability, anisotropic rock types and the tensile fracturing process which is essential to develop a more engineered approach to reservoir stimulation via hydraulic fracturing. This becomes even more important when the potential risks are considered, as every shale play has unique properties, which need to be addressed in

the treatment design, especially in highly populated areas like the UK or when applied in close vicinity of water-bearing rock formations.

Future Work

Through the course of the investigation, a number of challenges have been encountered which, due to the constraints of time, were not investigated fully yet would considerably improve the understanding of hydraulic fracturing and the interplay between mechanical and seismic responses as well as initial permeability, rock fabric and inherent anisotropy. A logical advance would be to use the AE to locate, in 3D, fracture events during hydraulic fracturing experiments and so to track fracture propagation in space and time. This would lead to more detailed information about the distinct fracture stages including the fracture mechanism during each distinctive stage. The three dimensional location of events could also improve the analysis of the effective fracture toughness as fracture length could be determined directly.

Another avenue for future work is the development of a forecast model using a combination of seismic and mechanical data. A preliminary analysis of the seismic data suggests that bulk parameters of AE hit rate can be used to forecast an approximate time to failure. Such a system not only could become a prediction/forecasting tool, but also a means to control the fracking process to prevent avoidable seismic events and fracture extend beyond the targeted lithology. A common method for rock failure forecast is the inverse seismic rate model (Kilburn, 2003) which considers the linkage of microcracks through time. This derives a forecast time of failure by taking an intercept time as the inverse rate approaches zero (representing an infinite seismic rate, or rock fracture rate). Although this model was originally designed for episodes of cyclical volcanic activity, the physics behind the model is appropriate for other areas of pure and applied research including that of forecasting rock mass failure during hydrofracture. The technique has been shown to work well for fracturing materials with few pre-exiting flaws, and this is represented in the following preliminary analysis. AE data from conduit-parallel and conduit-normal orientation (Figure 7-1) provide good agreement between failure prediction based on AE data and the known fracture initiation point which indicates that breakdown is imminent. For AE data of the shale in conduit-normal orientation, where the fracture is known to pass several beds (representing higher pre-exiting damage) the forecast failure time was less accurate. Although in some of the experiments the inverse AE trend for failure forecast only became apparent immediately prior to failure, in field operations this could amount to tens of seconds or minutes, giving enough time for an operator to react. However, this concept needs further development in combination with the mechanical data to provide a true “warning time”.

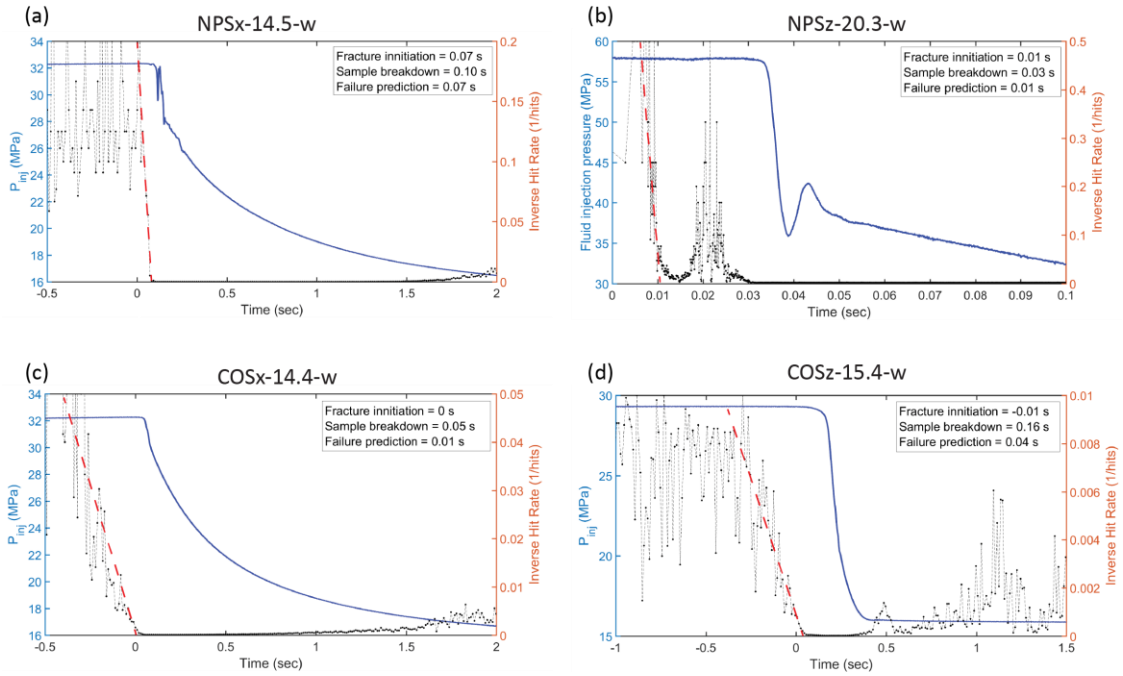

Figure 7-1: Failure time prediction via the inverse hit rate failure forecast model (Kilburn, 2003). This model uses the inverse seismic rate to determine a forecast time of failure as this parameter approaches zero; (a) NPSx – prediction of fracture initiation very accurate, but only possible immediately prior to failure; (b) NPSz – prediction of fracture initiation very accurate; (c) COSx - prediction very close to fracture initiation; (d) COSz – prediction very close to fracture initiation. Time scales zeroed at max fluid injection pressure, P_{inj} = fluid injection pressure.

References

Abou-Sayed, A. (1978). An experimental technique for measuring the fracture toughness of rock under downhole stress condition. *VDI-berichte*, 313, p.819–824.

Abou-Sayed, A., Brechtel, C. and Clifton, R. (1978). In situ stress determination by hydrofracturing: a fracture mechanics approach. *Journal of Geophysical Research: Solid Earth*, 83 (B6), p.2851–2862.

Aguilera, R. (2006). Effect of fracture compressibility on oil recovery from stress-sensitive naturally fractured reservoirs. *Journal of Canadian Petroleum Technology*, 45 (12), Petroleum Society of Canada.

Aki, K., Fehler, M. and Das, S. (1977). Source mechanism of volcanic tremor: Fluid-driven crack models and their application to the 1963 Kilauea eruption. *Journal of volcanology and geothermal research*, 2 (3), p.259–287.

Alber, M., Brenne, S., Molenda, M., Stöckhert, F., Braun, J. and others. (2015). Hydraulic Fractures in a Highly Anisotropic Slate on Laboratory Scale. In: *ISRM Regional Symposium-EUROCK 2015*, 2015.

Alpern, J., Marone, C., Elsworth, D., Belmonte, A., Connelly, P. and others. (2012). Exploring the physicochemical processes that govern hydraulic fracture through laboratory experiments. In: *46th US Rock Mechanics/Geomechanics Symposium*, 2012.

Amadei, B. (1982). The influence of rock anisotropy on measurement of stresses in situ. *University of California, Berkeley*, PhD thesis.

Amann, F., Kaiser, P. and Button, E. A. (2012). Experimental study of brittle behavior of clay shale in rapid triaxial compression. *Rock mechanics and rock engineering*, 45 (1), p.21–33.

Anderson, G. D. (1981). Effects of friction on hydraulic fracture growth near unbonded interfaces in rocks. *Society of Petroleum Engineers Journal*, 21 (01), p.21–29.

Anderson, T. L. (2017). *Fracture mechanics: fundamentals and applications*. CRC press.

Andrews, I. (2013). The Carboniferous Bowland Shale gas study: geology and resource estimation. *British Geological Survey for Department of Energy and Climate Change, London, UK*.

Andruleit, H., Bahr, A., Bönnemann, C., Erbacher, J., Franke, D., Gerling, J., Gestermann, N., Himmelsbach, T., Kosinowski, M. and Krug, S. (2012). *Abschätzung des Erdgaspotenzials aus dichten Tongesteinen (Schiefergas) in Deutschland*.

Arzani, N. (2004). Diagenetic evolution of mudstones: black shales to laminated limestones, an example from the Lower Jurassic of SW Britain. *Journal of sciences Islamic Republic of Iran*.

Atkinson, B. K. (1979a). A fracture mechanics study of subcritical tensile cracking of quartz in wet environments. *Pure and Applied Geophysics*, 117 (5), p.1011–1024.

Atkinson, B. K. (1979b). Fracture toughness of Tennessee sandstone and Carrara marble using the double torsion testing method. *International Journal of Rock Mechanics and Mining Sciences & Geomechanics Abstracts*, 16 (1), p.49–53.

Bame, D. and Fehler, M. (1986). Observations of long period earthquakes accompanying hydraulic fracturing. *Geophysical Research Letters*, 13 (2), p.149–152.

Barron, K. (1971). Detection of fracture initiation in rock specimens by the use of a simple ultrasonic listening device. In: *International Journal of Rock Mechanics and Mining Sciences & Geomechanics Abstracts*, 8 (1), 1971, p.55–59.

Baud, P., Klein, E. and Wong, T. (2004). Compaction localization in porous sandstones: spatial evolution of damage and acoustic emission activity. *Journal of Structural Geology*, 26 (4), p.603–624.

Bennion, D., Thomas, F., Bietz, R. and others. (1996). Low permeability gas reservoirs: problems, opportunities and solutions for drilling, completion, stimulation and production. In: *SPE Gas Technology Symposium*, 1996.

Benson, P. M. (2004). Experimental study of void space, permeability and elastic anisotropy in crustal rocks under ambient and hydrostatic pressure. *University College London*, PhD thesis.

Benson, P. M., Meredith, P. G. and Platzman, E. S. (2003). Relating pore fabric geometry to acoustic and permeability anisotropy in Crab Orchard Sandstone: A laboratory study using magnetic ferrofluid. *Geophysical research letters*, 30 (19).

Benson, P. M., Meredith, P. G. and Schubnel, A. (2006). Role of void space geometry in permeability evolution in crustal rocks at elevated pressure. *Journal of Geophysical Research: Solid Earth*, 111 (B12).

Benson, P. M., Thompson, B. D., Meredith, P. G., Vinciguerra, S. and Young, R. P. (2007). Imaging slow failure in triaxially deformed Etna basalt using 3D acoustic-emission location and X-ray computed tomography. *Geophysical research letters*, 34 (3).

Benson, P. M., Vinciguerra, S., Meredith, P. G. and Young, R. P. (2008). Laboratory simulation of volcano seismicity. *Science*, 322 (5899), American Association for the Advancement of Science, p.249–252.

Benson, P. M., Vinciguerra, S., Meredith, P. G. and Young, R. P. (2010). Spatio-temporal evolution of volcano seismicity: A laboratory study. *Earth and Planetary Science Letters*, 297 (1), p.315–323.

Benson, P. M., Vinciguerra, S., Nasseri, M. H. and Young, R. P. (2014). Laboratory simulations of fluid/gas induced micro-earthquakes: application to volcano seismology. *Frontiers in Earth Science*, 2, Frontiers, p.32.

Benson, P., Meredith, P., Platzman, E. and White, R. (2005). Pore fabric shape anisotropy in porous sandstones and its relation to elastic wave velocity and permeability anisotropy under hydrostatic pressure. *International Journal of Rock Mechanics and Mining Sciences*, 42 (7), p.890–899.

Bernabé, Y. (1987). The effective pressure law for permeability during pore pressure and confining pressure cycling of several crystalline rocks. *Journal of Geophysical Research: Solid Earth*, 92 (B1), p.649–657.

Bernier, F., Li, X., Bastiaens, W., Ortiz, L., Van Geet, M., Wouters, L., Frieg, B., Blümling, P., Desrues, J., Viaggiani, G. and others. (2007). Fractures and self-healing within the excavation disturbed zone in clays (SELFRAC). *Final report to EC (Project FIKW-CT2001-00182). EUR*, 22585.

Bidgoli, M. N. and Jing, L. (2014). Anisotropy of strength and deformability of fractured rocks. *Journal of Rock Mechanics and Geotechnical Engineering*, 6 (2), p.156–164.

Bieniawski, Z. (1967a). Mechanism of brittle fracture of rock: part I—theory of the fracture process. In: *International Journal of Rock Mechanics and Mining Sciences & Geomechanics Abstracts*, 4 (4), 1967, p.395–406.

Bieniawski, Z. (1967b). Mechanism of brittle fracture of rock: Part III—Fracture in tension and under long-term loading. In: *International Journal of Rock Mechanics and Mining Sciences & Geomechanics Abstracts*, 4 (4), 1967, p.425–430.

Bieniawski, Z. (1967c). Stability concept of brittle fracture propagation in rock. *Engineering Geology*, 2 (3), p.149–162.

Birch, F. (1960). The velocity of compressional waves in rocks to 10 kilobars: 1. *Journal of Geophysical Research*, 65 (4), p.1083–1102.

Blanton, T. L. (1982). An experimental study of interaction between hydraulically induced and pre-existing fractures. In: *SPE unconventional gas recovery symposium*, 1982.

Boitnott, G. and Scholz, C. (1990). Direct measurement of the effective pressure law: deformation of joints subject to pore and confining pressures. *Journal of Geophysical Research: Solid Earth*, 95 (B12), p.19279–19298.

Boone, T., Ingraffea, A. and Roegiers, J.-C. (1991). Simulation of hydraulic fracture propagation in poroelastic rock with application to stress measurement techniques. In: *International Journal of Rock Mechanics and Mining Sciences & Geomechanics Abstracts*, 28

(1), 1991, p.1–14.

Boulin, P., Bretonnier, P., Gland, N. and Lombard, J.-M. (2012). Contribution of the steady state method to water permeability measurement in very low permeability porous media. *Oil & Gas Science and Technology-Revue d'IFP Energies nouvelles*, 67 (3), Technip, p.387–401.

Bowker, K. A. (2007). Development of the barnett shale play, Fort Worth Basin. *AAPG Bulletin*, 91 (4), p.1–13.

Boyer, C., Clark, B., Jochen, V., Lewis, R. and Miller, C. K. (2011). Shale gas: A global resource. *Oilfield review*, 23 (3), p.28–39.

Brace, W. F. (1961). Dependence of fracture strength of rocks on grain size. In: *The 4th US Symposium on Rock Mechanics (USRMS)*, 1961.

Brace, W. F. (1964). Brittle fracture of rocks. *State of Stress in the Earth's Crust*, p.111–180.

Brace, W. and Kohlstedt, D. (1980). Limits on lithospheric stress imposed by laboratory experiments. *Journal of Geophysical Research: Solid Earth*, 85 (B11), p.6248–6252.

Brace, W., Walsh, J. and Frangos, W. (1968). Permeability of granite under high pressure. *Journal of Geophysical research*, 73 (6), p.2225–2236.

Brady, B. H. and Brown, E. T. (2005). *Rock mechanics: for underground mining*. Springer Netherlands.

Brassington, F. and Walthall, S. (1985). Field techniques using borehole packers in hydrogeological investigations. *Quarterly Journal of Engineering Geology and Hydrogeology*, 18 (2), Geological Society of London, p.181–193.

Brenne, S., Molena, M., Stoeckhert, F., Alber, M. and others. (2013). Hydraulic and sleeve fracturing laboratory experiments on 6 rock types. In: *ISRM International Conference for Effective and Sustainable Hydraulic Fracturing*, 2013.

Brenne, S., Molenda, M., Stoeckhert, F., Alber, M. and others. (2014). Hydraulic Fracturing of a Devonian Slate under confining pressure-with emphasis on cleavage inclination. In: *ISRM Regional Symposium-EUROCK 2014*, 2014.

Breyer, J. A., Denne, R., Funk, J., Kosanke, T. and Spaw, J. (2013). Stratigraphy and sedimentary facies of the Eagle Ford Shale (Cretaceous) between the Maverick Basin and the San Marcos Arch, Texas, USA. *Search and Discovery article*, 50899.

Broek, D. (2012). *Elementary engineering fracture mechanics*. Springer Netherlands.

Bruner, K. R. and Smosna, R. (2011). *A comparative study of the Mississippian Barnett shale, Fort Worth basin, and Devonian Marcellus shale, Appalachian basin*. US Department of

Energy.

Byerlee, J. D. (1967). Frictional characteristics of granite under high confining pressure. *Journal of Geophysical Research*, 72 (14), p.3639–3648.

Byerlee, J. D. and Lockner, D. (1977). Acoustic emission during fluid injection into rock. In: *Proceedings of 1st conference on acoustic emission/microseismic activity in geological structures and materials, Trans Tech Publications*, 1977, p.87–98.

Byerlee, J. and Summers, R. (1975). Stable sliding preceding stick-slip on fault surfaces in granite at high pressure. In: *Earthquake Prediction and Rock Mechanics*, p.63–68.

Carmichael, R. S. (1982). *CRC handbook of physical properties of Rocks*. CRC Press. Inc.

Chalmers, G. R. and Bustin, R. M. (2017). A multidisciplinary approach in determining the maceral (kerogen type) and mineralogical composition of Upper Cretaceous Eagle Ford Formation: Impact on pore development and pore size distribution. *International Journal of Coal Geology*, 171, p.93–110.

Chalmers, G. R., Bustin, R. M. and Power, I. M. (2012). Characterization of gas shale pore systems by porosimetry, pycnometry, surface area, and field emission scanning electron microscopy/transmission electron microscopy image analyses: Examples from the Barnett, Woodford, Haynesville, Marcellus, and Doig units. *AAPG bulletin*, 96 (6), p.1099–1119.

Chandler, M. R., Meredith, P. G., Brantut, N. and Crawford, B. R. (2016). Fracture toughness anisotropy in shale. *Journal of Geophysical Research: Solid Earth*, 121 (3), p.1706–1729.

Charalampidou, E.-M., Hall, S. A., Stanchits, S., Lewis, H. and Viggiani, G. (2011). Characterization of shear and compaction bands in a porous sandstone deformed under triaxial compression. *Tectonophysics*, 503 (1-2), p.8–17.

Chell, G. (1979). Elastic-plastic fracture mechanics. *Developments in fracture mechanics*, p.67–105.

Chen, Y., Nagaya, Y. and Ishida, T. (2015). Observations of fractures induced by hydraulic fracturing in anisotropic granite. *Rock Mechanics and Rock Engineering*, 48 (4), p.1455–1461.

Chitrala, Y., Moreno, C., Sondergeld, C. H., Rai, C. S. and others. (2010). Microseismic mapping of laboratory induced hydraulic fractures in anisotropic reservoirs. In: *Tight Gas Completions Conference*, 2010.

Chitrala, Y., Sondergeld, C. and Rai, C. (2012). Acoustic emission studies of hydraulic fracture evolution using different fluid viscosities. In: *46th US Rock Mechanics/Geomechanics Symposium*, 2012.

Chong, K. P., Kuruppu, M. D. and Kuszmaul, J. S. (1987). Fracture toughness determination of layered materials. *Engineering fracture mechanics*, 28 (1), p.43–54.

Chouet, B. (1988). Resonance of a fluid-driven crack: Radiation properties and implications for the source of long-period events and harmonic tremor. *Journal of Geophysical Research: Solid Earth*, 93 (B5), p.4375–4400.

Chouet, B. (2003). Volcano seismology. In: *Seismic Motion, Lithospheric Structures, Earthquake and Volcanic Sources: The Keiiti Aki Volume*, p.739–788.

Chouet, B. A. (1996). Long-period volcano seismicity: its source and use in eruption forecasting. *Nature*, 380 (6572), p.309–316.

Clifton, R., Simonson, E., Jones, A. and Green, S. (1976). Determination of the critical-stress-intensity factor K Ic from internally pressurized thick-walled vessels. *Experimental Mechanics*, 16 (6), p.233–238.

Collins, D. S., Pettitt, W. S. and Young, R. P. (2002). High-resolution mechanics of a microearthquake sequence. In: *The Mechanism of Induced Seismicity*, p.197–219.

Colmenares, L. and Zoback, M. (2002). A statistical evaluation of intact rock failure criteria constrained by polyaxial test data for five different rocks. *International Journal of Rock Mechanics and Mining Sciences*, 39 (6), p.695–729.

Cook, J. (1999). The effects of pore pressure on the mechanical and physical properties of shales. *Oil & Gas Science and Technology*, 54 (6), EDP Sciences, p.695–701.

Cook, N. G. (1965). The failure of rock. In: *International Journal of Rock Mechanics and Mining Sciences & Geomechanics Abstracts*, 2 (4), 1965, p.389–403.

Cosgrove, J. (1995). The expression of hydraulic fracturing in rocks and sediments. *Geological Society, London, Special Publications*, 92 (1), Geological Society of London, p.187–196.

Coulomb, C. A. (1776). *Essai sur une application des regles de maximis et minimis a quelques problemes de statique relatifs a l'architecture (essay on maximums and minimums of rules to some static problems relating to architecture)*.

Currie, J., Greenstone, M. and Meckel, K. (2017). Hydraulic fracturing and infant health: New evidence from Pennsylvania. *Science advances*, 3 (12), American Association for the Advancement of Science, p.e1603021.

Cuss, R., Wiseall, A., Hennissen, J., Waters, C. N., Kemp, S., Ougier-Simonin, A., Holyoake, S. and Haslam, R. (2015). *Hydraulic Fracturing: A review of theory and field experience*. British Geological Survey.

Daneshy, A. A. (1976). Rock properties controlling hydraulic fracture propagation. In: *SPE European Spring Meeting*, 1976.

Das, I. and Zoback, M. D. (2011). Long Period Long Duration Seismic Events During Hydraulic Stimulation of a Shale Gas Reservoir. *APG Annual Convention and Exhibition*.

Das, I. and Zoback, M. D. (2013). Long-period, long-duration seismic events during hydraulic stimulation of shale and tight-gas reservoirs—Part 1: Waveform characteristics. *Geophysics*, 78 (6), Society of Exploration Geophysicists, p.107–118.

Davy, C. A., Skoczylas, F., Barnichon, J.-D. and Lebon, P. (2007). Permeability of macro-cracked argillite under confinement: gas and water testing. *Physics and Chemistry of the Earth, Parts A/B/C*, 32 (8-14), p.667–680.

Denison, C., Carlson, W. and Ketcham, R. (1997). Three-dimensional quantitative textural analysis of metamorphic rocks using high-resolution computed X-ray tomography: Part I. Methods and techniques. *Journal of Metamorphic Geology*, 15 (1), p.29–44.

Detournay, E. and Carbonell, R. (1997). Fracture-mechanics analysis of the breakdown process in minifracture or leakoff test. *SPE production & facilities*, 12 (03), p.195–199.

Diaz, M., Jung, S., Zhuang, L., Kim, K., Yeom, S., Shin, H. and others. (2016). Effect of cleavage anisotropy on hydraulic fracturing behavior of Pocheon granite. In: *Proceedings of the 50th US rock mechanics/geomechanics symposium, Houston, ARMA*, 2016, p.16–143.

Dobson, K. J., Coban, S. B., McDonald, S. A., Walsh, J. N., Atwood, R. C. and Withers, P. J. (2016). 4-D imaging of sub-second dynamics in pore-scale processes using real-time synchrotron X-ray tomography. *Solid Earth*, 7 (4), p.1059.

Dropek, R., Johnson, J. and Walsh, J. (1978). The influence of pore pressure on the mechanical properties of Kayenta sandstone. *Journal of Geophysical Research: Solid Earth*, 83 (B6), p.2817–2824.

Dunn, D. E., LaFountain, L. J. and Jackson, R. E. (1973). Porosity dependence and mechanism of brittle fracture in sandstones. *Journal of Geophysical Research*, 78 (14), p.2403–2417.

Dusseault, M. B. (2013). Geomechanical aspects of shale gas development. In: *ISRM International Symposium-EUROCK 2013*, 2013.

Dyer, B., Schanz, U., Ladner, F., Häring, M. and Spillman, T. (2008). Microseismic imaging of a geothermal reservoir stimulation. *The Leading Edge*, 27 (7), p.856–869.

Eaton, D., van der Baan, M., Tary, J.-B., Birkelo, B., Spriggs, N., Cutten, S. and Pike, K. (2013). Broadband microseismic observations from a Montney hydraulic fracture treatment, northeastern BC, Canada. *Focus*.

Eberhardt, E., Stimpson, B. and Stead, D. (1999). Effects of grain size on the initiation and propagation thresholds of stress-induced brittle fractures. *Rock Mechanics and Rock Engineering*, 32 (2), p.81–99.

Eitzen, D. and Wadley, H. (1984). Acoustic emission: establishing the fundamentals. *Journal of research of the National Bureau of Standards*, 89 (1), p.75–100.

Elston, H. (2014). *Mineralogical and Geochemical Assessment of the Eagle Ford Shale*.

Enriquez Tenorio, O. (2016). *A Comprehensive Study of the Eagle Ford Shale Fracture Conductivity*.

Fairhurst, C. and Hudson, J. (1999). Draft ISRM suggested method for the complete stress-strain curve for intact rock in uniaxial compression. *International Journal of Rock Mechanics and Mining Sciences*, 36 (3), p.279–289.

Fauchille, A., Ma, L., Rutter, E., Chandler, M., Lee, P. and Taylor, K. (2017). An enhanced understanding of the Basinal Bowland shale in Lancashire (UK), through microtextural and mineralogical observations. *Marine and Petroleum Geology*, 86, p.1374–1390.

Fazio, M. (2017). Dynamic laboratory simulations of fluid-rock coupling with application to volcano seismicity and unrest. *University of Portsmouth*, PhD thesis.

Fazio, M., Benson, P. M. and Vinciguerra, S. (2017). On the generation mechanisms of fluid-driven seismic signals related to volcano-tectonics. *Geophysical Research Letters*, 44 (2), p.734–742.

Feldkamp, L., Davis, L. and Kress, J. (1984). Practical cone-beam algorithm. *JOSA A*, 1 (6), Optical Society of America, p.612–619.

Ferrazzini, V., Chouet, B., Fehler, M. and Aki, K. (1990). Quantitative analysis of long-period events recorded during hydrofracture experiments at Fenton Hill, New Mexico. *Journal of Geophysical Research: Solid Earth*, 95 (B13), p.21871–21884.

Fischer, G. (1992). The determination of permeability and storage capacity: Pore pressure oscillation method. *INTERNATIONAL GEOPHYSICS SERIES*, 51, p.187–187.

Forbes Inskip, N. D., Meredith, P. G., Chandler, M. R. and Gudmundsson, A. (2018). Fracture properties of Nash Point shale as a function of orientation to bedding. *Journal of Geophysical Research*, in review.

Fortin, J., Guéguen, Y. and Schubnel, A. (2007). Effect of pore collapse and grain crushing on ultrasonic velocities and Vp/Vs. *J. geophys. Res*, 112, p.B08207.

Fortin, J., Stanchits, S., Dresen, G. and Gueguen, Y. (2009). Acoustic emissions monitoring during inelastic deformation of porous sandstone: comparison of three modes of

deformation. In: *Rock Physics and Natural Hazards*, p.823–841.

Fortin, J., Stanchits, S., Dresen, G. and Guéguen, Y. (2006). Acoustic emission and velocities associated with the formation of compaction bands in sandstone. *Journal of Geophysical Research: Solid Earth*, 111 (B10).

Fredrich, J. T., Evans, B. and Wong, T.-F. (1990). Effect of grain size on brittle and semibrittle strength: Implications for micromechanical modelling of failure in compression. *Journal of Geophysical Research: Solid Earth*, 95 (B7), p.10907–10920.

Gan, Q., Elsworth, D., Alpern, J., Marone, C. and Connolly, P. (2015). Breakdown pressures due to infiltration and exclusion in finite length boreholes. *Journal of Petroleum Science and Engineering*, 127, p.329–337.

Gandossi, L. (2013). An overview of hydraulic fracturing and other formation stimulation technologies for shale gas production. *Eur. Commisison Jt. Res. Cent. Tech. Reports*.

Gangi, A. F. and Carlson, R. L. (1996). An asperity-deformation model for effective pressure. *Tectonophysics*, 256 (1-4), p.241–251.

Gasparik, M., Bertier, P., Gensterblum, Y., Ghanizadeh, A., Krooss, B. M. and Littke, R. (2014). Geological controls on the methane storage capacity in organic-rich shales. *International Journal of Coal Geology*, 123, p.34–51.

Gehne, S. and Benson, P. M. (2017). Permeability and permeability anisotropy in Crab Orchard sandstone: Experimental insights into spatio-temporal effects. *Tectonophysics*, 712, p.589–599.

Ghanizadeh, A., Gasparik, M., Amann-Hildenbrand, A., Gensterblum, Y. and Krooss, B. (2013). Lithological controls on matrix permeability of organic-rich shales: an experimental study. *Energy Procedia*, 40, p.127–136.

Goodfellow, S. D. (2015). *Quantitative Analysis Of Acoustic Emission From Rock Fracture Experiments*.

Goodman, R. E. (1963). Subaudible noise during compression of rocks. *Geological Society of America Bulletin*, 74 (4), p.487–490.

Gowd, T. and Rummel, F. (1977). Effect of fluid injection on the fracture behavior of porous rock. In: *International Journal of Rock Mechanics and Mining Sciences & Geomechanics Abstracts*, 14 (4), 1977, p.203–208.

Griffith, A. (1921). The phenomena of rupture and flow in solids. *Phil. Trans. R. Soc. Lond. A*, 221 (582-593), The Royal Society, p.163–198.

Griffith, A. (1924). The theory of rupture. In: *First Int. Cong. Appl. Mech*, 1924, p.55–63.

Grosse, C. U. and Ohtsu, M. (2008). *Acoustic emission testing*. Springer-Verlag Berlin Heidelberg.

Gudmundsson, A. and Brenner, S. L. (2001). How hydrofractures become arrested. *Terra Nova*, 13 (6), p.456–462.

Guéguen, Y. and Palciauskas, V. (1994). *Introduction to the physics of rocks*. Princeton University Press.

Guo, T., Zhang, S., Gao, J., Zhang, J. and Yu, H. (2013). Experimental study of fracture permeability for stimulated reservoir volume (SRV) in shale formation. *Transport in porous media*, 98 (3), p.525–542.

Haimson, B. and Avasthi, J. (1973). Stress measurements in anisotropic rock by hydraulic fracturing. In: *Proc. US Nat. Comm. for Rock Mech. Appl. of Rock Mech. Symp.;(United States)*, (CONF-7309108-), 1973.

Haimson, B. C. and Zhao, Z. (1991). Effect of borehole size and pressurization rate on hydraulic fracturing breakdown pressure. In: *The 32nd US Symposium on Rock Mechanics (USRMS)*, 1991.

Haimson, B. and Fairhurst, C. (1967). Initiation and extension of hydraulic fractures in rocks. *Society of Petroleum Engineers Journal*, 7 (03), p.310–318.

Haimson, B. and Fairhurst, C. (1969a). Hydraulic fracturing in porous-permeable materials. *Journal of Petroleum Technology*, 21 (07), p.811–817.

Haimson, B. and Fairhurst, C. (1969b). In-situ stress determination at great depth by means of hydraulic fracturing. In: *The 11th US symposium on rock mechanics (USRMS)*, 1969.

Handin, J., Hager Jr, R. V., Friedman, M. and Feather, J. N. (1963). Experimental deformation of sedimentary rocks under confining pressure: pore pressure tests. *Aapg Bulletin*, 47 (5), American Association of Petroleum Geologists, p.717–755.

Handin, J., Heard, H. and and Magouirk, J. (1967). Effects of the intermediate principal stress on the failure of limestone, dolomite, and glass at different temperatures and strain rates. *Journal of geophysical research*, 72 (2), p.611–640.

Hardy Jr, H. R. (2005). *Acoustic emission/microseismic activity: volume 1: principals, techniques and geotechnical applications*. CRC Press.

Harrington, R. M. and Benson, P. M. (2011). Analysis of laboratory simulations of volcanic hybrid earthquakes using empirical Green's functions. *Journal of Geophysical Research: Solid*

Earth, 116 (B11).

Harvey, T. and Gray, J. (2013). The unconventional hydrocarbon resources of Britain's onshore basins-shale gas. *Report by the British Geological Survey (BGS)*.

Hatzor, Y. and Palchik, V. (1997). The influence of grain size and porosity on crack initiation stress and critical flaw length in dolomites. *International Journal of Rock Mechanics and Mining Sciences*, 34 (5), p.805–816.

He, J., Afolagboye, L. O., Lin, C. and Wan, X. (2018). An Experimental Investigation of Hydraulic Fracturing in Shale Considering Anisotropy and Using Freshwater and Supercritical CO2. *Energies*, 11 (3), Multidisciplinary Digital Publishing Institute, p.557.

He, J., Lin, C., Li, X. and Wan, X. (2016). Experimental investigation of crack extension patterns in hydraulic fracturing with shale, sandstone and granite cores. *Energies*, 9 (12), Multidisciplinary Digital Publishing Institute, p.1018.

Heap, M. J. (2009). Creep: time-dependent brittle deformation in rocks. *University College London*, PhD thesis.

Heard, H. C. (1960). Transition from brittle fracture to ductile flow in Solenhofen limestone as a function of temperature, confining pressure, and interstitial fluid pressure. *Geological Society of America Memoirs*, 79, p.193–226.

Heller, R., Vermylen, J. and Zoback, M. (2014). Experimental investigation of matrix permeability of gas shales. *AAPG bulletin*, 98 (5), p.975–995.

Hellier, C. (2001). *Handbook of nondestructive evaluation*. Mcgraw-hill New York.

Hennissen, J. A., Hough, E., Vane, C. H., Leng, M. J., Kemp, S. J. and Stephenson, M. H. (2017). The prospectivity of a potential shale gas play: An example from the southern Pennine Basin (central England, UK). *Marine and Petroleum Geology*, 86, p.1047–1066.

Hillerborg, A. (1985). The theoretical basis of a method to determine the fracture energy of concrete. *Materials and structures*, 18 (4), p.291–296.

Hoagland, R. G., Hahn, G. T. and Rosenfield, A. R. (1973). Influence of microstructure on fracture propagation in rock. *Rock Mechanics*, 5 (2), p.77–106.

Hobbs, P., Entwisle, D., Northmore, K., Sumbler, M., Jones, L., Kemp, S., Self, S., Barron, M. and Meakin, J. (2012). *Engineering geology of British rocks and soils: Lias Group*. British Geological Survey.

Hoek, E. (1965). Rock fracture under static stress conditions. *University of Cape Town*, PhD thesis.

Hoek, E. and Bieniawski, Z. (1965). Brittle fracture propagation in rock under compression. *International Journal of Fracture Mechanics*, 1 (3), p.137–155.

Hoek, E. and Brown, E. T. (1980). Empirical strength criterion for rock masses. *Journal of Geotechnical and Geoenvironmental Engineering*, 106 (ASCE 15715).

Hoek, E. and Brown, E. T. (1997). Practical estimates of rock mass strength. *International Journal of Rock Mechanics and Mining Sciences*, 34 (8), p.1165–1186.

Hoek, E. and Franklin, J. A. (1967). *A simple triaxial cell for field or laboratory testing of rock*. Imperial College of Science and Technology, University of London.

Hoek, E. and Martin, C. (2014). Fracture initiation and propagation in intact rock-a review. *Journal of Rock Mechanics and Geotechnical Engineering*, 6 (4), p.287–300.

Houben, M., Barnhoorn, A., Lie-A-Fat, J., Ravestein, T., Peach, C. and Drury, M. (2016). Microstructural characteristics of the Whitby Mudstone formation (UK). *Marine and Petroleum Geology*, 70, p.185–200.

Hough, E., Vane, C. H., Smith, N. J. and Moss-Hayes, V. L. (2014). The Bowland Shale in the Roosecote Borehole of the Lancaster Fells Sub-Basin, Craven Basin, UK: a potential UK shale gas play? In: *SPE/EAGE European Unconventional Resources Conference and Exhibition*, 2014.

Howell, R. A. (2018). UK public beliefs about fracking and effects of knowledge on beliefs and support: a problem for shale gas policy. *Energy Policy*, 113, p.721–730.

Hu, H., Li, A. and Zavala-Torres, R. (2017). Long-period long-duration seismic events during hydraulic fracturing: implications for tensile fracture development. *Geophysical Research Letters*.

Hubbert, M. K. and Willis, D. G. (1957). Mechanics of hydraulic fracturing. *Petroleum Transactions, AIME*, 210, p.153–168.

Hudson, J. A. and Harrison, J. P. (2000). *Engineering rock mechanics: an introduction to the principals*.

Hugman III, R. and Friedman, M. (1979). Effects of texture and composition on mechanical behavior of experimentally deformed carbonate rocks. *AAPG Bulletin*, 63 (9), American Association of Petroleum Geologists, p.1478–1489.

Hurd, O. and Zoback, M. D. (2012). Stimulated Shale Volume Characterization: Multiwell Case Study from the Horn River Shale: I. Geomechanics and Microseismicity. In: *SPE Annual Technical Conference and Exhibition*, 2012.

Inglis, C. E. (1913). Stresses in a plate due to the presence of cracks and sharp corners. *Transactions of the institute of naval architects*, 55 (219-241), p.193–198.

Ingraffea, A. P., Heuze, F. E., Ko, H.-Y., Gerstle, K. and others. (1976). Fracture Propagation In Rock: Laboratory Tests And Finite-Element Analysis. In: *The 17th US Symposium on Rock Mechanics (USRMS)*, 1976.

Irwin, G. R. (1948). Fracture dynamics. *Fracturing of metals*, 152, ASM Cleveland.

Irwin, G. R. (1957). Analysis of stresses and strains near the end of a crack traversing a plate. *J. appl. Mech.*

Irwin, G. and de Wit, R. (1983). A summary of fracture mechanics concepts. *Journal of Testing and Evaluation*, 11 (1), ASTM International, p.56–65.

Ishida, T. (2001). Acoustic emission monitoring of hydraulic fracturing in laboratory and field. *Construction and Building Materials*, 15 (5), p.283–295.

Ishida, T., Aoyagi, K., Niwa, T., Chen, Y., Murata, S., Chen, Q. and Nakayama, Y. (2012). Acoustic emission monitoring of hydraulic fracturing laboratory experiment with supercritical and liquid CO2. *Geophysical Research Letters*, 39 (16).

Ishida, T., Chen, Q. and Mizuta, Y. (1997). Effect of injected water on hydraulic fracturing deduced from acoustic emission monitoring. In: *Seismicity Associated with Mines, Reservoirs and Fluid Injections*, p.627–646.

Ishida, T., Chen, Q., Mizuta, Y. and Roegiers, J.-C. (2004). Influence of fluid viscosity on the hydraulic fracturing mechanism. *Journal of energy resources technology*, 126 (3), p.190–200.

Ito, T. and Hayashi, K. (1991). Physical background to the breakdown pressure in hydraulic fracturing tectonic stress measurements. In: *International Journal of Rock Mechanics and Mining Sciences & Geomechanics Abstracts*, 28 (4), 1991, p.285–293.

Jackson, D. and Mulholland, P. (1993). Tectonic and stratigraphic aspects of the East Irish Sea Basin and adjacent areas: contrasts in their post-Carboniferous structural styles. In: *Geological Society, London, Petroleum Geology Conference series*, 4 (1), 1993, p.791–808.

Jaeger, J. (1963). Extension failures in rocks subject to fluid pressure. *Journal of Geophysical Research*, 68 (21), p.6066–6067.

Jaeger, J. C., Cook, N. G. and Zimmerman, R. (2009). *Fundamentals of rock mechanics*. John Wiley & Sons.

Jarvie, D. M. (2012a). *Shale resource systems for oil and gas: Part 1—Shale-gas resource systems*. 97, AAPG Special Volumes, p.69–87.

Jarvie, D. M. (2012b). *Shale resource systems for oil and gas: Part 2—Shale-oil resource systems*. AAPG Special Volumes.

Jennings, A. (2011). Shale gas developments: enabled by technology. *First Break*, 29 (5), p.127–131.

Jones, C. and Meredith, P. (1998). An Experimental Study of Elastic Wave Propagation Anisotropy and Permeability Anisotropy in an Illitic Shale. In: *SPE/ISRM Rock Mechanics in Petroleum Engineering*, 1998.

Kassis, S. and Sondergeld, C. H. (2010). Fracture permeability of gas shale: Effect of roughness, fracture offset, proppant, and effective stress. In: *International oil and gas conference and exhibition in China*, 2010.

Keaney, G. M., Meredith, P., Murrell, S., Barker, J. and others. (2004). Determination of the effective stress laws for permeability and specific storage in a low porosity sandstone. In: *Gulf Rocks 2004, the 6th North America Rock Mechanics Symposium (NARMS)*, 2004.

Kemeny, J. M. and Cook, N. G. (1987). *Determination of rock fracture parameters from crack models for failure in compression*.

Ketcham, R. A., Slottke, D. T. and Sharp, J. M. (2010). Three-dimensional measurement of fractures in heterogeneous materials using high-resolution X-ray computed tomography. *Geosphere*, 6 (5), p.499–514.

Kilburn, C. R. (2003). Multiscale fracturing as a key to forecasting volcanic eruptions. *Journal of Volcanology and Geothermal Research*, 125 (3), p.271–289.

King, M., Pettitt, W., Haycox, J. and Young, R. (2012). Acoustic emissions associated with the formation of fracture sets in sandstone under polyaxial stress conditions. *Geophysical Prospecting*, 60 (1), p.93–102.

Kirby, S. H. (1980). Tectonic stresses in the lithosphere: Constraints provided by the experimental deformation of rocks. *Journal of Geophysical Research: Solid Earth*, 85 (B11), p.6353–6363.

Kirsch, C. (1898). Die theorie der elastizitat und die bedurfnisse der festigkeitslehre. *Zeitschrift des Vereines Deutscher Ingenieure*, 42, p.797–807.

Klinkenberg, L. (1941). The permeability of porous media to liquids and gases. In: *Drilling and production practice*, 1941.

Knott, J. F. (1973). *Fundamentals of fracture mechanics*. Gruppo Italiano Frattura.

Kranz, R., Frankel, A., Engelder, T. and Scholz, C. (1979). The permeability of whole and jointed Barre granite. In: *International Journal of Rock Mechanics and Mining Sciences &*

Geomechanics Abstracts, 16 (4), 1979, p.225–234.

Kranz, R., Saltzman, J. and Blacic, J. (1990). Hydraulic diffusivity measurements on laboratory rock samples using an oscillating pore pressure method. In: *International Journal of Rock Mechanics and Mining Sciences & Geomechanics Abstracts*, 27 (5), 1990, p.345–352.

Kumagai, H. and Chouet, B. A. (2000). Acoustic properties of a crack containing magmatic or hydrothermal fluids. *Journal of Geophysical Research: Solid Earth*, 105 (B11), p.25493–25512.

Kumar, A., Hammack, R., Zorn, E., Harbert, W. and others. (2016). Long period, long duration (LPLD) seismicity observed during hydraulic fracturing of the Marcellus Shale in Greene County, Pennsylvania. In: *2016 SEG International Exposition and Annual Meeting*, 2016.

Kuuskraa, V., Stevens, S. H. and Moodhe, K. D. (2013). *Technically recoverable shale oil and shale gas resources: an assessment of 137 shale formations in 41 countries outside the United States*.

Kwon, O., Kronenberg, A. K., Gangi, A. F. and Johnson, B. (2001). Permeability of Wilcox shale and its effective pressure law. *Journal of Geophysical Research: Solid Earth*, 106 (B9), p.19339–19353.

Labuz, J., Shah, S., Dowding, C. and others. (1983). Post peak tensile load-displacement response and the fracture process zone in rock. In: *The 24th US Symposium on Rock Mechanics (USRMS)*, 1983.

Lancaster, D., McKetta, S. and Lowry, P. (1993). Research findings help characterize Fort Worth basin's Barnett Shale. *Oil and Gas Journal;(United States)*, 91 (10).

Lange, F. (1974). Origin and use of fracture mechanics. In: *Concepts, Flaws, and Fractography*, p.3–15.

Law, B. and Curtis, J. (2002). Introduction to unconventional petroleum systems. *AAPG bulletin*, 86 (11), American Association of Petroleum Geologists, p.1851–1852.

Lechtenböhmer, S., Altmann, M., Capito, S., Matra, Z., Weindrorf, W. and Zittel, W. (2012). *Impacts of shale gas and shale oil extraction on the environment and on human health: study*.

Lee, W. and Hopkins, C. (1994). Characterization of tight reservoirs. *Journal of Petroleum Technology*, 46 (11), p.956–964.

Li, X., Feng, Z., Han, G., Elsworth, D., Marone, C., Saffer, D. and Cheon, D.-S. (2016). Breakdown pressure and fracture surface morphology of hydraulic fracturing in shale with H 2 O, CO 2 and N 2. *Geomechanics and Geophysics for Geo-Energy and Geo-Resources*, 2 (2), p.63–76.

Lisle, R. and Strom, C. (1982). Least-squares fitting of the linear Mohr envelope. *Quarterly Journal of Engineering Geology and Hydrogeology*, 15 (1), Geological Society of London, p.55–56.

Lockner, D. (1993). The role of acoustic emission in the study of rock fracture. In: *International Journal of Rock Mechanics and Mining Sciences & Geomechanics Abstracts*, 30 (7), 1993, p.883–899.

Lockner, D. A. and Beeler, N. M. (2002). Rock failure and earthquakes. *International Geophysics Series*, 81 (A), p.505–538.

Lockner, D. and Byerlee, J. (1977). Hydrofracture in Weber sandstone at high confining pressure and differential stress. *Journal of Geophysical Research*, 82 (14), p.2018–2026.

Lockner, D., Byerlee, J., Kuksenko, V., Ponomarev, A. and Sidorin, A. (1991). Quasi-static fault growth and shear fracture energy in granite. *Nature*, 350 (6313), p.39.

Lockner, D., Summers, R., Moore, D. and Byerlee, J. (1982). Laboratory measurements of reservoir rock from the Geysers Geothermal Field, California. In: *International Journal of Rock Mechanics and Mining Sciences & Geomechanics Abstracts*, 19 (2), 1982, p.65–80.

Loucks, R. G. and Ruppel, S. C. (2007). Mississippian Barnett Shale: Lithofacies and depositional setting of a deep-water shale-gas succession in the Fort Worth Basin, Texas. *AAPG bulletin*, 91 (4), American Association of Petroleum Geologists (AAPG), p.579–601.

Lubinski, A. (1954). The theory of elasticity for porous bodies displaying a strong pore structure. In: *Proc*, 1954, p.247–256.

Ma, L., Taylor, K. G., Dowey, P. J., Courtois, L., Gholinia, A. and Lee, P. D. (2017). Multi-scale 3D characterisation of porosity and organic matter in shales with variable TOC content and thermal maturity: Examples from the Lublin and Baltic Basins, Poland and Lithuania. *International Journal of Coal Geology*, 180, p.100–112.

Ma, L., Taylor, K. G., Lee, P. D., Dobson, K. J., Dowey, P. J. and Courtois, L. (2016). Novel 3D centimetre-to nano-scale quantification of an organic-rich mudstone: The Carboniferous Bowland Shale, Northern England. *Marine and Petroleum Geology*, 72, p.193–205.

MacKenzie, W. S., Adams, A. E. and Brodie, K. H. (2017). *Rocks and Minerals in Thin Section: A Colour Atlas*. CRC Press.

Malkowski, P. and Ostrowski, L. (2017). The Methodology for the Young Modulus Derivation for Rocks and Its Value. *Procedia Engineering*, 191, p.134–141.

Malone, S. D., Boyko, C. and Weaver, C. S. (1983). Seismic precursors to the Mount St. Helens eruptions in 1981 and 1982. *Science*, 221 (4618), p.1376–1378.

Martin, C. and Chandler, N. (1994). The progressive fracture of Lac du Bonnet granite. In: *International Journal of Rock Mechanics and Mining Sciences & Geomechanics Abstracts*, 31 (6), 1994, p.643–659.

Martin, C. D. (1997). Seventeenth Canadian geotechnical colloquium: the effect of cohesion loss and stress path on brittle rock strength. *Canadian Geotechnical Journal*, 34 (5), NRC Research Press, p.698–725.

Martin, C., Kaiser, P. and McCreath, D. (1999). Hoek-Brown parameters for predicting the depth of brittle failure around tunnels. *Canadian Geotechnical Journal*, 36 (1), NRC Research Press, p.136–151.

May, V. and Hansom, J. D. (2003). *Coastal Geomorphology of Great Britain*. Joint Nature Conservation Committee.

McClintock, F. (1962). Friction on Griffith cracks in rocks under pressure. In: *Proc. 4th US Nat. Congr. Appl. Mech.*, 2, 1962, p.1015–1022.

McKernan, R., Mecklenburgh, J., Rutter, E. and Taylor, K. (2017). Microstructural controls on the pressure-dependent permeability of Whitby mudstone. *Geological Society, London, Special Publications*, 454 (1), p.39–66.

Meyer, R. (2002). Anisotropy of sandstone permeability. *CREWES Research Report*, 14, p.1–12.

Miller, R. K. and McIntire, P. (1987). Nondestructive testing handbook; v. 5', American Society for Nondestructive Testing. *INC., USA, ISBN 0-931403-02-2*.

Mitchell, C., Kurpan, J., Snelling, P. and others. (2013). Detecting long-period long-duration microseismic events during hydraulic fracturing in the Cline Shale Formation, West Texas: A case study. In: *2013 SEG Annual Meeting*, 2013.

Mogi, K. (1967). Effect of the intermediate principal stress on rock failure. *Journal of Geophysical Research*, 72 (20), p.5117–5131.

Mogi, K. (1968). Source locations of elastic shocks in the fracturing process in rocks. *Bull. Earthq. Res. Inst., Univ. Tokyo*, 46, p.1103–1125.

Mokhtari, M. (2015). Characterization of anisotropy in organic-rich shales: Shear and tensile failure, wave velocity, matrix and fracture permeability. *Colorado School of Mines*, PhD thesis.

Molenda, M., Stoeckhert, F., Brenne, S., Alber, M. and others. (2015). Acoustic emission monitoring of laboratory scale hydraulic fracturing experiments. In: *49th US Rock Mechanics/Geomechanics Symposium*, 2015.

Montgomery, C. T. and Smith, M. B. (2010). Hydraulic fracturing: History of an enduring technology. *Journal of Petroleum Technology*, 62 (12), p.26–40.

Mullen, J. (2010). Petrophysical characterization of the Eagle Ford Shale in south Texas. In: *Canadian Unconventional Resources and International Petroleum Conference*, 2010.

Murrell, S. (1963). A criterion for brittle fracture of rocks and concrete under triaxial stress and the effect of pore pressure on the criterion. *Rock mechanics*, p.563–577.

Murrell, S. (1964). The theory of the propagation of elliptical Griffith cracks under various conditions of plane strain or plane stress: Parts II and III. *British Journal of Applied Physics*, 15 (10), IOP Publishing, p.1211.

Murrell, S. A. F. (1965). The effect of triaxial stress systems on the strength of rocks at atmospheric temperatures. *Geophysical Journal International*, 10 (3), p.231–281.

Murrell, S. and Digby, P. (1970). The theory of brittle fracture initiation under triaxial stress conditions—I. *Geophysical Journal International*, 19 (4), p.309–334.

Nasseri, M., Goodfellow, S., Lombos, L. and Young, R. (2014). 3-D transport and acoustic properties of Fontainebleau sandstone during true-triaxial deformation experiments. *International Journal of Rock Mechanics and Mining Sciences*, 69, p.1–18.

Nasseri, M., Rao, K. and Ramamurthy, T. (2003). Anisotropic strength and deformational behavior of Himalayan schists. *International Journal of Rock Mechanics and Mining Sciences*, 40 (1), p.3–23.

Navarette, M., Chorn, L., Maucec, M. and others. (2013). A Holistic Approach to the Appraisal Stage of Shale Gas Resources. In: *SPE Unconventional Resources Conference and Exhibition-Asia Pacific*, 2013.

Nie, Y., Zhang, G., Tang, M., Zhao, B., Pan, R., Liu, Z., Xu, S., Yang, X. and others. (2017). Effect of Water-Oil Saturation on Fracture Toughness of Reservoir Rocks During Long-Term Production. In: *51st US Rock Mechanics/Geomechanics Symposium*, 2017.

Nygård, R., Gutierrez, M., Bratli, R. K. and Høeg, K. (2006). Brittle-ductile transition, shear failure and leakage in shales and mudrocks. *Marine and Petroleum Geology*, 23 (2), p.201–212.

Obert, L. (1977). The microseismic method: discovery and early history. In: *First conf. on acoustic emission/microseismic activity in geologic structures and materials*, 1977, p.11–12.

Ohminato, T. and Ereditato, D. (1997). Broadband seismic observations at Satsuma-Iwojima Volcano, Japan. *Geophysical research letters*, 24 (22), p.2845–2848.

Ohnaka, M. and Mogi, K. (1982). Frequency characteristics of acoustic emission in rocks under uniaxial compression and its relation to the fracturing process to failure. *Journal of geophysical research: Solid Earth*, 87 (B5), p.3873–3884.

Olsson, W. A. (1974). Grain size dependence of yield stress in marble. *Journal of Geophysical Research*, 79 (32), p.4859–4862.

Orowan, E. (1949). Fracture and strength of solids. *Reports on progress in physics*, 12 (1), IOP Publishing, p.185.

Parate, N. (1973). Influence of water on the strength of limestone. *Transactions of the Society of Mining, AIME*, 254, p.127–131.

Paris, P. C. and Sih, G. C. (1965). Stress analysis of cracks. In: *Fracture toughness testing and its applications*, ASTM International.

Paterson, M. S. and Wong, T. (2005). *Experimental rock deformation-the brittle field*. Springer-Verlag Berlin Heidelberg.

Paul, C., Allison, P. A. and Brett, C. E. (2008). The occurrence and preservation of ammonites in the Blue Lias Formation (lower Jurassic) of Devon and Dorset, England and their palaeoecological, sedimentological and diagenetic significance. *Palaeogeography, Palaeoclimatology, Palaeoecology*, 270 (3), p.258–272.

Pearson, C. (1981). The relationship between microseismicity and high pore pressures during hydraulic stimulation experiments in low permeability granitic rocks. *Journal of Geophysical Research: Solid Earth*, 86 (B9), p.7855–7864.

Peck, L. (1983). Stress corrosion and crack propagation in Sioux quartzite. *Journal of Geophysical Research: Solid Earth*, 88 (B6), p.5037–5046.

Du Plessis, A., Broeckhoven, C., Guelpa, A. and Le Roux, S. G. (2017). Laboratory x-ray micro-computed tomography: a user guideline for biological samples. *GigaScience*, 6 (6), Oxford University Press, p.1–11.

Power, J. A., Lahr, J. C., Page, R. A., Chouet, B. A., Stephens, C. D., Harlow, D. H., Murray, T. L. and Davies, J. N. (1994). Seismic evolution of the 1989-1990 eruption sequence of Redoubt Volcano, Alaska. *Journal of Volcanology and Geothermal Research*, 62 (1-4), p.69–94.

Pradhan, S., Stroisz, A. M., Fjær, E., Stenebråten, J. F., Lund, H. K. and Sønstebø, E. F. (2015). Stress-induced fracturing of reservoir rocks: acoustic monitoring and microCT image analysis. *Rock Mechanics and Rock Engineering*, 48 (6), p.2529–2540.

Price, N. (1960). The compressive strength of coal measure rocks. *Colliery Engineering*, 37 (437), p.283–292.

Reinicke, A., Rybacki, E., Stanchits, S., Huenges, E. and Dresen, G. (2010). Hydraulic fracturing stimulation techniques and formation damage mechanisms—Implications from laboratory testing of tight sandstone-proppant systems. *Chemie der Erde-Geochemistry*, 70, p.107–117.

Renard, F., Bernard, D., Desrues, J. and Ougier-Simonin, A. (2009). 3D imaging of fracture propagation using synchrotron X-ray microtomography. *Earth and Planetary Science Letters*, 286 (1), p.285–291.

Robinson Jr, L. (1959). *Effects of Pore and Confining Pressures on Failure Characteristics of Sedimentary Rocks*. Society of Petroleum Engineers.

Rubin, A. M. (1993). Tensile fracture of rock at high confining pressure: implications for dike propagation. *Journal of Geophysical Research: Solid Earth*, 98 (B9), p.15919–15935.

Rummel, F. (1987). Fracture mechanics approach to hydraulic fracturing stress measurement. *Fracture mechanics of rock*, p.217.

Rushing, J., Newsham, K., Lasswell, P., Cox, J., Blasingame, T. and others. (2004). Klinkenerg-corrected permeability measurements in tight gas sands: steady-state versus unsteady-state techniques. In: *SPE Annual Technical Conference and Exhibition*, 2004.

Rutledge, J. T. and Phillips, W. S. (2003). Hydraulic stimulation of natural fractures as revealed by induced microearthquakes, Carthage Cotton Valley gas field, east Texas. *Geophysics*, 68 (2), Society of Exploration Geophysicists, p.441–452.

Rutter, E. H. (1972). The influence of interstitial water on the rheological behaviour of calcite rocks. *Tectonophysics*, 14 (1), p.13–33.

Rutter, E. H. and Mecklenburgh, J. (2017). Hydraulic conductivity of bedding-parallel cracks in shale as a function of shear and normal stress. *Geological Society, London, Special Publications*, 454 (1), Geological Society of London, p.67–84.

Rutter, E., McKernan, R., Mecklenburgh, J. and May, S. (2013). Permeability of stress sensitive formations: its importance for shale gas reservoir simulation and evaluation. *Petro Industry News*, 14, p.44–45.

Rybacki, E., Reinicke, A., Meier, T., Makasi, M. and Dresen, G. (2015). What controls the mechanical properties of shale rocks?-Part I: Strength and Young's modulus. *Journal of Petroleum Science and Engineering*, 135, p.702–722.

Saif, T., Lin, Q., Bijeljic, B. and Blunt, M. J. (2017). Microstructural imaging and characterization of oil shale before and after pyrolysis. *Fuel*, 197, p.562–574.

Sammonds, P. (1999). Understanding the fundemental physics governing the evolution and dynamics of the Earth'crust and ice sheets. *Philosophical Transactions of the Royal Society of*

London A: Mathematical, Physical and Engineering Sciences, 357 (1763), p.3377–3401.

Sayers, C. M. (1999). Stress-dependent seismic anisotropy of shales. *Geophysics*, 64, p.93.

Scheidegger, A. (1962). Stresses in the earth's crust as determined from hydraulic fracturing data. *Geologie und Bauwesen*, 27 (2), p.1.

Schieber, J., Lazar, R., Bohacs, K., Klimentidis, R., Dumitrescu, M. and Ottmann, J. (2016). *An SEM Study of Porosity in the Eagle Ford Shale of Texas—Pore Types and Porosity Distribution in a Depositional and Sequence-stratigraphic Context*. AAPG Special Volumes.

Schmidt, R. A. (1980). A microcrack model and its significance to hydraulic fracturing and fracture toughness testing. In: *The 21st US Symposium on Rock Mechanics (USRMS)*, 1980.

Schmidt, R. and Huddle, C. (1977). Effect of confining pressure on fracture toughness of Indiana limestone. In: *International Journal of Rock Mechanics and Mining Sciences & Geomechanics Abstracts*, 14 (5-6), 1977, p.289–293.

Schmitt, D. R. and Zoback, M. D. (1992). Diminished pore pressure in low-porosity crystalline rock under tensional failure: Apparent strengthening by dilatancy. *Journal of Geophysical Research: Solid Earth*, 97 (B1), p.273–288.

Schmitt, D. and Zoback, M. (1989). Laboratory tests of the effects of pore pressure on tensile failure. In: *ISRM International Symposium*, 1989.

Schmitt, D. and Zoback, M. (1993). Infiltration effects in the tensile rupture of thin walled cylinders of glass and granite: Implications for the hydraulic fracturing breakdown equation. In: *International journal of rock mechanics and mining sciences & geomechanics abstracts*, 30 (3), 1993, p.289–303.

Scholz, C. (1968a). Experimental study of the fracturing process in brittle rock. *Journal of Geophysical Research*, 73 (4), p.1447–1454.

Scholz, C. (1968b). Microfracturing and the inelastic deformation of rock in compression. *Journal of Geophysical Research*, 73 (4), p.1417–1432.

Schormair, N., Thuro, K. and Plinninger, R. (2006). The influence of anisotropy on hard rock drilling and cutting. *The Geological Society of London, IAEG, Paper*, (491), p.1–11.

Selley, R. C. (2012). UK shale gas: the story so far. *Marine and petroleum geology*, 31 (1), p.100–109.

Serdengecti, S. and Boozer, G. (1961). The effects of strain rate and temperature on the behavior of rocks subjected to triaxial compression. In: *The 4th US Symposium on Rock Mechanics (USRMS)*, 1961.

Seto, M., Nag, D., Vutukuri, V. and Katsuyama, K. (1997). Effect of chemical additives on the strength of sandstone. *International Journal of Rock Mechanics and Mining Sciences*, 34 (3-4), p.280–e1.

Simms, M., Chidlaw, N., Morton, N. and Page, K. (2004). British Lower Jurassic stratigraphy: an introduction. *GEOLOGICAL CONSERVATION REVIEW SERIES*, 30, p.1–50.

Smith, N., Turner, P. and Williams, G. (2010). UK data and analysis for shale gas prospectivity. In: *Geological Society, London, Petroleum Geology Conference Series*, 7 (1), 2010, p.1087–1098.

Solberg, P., Lockner, D. and Byerlee, J. (1980). Hydraulic fracturing in granite under geothermal conditions. In: *International Journal of Rock Mechanics and Mining Sciences & Geomechanics Abstracts*, 17 (1), 1980, p.25–33.

Sondergeld, C. H., Ambrose, R. J., Rai, C. S., Moncrieff, J. and others. (2010). Micro-structural studies of gas shales. In: *SPE Unconventional Gas Conference*, 2010.

Sone, H. and Zoback, M. D. (2013a). Mechanical properties of shale-gas reservoir rocks—Part 1: Static and dynamic elastic properties and anisotropy. *Geophysics*, 78 (5), Society of Exploration Geophysicists, p.D381–D392.

Sone, H. and Zoback, M. D. (2013b). Mechanical properties of shale-gas reservoir rocks—Part 2: Ductile creep, brittle strength, and their relation to the elastic modulusMechanical properties of gas shale—Part 2. *Geophysics*, 78 (5), GeoScienceWorld, p.D393–D402.

Song, I. and Haimson, B. (2001). Effect of pressurization rate and initial pore pressure on the magnitude of hydrofracturing breakdown pressure in Tablerock sandstone. In: *DC Rocks 2001, The 38th US Symposium on Rock Mechanics (USRMS)*, 2001.

Stanchits, S., Burghardt, J., Surdi, A., Edelman, E. and Suarez-Rivera, R. (2014a). Acoustic Emission Monitoring of Heterogeneous Rock Hydraulic Fracturing. *48th US Rock Mechanics/Geomechanics Symposium, American Rock Mechanics Association*.

Stanchits, S., Fortin, J., Gueguen, Y. and Dresen, G. (2009). Initiation and propagation of compaction bands in dry and wet Bentheim sandstone. *Pure and Applied Geophysics*, 166 (5-7), p.843–868.

Stanchits, S., Mayr, S., Shapiro, S. and Dresen, G. (2011). Fracturing of porous rock induced by fluid injection. *Tectonophysics*, 503 (1), p.129–145.

Stanchits, S., Surdi, A., Edelman, E. and Suarez-Rivera, R. (2012a). Acoustic emission and ultrasonic transmission monitoring of hydraulic fracture propagation in heterogeneous rock samples. *46th U.S. Rock Mechanics/Geomechanics Symposium, 24-27 June, Chicago, Illinois*.

Stanchits, S., Surdi, A., Gathogo, P., Edelman, E. and Suarez-Rivera, R. (2014b). Onset of hydraulic fracture initiation monitored by acoustic emission and volumetric deformation measurements. *Rock Mechanics and Rock Engineering*, 47 (5), p.1521–1532.

Stanchits, S., Surdi, A. and Suarez-Rivera, R. (2012b). Monitoring hydraulic fracturing of tight shale by acoustic emission and ultrasonic transmission techniques. In: *Proceeding of 74th EAGE conference and exhibition incorporating SPE EUROPEC*, 2012.

Stoeckhert, F., Brenne, S., Molenda, M. and Alber, M. (2016). Mode I fracture toughness of rock under confining pressure. *Rock Mechanics and Rock Engineering: From the Past to the Future*, CRC Press, p.313.

Stoeckhert, F., Brenne, S., Molenda, M., Alber, M. and others. (2014). Fracture mechanical evaluation of hydraulic fracturing laboratory experiments. In: *ISRM Regional Symposium-EUROCK 2014*, 2014.

Stoeckhert, F., Molenda, M., Brenne, S. and Alber, M. (2015). Fracture propagation in sandstone and slate-Laboratory experiments, acoustic emissions and fracture mechanics. *Journal of Rock Mechanics and Geotechnical Engineering*, 7 (3), p.237–249.

Tada, H., Paris, P. C. and Irwin, G. R. (1973). The stress analysis of cracks. *Handbook, Del Research Corporation*.

Tan, Y., Pan, Z., Liu, J., Feng, X.-T. and Connell, L. D. (2018). Laboratory study of proppant on shale fracture permeability and compressibility. *Fuel*, 222, p.83–97.

Terzaghi, K. von. (1936). The shearing resistance of saturated soils and the angle between the planes of shear. In: *First international conference on soil Mechanics, 1936*, 1, 1936, p.54–59.

Thallak, S., Holder, J., Gray, K. and others. (1993). The pressure dependence of apparent hydrofracture toughness. In: *The 34th US Symposium on Rock Mechanics (USRMS)*, 1993.

Thompson, B. D. (2006). Acoustic emission investigation of fracture and fault mechanics in the laboratory. *University of Liverpool*, PhD thesis.

Thompson, B. D., Young, R. P. and Lockner, D. A. (2005). Observations of premonitory acoustic emission and slip nucleation during a stick slip experiment in smooth faulted Westerly granite. *Geophysical research letters*, 32 (10).

Thompson, B., Young, R. and Lockner, D. A. (2009). Premonitory acoustic emissions and stick-slip in natural and smooth-faulted Westerly granite. *Journal of Geophysical Research: Solid Earth*, 114 (B2).

Timoshenko, S. P. and Goodier, J. N. (1970). *Theory of elasticity*. McGraw-Hill, New York London.

Tuffen, H. and Dingwell, D. (2005). Fault textures in volcanic conduits: evidence for seismic trigger mechanisms during silicic eruptions. *Bulletin of Volcanology*, 67 (4), p.370–387.

Ulusay, R. (2014). *The ISRM suggested methods for rock characterization, testing and monitoring: 2007-2014*. Springer.

Unglert, K. and Jellinek, A. (2015). Volcanic tremor and frequency gliding during dike intrusions at Kīlauea—A tale of three eruptions. *Journal of Geophysical Research: Solid Earth*, 120 (2), p.1142–1158.

De Vallejo, L. G. and Ferrer, M. (2011). *Geological engineering*. CRC Press.

Vermylen, J. P. (2011). Geomechanical studies of the Barnett shale, Texas, USA. *Stanford University, PhD thesis*.

Vermylen, J. and Zoback, M. D. (2011). Hydraulic fracturing, microseismic magnitudes, and stress evolution in the Barnett Shale, Texas, USA. In: *SPE Hydraulic Fracturing Technology Conference*, 2011.

Vidic, R. D., Brantley, S. L., Vandenbossche, J. M., Yoxtheimer, D. and Abad, J. D. (2013). Impact of shale gas development on regional water quality. *Science (New York, N.Y.)*, 340 (6134), p.1235009. [Online]. Available at: doi:10.1126/science.1235009.

Vinciguerra, S., Meredith, P. G. and Hazzard, J. (2004). Experimental and modeling study of fluid pressure-driven fractures in Darley Dale sandstone. *Geophysical research letters*, 31 (9).

Walder, J. and Nur, A. (1986). Permeability measurement by the pulse-decay method: Effects of poroelastic phenomena and non-linear pore pressure diffusion. In: *International Journal of Rock Mechanics and Mining Sciences & Geomechanics Abstracts*, 23 (3), 1986, p.225–232.

Walls, J. and Sinclair, S. (2011). Eagle Ford Shale characterization by digital rock physics (DRP). *SPWLA Short Course "Lab Measurements of Shale Gas Cores" (Colorado Springs, CO,)*.

Walsh, J. (1981). Effect of pore pressure and confining pressure on fracture permeability. In: *International Journal of Rock Mechanics and Mining Sciences & Geomechanics Abstracts*, 18 (5), 1981, p.429–435.

Wang, Q., Chen, X., Jha, A. N. and Rogers, H. (2014). Natural gas from shale formation - The evolution, evidences and challenges of shale gas revolution in United States. *Renewable and Sustainable Energy Reviews*, 30, p.1–28.

Warner, D. (2011). Shale gas in Australia: a great opportunity comes with significant challenges. *Preview*, 2011 (155), p.18–21.

Warpinski, N. R., Clark, J. A., Schmidt, R. A. and Huddle, C. W. (1981). *Laboratory investigation on the effect of in situ stresses on hydraulic fracture containment*.

Warpinski, N. R., Du, J. and Zimmer, U. (2012). Measurements of hydraulic-fracture-induced seismicity in gas shales. *SPE Production & Operations*, 27 (03), p.240–252.

Warpinski, N., Wolhart, S. and Wright, C. (2004). Analysis and prediction of microseismicity induced by hydraulic fracturing. *SPE Journal*, 9 (1), p.24–33.

Wawersik, W. and Fairhurst, C. (1970). A study of brittle rock fracture in laboratory compression experiments. In: *International Journal of Rock Mechanics and Mining Sciences & Geomechanics Abstracts*, 7 (5), 1970, p.561–575.

Weedon, G. (1986). Hemipelagic shelf sedimentation and climatic cycles: the basal Jurassic (Blue Lias) of South Britain. *Earth and Planetary Science Letters*, 76 (3-4), p.321–335.

Whittaker, B. N., Singh, R. N. and Sun, G. (1992). Rock fracture mechanics principals, design and applications, developments in geotechnical engineering. *Netherlands: Elsevier Publishers*.

Winter, R.-B. (1983). *Bruchmechanische Gesteinsuntersuchungen mit dem Bezug zu hydraulischen Frac-Versuchen in Tiefbohrungen*.

Wong, R. H., Chau, K. and Wang, P. (1996). Microcracking and grain size effect in Yuen Long marbles. In: *International journal of rock mechanics and mining sciences & geomechanics abstracts*, 33 (5), 1996, p.479–485.

Wong, T. (1982). Shear fracture energy of Westerly granite from post-failure behavior. *Journal of Geophysical Research: Solid Earth*, 87 (B2), p.990–1000.

Wyllie, D. C. and Mah, C. (2014). *Rock slope engineering*. Spon Press, London and New York.

Zaki, A., Chai, H. K., Aggelis, D. G. and Alver, N. (2015). Non-destructive evaluation for corrosion monitoring in concrete: A review and capability of acoustic emission technique. *Sensors*, 15 (8), Multidisciplinary Digital Publishing Institute, p.19069–19101.

Zhang, A., Wagner, F., Stanchits, S., Dresesn, G., Andrsen, R. and Haidekker, M. (1998). Source analysis of acousic emission in aue granite cores under symmetric and asymmetric compressive load. *Geophys. J. Int*, 135, p.1113–1130.

Zhang, J., Kamenov, A., Zhu, D. and Hill, A. (2013). Laboratory measurement of hydraulic fracture conductivities in the Barnett shale. In: *IPTC 2013: International Petroleum Technology Conference*, 2013.

Zhang, S., Sheng, J. J. and Shen, Z. (2017). Effect of hydration on fractures and permeabilities in Mancos, Eagleford, Barnette and Marcellus shale cores under compressive stress

conditions. *Journal of Petroleum Science and Engineering*, 156, p.917–926.

Zhu, X.-K. and Joyce, J. A. (2012). Review of fracture toughness (G, K, J, CTOD, CTOA) testing and standardization. *Engineering Fracture Mechanics*, 85, p.1–46.

Zoback, M. D. (2007). *Reservoir geomechanics*. Cambridge University Press, Cambridge.

Zoback, M. D. and Byerlee, J. (1975). Permeability and effective stress: geologic notes. *AAPG Bulletin*, 59 (1), p.154–158.

Zoback, M. D. and Pollard, D. D. (1978). Hydraulic fracture propagation and the interpretation of pressure-time records for in-situ stress determinations. In: *19th US Symposium on Rock Mechanics (USRMS)*, 1978.

Zoback, M., Rummel, F., Jung, R. and Raleigh, C. (1977). Laboratory hydraulic fracturing experiments in intact and pre-fractured rock. In: *International Journal of Rock Mechanics and Mining Sciences & Geomechanics Abstracts*, 14 (2), 1977, p.49–58.

Appendices

Appendix A.1: List of references for hydraulic fracturing laboratory experiments

Appendix A.1: List of references for hydraulic fracturing laboratory experiments.

Abbreviations: cyl = cylindrical specimens, cub = cuboid specimens, sleeve = experiments with jacketed boreholes.

Sample material: and = andesite, cem = cement, dia = diatomite, dol = dolomite, gab = gabbro, gla = glass, grn = granite, hyd = hydrostone, lim = limestone, mrb = marble, phy = pyrophyllite, pls = plaster, PMMA = polymethyl methacrylate, rhy = rhyolite, sha = shale, sla = slate, slt = rock salt, sst = sandstone.

Author	Focus of experiments	Cyl	Cub	Sleeve	Material	Outer diameter (mm)	Edge length (mm)	BH diameter (mm)	BH length	Anisotropy	Orientation of fracture	Injection fluid	AE	CT and fracture pattern analysis	Radial deformation
Hubbert and Willis (1957)	Confirm theoretical results	x			gelatin							plaster slurry	no	no	no
Haimson and Fairhurst (1969b)	Initiation, orientation and location of hydrofractures, development of theoretical criteria	x	x		hyd	127	127x127x140	7.6	half	isotropic		oils with different viscosity	no	no	no
Haimson and Fairhurst (1969b)	Effect of fluid infiltration	x	x		mrb, grn, dol, sst, hyd	127	127x127x140	7.6 (11–36)							
Haimson and Avasthi (1973)		x	x		sla	100	100x100x200	7.6							
Zoback et al. (1977)	Effect of pressurisation rate and influence of pre-existing cracks	x			sst, gab	30		2–3	full	isotropic		oil	yes	no	no
Zoback et al. (1977)	Effect of pressurisation rate and influence of pre-existing cracks		x		sst, gab		120	10.5	half	isotropic		oil and oil/water mixture	yes	no	no
Lockner and Byerlee (1977)	Location and orientation of fracture planes	x			sst	25.4 and 76.2		1.6	full	isotropic		oil	yes	no	no
Abou-Sayed et al. (1978)	Supply material properties for field interpretations	x		x	sha	96.5		92.7	full	anisotropic					
Daneshy (1976)	Effect of rock properties on fracture propagation	x			sst, lim		76–152x304	2.54							
Solberg et al. (1980)		x			grn	15.9		1.6							
Anderson (1981)			x		sst, lim	50–100		6.35							
Warpinski et al. (1981)		x			sst, tuff	200		19							

Author	Focus of experiments	Cyl	Cub	Sleeve	Material	Outer diameter (mm)	Edge length (mm)	BH diameter (mm)	BH length	Anisotropy	Orientation of fracture	Injection fluid	AE	CT and fracture pattern analysis	Radial deformation
Blanton (1982)			x		sst, lim		305x305x380	3							
Lockner et al. (1982)		x			greywacke	76.2		1.6							
Winter (1983)		x		x	sst	30		2.5							
Rummel (1987)	Derive material properties for field data interpretation	x	x		grn, sst, lim, mrb, gab, slt	30		2.5	full	isotropic		oil	no	no	no
Ito and Hayashi (1991)	To verify theoretical breakdown pressures		x	x	and		300x300x300	10,15,30	half	anisotropic	parallel	water	yes	no	no
Haimson and Zhao (1991)	Size and pressurisation rate effects on hydraulic fracturing	x			grn, lim	20-250		3.2–50.8		isotropic		water and oil	yes	no	no
Schmitt and Zoback (1992)	Diminished pore pressures and dilatancy prior failure	x			grn	110		64.0	full	isotropic		kerosene	no	no	yes
Schmitt and Zoback (1993)	Infiltrations effects during hydraulic fracturing	x			grn, glass	110-150		64.0	sealed section	isotropic		kerosene	no	no	yes
Ishida et al. (1997)	Effect of injected water in hydraulic fracturing		x	x	grn		190x190x190	20							
Song and Haimson (2001)	Effect of pressurisation rate and initial pore pressure	x			sst	102		13	full	isotropic		oil	yes	no	no
Ishida (2001)	Effect of viscosity of injection fluid		x	x	grn		200x200x200	10	sealed section (60mm)	anisotropic	parallel	water, oil and with sleeve	yes	no	no
Ishida et al. (2004)	Effect of viscosity of injection fluid		x	x	grn		190x190x190	20							
Vinciguerra et al. (2004)	Comparison of experimental and numerical results for MHF	x		x	sst	40		8	full	isotropic		water	yes	no	no
Chitrala et al. (2010)		x			lim, sst, phy	100		6.35							
Chitrala et al. (2012)	Microseismicity and fracture morphology	x			sst, phy	100		10	half	sst isotropic and phy anisotropic		water	yes	no	no

Author	Focus of experiments	Cyl	Cub	Sleeve	Material	Outer diameter (mm)	Edge length (mm)	BH diameter (mm)	BH length	Anisotropy	Orientation of fracture	Injection fluid	AE	CT and fracture pattern analysis	Radial deformation
Stanchits et al. (2012a)	Initiation and growth of hydrofractures in sandstone		x		sst		279x279x381	25.4	half	isotropic		oil	yes	no	yes
Stanchits et al. (2012b)	Effect of fluid viscosity on fracture initiation and propagation		x		sha		279x279x381	25.4	full	anisotropic	parallel	water and oil	yes	no	yes
Alpern et al. (2012)	Effect of different fluids		x		PMMA		101 and 121	3.66		isotropic			no	no	no
Brenne et al. (2013)	Comparison of sleeve and non-sleeve fracturing	x		x	mrb, lim, sst, and, rhy	40 and 62		4 and 6	full	isotropic and anisotropic	parallel	water	yes	no	no
Brenne et al. (2014)	Effect of bedding orientation	x		x	sla	40		4.0	full	anisotropic	various angles	water	yes	no	yes
Stoeckhert et al. (2014)	Effect of bedding orientation and pressurisation rates	x			and, rhy, sst, lst, sla, mrb	40 and 62		4 and 6.2	full	sla anisotropic, rest isotropic	various for the slate	water	yes	no	no
Stanchits et al. (2014a)	Effect of discontinuities in sandstone and shale		x		sst, sha		279x279x381	25.4	full and half	Sha anisotropic, sst isotropic	parallel	water and high viscosity fluid	yes	no	no
Stanchits et al. (2014b)	Onset of hydraulic fracture initiation in sandstone		x		sst		279x279x381	25.4	half	isotropic		oils with different viscosity	yes	no	no
Goodfellow (2015)	Energy budget of hydraulic fracturing	x			grn	50		6.35	half	isotropic		water	yes	CT	yes
Gan et al. (2015)	Effect of fluid infiltration and exclusion on breakdown pressures		x		PMMA		101 and 121mm	3.66	half	isotropic		He, N_2, CO_2, Ar, sulfur hexa-fluoride, water	no	no	no

Author	Focus of experiments	Cyl	Cub	Sleeve	Material	Outer diameter (mm)	Edge length (mm)	BH diameter (mm)	BH length	Anisotropy	Orientation of fracture	Injection fluid	AE	CT and fracture pattern analysis	Radial deformation
Molenda et al. (2015)	AE location		x	x	rhy, sst, sla		150	13	full	sla anisotropic, rest isotropic	parallel	water	yes	no	no
Alber et al. (2015)	Effect of bedding orientation		x	x	sla					anisotropic	various degrees relative to bedding	water	no	no	no
Stoeckhert et al. (2015)	Fracture propagation in slate and sandstone		x	x	sst, sla			5	full	sla anisotropic, sst isotropic	parallel	water	yes	no	no
Chen et al. (2015)	Effect of viscosity on fracture propagation and morphology		x		grn		170x170x170	20	packer (60mm)	anisotropic	parallel	CO_2, water and oil	yes	yes	no
Pradhan et al. (2015)	Fracture behaviour and morphology	x			sst, chalk	51		10.5	full	isotropic		silicon oil	yes	yes	yes
Li et al. (2016)	Effect of different gas compositions on fracture propagation and morphology	x			sh	25		2.5	half	anisotropic		water, CO_2 and N_2	yes	no	no
Diaz et al. (2016)	Effect of cleavage anisotropy on fracture behaviour in granite	x			grn	50		8	full	anisotropic	various	water	no	yes	no
He et al. (2016)	Fracture pattern comparison of three rock types	x			sst, grn, sha	50		8	full	isotropic sst and granite, anisotropic sha	various for the shale	water	no	yes	yes
He et al. (2018)	Effect of bedding orientation on fracture propagation direction	x			sha	50		8	half	anisotropic	various	water and CO_2	no	no	no

Appendix A.2: Functions for linear fracture mechanics model

Table A.2-1: Values for functions $f(a_0/r_i)$ and $g(a_0/r_i)$ determined by Paris and Sih (1965)

a_0/r_i	One radial crack		Two symmetrical radial cracks	
	$f(a_0/r_i)$	$g(a_0/r_i)$	$f(a_0/r_i)$	$g(a_0/r_i)$
0.00	2.26	3.39	2.26	3.39
0.10	1.98	2.73	2.06	2.93
0.20	1.82	2.30	1.83	2.41
0.30	1.69	2.04	1.70	2.15
0.40	1.58	1.86	1.61	1.96
0.50	1.49	1.73	1.57	1.83
0.60	1.42	1.64	1.52	1.71
0.80	1.32	1.47	1.43	1.58
1.00	1.22	1.37	1.38	1.45
1.50	1.06	1.18	1.26	1.29
2.00	1.01	1.06	1.20	1.21
3.00	0.93	0.94	1.13	1.14
5.00	0.81	0.81	1.06	1.07
10.00	0.75	0.75	1.03	1.03
∞	0.707	0.707	1.00	1.00

Appendix A.3: Technical drawings waterguide (fracker)

RevNo	Revision note	Date	Signature	Checked
B	Adding 4 o-rings along the stick	22/03/16		

Top view

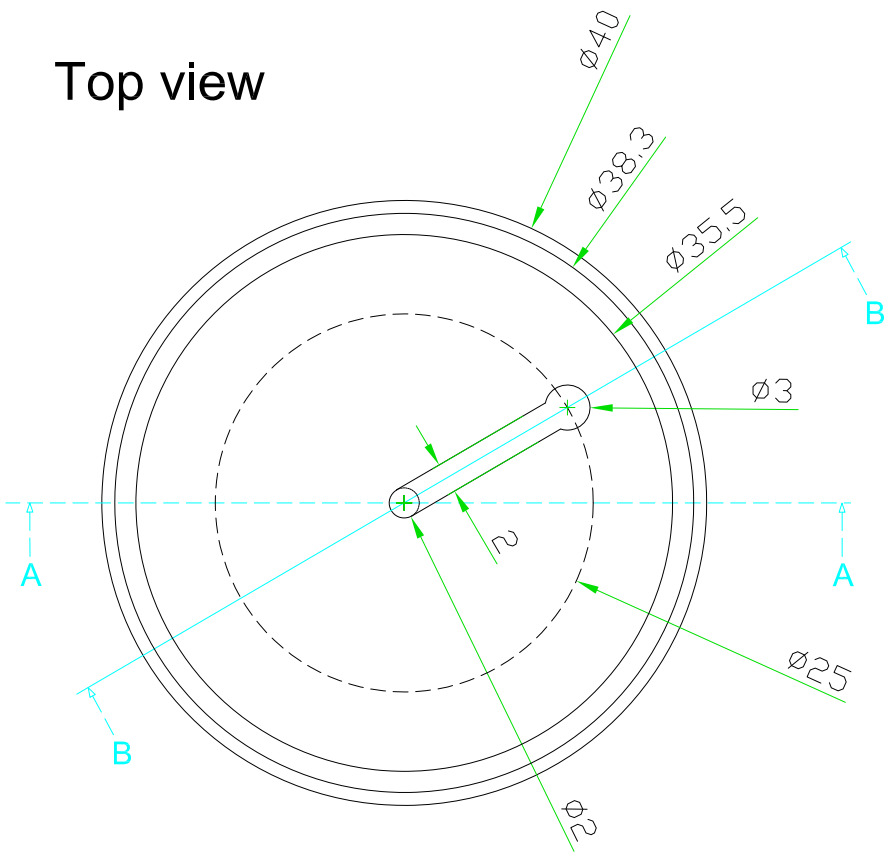

Section A-A

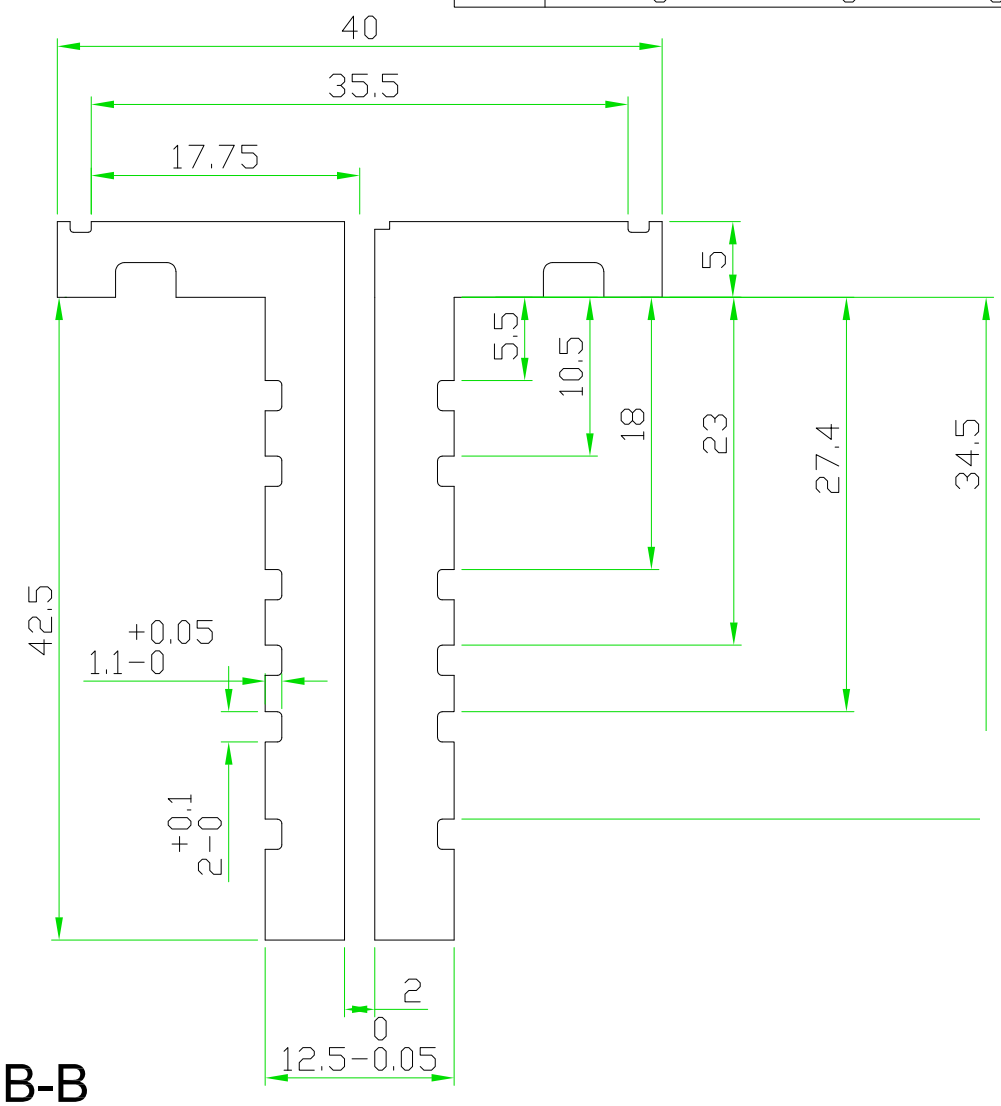

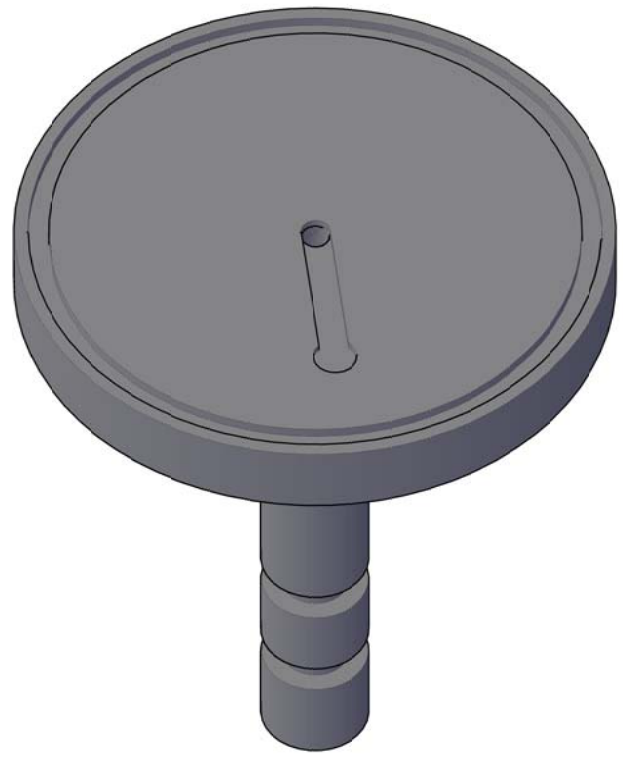

Bottom view

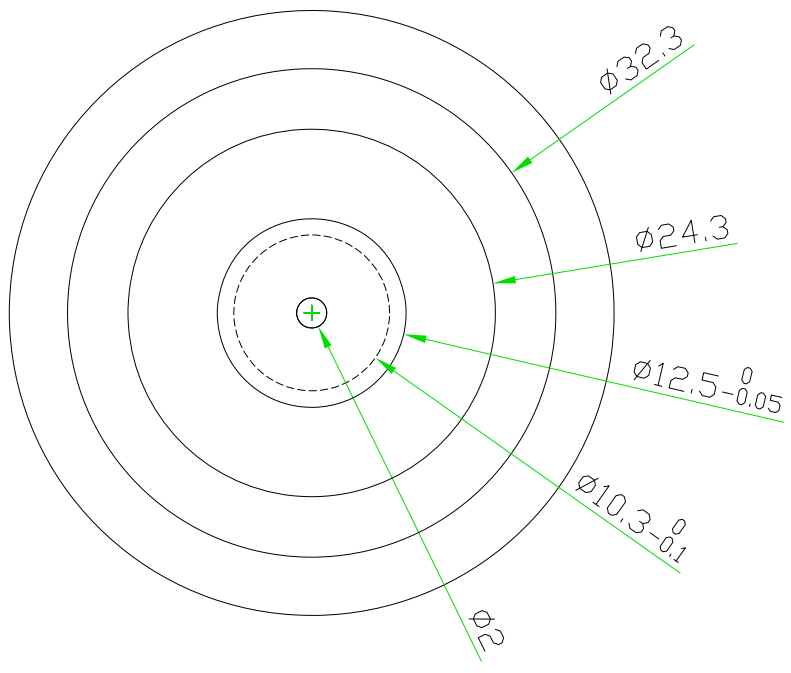

Section B-B

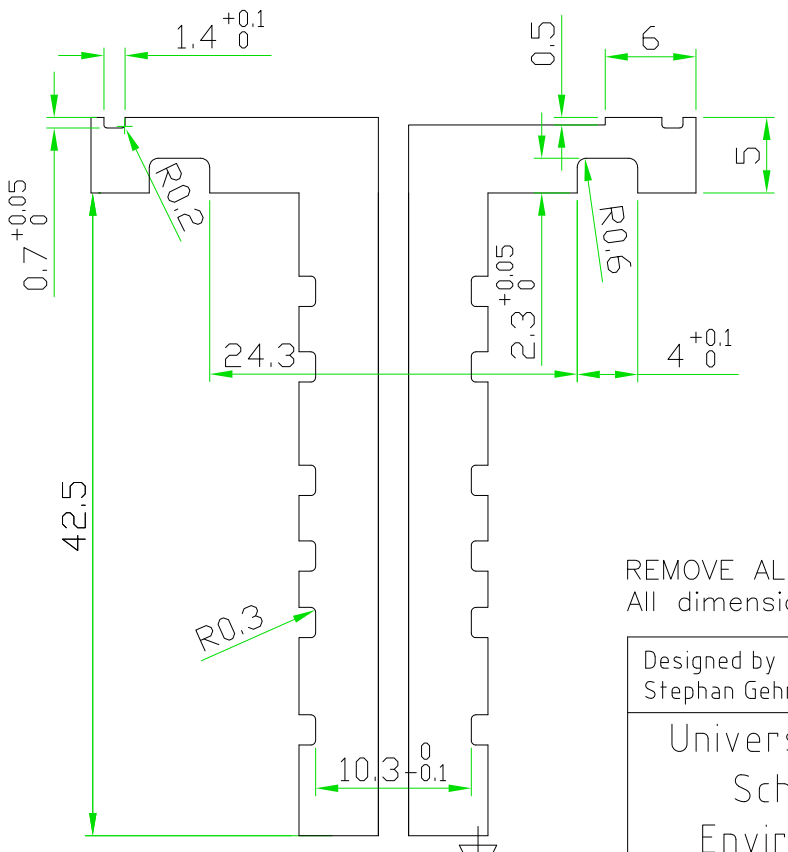

REMOVE ALL BURRS & SHARP EDGES
All dimensions are in millimeter unless otherwise shown

Material:	Tolerances:
316 SS	DECIMAL DIMENSIONS ±0.1 NON DECIMAL DIMENSIONS ±0.5 SURFACE FINISH - 0.8µm Ra UNLESS OTHERWISE STATED

Designed by	Approved by - date	Date	Unit	Scale
Stephan Gehne	22/10/15	22/10/15		

University of Portsmouth
School of Eart and
Environmental Science

TRX Fracker-F2

RML-PD-FRACSEIS-StG-2015-021-B	Edition B	Sheet 1/1

RevNo	Revision note	Date	Signature	Checked

Top view

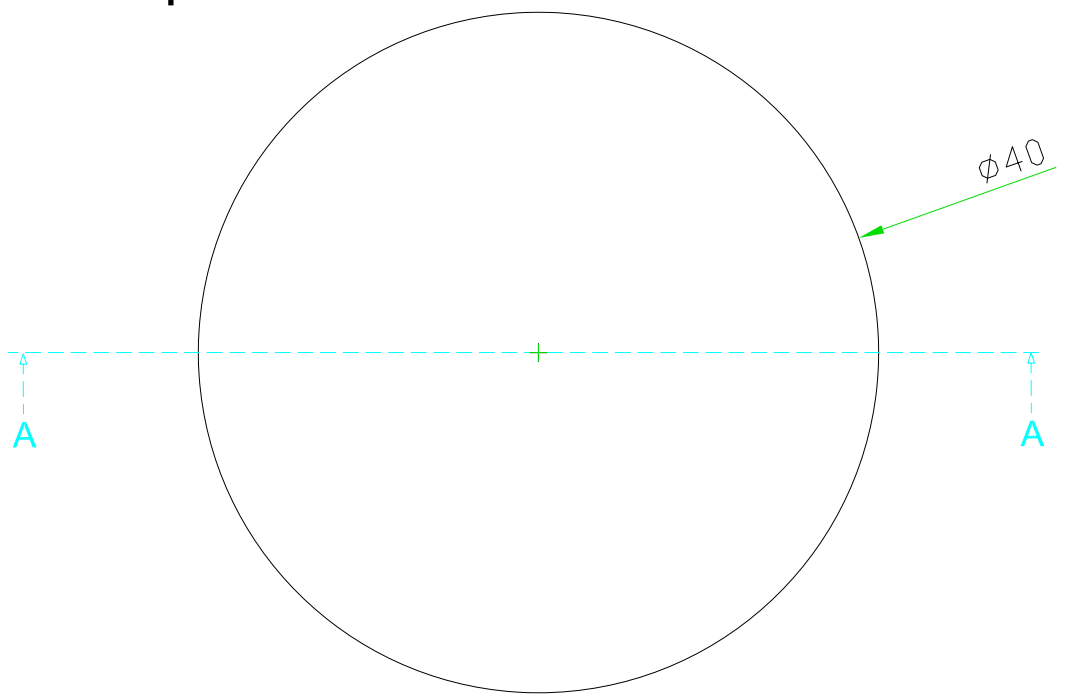

Bottom view

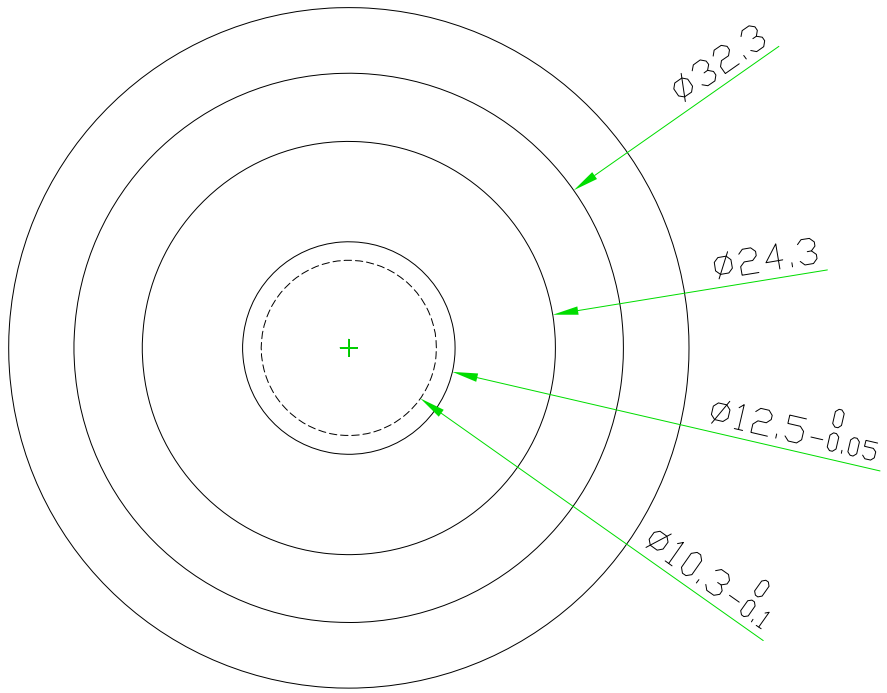

Section A-A

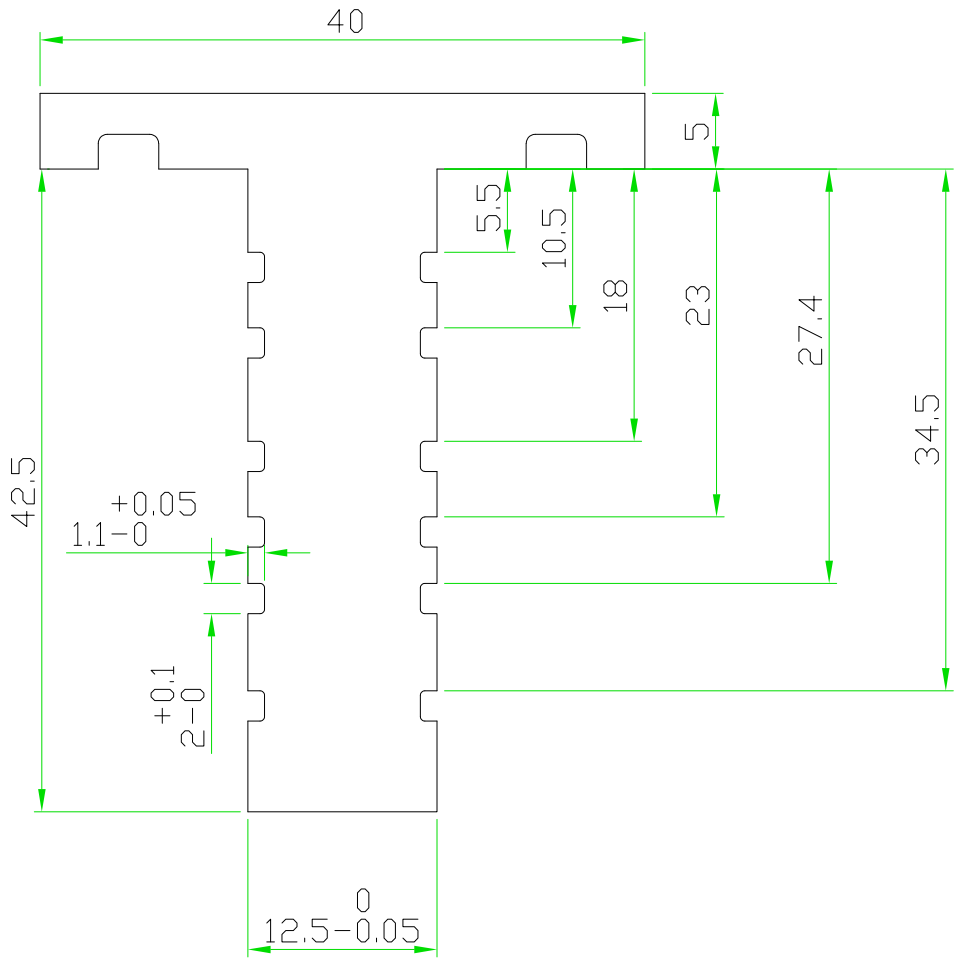

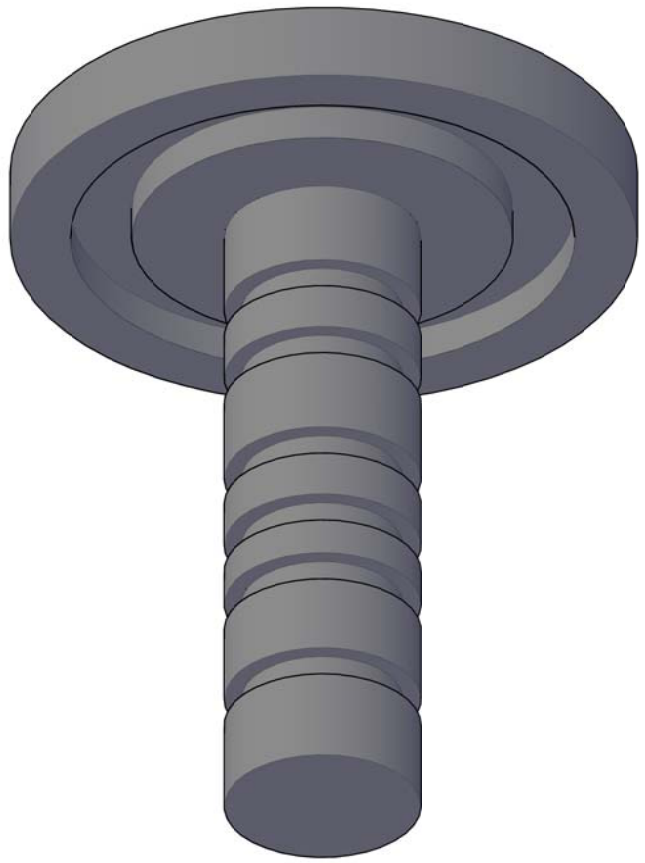

Section A-A

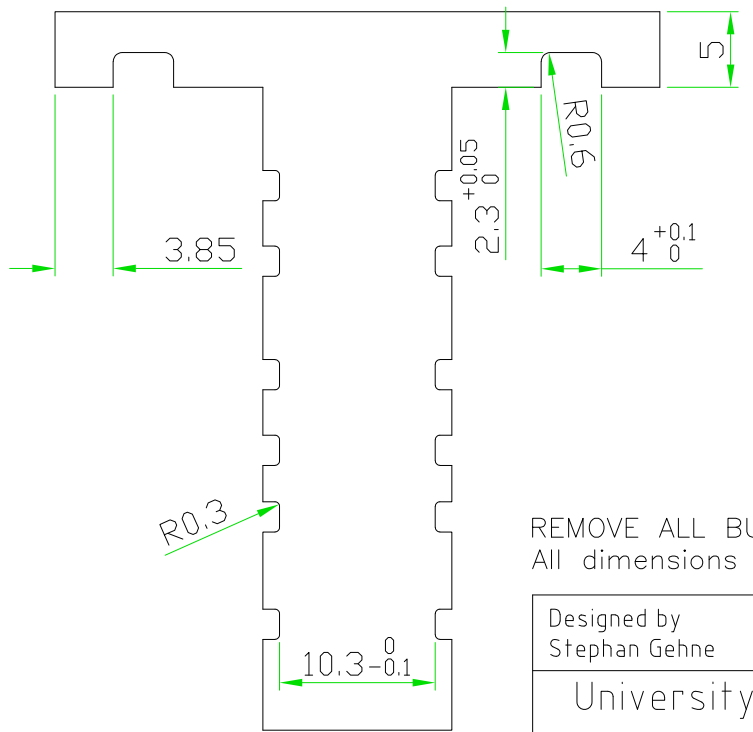

REMOVE ALL BURRS & SHARP EDGES
All dimensions are in millimeter unless otherwise shown

Material:	Tolerances:
316 SS	DECIMAL DIMENSIONS ±0.1 NON DECIMAL DIMENSIONS ±0.5 SURFACE FINISH - 0.8µm Ra UNLESS OTHERWISE STATED

Designed by	Approved by - date	Date	Unit	Scale
Stephan Gehne	03/05/16	03/05/16		

University of Portsmouth
School of Eart and
Environmental Science

TRX Fracker-Plug 12.5

RML-PD-FRACSEIS-StG-2016-24-A	Edition A	Sheet 1/1

Appendix A.4: Technical drawings radial extensometer

RevNo	Revision note	Date	Signature	Checked

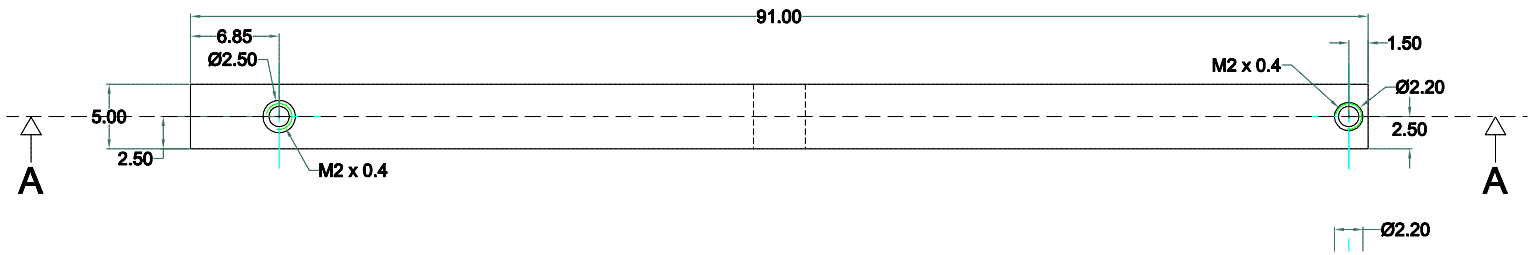

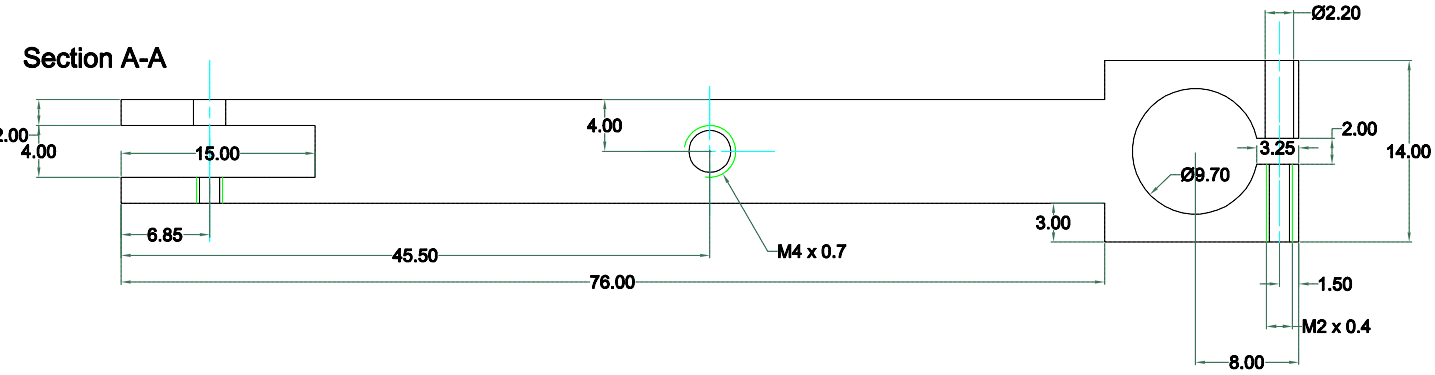

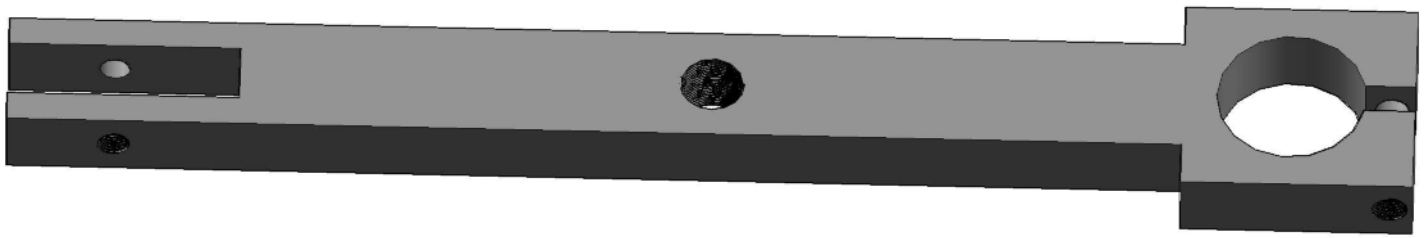

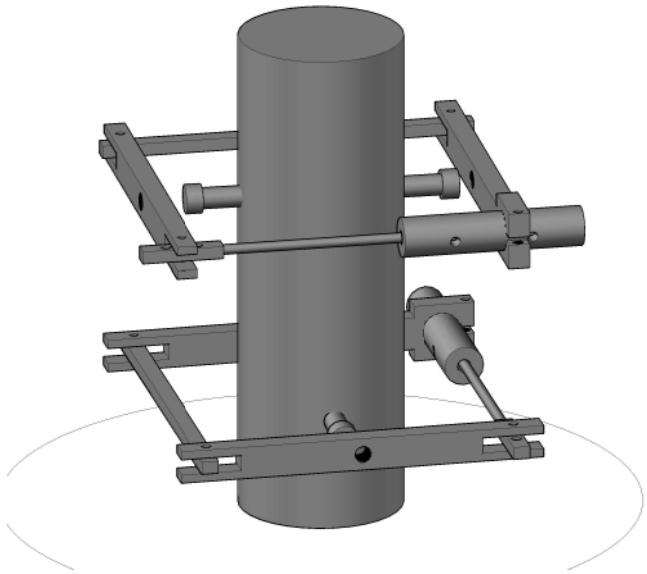

REMOVE ALL BURRS & SHARP EDGES
All dimensions are in millimeter unless otherwise shown

Material:	Tolerances:
316 SS	DECIMAL DIMENSIONS ±0.1 NON DECIMAL DIMENSIONS ±0.5 SURFACE FINISH - 0.8µm Ra UNLESS OTHERWISE STATED

Designed by	Approved by - date	Date	Unit	Scale
StG	23/06/2015	23/06/2015	Metric	1:1

Rock Mechanics Laboratory
University of Portsmouth
School of Earth and
Environmental Science

Radial extensometer - LVDT Bridge

RML-PD-FRACSEIS-StG-2015-19.2-A	Edition	Sheet
	A	1/1

LVDT Extension - Part 1

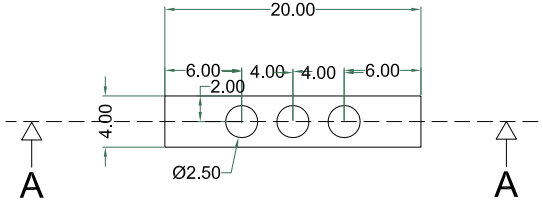

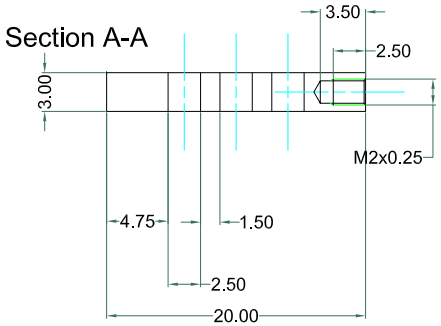

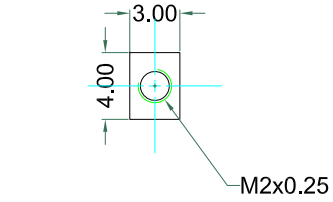

LVDT Extension - Part 2

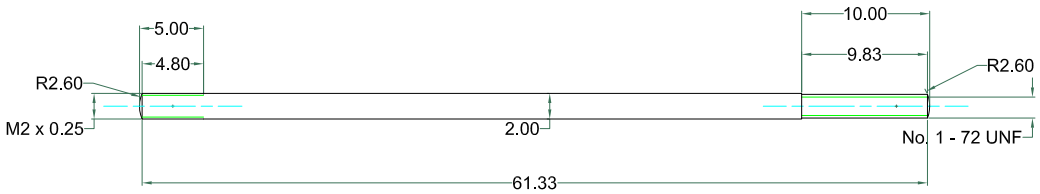

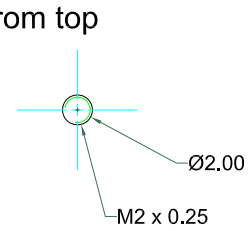

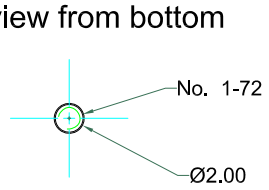

LVDT Extension - Assembly

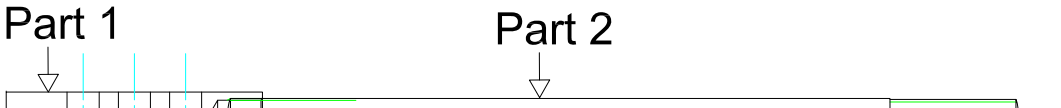

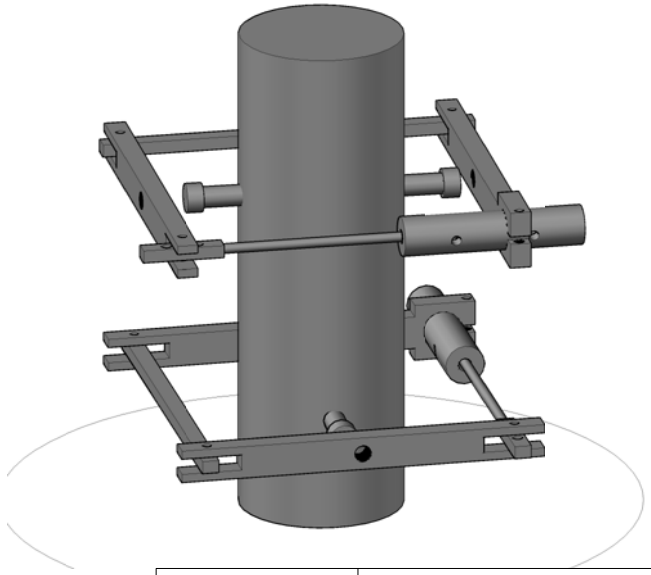

RevNo	Revision note	Date	Signature	Checked

REMOVE ALL BURRS & SHARP EDGES
All dimensions are in millimeter unless otherwise shown

Material:	Tolerances:
316 SS	DECIMAL DIMENSIONS ±0.1 NON DECIMAL DIMENSIONS ±0.5 SURFACE FINISH - 0.8µm Ra UNLESS OTHERWISE STATED

Designed by	Approved by - date	Date	Unit	Scale
StG	10/08/2015	10/08/2015	Metric	1:1

Rock Mechanics Laboratory
University of Portsmouth
School of Earth and
Environmental Science

Radial extensometer - LVDT extension

RML-PD-FRACSEIS-StG-2015-19.4-B	Edition	Sheet
	B	1/1

RevNo	Revision note	Date	Signature	Checked

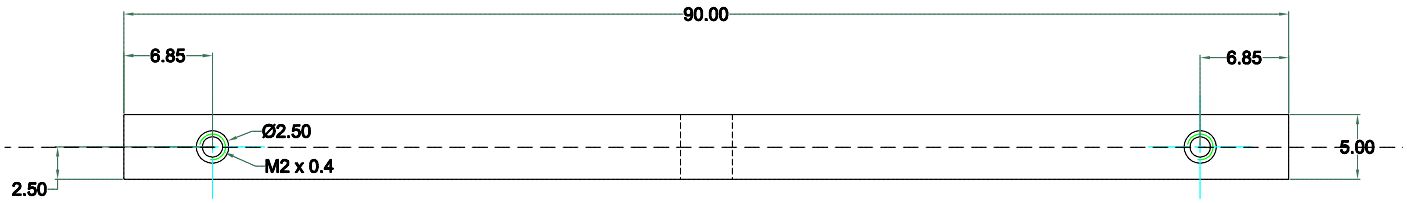

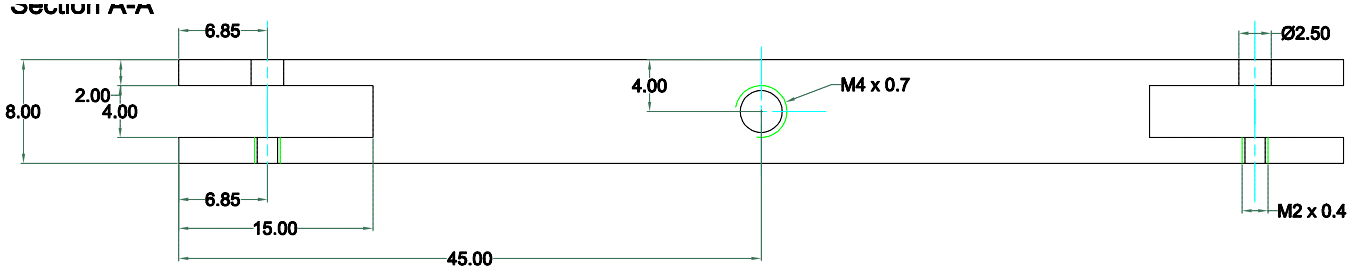

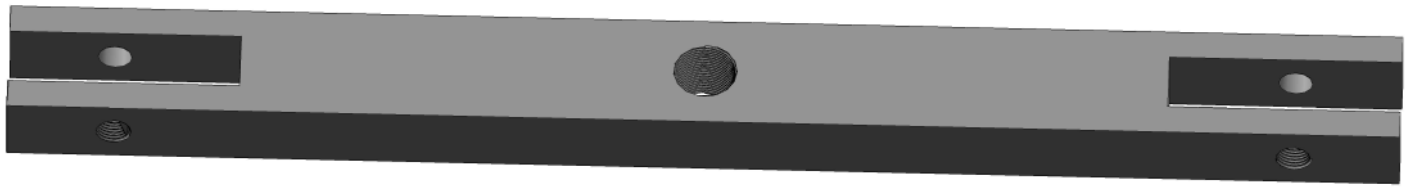

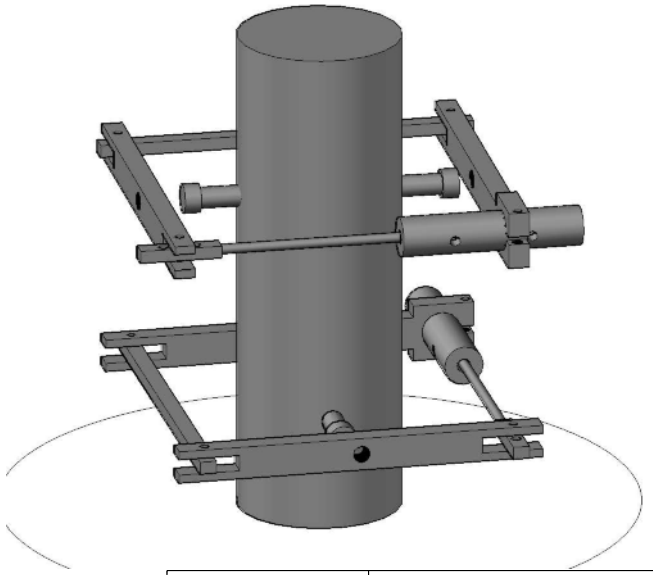

REMOVE ALL BURRS & SHARP EDGES
All dimensions are in millimeter unless otherwise shown

Material:	Tolerances:
316 SS	DECIMAL DIMENSIONS ±0.1 NON DECIMAL DIMENSIONS ±0.5 SURFACE FINISH - 0.8µm Ra UNLESS OTHERWISE STATED

Designed by	Approved by - date	Date	Unit	Scale
StG	23/06/2015	23/06/2015	Metric	1:1

Rock Mechanics Laboratory
University of Portsmouth
School of Earth and
Environmental Science

Radial extensometer - Bridge 1

RML-PD-FRACSEIS-StG-2015-19.1-A	Edition A	Sheet 1/1

RevNo	Revision note	Date	Signature	Checked

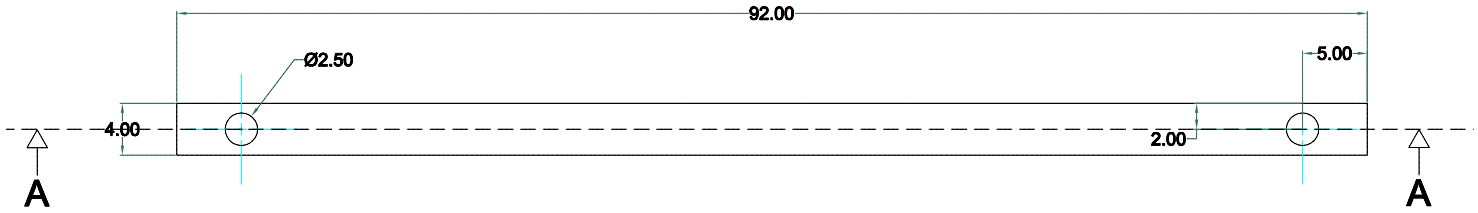

Section A-A

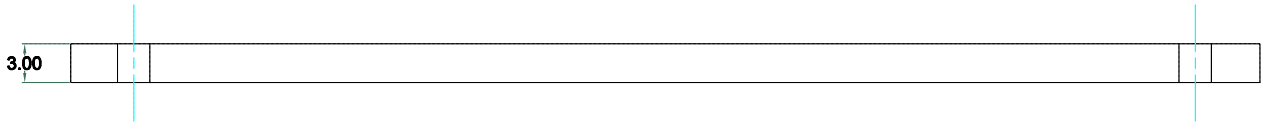

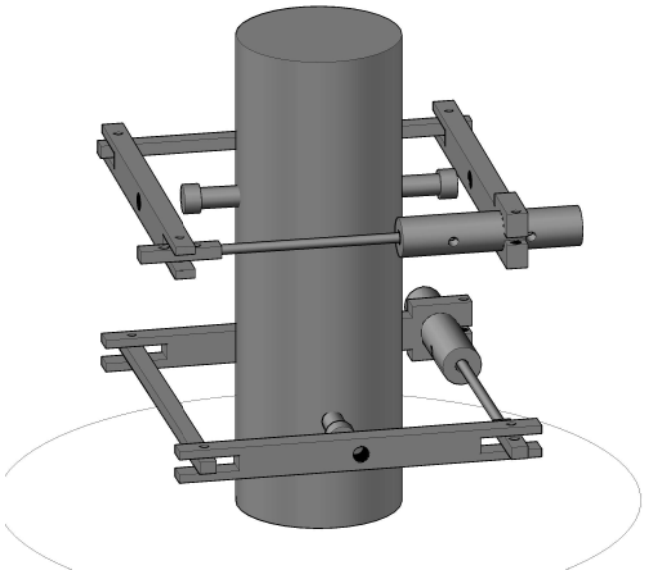

REMOVE ALL BURRS & SHARP EDGES
All dimensions are in millimeter unless otherwise shown

Material:	Tolerances:
316 SS	DECIMAL DIMENSIONS ±0.1 NON DECIMAL DIMENSIONS ±0.5 SURFACE FINISH - 0.8µm Ra UNLESS OTHERWISE STATED

Designed by	Approved by - date	Date	Unit	Scale
StG	23/06/2015	23/06/2015	Metric	1:1

Rock Mechanics Laboratory
University of Portsmouth
School of Earth and
Environmental Science

Radial extensometer - Bridge 2

RML-PD-FRACSEIS-StG-2015-19.3-A	Edition	Sheet
	A	1/1

Appendix A.5: Technical drawings fluid separator

REMOVE ALL BURRS & SHARP EDGES

RevNo	Revision note	Date	Signature	Checked

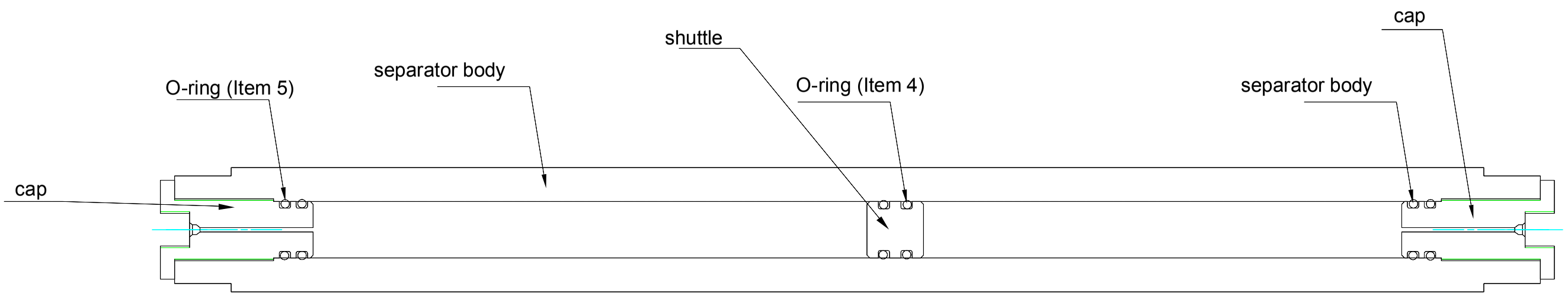

Parts List - TRX fluid separator

Item	Qty	Description	Standard	Material
1	1	Separator body	TRX_2015_FSbody_E	316 SS
2	2	Separator cap	TRX_2015_FScap_B	316 SS
3	1	Separator shuttle	TRX_2015_FSshuttle_B	316 SS
4	2	Polymax O-ring	14x3N70 (CS 3mm, ID 14mm)	NBR (Nitrile)
5	4	Polymax O-ring	15x3N70 (CS 3mm, ID 15mm)	NBR (Nitrile)

Material:	Tolerances:
316 SS	DECIMAL DIMENSIONS ±0.1 NON DECIMAL DIMENSIONS ±0.5 SURFACE FINISH - 0.8µm Ra UNLESS OTHERWISE STATED

Designed by	Approved by - date	Date	Unit	Scale
St. Gehne	21/04/2015	21/04/15	Metric	

University of Portsmouth-
School of Earth and
Environmental Science

Fluid separator - Assembly

TRX_2015_FSassembly_A	Edition	Sheet
	A	1/1

REMOVE ALL BURRS & SHARP EDGES

RevNo	Revision note	Date	Signature	Checked
1	Circular body with flats at each end instead of hexagonal body	17/04/15	StG	
2	Outer and BH diameter decreased	17/04/15	StG	
3	Outer and BH diameter deceased , length decreased, thread size decreased, thread length increased	20/04/15	StG	

A-A

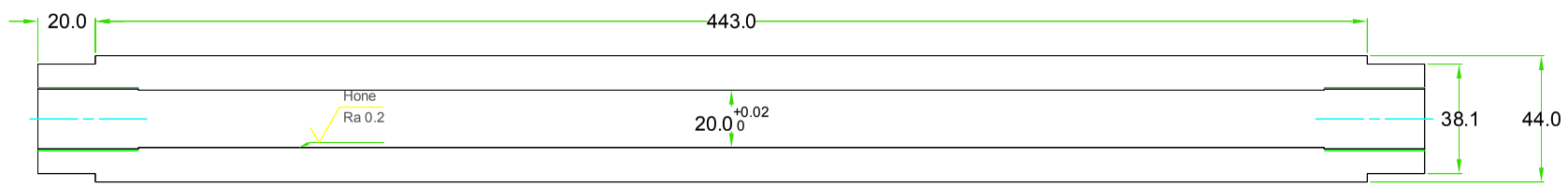

B-B

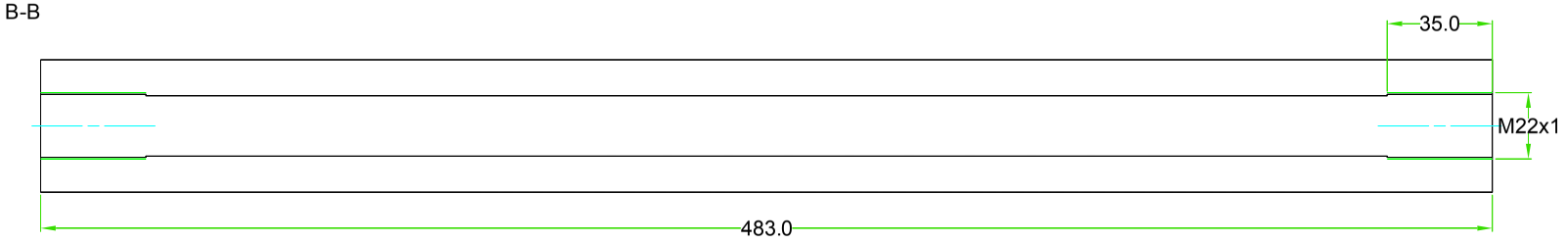

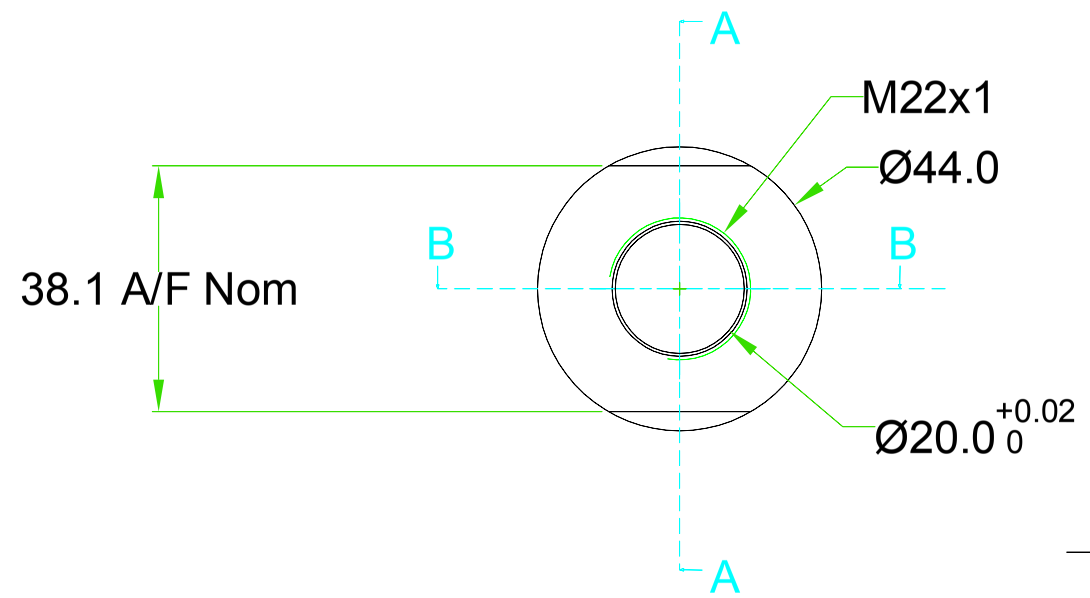

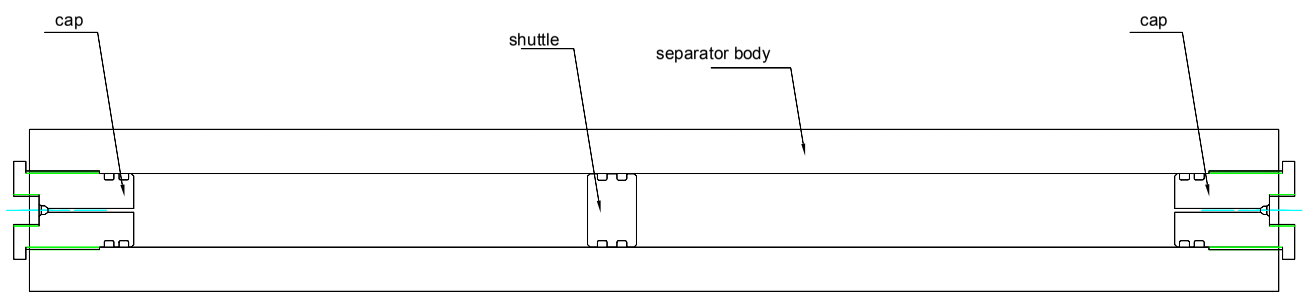

Note:
Machining at both ends is identical

Material:	Tolerances:
316 SS	DECIMAL DIMENSIONS ±0.1 NON DECIMAL DIMENSIONS ±0.5 SURFACE FINISH - 0.8µm Ra UNLESS OTHERWISE STATED

Designed by	Approved by - date	Date	Unit	Scale
St. Gehne	20/04/2015	20/04/15	Metric	

University of Portsmouth-
School of Earth and
Environmental Science

Separator Body

TRX_2015_FSbody_E	Edition	Sheet
	E	1/1

REMOVE ALL BURRS & SHARP EDGES

RevNo	Revision note	Date	Signature	Checked
1	Change of outer dimensions and dimensions of the groove	20/04/15	StG	

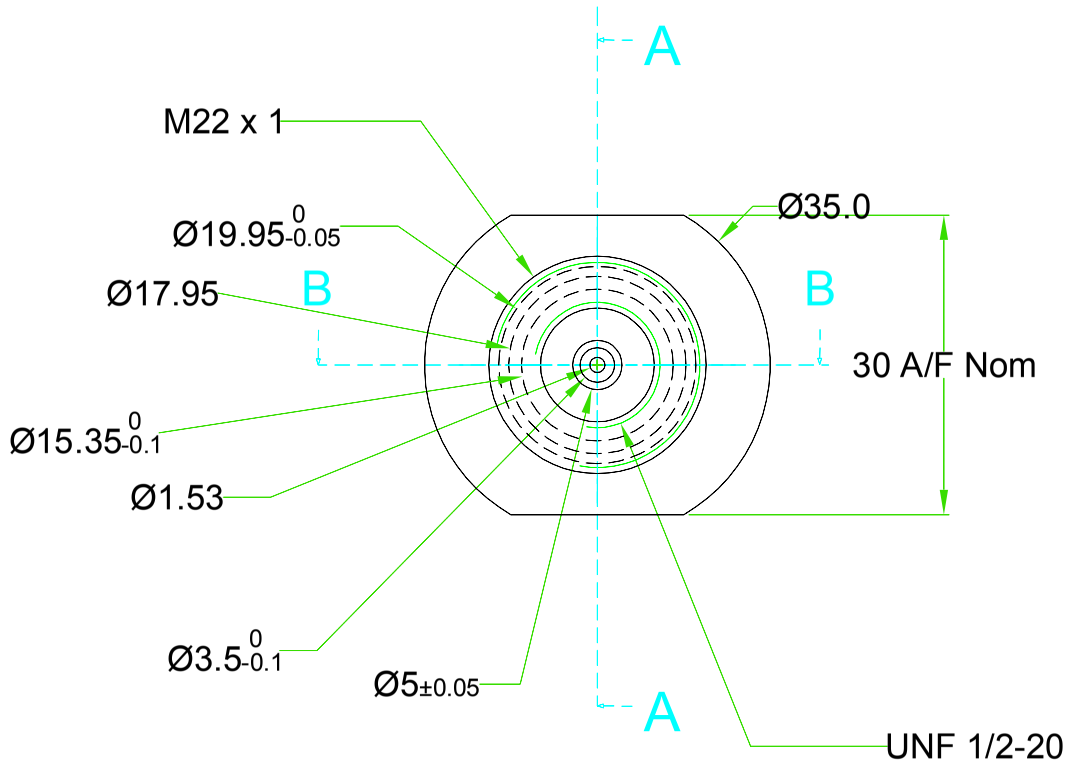

A-A

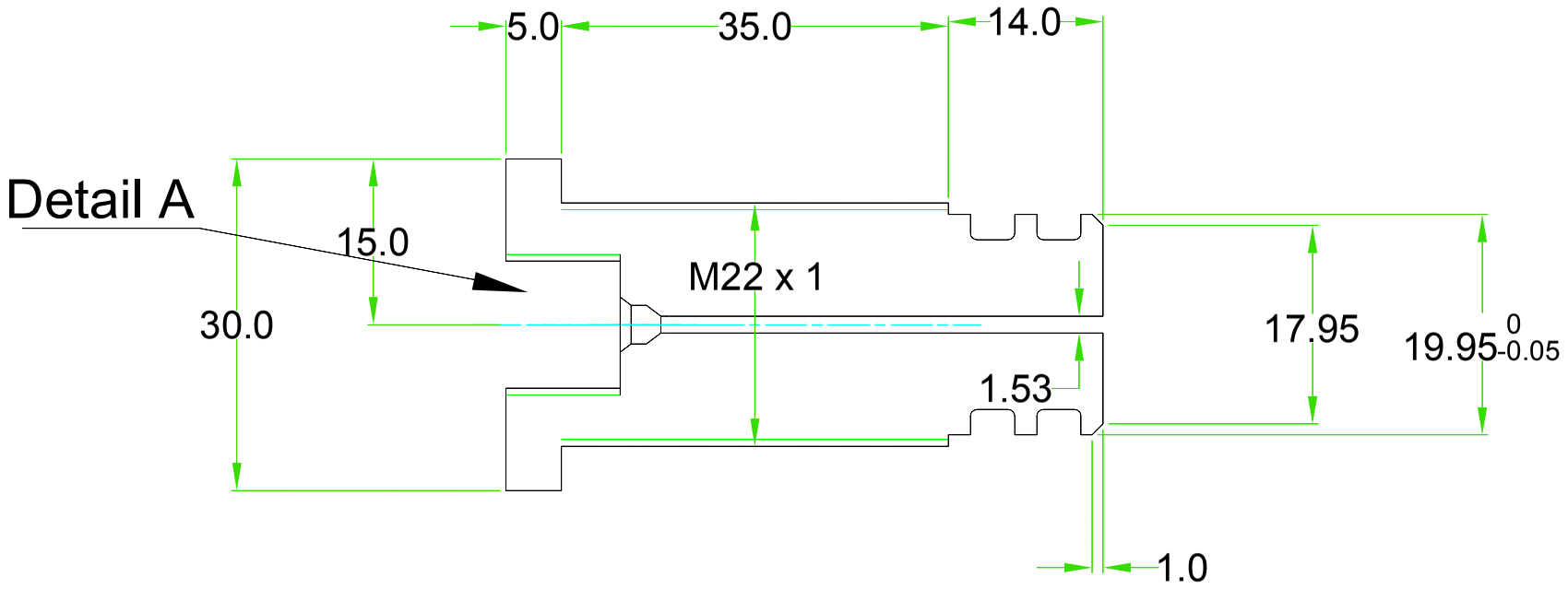

Detail A

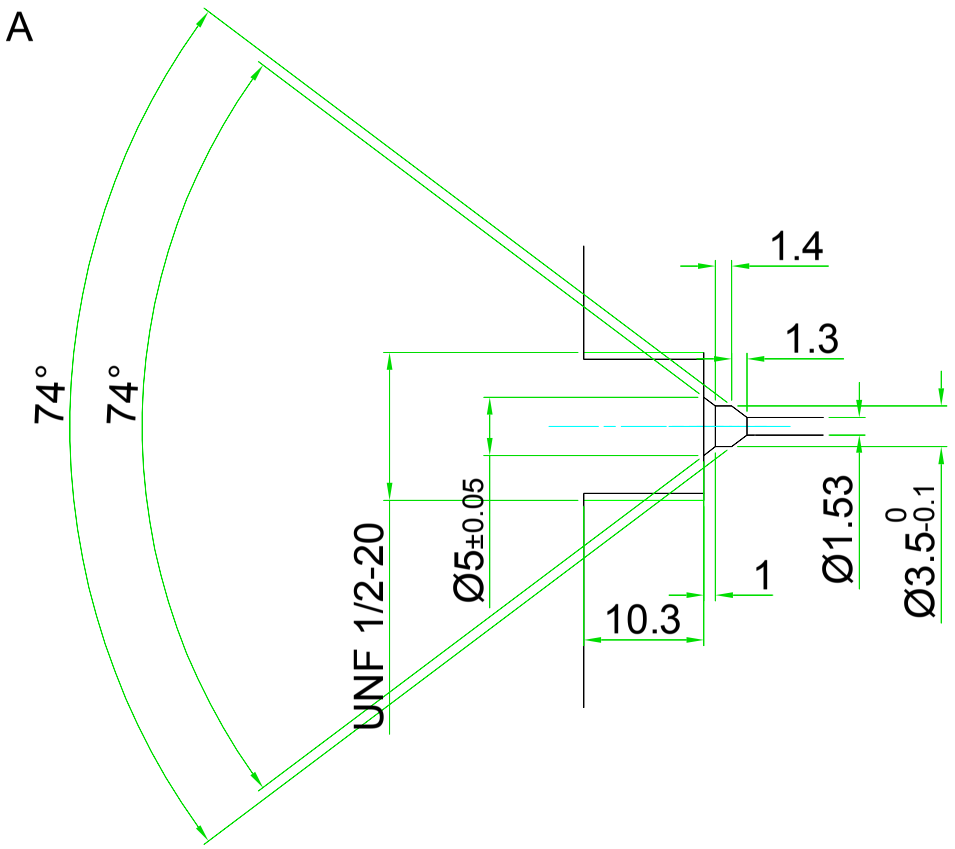

B-B

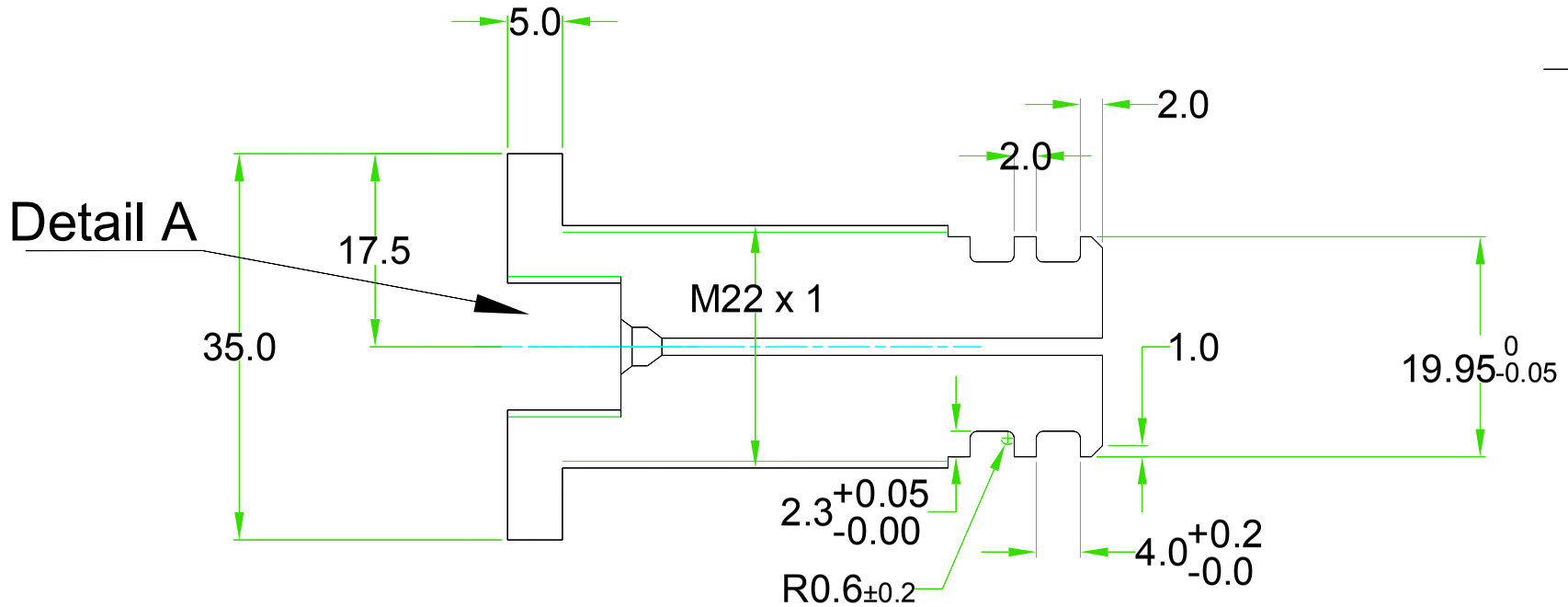

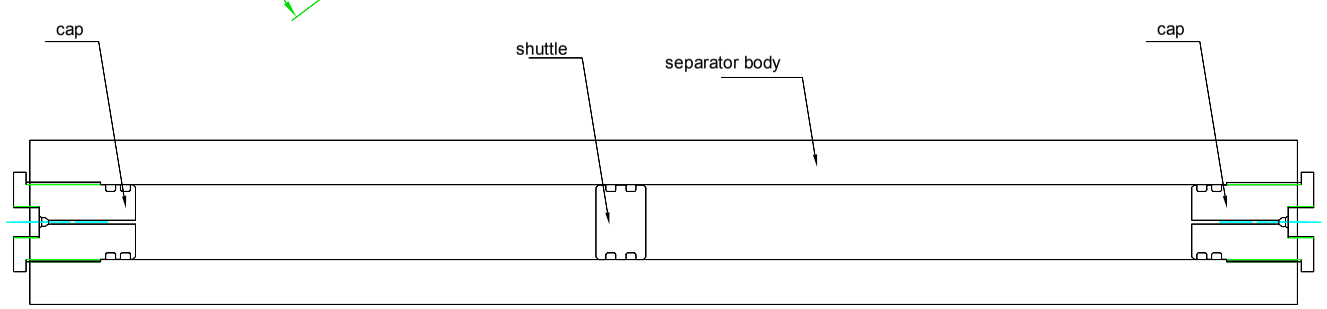

Material:	Tolerances:
316 SS	DECIMAL DIMENSIONS ±0.1 NON DECIMAL DIMENSIONS ±0.5 SURFACE FINISH - 0.8µm Ra UNLESS OTHERWISE STATED

Designed by	Approved by - date	Date	Unit	Scale
St. Gehne	20/04/2015	20/04/15	Metric	

University of Portsmouth-
School of Earth and
Environmental Science

Separator Cap

	Edition	Sheet
TRX_2015_FScap_B	B	1/1

REMOVE ALL BURRS & SHARP EDGES

RevNo	Revision note	Date	Signature	Checked
1	Change of outer dimensions and dimensions of the groove	20/04/15	StG	

A-A

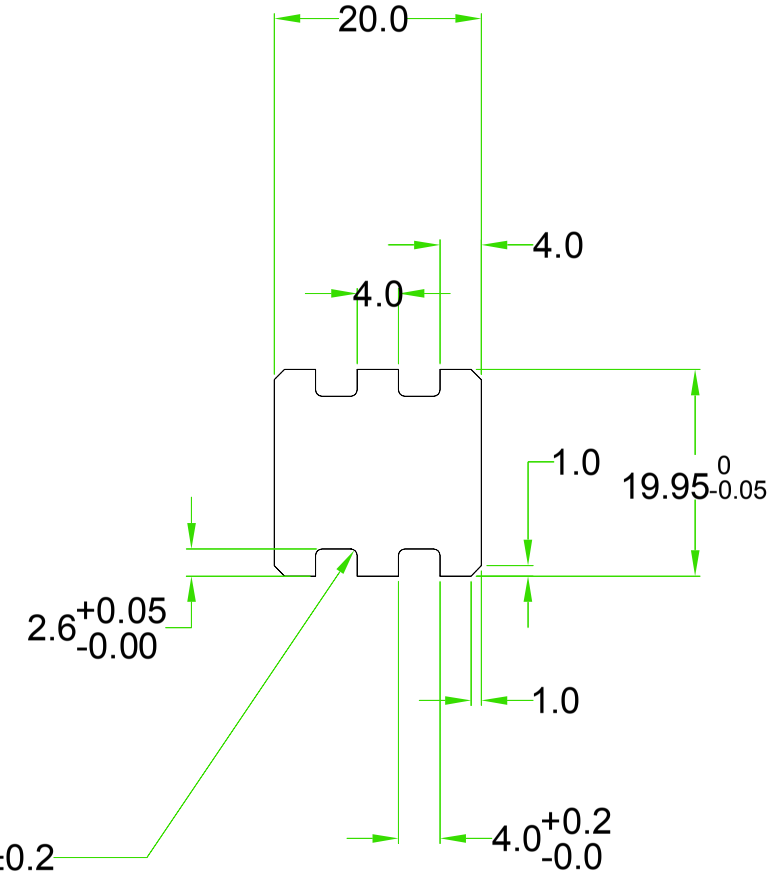

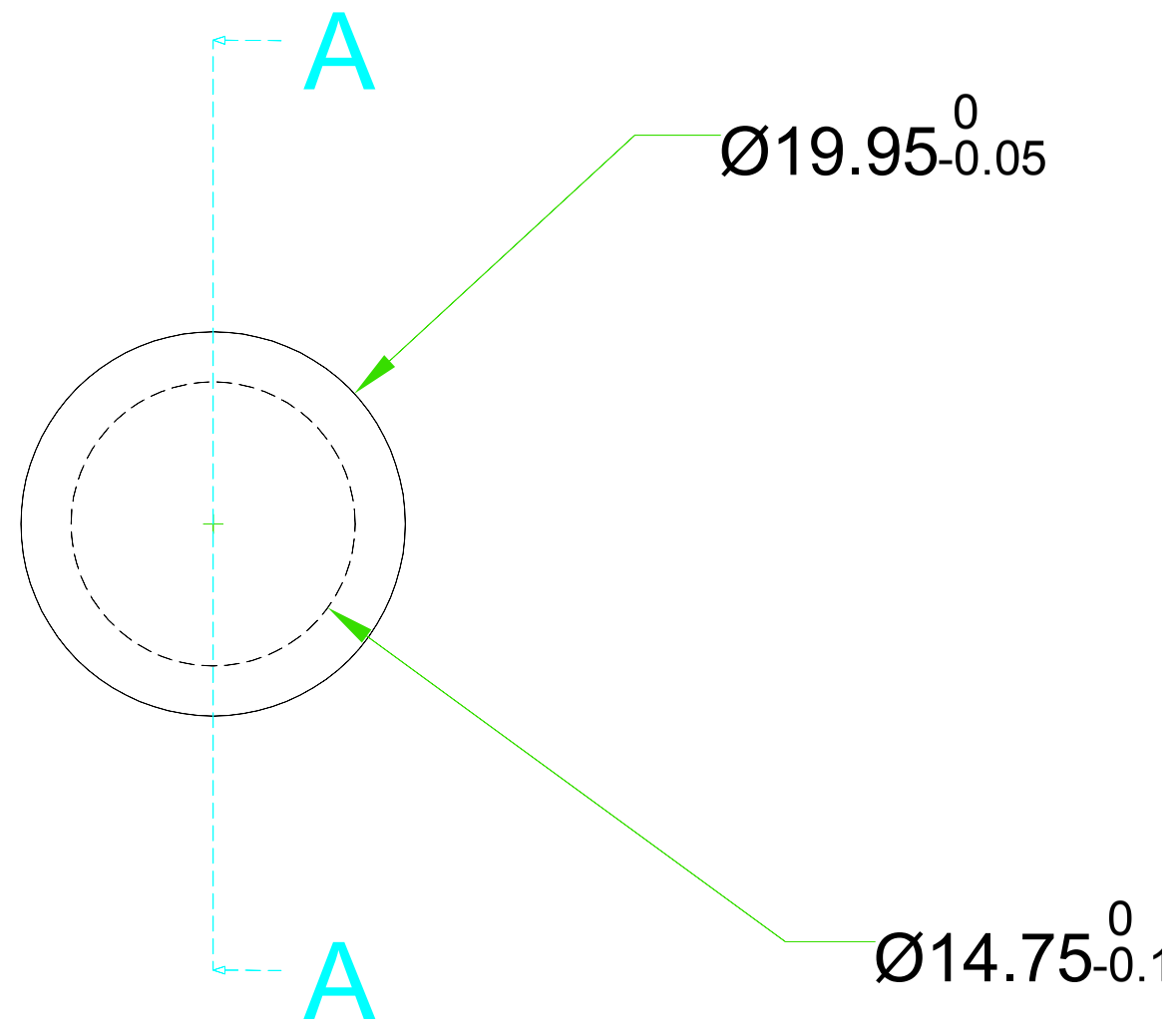

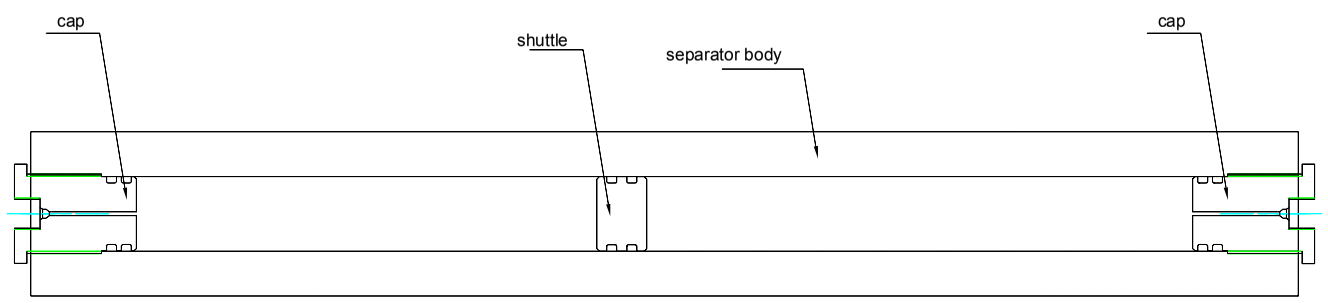

Material:	Tolerances:
316 SS	DECIMAL DIMENSIONS ±0.1 NON DECIMAL DIMENSIONS ±0.5 SURFACE FINISH - 0.8µm Ra UNLESS OTHERWISE STATED

Designed by	Approved by - date	Date	Unit	Scale
St. Gehne	20/04/2015	20/04/15	Metric	

University of Portsmouth-
School of Earth and
Environmental Science

Separator Shuttle

TRX_2015_FSshuttle_B	Edition	Sheet
	B	1/1

Appendix A.6: High-speed recording system – program code and user interface

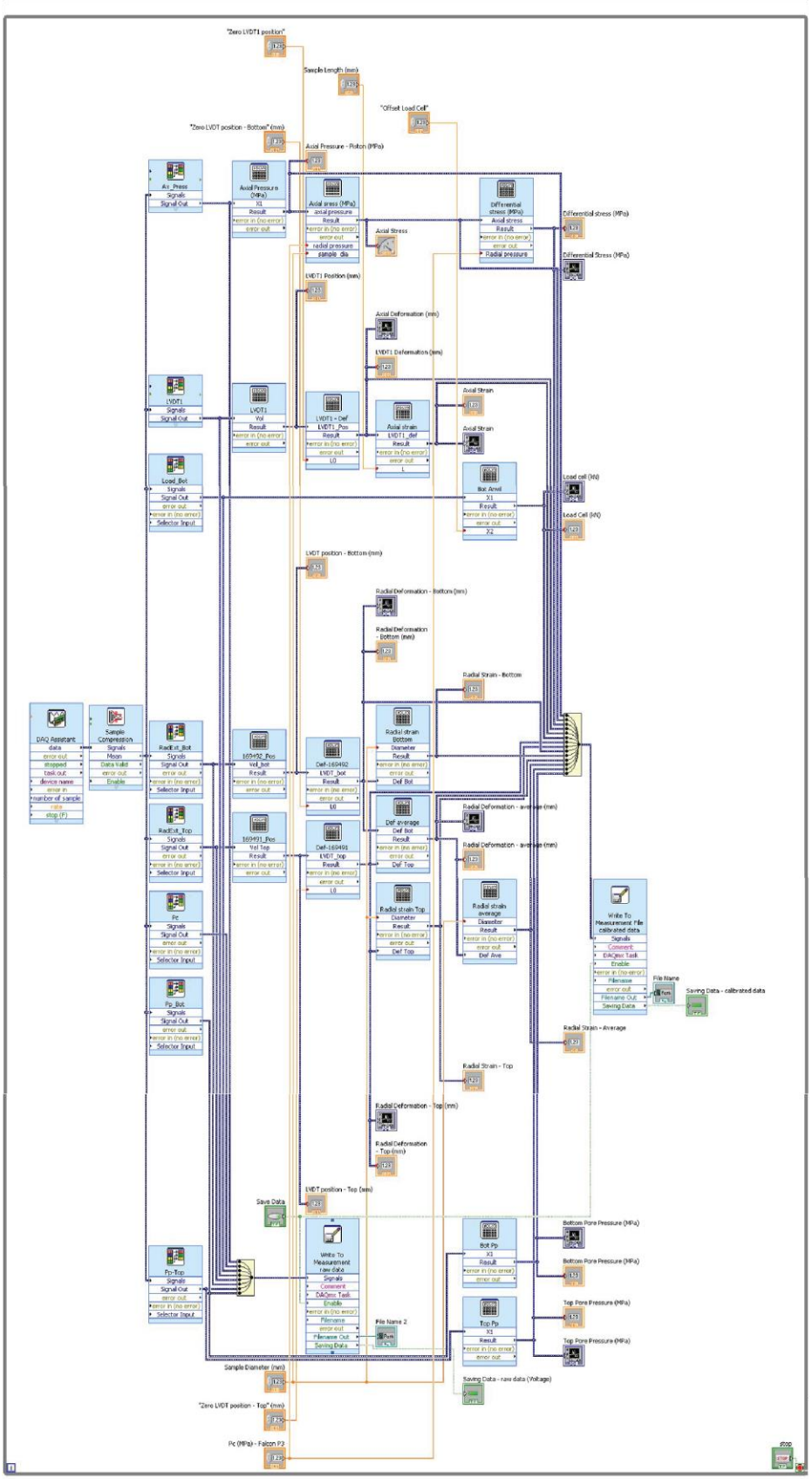

Figure A.6-1: High-speed recording system Labview code

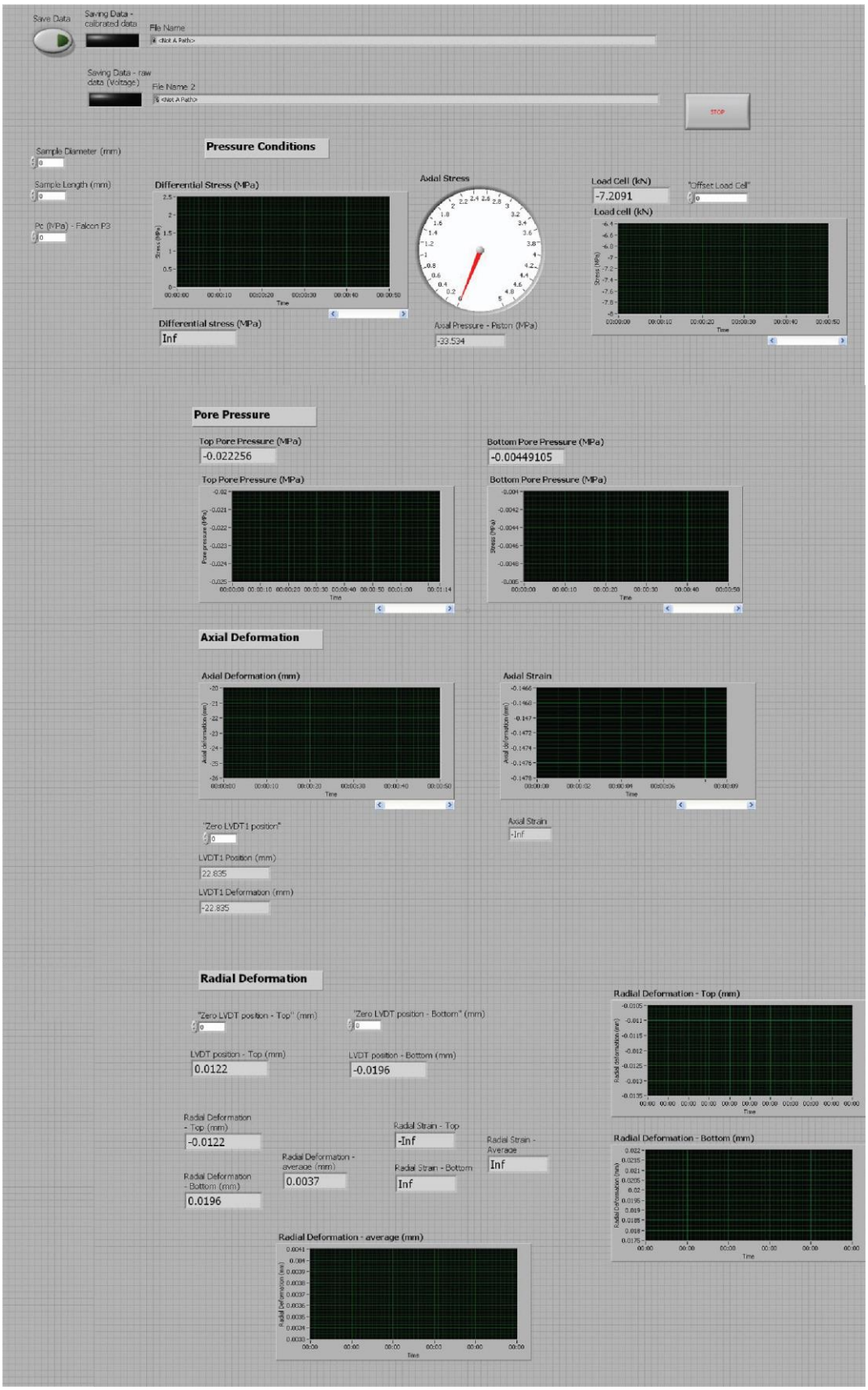

Figure A.6-2: User interface of high-speed recording system

Appendix A.7: Laboratory data from Indirect Tensile Strength test

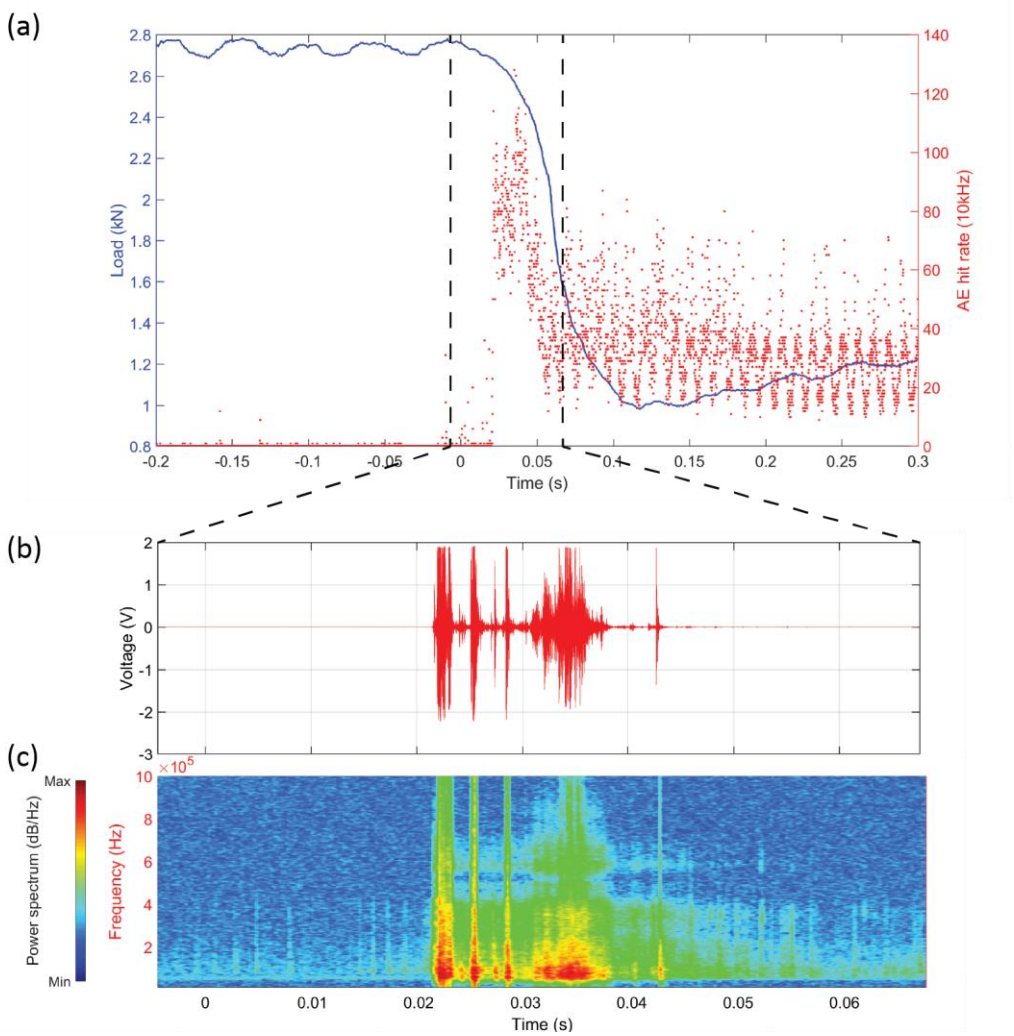

Figure A.7-1: Laboratory data from Indirect Tensile Strength test (Brazilian test) on NPS at ambient pressure in the Short-Transverse orientation; (a) Time-record of load (blue line) and AE hit counts (red dots). (b) Snapshot of the continuous waveform (red line) including the signal envelope at the time of failure. (c) Respective spectrogram at the time of failure. The spectrogram data illustrates the frequency range exhibiting power (colour) with time. Time scales zeroed at load decrease.

Appendix A.8: Hydraulic fracturing pressure parameters

Table A.8-1: Overview of distinct pressures recorded during hydraulic fracturing of Nash Point Shale and Crab Orchard Sandstone.

Sample	Max P_{inj} (MPa)	Fracture initiation pressure (MPa)	Breakdown pressure (MPa)	Confining Pressure (MPa)	Pressurised fluid
NPSx-0.0-w	5.35		5.28	0	water
NPSx-2.2-w	10.39	10.35	10.08	2.21	water
NPSx-2.3-w	4.84	4.83	4.82	2.3	water
NPSx-14.5-w	32.36	32.3	32.12	14.48	water
NPSx-25.4-w	36.35	36.18	35.55	25.4	water
NPSx-15.3-oil	26.36	26.23	26.04	15.3	oil
NPSz-4.5-w	30.3	30.28	30.0	4.5	water
NPSz-15.3-w	55.11	55.07	53.79	15.3	water
NPSz-20.3-w	57.98	57.85	57.47	20.28	water
COSx-14.4-w	32.23	32.26	32.13	14.39	water
COSx-15.5-oil	48.17	48.16	47.96	15.5	oil
COSz-15.4-w	29.34	29.35	28.68	15.43	water

Appendix A.9: Apparent fracture toughness analysis

Short-Transverse orientation

NPSx-2.2-w

- Two fractures
- End of radial fracture propagation indicated by end of drastic AE energy increase and decrease in fluid pressure decay rate
- Further energy increase due to continuing axial fracture propagation and increase in radial deformation as sample can open up

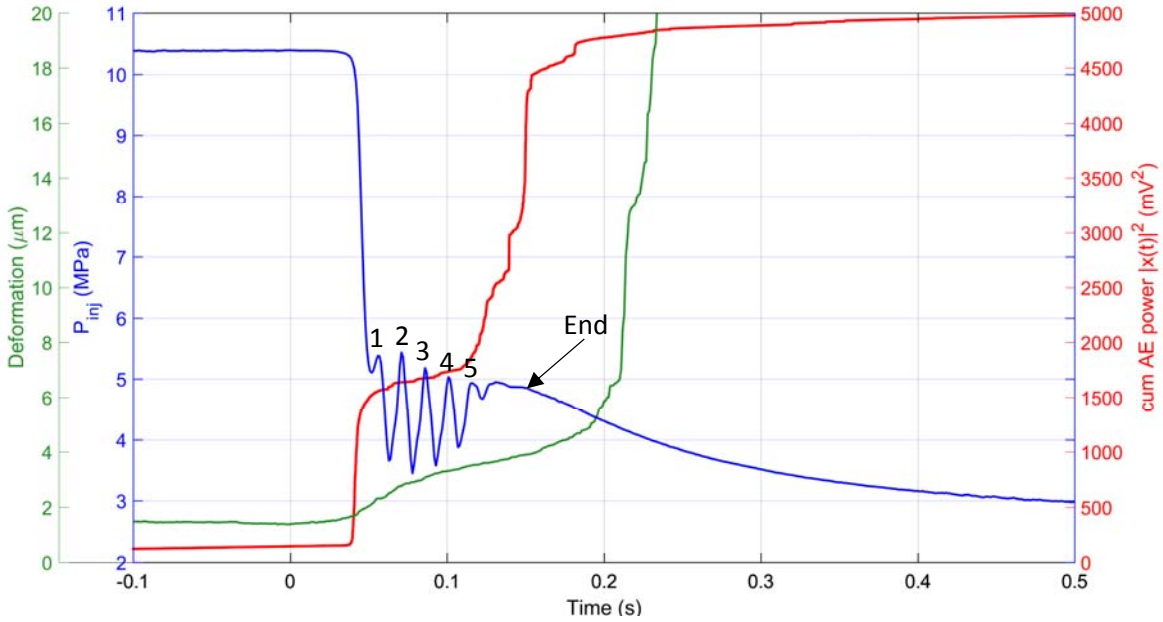

Peak	Effective fluid pressure (MPa)	a_0 (mm)	aK_{IC} (MPa.m$^{1/2}$)	Fracture orientation
1	3.2	5.25	0.58	S-T
2	3.2	5.55	0.56	S-T
3	3.0	5.74	0.53	S-T
4	2.8	5.94	0.51	S-T
5	2.7	6.16	0.50	S-T

Average aK_{IC} = 0.53MPa.m$^{1/2}$ ±0.02

NPSx-6.1-w

- Single fracture
- End of radial fracture propagation based on AE hit count rate and decrease in fluid pressure decay rate

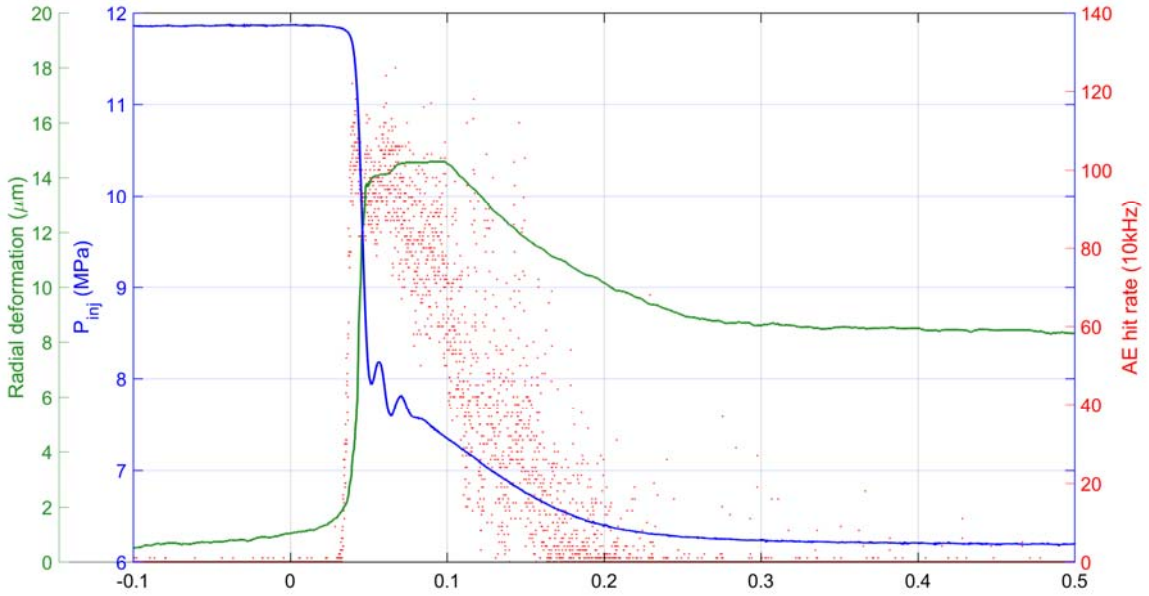

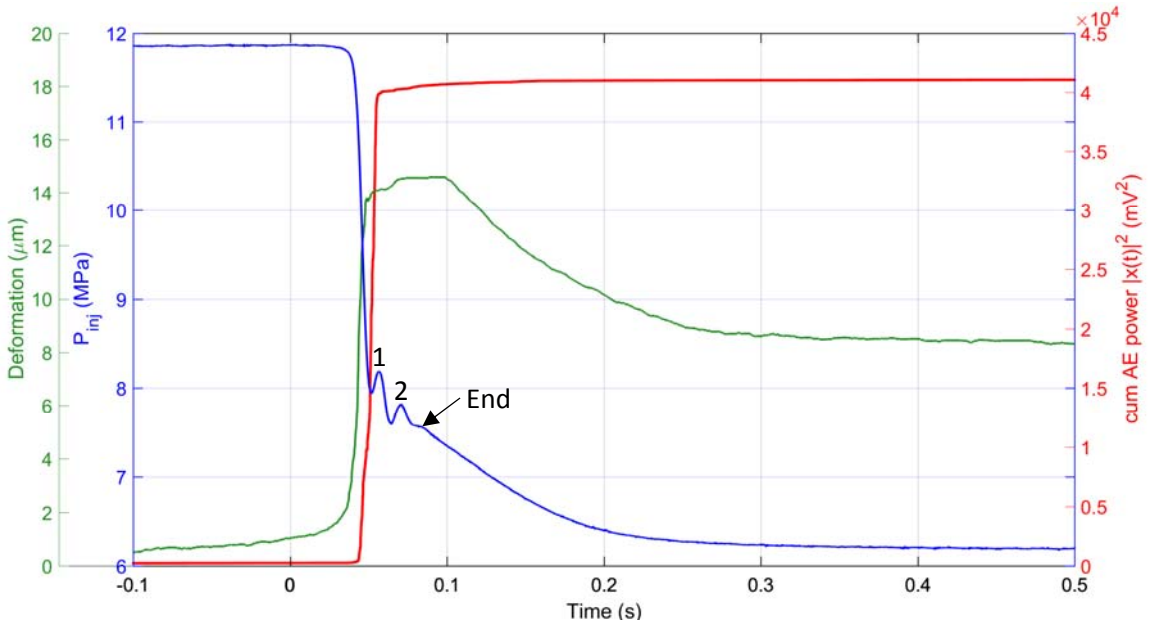

Peak	Effective fluid pressure (MPa)	a_0 (mm)	aK_{IC} (MPa.m$^{1/2}$)	Fracture orientation
1	2.1	6.37	0.39	S-T
2	1.7	13.6	0.36	S-T

Average aK_{IC} = 0.37MPa.m$^{1/2}$ ±0.02

NPSx-12.1-w

- Single fracture
- End of radial fracture propagation based on AE hit count rate and fluid pressure decay rate.

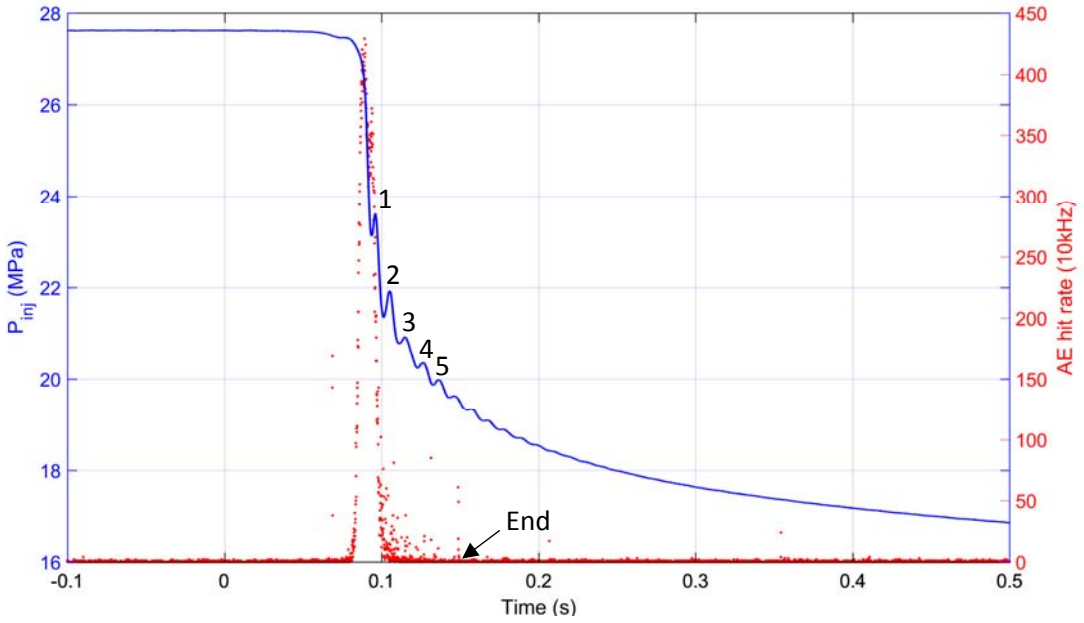

Peak	Effective fluid pressure (MPa)	a_0 (mm)	aK_{IC} (MPa.m$^{1/2}$)	Fracture orientation
1	11.5	11.73	2.34	S-T
2	9.8	12.81	2.09	S-T
3	8.8	13.11	1.90	S-T
4	8.3	13.35	1.79	S-T
5	7.9	13.55	1.64	S-T

Average aK_{IC} = 1.95MPa.m$^{1/2}$ ±0.27

NPSx-14.3-w

- Single fracture
- End of radial fracture propagation based on AE hit count rate, decrease in fluid pressure decay rate and change in radial deformation.

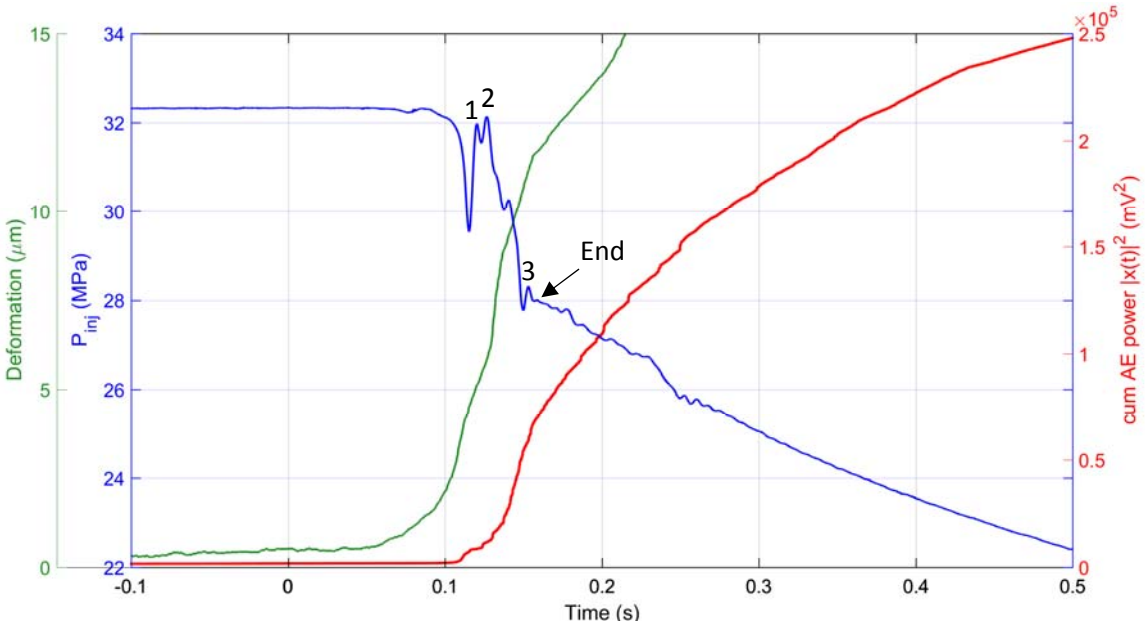

Peak	Effective fluid pressure (MPa)	a_0 (mm)	K_{IC} (MPa.m$^{1/2}$)	Fracture orientation
1	17.68	1.13	2.08	S-T
2	17.84	1.50	2.23	S-T
3	14.01	10.98	2.76	S-T

There are no obvious reasons why the values of the first two peaks are lower despite the higher effective fluid pressure. Furthermore, these two peaks show a rather unusual behaviour as they reache a similar level than the maximum fluid injection pressure, whereas in all other experiments oscillations only showed a small pressure increase relative to maximum fluid injection pressure preceded by a significant pressure drop. The behaviour seen in this sample could be due to shell or lithic fragment temporally stopping fracture propagation. Therefore, only the value of the third oscillating peak is considered.

NPSx-20.5-w

- End of radial fracture propagation based on AE hit count rate decrease and decrease in fluid pressure decay rate

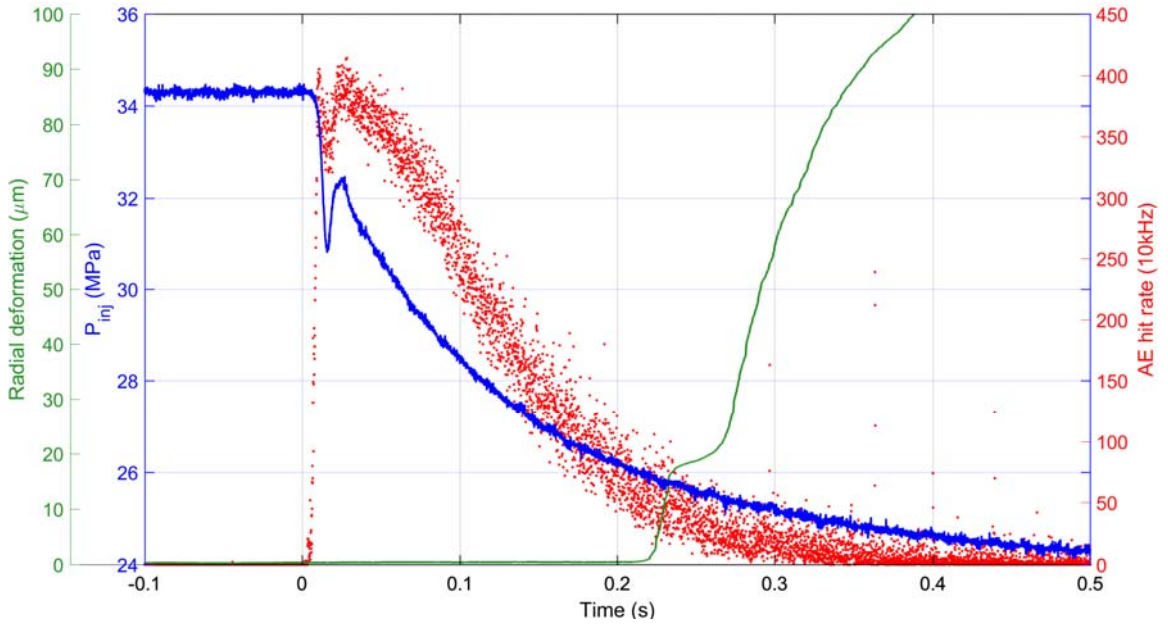

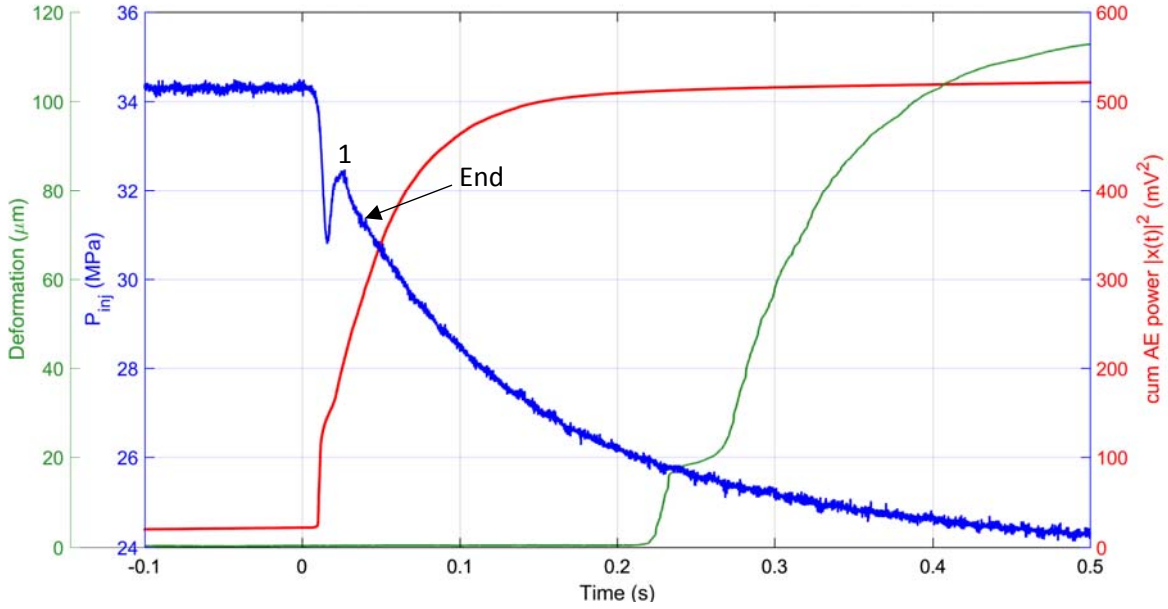

Peak	Effective fluid pressure (MPa)	a_0 (mm)	K_{IC} (MPa.m$^{1/2}$)	Fracture orientation
1	12.0	7.03	2.17	S-T

NPSx-25.3-w

- Single fracture
- End of radial fracture propagation based on AE hit count rate decrease and decrease in fluid pressure decay rate

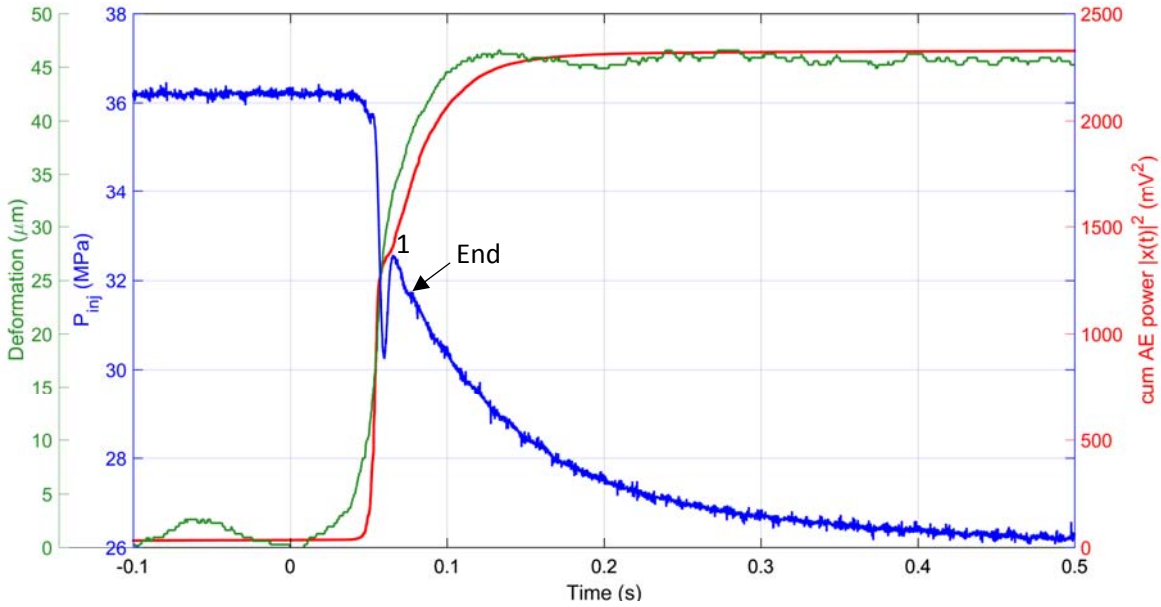

Peak	Effective fluid pressure (MPa)	a_0 (mm)	K_{IC} (MPa.m$^{1/2}$)	Fracture orientation
1	7.3	10.98	1.41	S-T

Divider orientation

NPSz-4.5-w

- Single fracture
- End of radial fracture propagation based on AE hit count rate decrease, decrease in fluid pressure decay rate and plateau of radial deformation

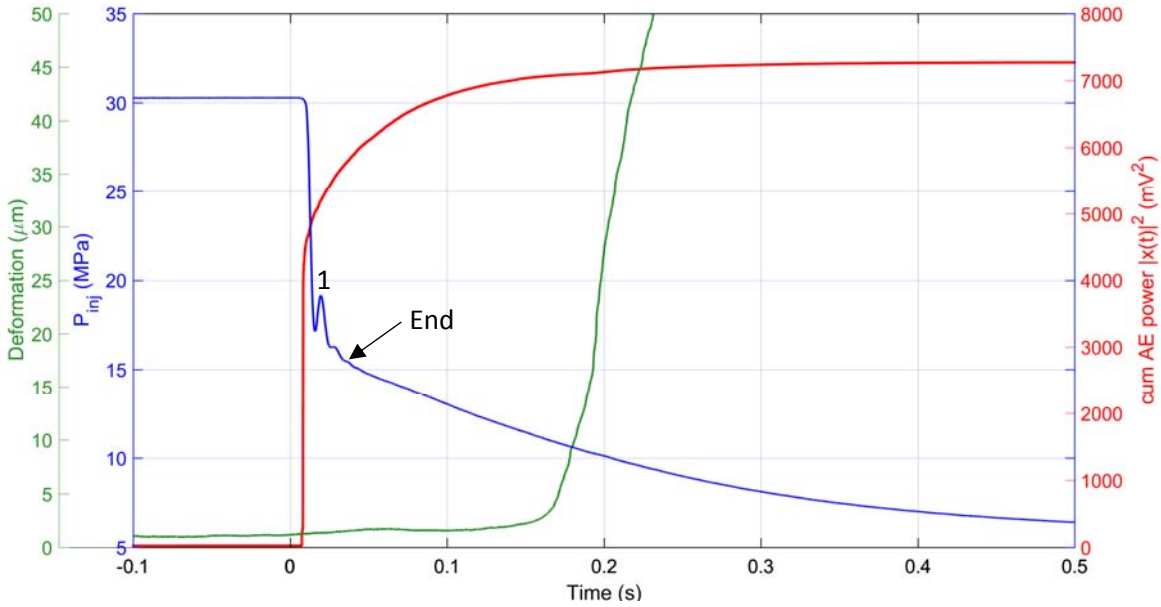

Peak	Effective fluid pressure (MPa)	a_0 (mm)	K_{IC} (MPa.m$^{1/2}$)	Fracture orientation
1	14.6	11.72	2.98	Div

NPSz-15.3-w

- Multiple fractures
- End of radial fracture propagation based on AE hit count rate decrease, decrease in fluid pressure decay rate and plateau of radial deformation

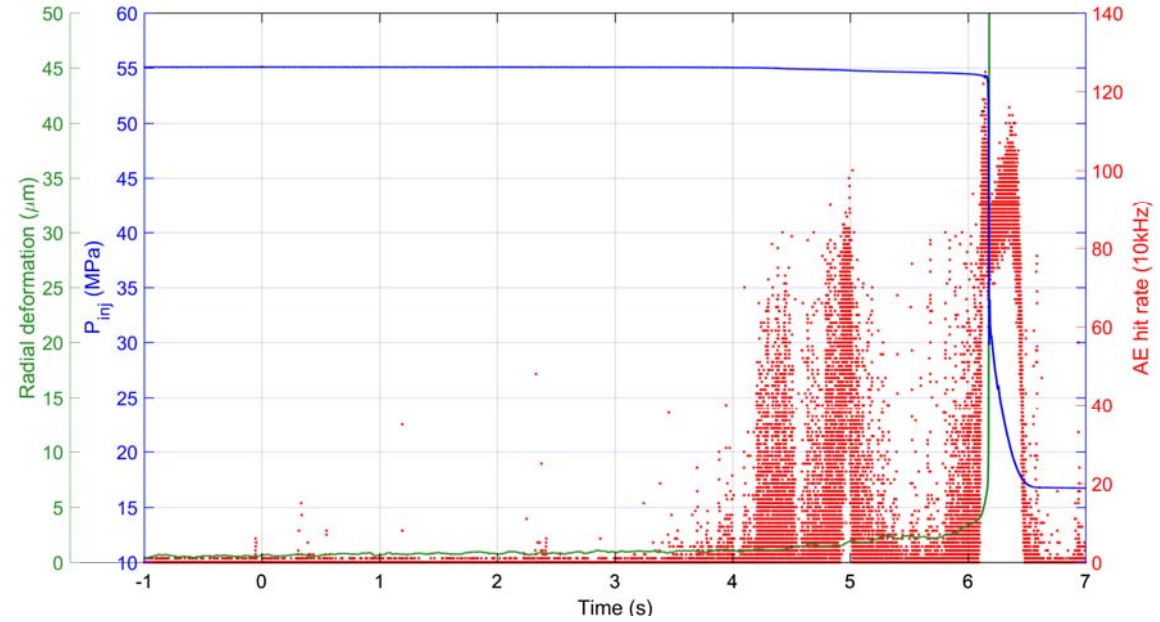

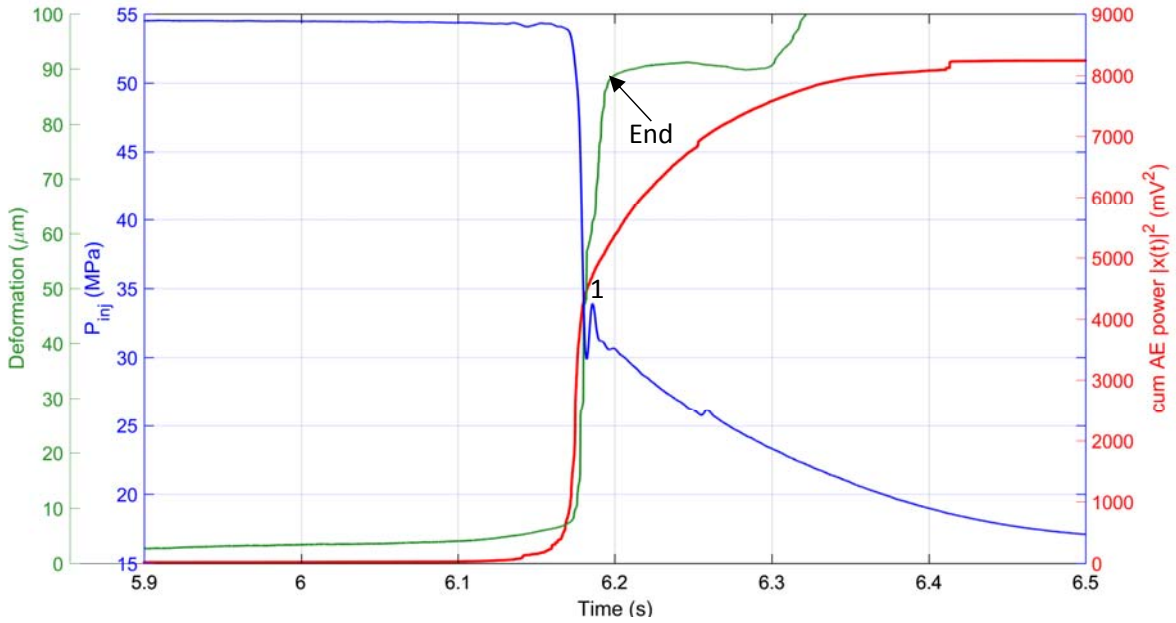

Peak	Effective fluid pressure (MPa)	a_0 (mm)	K_{IC} (MPa.m$^{1/2}$)	Fracture orientation
1	18.6	12.22	3.86	Div

NPSz-20.4-w

- Single fracture
- End of radial fracture propagation based on AE hit count rate decrease, decrease in fluid pressure decay rate and plateau of radial deformation

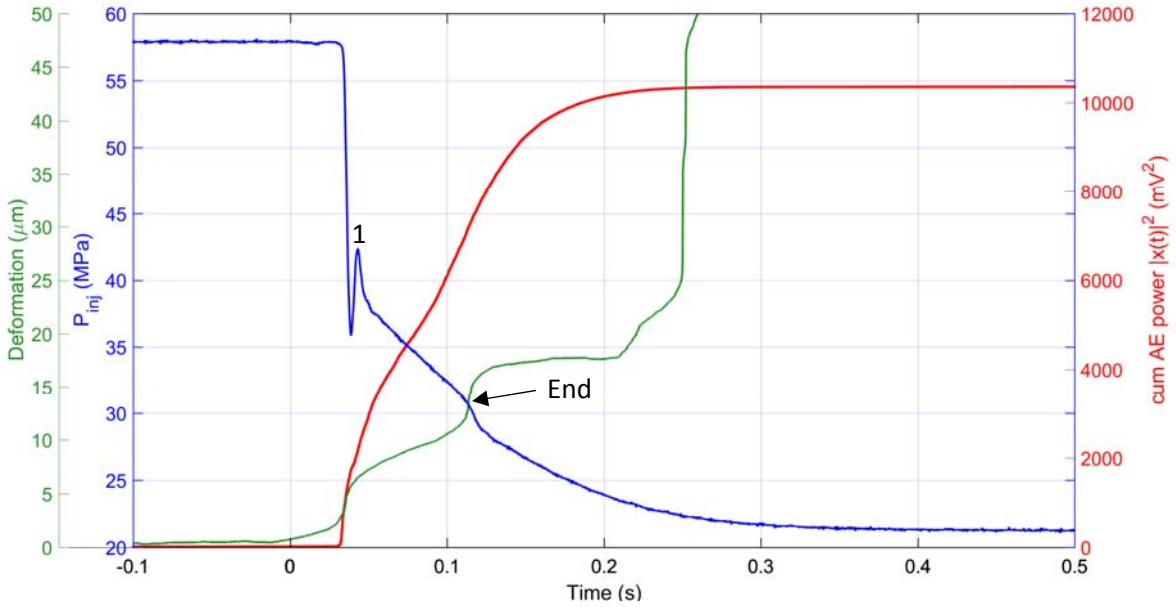

Peak	Effective fluid pressure (MPa)	a_0 (mm)	K_{IC} (MPa.m$^{1/2}$)	Fracture orientation
1	22	7.27	4.05	Div

Appendix A.10 - Certificate of Ethics Review

FORM UPR16

Research Ethics Review Checklist

Please include this completed form as an appendix to your thesis (see the Research Degrees Operational Handbook for more information

UNIVERSITY OF PORTSMOUTH

Postgraduate Research Student (PGRS) Information				**Student ID:**	472996
PGRS Name:	Stephan Gehne				
Department:	SEES	**First Supervisor:**	Dr Philip Benson		
Start Date: (or progression date for Prof Doc students)	**01.09.2014**				
Study Mode and Route:	Part-time ☐	MPhil ☐	MD ☐		
	Full-time ☒	PhD ☐	Professional Doctorate ☐		

Title of Thesis:	A laboratory study of fluid-driven tensile fracturing in anisotropic rocks
Thesis Word Count: (excluding ancillary data)	64055

If you are unsure about any of the following, please contact the local representative on your Faculty Ethics Committee for advice. Please note that it is your responsibility to follow the University's Ethics Policy and any relevant University, academic or professional guidelines in the conduct of your study

Although the Ethics Committee may have given your study a favourable opinion, the final responsibility for the ethical conduct of this work lies with the researcher(s).

UKRIO Finished Research Checklist: (If you would like to know more about the checklist, please see your Faculty or Departmental Ethics Committee rep or see the online version of the full checklist at: http://www.ukrio.org/what-we-do/code-of-practice-for-research/)	
a) Have all of your research and findings been reported accurately, honestly and within a reasonable time frame?	YES ☒ NO ☐
b) Have all contributions to knowledge been acknowledged?	YES ☒ NO ☐
c) Have you complied with all agreements relating to intellectual property, publication and authorship?	YES ☒ NO ☐
d) Has your research data been retained in a secure and accessible form and will it remain so for the required duration?	YES ☒ NO ☐
e) Does your research comply with all legal, ethical, and contractual requirements?	YES ☒ NO ☐

Candidate Statement:	
I have considered the ethical dimensions of the above named research project, and have successfully obtained the necessary ethical approval(s)	
Ethical review number(s) from Faculty Ethics Committee (or from NRES/SCREC):	534816
If you have *not* submitted your work for ethical review, and/or you have answered 'No' to one or more of questions a) to e), please explain below why this is so:	
Signed *(PGRS)*: 	**Date:** 25/07/2018

Certificate of Ethics Review

Project Title:	Seismo-mechanical response of anisotropic rocks under simulated hydraulic fracture conditions: new experimental insights.
User ID:	534816
Name:	Stephan Gehne
Application Date:	02/05/2018 12:45:46

You must download your certificate, print a copy and keep it as a record of this review.

It is your responsibility to adhere to the University Ethics Policy and any Department/School or professional guidelines in the conduct of your study including relevant guidelines regarding health and safety of researchers and University Health and Safety Policy.

It is also your responsibility to follow University guidance on Data Protection Policy:

- General guidance for all data protection issues
- University Data Protection Policy

You are reminded that as a University of Portsmouth Researcher you are bound by the UKRIO Code of Practice for Research; any breach of this code could lead to action being taken following the University's Procedure for the Investigation of Allegations of Misconduct in Research.

Any changes in the answers to the questions reflecting the design, management or conduct of the research over the course of the project must be notified to the Faculty Ethics Committee. Any changes that affect the answers given in the questionnaire, not reported to the Faculty Ethics Committee, will invalidate this certificate.

This ethical review should not be used to infer any comment on the academic merits or methodology of the project. If you have not already done so, you are advised to develop a clear protocol/proposal and ensure that it is independently reviewed by peers or others of appropriate standing. A favourable ethical opinion should not be perceived as permission to proceed with the research; there might be other matters of governance which require further consideration including the agreement of any organisation hosting the research.

GovernanceChecklist
A1-BriefDescriptionOfProject: The project investigates the dependence and fracture mechanics behaviour of the fluid driven mechanical fracture process to assess the competition between permeability and overpressure upon the derived fracture pattern. In addition, new data is being generated to test the link between the measured seismicity and the accuracy of the rupture pattern with the aim of calculating the permeability of the fracture network remotely.
A2-Faculty: Science

A3-VoluntarilyReferToFEC: No
A5-AlreadyExternallyReviewed: No
B1-HumanParticipants: No
HumanParticipantsDefinition
B2-HumanParticipantsConfirmation: Yes
C6-SafetyRisksBeyondAssessment: No
D2-PhysicalEcologicalDamage: No
D4-HistoricalOrCulturalDamage: No
E1-ContentiousOrIllegal: No
E2-SociallySensitiveIssues: No
F1-InvolvesAnimals: No
F2-HarmfulToThirdParties: No
G1-ConfirmReadEthicsPolicy: Confirmed
G2-ConfirmReadUKRIOCodeOfPractice: Confirmed
G3-ConfirmReadConcordatToSupportResearchIntegrity: Confirmed
G4-ConfirmedCorrectInformation: Confirmed